# Biological Targeting of Inflammation in Atherosclerosis using Iron Oxide Particles and MRI

**Joyce Man Sum Chan**

Department of Vascular Surgery, St Mary's Hospital

Imperial College Healthcare NHS Trust

Imperial College London

Feb 2014

**Supervisors:**

Mr Richard G. J. Gibbs MD, FRCS

Professor Claudia Monaco MD, PhD, FESC

Professor Kishore Bhakoo PhD

A thesis submitted for the degree of

Doctor of Philosophy at Imperial College London

# ABSTRACT

Atherosclerosis is now widely viewed as an inflammatory disease. Intraplaque inflammation drives the progression and destabilisation of atherosclerotic lesions, converting chronic stable asymptomatic lesions into acute lesions with ensuing clinical sequelae, including acute coronary syndrome, transient ischaemic attack or stroke. There is currently no clinical imaging technique available to assess the degree of inflammation associated with plaques. The purpose of this work is to develop and utilise novel *in vivo* magnetic resonance imaging (MRI) methodologies to assess inflammation in atherosclerotic plaques. This thesis describes the development of antibody-conjugated iron oxide particles targeted against endothelial adhesion molecules in order to act as a contrast agent for MRI of inflammation in atherosclerosis. This study aims at visualising and characterising atherosclerosis using targeted iron oxide particles as an MRI probe for detecting inflamed plaque disease in both human atherosclerotic tissue and an apolipoprotein E-deficient (ApoE-/-) mouse model.

This study is comprised of four main experimental stages. The initial *in vitro* feasibility study confirmed MRI detection of activated endothelial cells using anti-E-selectin antibody and anti-VCAM-1 antibody conjugated superparamagnetic iron oxide particles (SPIO). Subsequent *ex vivo* studies demonstrated MRI detection and characterisation of inflammatory markers on human atherosclerotic plaques using anti-VCAM-1 antibody and anti-E-selectin antibody conjugated SPIO with confirmatory immunohistochemistry. Further,

the *ex vivo in situ* stage consisted of MRI detection of atherosclerotic lesions in the aortic root of ApoE-/- mice using a new improvised version of iron oxide particles – the dual antibody-conjugated microparticles of iron oxide (MPIO) against VCAM-1 and P-selectin. The final *in vivo* stage involved detection and characterisation of atherosclerotic lesions in the aortic root and aortic arch of ApoE-/- mice by *in vivo* MRI using the dual-targeted MPIO. Following this, an animal model (ApoE-/- mouse) with focal atherosclerotic lesions in carotid arteries was developed by means of peri-arterial cuff placement to allow *in vivo* molecular MRI using these probes.

The *in vitro* cellular model of endothelial inflammation demonstrated stimulated bovine aortic endothelial cells were detectable on MRI using targeted SPIO as a contrast agent, confirmed by immunocytochemistry. Inflammation of human atherosclerotic plaques was similarly detectable by *ex vivo* MRI. Further, we have demonstrated that the MR contrast effect induced by endothelial-bound dual-ligand MPIO quantitatively tracked with macrophage content within the aortic root lesions of ApoE-/- mice by *in vivo* MRI. In the final *in vivo* mouse carotid stage, we have utilised the shear stress modifying cuff to generate both stable and rupture-prone lesions in the murine carotid artery. Using dual-targeted MPIO, we have subsequently identified these high-risk inflamed carotid plaque lesions by *in vivo* MRA. The *in vivo* MRI combined with dual-targeted MPIO approach will potentially allow real time *in vivo* characterisation of plaque vulnerability, leading to accurate risk stratification in individual patients, thereby contributing a personalised approach to the management of carotid atherosclerotic disease in the future.

# CONTENTS

ABSTRACT ..... 2

CONTENTS ..... 4

LIST OF FIGURES ..... 11

LIST OF TABLES ..... 14

ABBREVIATIONS ..... 15

COPYRIGHT ..... 18

STATEMENT OF ORIGINALITY ..... 19

AWARDS AND GRANTS ..... 20

LIST OF PRESENTATIONS ..... 22

Presentations: International Level ..... 22

Presentations: National Level ..... 25

ACKNOWLEDGEMENTS ..... 27

**CHAPTER 1: INTRODUCTION ..... 29**

1.1 ATHEROSCLEROSIS ..... 30

1.1.1 Endothelial Dysfunction ..... 31

1.1.2 Initiation of Inflammation and Atherosclerosis ..... 32

1.1.3 Progression of Atherosclerosis ..... 32

1.1.4 Fate of the Vulnerable Plaque ..... 33

1.2 THE CLINICAL NEED FOR NEW ADJUNCTIVE IMAGING STRATEGIES 35

1.2.1 Identifying the 'High-risk' Patients ..... 35

1.2.2 Limitations of Current Conventional Clinical Imaging Tools ..... 37

1.3 NEW ADJUNCTIVE IMAGING STRATEGIES ..... 39

1.3.1 Ultrasound ..... 39

1.3.1.1 Plaque morphology ..... 39

1.3.1.2 Detection of emboli ..... 40
1.3.1.3 Contrast-enhanced ultrasound ..... 41
1.3.2 Computed Tomography ..... 42
1.3.3 Hybrid Imaging Systems ..... 42
1.3.4 High Resolution MRI ..... 44
1.3.4.1 Plaque morphology ..... 44
1.3.4.2 Flow and Stress ..... 45
1.4 MOLECULAR MRI ..... 47
1.4.1 Gadolinium based Contrast Agents ..... 48
1.4.2 Iron Oxide based Contrast Agents ..... 49
1.4.2.1 USPIO ..... 51
1.4.2.2 SPIO ..... 51
1.4.2.3 MPIO ..... 52
1.5 TARGETED MPIO ..... 54
1.6 ENDOTHELIAL ADHESION MOLECULES: POTENTIAL TARGETS FOR IMAGING WITH MPIO ..... 55
1.6.1 E-selectin ..... 56
1.6.2 P-selectin ..... 56
1.6.3 VCAM-1 ..... 57
1.7 PURPOSE AND HYPOTHESIS ..... 59
1.8 OBJECTIVES SUMMARY ..... 61
*In vitro* stage ..... 61
*Ex vivo* stage ..... 61
*Ex vivo in situ* stage ..... 62
*In vivo* stage (mouse aortic root and aortic arch) ..... 62
*In vivo* stage (mouse carotid artery) ..... 62
**CHAPTER 2: *IN VITRO* ENDOTHELIAL CELL STAGE ..... 64**
2.1 INTRODUCTION ..... 65

2.2 MATERIALS AND METHODS ..... 66
2.2.1 Induction of Inflammation on Endothelial Cells by TNFα ..... 66
2.2.2 Detection and Characterisation of Inflammatory Markers on Endothelial Cells by Immunocytochemistry ..... 66
2.2.3 Detection, Characterisation and Imaging of Inflammatory Markers on Endothelial Cells by Biotinylated Antibody-Conjugated Streptavidin Microbeads ..... 67
2.2.4 Activated Endothelial Cells Labelled with Biotinylated Anti-E-selectin and Anti-VCAM-1 Antibody ..... 68
2.2.5 Activated Endothelial Cells Labelled with Streptavidin Microbeads ..... 69
2.2.6 Cell Phantom MRI ..... 70
2.3 RESULTS ..... 71
2.3.1 Immunocytochemistry of bAEC ..... 71
2.3.2 MRI of Cell Phantom ..... 73
2.4 DISCUSSION ..... 76
2.5 CONCLUSION ..... 77

**CHAPTER 3: *EX VIVO* HUMAN CAROTID PLAQUE STAGE ..... 78**

3.1 INTRODUCTION ..... 79
3.2 MATERIALS AND METHODS ..... 80
3.2.1 Study Population ..... 80
3.2.2 Tissue Collection ..... 81
3.2.3 Detection, Characterisation and Imaging of Inflammatory Markers on Human Carotid Plaques by Biotinylated Antibody-Conjugated Streptavidin Microbeads ..... 83
3.2.4 *Ex Vivo* MRI of Human Carotid Plaques ..... 84
3.2.4.1 Quantitative MR image analysis ..... 86
3.2.5 Immunohistochemistry ..... 87
3.2.5.1 Fixation and paraffin embedding of tissue ..... 87
3.2.5.2 Preparation of paraffin sections for immunohistochemistry ..... 88
3.2.5.3 Immunohistochemical staining of paraffin embedded tissues ..... 89

3.2.5.4 Microscopy and quantification of immunostaining .....93
3.2.6 Statistical Methods ..... 95
3.3 RESULTS ..... 96
3.3.1 Baseline Demographics ..... 96
3.3.2 Immunohistochemistry ..... 97
3.3.3 Intra-observer and Inter-observer Variability in Quantification of SPIO-induced Contrast Effect ..... 97
3.3.4 Relationship between Mean Macrophage Content and Mean 1/ $T_2$ of Whole Plaque ..... 102
3.3.5 Relationship between Expression of Histological Markers (VCAM-1, E-selectin, CD68 and Perls' iron stain) and 1/ $T_2$ .....105
3.3.6 Synergistic Relationship of E-selectin and VCAM-1 Expression on 1/$T_2$ ..... 106
3.4 DISCUSSION ..... 108
Limitations and future work ..... 110
3.5 CONCLUSION..... 112
**CHAPTER 4: *EX VIVO IN SITU* APOE-/- MOUSE MODEL STAGE ..... 113**
4.1 INTRODUCTION ..... 114
ApoE-/- mice as atherosclerotic model ..... 115
4.2 MATERIALS AND METHODS ..... 118
4.2.1 Dual Antibody Conjugation to MPIO ..... 118
4.2.2 *In Vivo* Systemic Administration of Dual-Targeted MPIO ..... 119
4.2.3 Vascular Perfusion Fixation of ApoE-/- Mice ..... 120
4.2.4 Ex Vivo In Situ MRI ..... 121
4.3 RESULTS ..... 123
*In Vivo* Dual-Targeted MPIO Binding to Atherosclerosis and *Ex Vivo In Situ* MRI ... 123
4.4 DISCUSSION ..... 125
4.5 CONCLUSION..... 129

**CHAPTER 5: *IN VIVO* APOE-/- MOUSE MODEL STAGE: AORTIC ROOT AND AORTIC ARCH ..... 130**

5.1 INTRODUCTION ..... 131

5.2 MATERIALS AND METHODS ..... 133

5.2.1 *In Vivo* MRI of Aortic Root and Aortic Arch ..... 133

5.2.2 Analysis of MR Imaging of the Aortic Root ..... 136

5.2.2.1 Qualitative MR Image Analysis ..... 136

5.2.2.2 Quantitative MR Image Analysis ..... 138

5.2.3 Histological Staining of Aortic Root and Aortic Arch ..... 139

5.2.3.1 CD31 ..... 140

5.2.3.2 VCAM-1 ..... 142

5.2.3.3 Mac-3 ..... 144

5.2.3.4 αSMA ..... 146

5.2.4 Analysis Of Histological Staining Of Aortic Root ..... 148

5.2.4.1 Qualitative Histological Image Analysis ..... 148

5.2.4.2 Quantitative Histological Image Analysis ..... 149

5.2.5 Statistical Analysis ..... 150

5.2.5.1 Qualitative Analysis of MR Image and Histological Staining of the Aortic Root ..... 150

5.2.5.2 Quantitative Analysis of MR Image of the Aortic Root ..... 150

5.2.5.3 Comparative Analyses between MR Image and Histology ..... 151

5.2.5.4 Quantitative Analysis of Histology of the Aortic Root ..... 152

5.3 RESULTS ..... 153

5.3.1 Qualitative Analysis of MR Image and Histological Staining of the Aortic Root 153

5.3.1.1 Detection of MPIO-Induced Signal Effect in the Aortic Root ..... 153

5.3.1.2 Agreement between Location of MR Signal Loss and Location of MPIO-labeled Cells ..... 156

5.3.1.3 Intra-observer and Inter-observer Agreement on MR Signal Loss ... 157

5.3.1.4 Intra-observer and Inter-observer Agreement on the Presence of Perls' Stain ..... 159
5.3.1.5 Intra-observer and Inter-observer Agreement on the Presence of Advanced Atherosclerotic Disease ..... 160
5.3.2 Quantitative Analysis of MR Images and Histology of the Aortic Root ..... 161
5.3.2.1 Quantification of MPIO-Induced Signal Effect in Aortic Root ..... 161
5.3.2.2 Comparative Analyses Between MR and Histology ..... 167
5.3.3 Histological Analysis Of the Aortic Root ..... 169
5.3.3.1 Qualitative Histological Image Analysis ..... 169
5.3.3.2 Quantitative Histological Image Analysis ..... 174
5.3.4 *In Vivo* MRI of Aortic Arch ..... 176
5.4 DISCUSSION ..... 180
5.4.1 *In Vivo* Imaging of Atherosclerosis in Mice Using Dual-Targeted MPIO ..... 181
5.4.2 Dual-targeted MPIO Selectively Bind to Atherosclerosis-Susceptible Sites ..... 185
5.4.3 Dual-Targeted MPIO Bind to Activated Endothelial Cells Overlying Atherosclerotic Lesions ..... 186
5.4.4 Dual-targeted MPIO induced MR Contrast Effect Tracks Quantitatively with Lesion Macrophage Burden ..... 188
5.4.5 Statistics ..... 192
5.4.6 Limitations ..... 193
5.5 CONCLUSIONS ..... 195
**CHAPTER 6: *IN VIVO* APOE-/- MOUSE MODEL STAGE: CAROTID ARTERY ..... 196**
6.1 INTRODUCTION ..... 197
6.2 MATERIALS AND METHODS ..... 200
6.2.1 The Shear Stress Modifying Cuff ..... 200
6.2.2 Implantation of Carotid Cuff ..... 202
6.2.3 *In Vivo* MRI ..... 205

6.2.4 Explantation of Carotid Cuff and Carotid Arteries ..... 206
6.2.5 Histological Staining of Carotid Arteries ..... 207
6.2.5.1 Picrosirius Red ..... 208
6.3 RESULTS ..... 209
6.3.1 *In Vivo* Detection of Vulnerable Plaque Lesions in Mouse Carotid Arteries using Dual-Targeted MPIO ..... 209
6.3.2 Histological Analysis ..... 214
6.3.2.1 Low Shear Stress and Oscillatory Shear Stress Both Induce Atherosclerotic Plaque Formation, Whereas High Shear Stress Protects Against Atherosclerosis ..... 214
6.3.2.2 Low Shear Stress Induces Formation of Lesions With Vulnerable Plaque Phenotype, Whereas Oscillatory Shear Stress Induces Development of Stable Lesions ..... 215
6.3.2.3 Dual-targeted MPIO Selectively Bind to Lesions With Vulnerable Plaque Phenotype but Not to Stable Lesions ..... 216
6.3.2.4 Dual-targeted MPIO Selectively Bind to Endothelium Overlying Lesions With Vulnerable Plaque Phenotype ..... 221
6.4 DISCUSSION ..... 230
6.5 CONCLUSIONS ..... 242
**CHAPTER 7: CONCLUSION ..... 244**
7.1 CONCLUSION ..... 245
7.2 LIMITATIONS ..... 248
7.3 FUTURE WORK ..... 250
**REFERENCES ..... 253**
**APPENDIX A ..... 280**
**APPENDIX B ..... 295**

# LIST OF FIGURES


| | | |
|---|---|---|
| 2.1 | Experimental design of *in vitro* endothelial cells stage | 67 |
| 2.2 | Experimental design of *in vitro* endothelial cell stage | 68 |
| 2.3 | Immunocytochemistry for VCAM-1 and E-selectin on quiescent control bAEC and activated bAEC | 72 |
| 2.4 | The transaxial view of MR image of cell phantom | 74 |
| 2.5 | Signal-to-noise ratio of cell phantom MRI | 75 |
| 3.1 | Carotid endarterectomy specimen | 82 |
| 3.2 | Carotid endarterectomy specimen cut into sections | 82 |
| 3.3 | Experimental design of *ex vivo* human plaque stage | 84 |
| 3.4 | Human carotid plaque sections embedded in agarose block | 85 |
| 3.5 | Representative images of human atherosclerotic plaque sections of positive and negative antibody control for CD31, VCAM-1, E-selectin and CD68 staining | 91 |
| 3.6 | Objective quantification of immunostaining | 94 |
| 3.7 | Representative histology images of human carotid plaque and control femoral artery | 98 |
| 3.8 | The Bland-Altman plot for intra-observer variability | 100 |
| 3.9 | The Bland-Altman plot for inter-observer variability | 101 |
| 3.10 | Spectrum of MR images and histological images of phenotypically symptomatic plaques, asymptomatic plaques and control femoral artery | 104 |
| 3.11 | The relationship between intraplaque inflammation and MR contrast effect | 105 |
| 4.1 | Experimental design of *ex vivo in situ* ApoE-/- mouse model stage | 119 |
| 4.2 | *Ex vivo in situ* MRI of aortic root at 30 minutes post-injection | 124 |

of either dual-targeted MPIO or negative control IgG-MPIO
5.1 Experimental design of in vivo ApoE-/- mouse model stage 134
5.2 Experimental design of *in vivo* ApoE-/- mouse model stage 135
5.3 MR image analysis 137
5.4 Quantitative MR image analysis 138
5.5 Histological cross-sections of the aortic root showing three levels of cutting of the aortic valve 140
5.6 Representative images of mouse artery sections of positive and negative antibody control for CD31 staining 142
5.7 Representative images of mouse artery sections of positive and negative antibody control for VCAM-1 staining 144
5.8 Representative images of mouse artery sections of positive and negative antibody control for Mac-3 staining 146
5.9 Representative images of mouse artery sections of positive and negative antibody control for αSMA staining 147
5.10 Representative MR and histological images of the aortic root. 155
5.11 Bar chart comparing detection of hypointensity signal effect in the aortic root between dual-targeted MPIO group and control IgG-MPIO group 156
5.12 The profile plot of pre-contrast and post-contrast SNR comparison in dual-targeted MPIO group and control IgG-MPIO group 163
5.13 The Bland-Altman plot for intra-observer variability 165
5.14 The Bland-Altman plot for inter-observer variability 166
5.15 Representative serial histological images of aortic root 171
5.16 Representative serial histological images of aortic root in the dual-targeted MPIO group and control IgG-MPIO group 173
5.17 Representative serial histological images of aortic root atherosclerotic lesion of positive and negative antibody control for CD31 and VCAM-1 staining 174

| | | |
|---|---|---|
| 5.18 | Representative MR and histological images of aortic arch | 178 |
| 5.19 | Representative MR images of aortic arch | 179 |
| 6.1 | The shear stress modifying cuff around the common carotid artery | 201 |
| 6.2 | Regions of different flow dynamics and shear stress | 201 |
| 6.3 | Experimental design of *in vivo* ApoE-/- mouse model stage | 204 |
| 6.4 | Surgical implantation of shear stress modifier cuff around the right common carotid artery | 205 |
| 6.5 | Representative images of *in vivo* MRA of carotid arteries in dual-targeted MPIO group | 211 |
| 6.6 | Representative images of *in vivo* MRA of carotid arteries in control IgG-MPIO group | 213 |
| 6.7 | Representative histological images of carotid arteries of ApoE double knockout mouse in dual-targeted group under high fat diet 9 weeks after implantation of cuff | 218 |
| 6.8 | Representative histological images of carotid arteries of ApoE double knockout mouse in control IgG-MPIO group under high fat diet 9 weeks after implantation of cuff | 220 |
| 6.9 | Representative histological images at higher magnification of carotid arteries of ApoE double knockout mouse in dual-targeted group 9 weeks after implantation of cuff | 222 |
| 6.10 | Representative histological images at higher magnification of carotid arteries of ApoE double knockout mouse in dual-targeted group 9 weeks after implantation of cuff | 225 |
| 6.11 | Representative histological images at higher magnification of carotid arteries of ApoE double knockout mouse in control IgG-MPIO group 9 weeks after implantation of cuff | 228 |

# LIST OF TABLES


| | | |
|---|---|---|
| 3.1 | Primary antibodies used in immunohistochemical staining of paraffin embedded human carotid plaque sections | 92 |
| 3.2 | Patient clinical characteristics | 96 |
| 4.1 | Lesion stage and time frame for development in both ApoE-/- and LDLR-/- Mice | 116 |
| 5.1 | Kappa Coefficient Estimates of Location of MR Signal Effect and Location of Iron-Positive Cells on Histology | 157 |
| 5.2 | Kappa Coefficient Estimates of intra-observer agreement on signal loss in each combination of slices and quadrants of MR images | 158 |
| 5.3 | Kappa Coefficient Estimates of inter-observer agreement on signal loss in each combination of slices and quadrants of MR images | 158 |
| 5.4 | Kappa Coefficient Estimates of intra-observer agreement on the presence of Perls' stain in each combination of slices and quadrants of histological images | 159 |
| 5.5 | Kappa Coefficient Estimates of inter-observer agreement on the presence of Perls' stain in each combination of slices and quadrants of histological images | 160 |
| 5.6 | Kappa Coefficient Estimates of intra-observer agreement on the presence of atherosclerotic disease in each combination of slices and quadrants of histological images | 160 |
| 5.7 | Kappa Coefficient Estimates of inter-observer agreement on the presence of atherosclerotic disease in each combination of slices and quadrants of histological images | 161 |

# ABBREVIATIONS

| | |
|---|---|
| αSMA | α Smooth Muscle Actin |
| ABC | Avidin-Biotin-Complex |
| ACAS | Asymptomatic Carotid Artery Stenosis |
| ACES | Asymptomatic Carotid Emboli Study |
| ACSRS | Asymptomatic Carotid Stenosis and Risk of Stroke |
| ACST | Asymptomatic Carotid Surgery Trial |
| AHA | American Heart Association |
| ANOVA | Analysis Of Variance |
| ApoE | Apolipoprotein E |
| ApoE-/- mice | Apolipoprotein E-deficient mice |
| bAEC | Bovine Aortic Endothelial Cells |
| CAS | Carotid Artery Stenting |
| CD62E | E-selectin |
| CD62P | P-selectin |
| CEA | Carotid Endarterectomy |
| CEUS | Contrast-Enhanced Ultrasound |
| CT | Computed Tomography |
| CTA | Computed Tomography Angiography |
| CVD | Cardiovascular Diseases |
| DAB | 3,3'-Diaminobenzidine |
| DCE-MRI | Dynamic Contrast-Enhanced MRI |
| ECST | European Carotid Surgery Trial |
| EDTA | Ethylenediaminetetraacetic Acid |
| Fab | Antibody Fragments |
| FDA | Food and Drug Administration |
| FDG | 18F-fluorodeoxyglucose |
| FLASH | Fast Low Angle Shot |
| FOV | Field Of View |
| Gd-DTPA | Gadolinium Diethylene-Triamine-Pentaacetic Acid |
| GEE | Generalised Estimating Equations |

| | |
|---|---|
| GLM | General Linear Model |
| GSM | Gray-Scale Median |
| H&E | Haematoxylin and Eosin |
| HDL | High Density Lipoprotein |
| ICA | Internal Carotid Artery |
| ICAM-1 | Intercellular Adhesion Molecule-1 |
| IgG | Immunoglobulin G |
| IL | Interleukin |
| IPH | Intraplaque Haemorrhage |
| JBA | Juxta-luminal Black Area |
| LDL | Low-Density Lipoproteins |
| LDLR | LDL Receptor |
| LDLR-/-mice | Low-Density Lipoprotein Receptor-Deficient mice |
| LP-CEUS | Late-Phase Contrast-Enhanced Ultrasound |
| LRNC | Lipid-Rich Necrotic Core |
| MMP | Matrix Metalloproteinase |
| MPIO | Microparticles of Iron Oxide |
| MRA | Magnetic Resonance Angiography |
| MRI | Magnetic Resonance Imaging |
| NASCET | North American Symptomatic Carotid Endarterectomy Trial |
| NBF | Neutral Buffered Formalin |
| NF-κB | Nuclear Factor-kappa B |
| NO | Nitric Oxide |
| PBS | Phosphate Buffered Saline |
| PET | Positron Emission Tomography |
| PFA | Paraformaldehyde |
| PLGA | Poly(Lactide-co-Glycolide) |
| PSGL-1 | P-Selectin Glycoprotein Ligand-1 |
| RES | Reticulo-Endothelial System |
| ROI | Region Of Interest |
| ROS | Reactive Oxygen Species |
| SAS | Statistical Analysis System |

| | |
|---|---|
| SD | Standard Deviation |
| SMC | Smooth Muscle Cells |
| S/N | Signal-to-Noise Ratio |
| SPECT | Single Photon Emission Computed Tomography |
| SPIO | Superparamagnetic Particles of Iron Oxide |
| TCD | Transcranial Doppler |
| TE | Echo Time |
| TIA | Transient Ischaemic Attack |
| TNFα | Tumour Necrosis Factor-α |
| TOF | Time Of Flight |
| TR | Repetition Time |
| UK | United Kingdom |
| USPIO | Ultrasmall Superparamagnetic Particle of Iron Oxide |
| VCAM-1 | Vascular Cell Adhesion Molecule-1 |
| VLA-4 | Very Late Antigen |
| VLDL | Very Low Density Lipoprotein |

# COPYRIGHT

The copyright of this thesis rests with the author and is made available under a Creative Commons Attribution-Non Commercial-No Derivatives license. Researchers are free to copy, distribute or transmit the thesis on the condition that they attribute it, that they do not use it for commercial purposes and that they do not alter, transform or build upon it. For any reuse or distribution, researchers must make clear to others the license terms of this work.

# STATEMENT OF ORIGINALITY

I hereby declare that this submission is my own work and to the best of my knowledge it contains no materials previously published or written by another person, except where due acknowledgement is made in the thesis. I also declare that the intellectual content of this thesis is the product of my own work and that all the assistance received in preparing this thesis and sources have been acknowledged.

# AWARDS AND GRANTS

A list of awards and grants that have been received based on the material in this thesis are provided below:

| | | |
|---|---|---|
| Jan 2012 | **WOLFE VASCULAR TRUSTEES' FUND**<br>Imperial College Healthcare NHS Trust,<br>London, U.K. | **£10,000** |
| Feb 2012 | **IMPERIAL COLLEGE ENGINEERING AND MEDICINE RESEARCH COLLABORATION KICK-START GRANT**<br>Imperial College London, U.K. | **£20,000** |
| Oct 2011 | **THE ASIAN SOCIETY FOR VASCULAR SURGERY FIRST PRIZE AWARD FOR THE BEST SCIENTIFIC PAPER**<br>The 12th Annual Congress Of Asian Society<br>For Vascular Surgery, Taipei, Taiwan | **US$1,000** |
| Nov 2011 | **THE BRITISH JOURNAL OF SURGERY PRIZE FOR THE BEST SCIENTIFIC PAPER**<br>The Vascular Society of Great Britain and<br>Ireland Conference, Brighton, U.K. | **£600** |
| Sep 2011 | **EUROPEAN SOCIETY FOR VASCULAR SURGERY TRAVEL GRANT**<br>The European Society for Vascular Surgery,<br>Copenhagen, Denmark | **€1,000** |

| | | |
|---|---|---|
| Oct 2010 | **EUROPEAN SOCIETY FOR VASCULAR SURGERY RESEARCH GRANT**<br>The European Society for Vascular Surgery, Copenhagen, Denmark | **€19,821** |
| Jul 2010 | **FIRST RUNNER-UP POSTER COMPETITION**<br>The Fourth Symposium of Cardiovascular Technology Network Symposium, Imperial College, London, U.K. | **£75** |
| Oct 2009 | **THE ASIAN SOCIETY FOR VASCULAR SURGERY TRAVEL AWARD**<br>10th Annual Congress of Asian Society for Vascular Surgery, Busan, Korea | **US$500** |
| Mar 2009 | **BRITISH ATHEROSCLEROSIS SOCIETY & BRITISH SOCIETY FOR CARDIOVASCULAR RESEARCH TRAVEL GRANT**<br>Joint Spring Meeting Of British Atherosclerosis Society And British Society For Cardiovascular Research, Oxford, U.K. | **£100** |
| Aug 2009 | **PUMP PRIMING RESEARCH GRANT**<br>The Royal College Of Surgeons Of England, London, U.K. | **£8,500** |

# LIST OF PRESENTATIONS

A list of presentations that have been delivered based on the material in this thesis are provided below:

## Presentations: International Level

| | |
|---|---|
| 12-16 Oct 2011 | **ENDOVASCOLOGY INTERNATIONAL CONGRESS, SHANGHAI, CHINA**<br>Oral presentation: *"Imaging of the vulnerable carotid plaque: Biological targeting of inflammation using superparamagnetic particles of iron oxide (SPIO) and MRI"* |
| 29 Sept - 2 Oct 2011 | **THE 12TH ANNUAL CONGRESS OF ASIAN SOCIETY FOR VASCULAR SURGERY (ASVS), TAIPEI, TAIWAN**<br>Awarded **The Asian Society for Vascular Surgery First Prize** for the best scientific paper:<br>Oral presentation: *"Molecular Imaging of the vulnerable carotid plaque"* |
| 22-25 Sep 2011 | **THE 25TH EUROPEAN SOCIETY FOR VASCULAR SURGERY (ESVS), ATHENS, GREECE**<br>Oral presentation: *"Imaging of the vulnerable carotid plaque: Biological targeting of inflammation using superparamagnetic particles of iron oxide (SPIO) and MRI"* |
| 7-10 Sep 2011 | **WORLD MOLECULAR IMAGING CONGRESS (WMIC), SAN DIEGO, U.S.**<br>Poster presentation: *"Imaging of the vulnerable carotid plaque: Biological targeting of inflammation using superparamagnetic particles of iron oxide (SPIO) and MRI"* |

| | |
|---|---|
| 13-16 Oct 2010 | **THE 7TH WORLD STROKE CONGRESS, SEOUL, KOREA**<br>Oral presentation: *"Visualising inflamed atherosclerotic plaques: Molecular imaging using MRI and targeted superparamagnetic particles of iron oxide (SPIO)"* |
| 8-11 Sep 2010 | **WORLD MOLECULAR IMAGING CONGRESS (WMIC), KYOTO, JAPAN**<br>Poster presentation: *"MR imaging of vulnerable carotid plaques: Biological targeting of inflammation using superparamagnetic particles of iron oxide (SPIO)"* |
| 29 Jun - 2 Jul 2010 | **THE 11TH ANNUAL CONGRESS OF ASIAN SOCIETY FOR VASCULAR SURGERY (ASVS), KYOTO, JAPAN**<br>Oral presentation: *"Visualising inflamed atherosclerotic plaques: Molecular imaging using MRI and targeted superparamagnetic particles of iron oxide (SPIO)"* |
| 20 - 24 Jun 2010 | **THE 16TH INTERNATIONAL VASCULAR BIOLOGY MEETING (IVBM), UCLA, LOS ANGELES, U.S.**<br>Oral presentation: *"Visualising inflamed atherosclerotic plaques: Molecular imaging using MRI and targeted superparamagnetic particles of iron oxide (SPIO)"* |
| 14 - 17 Oct 2009 | **THE 10TH ANNUAL CONGRESS OF ASIAN SOCIETY FOR VASCULAR SURGERY (ASVS), BUSAN, KOREA**<br>Oral presentation: *"MRI of endothelial adhesion molecules in carotid atherosclerosis using targeted superparamagnetic particles of iron oxide (SPIO)"* |

| | |
|---|---|
| 10 - 12 Sep 2009 | **ARTERY 9, CAMBRIDGE, U.K.**<br>Oral presentation: *"MRI of endothelial adhesion molecules in carotid atherosclerosis using targeted superparamagnetic particles of iron oxide – Towards an in vivo model"* |
| 14 - 18 Jun 2009 | **XV INTERNATIONAL SYMPOSIUM ON ATHEROSCLEROSIS, BOSTON, U.S.**<br>Poster presentation: *"Visualising inflamed endothelial cells: Molecular imaging using MRI and targeted SPIOs"* |
| 20 - 24 May 2009 | **THE 6TH METABOLIC SYNDROME, TYPE II DIABETES AND ATHEROSCLEROSIS CONGRESS, BERLIN**<br>Poster presentation: *"MRI of carotid atherosclerosis using targeted superparamagnetic particles of iron oxide"* |

## Presentations: National Level

| | |
|---|---|
| 24 - 26 Nov 2010 | **THE VASCULAR SOCIETY OF GREAT BRITAIN AND IRELAND CONFERENCE, BRIGHTON, U.K.**<br>Awarded **The British Journal of Surgery Prize** for the best scientific paper.<br>Oral presentation: *"Imaging of the vulnerable carotid plaque: Biological targeting of inflammation using superparamagnetic particles of iron oxide (SPIO) and MRI"* |
| 9-10 Sep 2010 | **BRITISH ATHEROSCLEROSIS SOCIETY MEETING, OXFORD, U.K.**<br>Poster presentation: *"Visualising inflamed atherosclerotic plaques: Molecular imaging using MRI and targeted SPIO"* |
| 7 - 8 Jun 2010 | **JOINT MEETING OF BRITISH ATHEROSCLEROSIS SOCIETY AND BRITISH SOCIETY FOR CARDIOVASCULAR RESEARCH: NEW FRONTIERS IN CARDIOVASCULAR RESEARCH, MANCHESTER, U.K.**<br>Poster presentation: *"Visualising inflamed atherosclerotic plaques: Molecular imaging using MRI and targeted SPIO"* |
| 2 - 3 Apr 2009 | **JOINT MEETING OF BRITISH ATHEROSCLEROSIS SOCIETY AND BRITISH SOCIETY FOR CARDIOVASCULAR RESEARCH, OXFORD, U.K.**<br>Poster presentation: *"MRI of endothelial adhesion molecules in carotid atherosclerosis using targeted superparamagnetic particles of iron oxide (SPIO)"* |

3 Dec 2008 **SURGICAL SPR PRIZE MEETING (MIA PRIZE), ROYAL SOCIETY OF MEDICINE, LONDON, U.K.**

Oral presentation: *"MRI of endothelial adhesion molecules in carotid atherosclerosis using targeted superparamagnetic particles of iron oxide (SPIO) - Towards an in vivo model"*

# ACKNOWLEDGEMENTS

The work contained within this thesis could not have been realised without the support of those around me. Firstly, I would like to express my sincere gratitude to my supervisors, Mr Richard Gibbs, Professor Claudia Monaco and Professor Kishore Bhakoo, for their invaluable tutelage throughout this research, without which I would not have progressed this far. I am extremely grateful to Mr Gibbs for providing me with the Research Fellow post at the Regional Vascular Unit at St Mary's Hospital and his enormous support throughout my clinical and research career; Professor Monaco for her scientific support particularly in the animal model experiments; Professor Bhakoo for inspiring me to pursue in this research area since the start and his scientific support particularly in the synthesis of iron oxide particles.

I would like to thank the Biological Imaging Centre at Hammersmith Hospital and the Cytokine Biology of Atherosclerosis Group at Kennedy Institute of Rheumatology, which provided not only a scientifically inspiring environment but also a good companionship. More specifically, I would like to thank Dr Marzena Wylezinska-Arridge for her input and expertise with the MRI experiments, Dr Jordi Tremoleda for his help with the *in vivo* experiments, and Mr Michael Goddard and Dr Jennifer Cole for their help with the animal model experiments.

However, much of the work contained within this thesis was inspired by conversations with a variety of people within St Mary's Hospital. Consequently,

I would also like to extend my gratitude to the Regional Vascular Unit at St Mary's Hospital for providing a fantastic, stimulating forum that allowed me to explore the clinical translation issues of this imaging technique.

Of course, none of this would be possible without the financial support of The European Society for Vascular Surgery, The Wolfe Vascular Trustees' Fund and The Royal College of Surgeons of England, which not only supported my research, but also provided the means for me to present results at 12 international conferences across different continents – a truly eye-opening experience. Of particular note, I am indebted to Mr John Wolfe who has believed in this research from the beginning and generously funded the critical stage at the end, without which the final part of the validation experiments would not have been possible.

Finally, I would like to thank my family, uncle Dennis, aunt Lancy, Dennis, Royce and Vils, who have always been there for me and provided encouragement through the difficult times of this adventurous journey. This is as much your work as mine.

# CHAPTER 1:

# Introduction

# 1.1 ATHEROSCLEROSIS

Cardiovascular diseases (CVD) are the leading cause of death and disability worldwide.[1] The total global mortality from CVD was estimated to be 17.3 million in 2008, representing 30% of all deaths. Of these, 7.3 million were attributed to coronary heart disease and 6.2 million to stroke. Furthermore, the World Health Organisation predicts CVD will claim almost 25 million lives by 2030 and will continue to dominate as the single leading cause of mortality worldwide.[1] Atherosclerosis is the major cause of coronary, cerebrovascular, and peripheral arterial diseases.[2]

Atherosclerosis has traditionally been viewed as a pathological lipid deposition within the vessel wall of medium-sized and large arteries.[3] This concept, however, has been redefined by the more complex concept of an ongoing inflammatory response.[3] Current views regard atherosclerosis as a dynamic, progressive disease arising from the combination of endothelial dysfunction and inflammation. It is characterised by a specific series of cellular and molecular events, from early inflammatory lesions ('fatty streaks'), comprised of monocyte-derived macrophages and T lymphocytes, to the development of mature plaque, and eventually rupture and thrombosis.[4]

### 1.1.1 Endothelial Dysfunction

It is suggested that endothelial dysfunction, triggered by factors such as elevated low-density lipoproteins (LDL), free radicals, cigarette toxins and hypertension, leads to a compensatory inflammatory response.[5] Endothelial dysfunction is typified by decreased synthesis of nitric oxide (NO) and an imbalance between endothelium-derived relaxing and contracting factors, such as angiotensin and oxidants, making the vascular endothelium become susceptible to atheroma formation.[6]

As the key endothelium-derived relaxing factor, NO plays an essential role in vasodilatation[7] and protection against vascular injury, inflammation and thrombosis.[8] However, the defence of the endothelium begins to break down in the presence of atherosclerosis risk factors, such as hypercholesterolaemia and hypertension. Hypercholesterolaemia facilitates leukocyte adhesion to the vasculature.[8] Local oxidation of circulating lipoproteins causes endothelial activation, mediated by a decreased availability of NO.[9] Angiotensin II is a vasoconstrictor associated with hypertension. It not only antagonises the action of NO, but also triggers the production of intracellular reactive oxygen species (ROS), increases the concentration of the proinflammatory cytokines such as interleukin (IL)-6 and upregulates the expression of adhesion molecules such as vascular cell adhesion molecule-1 (VCAM-1) on the surface of endothelial cells.[10] Therefore, endothelial dysfunction and evolving vascular inflammation are critical in the initiation of atherosclerotic plaques.

### 1.1.2 Initiation of Inflammation and Atherosclerosis

During endothelial activation, proinflammatory cytokines, such as IL-1β, IL-6 and tumour necrosis factor-α (TNFα), increase the level of expression of endothelial adhesion molecules, such as selectins, VCAM-1, and intercellular adhesion molecule-1 (ICAM-1).[3] Upregulation of these molecules facilitates adherence of monocytes to the dysfunctional endothelium and their subsequent transmigration across the vessel wall.[3]

Once within the arterial intima, the monocytes develop into macrophages and express scavenger receptors that internalise modified lipoproteins.[11] Internalisation of these lipoproteins gives rise to lipid laden macrophages or foam cells, which characterise the early form of atheromatous plaques. The foam cells within these lesions begin to release proinflammatory cytokines to perpetuate the inflammatory response.[8] In addition to macrophages, T cells, mast cells and dendritic cells are also recruited into atherosclerotic lesions via binding to the adhesion molecules.[12] Once within the lesions, T cells are activated and secrete cytokines to influence macrophage activity. In the presence of persisting atherosclerotic risk factors, the atheroma will eventually evolve from an early inflammatory lesion (‘fatty streak’) towards a more advanced lesion.[8]

### 1.1.3 Progression of Atherosclerosis

The progression of a fatty streak to a complex lesion is characterised by the proliferation of smooth muscle cells (SMC) and their reduction in collagen synthesis. By releasing proinflammatory cytokines, activated endothelial cells,

T cells and foam cells not only perpetuate inflammation within the atheroma, but also enhance SMC proliferation and upregulate the activity of matrix metalloproteinase (MMP).[13] In addition to SMC proliferation, neovascularisation within the plaque and the rupture of these fragile vessels are thought to result in an acute expansion of the lesion.[14]

MMPs are a family of interstitial collagenases and gelatinases, playing an essential role in vascular remodelling, allowing for adaptation and repair. However, excessive MMP activity can lead to inappropriate vascular remodelling and atherosclerosis.[15] Mediated by IL-1, TNFα, ROS and oxLDL, over-expression of MMP degrades supportive collagen, and leads to thinning of the fibrous cap. Once the fibrous cap is weakened, the plaque is destabilised and becomes vulnerable to rupture, precipitating acute thromboembolic events.[13] Among the family of MMPs, MMP-9 protein activity was shown to be closely associated with the early (less than 4 weeks) occurrence of cerebrovascular accidents in patients with high-grade stenosis of internal carotid artery, suggesting a role in the destruction of the fibrous cap of atherosclerotic plaques.[16]

### 1.1.4 Fate of the Vulnerable Plaque

Haemodynamic stress can disrupt the vulnerable atherosclerotic plaque, causing exposure of the prothrombotic subendothelium and embolisation of plaque contents into the circulation. This in turn activates coagulation and thrombin formation, converting the atherosclerotic plaque into a source of thromboembolism.[8] In summary, inflammation participates in all steps of

atherosclerosis. It is not only instrumental in the development of atheromatous plaques, but, more importantly plays a critical role in plaque destabilisation, thus converting chronic atherosclerosis into an acute thromboembolism with ensuing clinical sequelae, including acute coronary syndrome, transient ischaemic attack and stroke.[8]

# 1.2 THE CLINICAL NEED FOR NEW ADJUNCTIVE IMAGING STRATEGIES

Stroke is defined as a rapid onset of focal neurological deficit due to a vascular lesion, with symptoms exceeding 24 hours (or leading to death). A transient ischaemic attack (TIA) has the same definition but with symptoms resolved within 24 hours.[17] Stroke is the third leading cause of death in developed countries and is the principal cause of neurological disability.[18, 19] The total clinical and social cost of stroke is estimated to be £9 billion in the United Kingdom (UK), contributing to 5% of national healthcare expenditure annually.[20] Ischaemic stroke accounts for 80% of all strokes, and approximately 30% of these are caused by thromboembolism originating from a culprit carotid plaque.[21,22] It is estimated that more than 2% of the population over 60 years of age have this detectable and modifiable risk factor for stroke.[23]

## 1.2.1 Identifying the 'High-risk' Patients

Carotid artery disease is one of the most scientifically examined conditions in medicine. Two landmark randomised, controlled trials, namely the European Carotid Surgery Trial (ECST) and North American Symptomatic Carotid Endarterectomy Trial (NASCET) led to worldwide consensus in the surgical treatment of recently symptomatic patients.[24, 25] The Asymptomatic Carotid Surgery Trial (ACST)[26] and Asymptomatic Carotid Artery Stenosis (ACAS) [27]

trials concluded that carotid endarterectomy (CEA) conferred a small, but significant benefit over medical treatment alone, but there is a lack of global consensus regarding the optimal way of treating asymptomatic patients. Some groups advocate carotid intervention for all threshold asymptomatic lesions,[28-32] whilst others challenge the 'one size fits all' strategy of mass intervention[33] and support the treatment of all asymptomatic patients with current best medical therapy.[34-39] Evidence shows that a policy of mass intervention in asymptomatic patients could only ever prevent about 1-4% of all strokes.[37, 40] 94% of CEA and carotid artery stenting (CAS) procedures are ultimately unnecessary, costing $2.1 billion per year,[37, 38] and placing patients at risk of periprocedural stroke. Furthermore, significant advances in best medical therapy, particularly the introduction of statin treatment, has substantially reduced risk of stroke,[33, 41, 42] thereby altering the risk-benefit ratio for intervention. To summarise, the 'one size fits all' strategy of mass intervention in asymptomatic patients is both ineffective and unsustainable. On the other hand, invasive intervention will undoubtedly confer benefit in a small cohort of high-risk asymptomatic patients. This mandates the goal of identification and treatment of this high-risk subgroup, rather than continuation of a policy of mass intervention that consumes vast amounts of resources but benefits very few patients in the long term.[33] This view is also supported by the 2011 American Heart Association (AHA) and intersociety guidelines, recommending that CEA or CAS should only be used in ‘highly selected’ cases.[28, 29] Therefore, imaging strategies for risk stratification are needed to identify the high-risk asymptomatic patients, thereby optimising resource allocation to target the appropriate cohort.

### 1.2.2 Limitations of Current Conventional Clinical Imaging Tools

Current selection criteria for surgical intervention of carotid artery disease are still primarily determined by symptomatology and the degree of luminal stenosis as assessed by conventional angiographic techniques, including intra-arterial digital subtraction angiography, duplex ultrasound, computed tomography angiography (CTA), and magnetic resonance angiography (MRA). However, it is now widely accepted that luminal stenosis alone does not adequately reflect the true disease burden due to the process of arterial remodeling.[43] Remodelling may produce normal luminal angiographic measurements despite a large atherosclerotic lesion *in situ* which may be at risk of rupture and subsequent embolisation.[44, 45] Supporting this, neither the ACST[26] nor ACAS[27] trials showed any evidence that stenosis severity were predictive of an increased risk of late stroke. The non- randomised Asymptomatic Carotid Stenosis and Risk of Stroke (ACSRS) study,[46] however, revealed that patients with asymptomatic 50–69% stenoses had a 0.8% annual stroke risk, compared with 1.4% for 70–89% stenoses, increasing to 2.4% for 90–99% stenoses. To date, stenosis severity has not been effective in identifying a high-risk asymptomatic subgroup.[33] Similarly, in the ECST, 43.8% of the 3,018 trial participants with symptomatic carotid disease had <30% stenosis.[24] In the NASCET, the 5-year rate of any ipsilateral stroke for patients with <50% stenosis was 22.2%.[25] Moreover, managing carotid artery disease based on degree of luminal stenosis alone has led to only a 7% reduction in stroke between 1996 to 2006.[47] This has directed the search for new adjunctive imaging strategies that characterise and identify vulnerable plaques to improve carotid disease evaluation.

Atherosclerotic plaques can behave in a benign and quiescent fashion, remaining clinically silent, but always have the potential to phenotypically change their biological behaviour. 'Vulnerable plaques' undergo rapid progression and a high likelihood of rupture, causing acute clinical thromboembolic complications. This vulnerability is dictated by plaque morphology, composition, and the presence of inflammation, which in turn are influenced by underlying pathophysiological mechanisms at the cellular and molecular level. There are now promising non-invasive imaging techniques, such as contrast-enhanced ultrasound, high resolution MRI and hybrid imaging, which have been used to interrogate plaque vulnerability *in vivo* and provide morphological and functional information, adding further prognostic information to luminal stenosis alone.

# 1.3 NEW ADJUNCTIVE IMAGING STRATEGIES

## 1.3.1 Ultrasound

### 1.3.1.1 Plaque morphology

Ultrasound provides relatively low resolution anatomical data, but with the great advantages of being widely available, cheap, and portable. In addition to luminal stenosis, ultrasound has also been used for evaluating plaque morphology. The ACSRS study investigators developed several computerised plaque analysis techniques for predicting late stroke.[46, 48-54] Plaques were ascribed to 1) a grade based on echolucency, a widely accepted marker of high-risk lesions, with type 1 being the most echolucent and type 4 the most echogenic; and 2) pixel gray-scale values.[51] Type 4 plaques were associated with a 0.4% annual risk of stroke, compared with 0.8% for type 3 plaques, increasing to 3.0% for type 1 and type 2 plaques. The Gray-Scale Median (GSM) is a standardised, computerised measurement of the gray values of all the plaque pixels.[49, 50, 54] This represents an index of echogenicity, with low GSM scores associated with echolucent plaques, whilst high GSM scores correspond to echogenic plaques. Patients with plaques of a GSM >30 incurred a 0.6% annual risk of ipsilateral stroke, compared to 1.6% in patients with a score of 15–30, increasing to 3.6% in those with a score <15.[49] GSM, however, has some drawbacks: since GSM measures the median brightness of the entire plaque, regional instability may exist within a plaque even with a high GSM value.

Plaque area and juxta-luminal black area (JBA) were the other ultrasonography-based parameters used in the ACSRS study to predict late stroke.[49, 52, 53] Patients with a greater plaque area (>80mm$^2$) had a higher annual risk of stroke (4.6%) compared with 1.0% in patients with a smaller plaque area (<40mm$^2$).[49] JBAs are synonymous with softer elements within the plaque (such as the necrotic core, or intraplaque haemorrhage). Similarly, patients with larger JBAs >8mm$^2$ incurred a higher annual stroke rate (4.6%) compared to 0.6% in patients with smaller JBAs <8mm$^2$.[49] However, this type of univariate analysis limits its practical value to the clinicians as these ultrasonography-based parameters can exhibit confounding factors.[33] For instance, an echolucent type 1 or type 2 plaque will have a low GSM and a large JBA. To overcome this, the investigators in ACSRS study subsequently used multi-regression analyses to devise an individualised scoring system for the annual risk of late stroke, which comprised of stenosis severity, presence or absence of contralateral symptoms, and two computerised plaque analyses (plaque area and GSM).[33] This system, however, remains to be validated prospectively.

#### 1.3.1.2 Detection of emboli

The predictive role of spontaneous embolisation detected by transcranial Doppler (TCD) ultrasonography in patients with asymptomatic carotid artery disease has been evaluated.[55-57] The Asymptomatic Carotid Emboli Study (ACES) demonstrated that patients with spontaneous embolisation had a sevenfold excess risk of late ipsilateral stroke.[55] In a prospective cohort of 468

asymptomatic patients TCD ultrasonography has also been used to show that an aggressive approach to medical treatment substantially reduces spontaneous embolisation.[56] Embolisation detected on TCD ultrasonography is a relatively simple but important way of monitoring the response to treatment, as well as being a screening test to direct carotid intervention to high-risk cohorts with ongoing embolisation.

#### 1.3.1.3 Contrast-enhanced ultrasound

Using microbubbles as 'surrogate red blood cells' and intravascular tracers, contrast-enhanced ultrasound (CEUS) has been adopted to study intraplaque neovascularisation, one of the features of plaque vulnerability. Carotid plaque contrast-agent enhancement correlates with histological density of neovessels and is associated with plaque echolucency.[58] Recently, late-phase contrast-enhanced ultrasound (LP-CEUS) was developed to quantify microbubble contrast retention within carotid atherosclerosis, and demonstrated that microbubbles were retained in areas of plaque inflammation and angiogenesis.[59] Moreover, through the use of targeted gas-filled microbubbles, it has been possible to image a range of targets, including VCAM-1,[60] P-selectin,[61] and ICAM-1.[62] Therefore, CEUS may provide valuable information for further risk stratification of echolucent atherosclerotic lesions and carotid artery stenosis of different degrees, beyond that provided by standard ultrasound imaging.

### 1.3.2 Computed Tomography

Computed tomography (CT) is able to identify some features of the high-risk atherosclerotic lesions, for example plaque ulceration, speckled pattern of calcification, presence of lipid core, and positive remodelling of the arterial wall. It has also been reported that enhancement of the vasa vasorum overlying a carotid plaque may be a marker of local inflammatory change. A study has shown that CTA enhancement of the internal carotid artery (ICA) wall is significantly more common in symptomatic than in asymptomatic patients with 70% ICA stenosis.[63] This is consistent with previous histological studies that have demonstrated the presence of neovascularisation of the adventitial vasa vasorum in symptomatic ICA walls.[64] CT can also be used to image the brain, and there is evidence to suggest that asymptomatic patients with CT scan evidence of silent infarction bear a higher risk of late stroke. The ACSRS study showed that CT scan evidence of silent embolic infarction was associated with a threefold increase in the risk of ipsilateral stroke (1.0% versus 3.6%, P = 0.002).[48] The presence of silent cerebral infarction potentially offers a simple approach to identify high-risk patients.

### 1.3.3 Hybrid Imaging Systems

Hybrid imaging systems such as co-registered positron emission tomography (PET)/CT and PET/ magnetic resonance imaging (MRI) are now becoming available. They enable integration of the extreme sensitivity (picomolar range) and quantitative outputs of nuclear imaging techniques - SPECT (single photon emission computed tomography) and PET with the excellent spatial

resolution of anatomical imaging modalities – CT and MRI, providing both structural and metabolic information about the plaque status.

Co-registration of SPECT with CT imaging was used to show that the recruitment and accumulation of indium-labeled monocytes to plaque in atherosclerotic mice was slowed by statin treatment.[65] The PET tracer 18F-fluorodeoxyglucose (FDG), a biological glucose analogue which is taken up by metabolically active tissue, has been extensively evaluated for measuring intraplaque inflammation in atherosclerotic lesions.[66-68] Davies *et al* have used combined FDG-PET and high resolution MRI to assess the degree of inflammation in stenotic and non-stenotic plaques.[66] In a prospective study, PET demonstrated that symptomatic carotid plaques accumulated approximately 30% more FDG compared to the asymptomatic plaques.[67] Despite ample evidence, concerns have been raised about specificity of this tracer for imaging inflammatory cells as FDG is taken up by any metabolically active tissue.[69] This led to development of novel 'radio-ligands', such as imaging probes that target MMP,[70] apoptosis,[71] and 11C-PK11195, a selective ligand of the translocator protein highly expressed by activated macrophages,[72] which enhanced the diagnostic performance to detect vulnerable plaques. While PET or SPECT has much greater detection sensitivity than MRI or CT, and much better tissue penetration than ultrasound, the disadvantages of nuclear imaging modalities include limited spatial resolution, logistics of isotope provision, substantial radiation exposure and expense.

## 1.3.4 High Resolution MRI

### 1.3.4.1 Plaque morphology

High resolution MRI has emerged as a leading non-invasive imaging modality for assessing atherosclerosis, due to its excellent spatial resolution at a sub-millimeter level, soft tissue contrast, and high signal-to-noise ratio. The significant advantage of MRI over duplex ultrasound and CT is the versatility to acquire and combine multiple different contrast weightings to characterise tissue composition within the vessel wall, resulting in vast quantity of data obtainable with MRI. Moreover, the ability of *in vivo* carotid MRI to quantify the main plaque components such as intraplaque haemorrhage (IPH), lipid-rich necrotic core (LRNC), calcification, and surface disruption has been meticulously validated with histology.[73] MRI-based carotid plaque characterisation has been shown to be accurate and reproducible with good to excellent intra-observer and inter-observer as well as inter-scanner reproducibility.[74] Since MRI does not involve ionising radiation, serial imaging can be performed safely over time within the same patient for monitoring disease progression and regression.

Amongst all the principal components of carotid lesions, IPH and LRNC have emerged as the most decisive indicators of lesion severity currently visualised by MRI.[75] The crucial role of MR-depicted IPH in differentiating unstable plaque lesions from indolent lesions has been demonstrated. In a prospective study, Takaya *et al* showed that patients with an asymptomatic 50–79% stenosis and MRI evidence of thinned or ruptured fibrous caps, IPH, or large lipid cores had higher rates of ipsilateral stroke than patients without these

features.[76] Altaf *et al* showed that IPH as assessed by MRI was a good predictor of ipsilateral stroke and TIA with a hazard ratio of 9.8 (p=0.03) in patients with symptomatic mild to moderate (30-69%) carotid stenosis.[77] In a cohort with asymptomatic moderate carotid stenosis, MR-depicted IPH was also found to be associated with future ipsilateral cerebrovascular events. Conversely, patients without MR-depicted IPH remained asymptomatic during the 2-year follow-up, suggesting that the absence of IPH at MRI may be a reassuring marker of plaque stability and of a lower risk of thromboembolism.[78] Studies have demonstrated that LRNC in the carotid artery is the strongest *in vivo* predictor of future surface disruption, which is associated with the development of future ipsilateral cerebrovascular events.[75] In a histological assessment of 526 symptomatic carotid plaques, Redgrave *et al* demonstrated that fibrous cap rupture showed strong positive associations with several other adverse histological features, including large lipid core, haemorrhage, and marked cap inflammation.[79]

### 1.3.4.2 Flow and Stress

By extracting quantitative vessel wall morphology and composition information, MRI can be used to test models of flow and biomechanical stress on carotid plaques. Biomechanical stress is regarded as one of the major contributing factors of plaque vulnerability. Plaque rupture can be viewed as a structural failure when the structure of plaque becomes inadequate to resist haemodynamic pressure and shear stress. Using finite element analysis and *in vivo* MRI, Li *et al* demonstrated that maximum stresses within the plaques of symptomatic patients were higher than those of asymptomatic patients,

suggesting the possibility that plaques with higher stresses may be more prone to become symptomatic and rupture.[80] Tang *et al* [81] have developed a 3-dimensional MRI-based computational model for vessel wall strain/stress analysis for human carotid plaques, and reported that large LRNC covered by thin plaque caps are associated with both extreme maximum (stretch) and minimum (compression) stress/strain levels, further supporting the fact that thin fibrous cap is an indicator of vulnerable plaque. Large cyclic stress/strain variations in the plaque under pulsating pressure may lead to artery fatigue and possible plaque rupture. Moreover, it has been reported that there is an association between biomechanical stress and ultrasmall superparamagnetic particle of iron oxide (USPIO) enhanced MR-defined inflammation within carotid plaques, both known risk factors for plaque vulnerability.[82] This highlights the complex interaction between physiological processes and biomechanical mechanisms in the development of carotid plaques.

## 1.4 MOLECULAR MRI

Molecular imaging is a rapidly evolving field, which opens new avenues to shift emphasis from imaging plaque structure to directly reporting the biological processes of atherosclerosis at the molecular and cellular levels.[83] Targeted or 'active' molecular imaging exploits specific 'inducible' molecular targets, or cellular events in diseases to generate the image contrast.[84] By specifically targeting molecules differentially expressed between physiological and pathological states, molecular imaging permits disease characterisation at a cellular or tissue level. As a molecular imaging modality, MRI has the distinct advantage of providing precise soft tissue and functional information *in vivo* by exploring biochemical contrasts, proton density and perfusion. This enables co-registration of molecular with anatomical information into a single imaging modality, hence fully capitalising on the diagnostic potential of MRI. Molecular MRI of atherosclerosis aims at accelerating diagnosis, refining risk stratification (identifying the high-risk subgroup), providing insights that reveal disease diversity, guiding specific therapies, and monitoring response to therapeutic intervention.[85]

MR images are determined by the density and local environment of water protons.[86] MRI contrast agents exert indirect effects by altering the properties of these protons and their local environment.[86] They increase sensitivity and facilitate diagnosis by enhancing T1 and T2 relaxation times, and can thus be thought of as relaxation catalysts. Agents that preferentially

reduce T1 relaxation times are 'T1 agents'; agents that primarily shorten T2 relaxation times are 'T2 agents'. There are two types of MRI contrast agents, namely paramagnetic and superparamagnetic, that differ in their structures and effects on signal intensity.[87]

### 1.4.1 Gadolinium based Contrast Agents

Paramagnetic contrast agents are typically composed of gadolinium chelates, such as gadolinium diethylene-triamine-pentaacetic acid (Gd-DTPA). Gadolinium chelates enhance the longitudinal magnetisation (T1) of nearby water protons, shortening T1 relaxation time, inducing a positive signal enhancement or bright appearance on T1-weighted images.[87]

One approach for assessing inflammatory activity in plaque by MRI is to measure the degree of plaque neovascularisation - a known feature of plaque inflammation.[88] Dynamic contrast-enhanced MRI (DCE-MRI) is emerging as a non-invasive tool to study neovascularisation and inflammation in carotid atherosclerotic plaques. It involves the acquisition of serial MR images with high temporal resolution before and after the administration of gadolinium-based contrast agents. After the injection of gadolinium-based contrast agents, carotid atherosclerotic plaques exhibit variable contrast enhancement rates in dynamic MR imaging sequences. Strong contrast enhancement suggests increased endothelial permeability and neovasculature growth into the plaque. Hence, plaque enhancement has been taken to be a sign of plaque inflammation. Kerwin *et al* showed that the rate of plaque contrast enhancement was significantly correlated with neovasculature and

macrophage content in human carotid plaques.[89, 90] In addition, DCE-MRI offers the advantage of using a readily available Food and Drug Administration (FDA)-approved MRI contrast agent.

Due to the low intrinsic relaxivity, however, gadolinium-based contrast agents must reach a micromolar range of concentrations in tissues to allow detection.[91] A range of strategies have been adopted in molecular imaging to amplify the gadolinium contrast effects. Specific peptides or antibodies have been attached to lipid-based nanoparticles, such as liposomes, perfluorocarbon lipid emulsions and micelles carrying substantial payloads of gadolinium.[92] Lipoprotein micelles enriched with gadolinium chelates have also been constructed for targeting macrophages within atherosclerotic plaques.[93-95] Nonetheless, compared to superparamagnetic iron oxide-based agents, the gadolinium contrast effects achievable remain relatively modest.[93, 96] Another disadvantage of gadolinium chelates is the potential severe long-term toxicity effects, including nephrogenic sclerosing fibrosis in patients with impaired renal function.[97]

### 1.4.2 Iron Oxide based Contrast Agents

In contrast to paramagnetic contrast agents that create hyperintense signals ("positive" contrast) in T1-weighted images, superparamagnetic contrast agents shorten the transverse T2 and T2* relaxation times, resulting in hypointense signals that appear black on T2- and T2*-weighted MR images ("negative" contrast).[87] These superparamagnetic agents are based on iron

oxide particles, which are composed of a core of iron oxides, coated by a biocompatible inert polymer, usually dextran.[98]

Iron oxide particles have become the favored contrast agent for the following reasons. Firstly, they have a known biocompatibility profile with their degradation occurring through normal physiologic iron-handling pathways. Iron oxide particles were originally developed to treat anaemia over half a century ago, and have been used successfully without any serious long-term side effects.[99] Furthermore, it has been shown that iron oxide particles are assimilated *in vivo*, where the iron is incorporated into the iron cycle.[100] Iron oxide is therefore an ideal candidate for cellular or molecular imaging as it is known to be broken down *in vivo* into non-toxic products. Conversely, little is known about the long-term cytotoxicity of gadolinium chelates as they are cleared from the body swiftly.[101] However, it is known that gadolinium ions can affect certain cell populations *in vivo*, such as reducing the number of Kuppfer cells,[102] hence making it potentially unsuitable for internal labelling of cells. Secondly, iron oxide agents confer superior sensitivity in MR contrast than gadolinium chelates due to iron oxide's inherent superparamagnetism, which distort magnetic fields, creating marked contrast effects far exceeding their physical size. As a result, either greater contrast effect is afforded with the same concentration of iron oxide compared to gadolinium or less iron oxide needs to be incorporated into the cells.[103]

Three classes of iron oxide particles are currently used for atheroma imaging. They can be classified according to particle size: ultrasmall superparamagnetic

particles of iron oxide (USPIO) (15 to 30nm diameter), superparamagnetic particles of iron oxide (SPIO) (50 to 300 nm) and microparticles of iron oxide (MPIO) (0.9–5μm).[85, 91]

#### 1.4.2.1 USPIO

USPIO, such as Ferumoxtran, have a thick and complete dextran coating to provide a magnetic 'shield' that prevents aggregation of particles. Hence, they remain monodisperse in solution and are cleared from the circulation very slowly by the reticulo-endothelial system (RES). The blood half-life of Ferumoxtran in humans is around 24 hours.[98] Due to their long blood half life and small particle size, USPIO have been used as passive contrast agents to identify plaque macrophages as surrogate markers of plaque inflammation in the assessment of atherosclerosis in humans.[104, 105] While being a positive attribute for macrophage imaging, the prolonged blood half life poses some drawbacks in targeted contrast agents including the high background contrast for an extended period, and the extensive 36-hour delay after USPIO injection before imaging.[105] Moreover, because USPIO can be taken up non-specifically and can extravasate passively,[106] particularly in the sites of inflammation with increased endothelial permeability, there is potential to compromise the specificity of molecular targeting.

#### 1.4.2.2 SPIO

In contrast to USPIO, SPIO, such as the Ferumoxides, have a thin and incomplete dextran coating, causing them to aggregate in solution into large clusters that are rapidly cleared from the circulation by the

RES. Ferumoxides in humans have a blood half-life of around 5 minutes.[98] Like USPIO, the small particle size allows SPIO to enter atherosclerotic plaques. Even though both classes of particles are phagocytosed by macrophages, their uptake mechanisms differ. While the mechanism of USPIO uptake in macrophages has not been fully understood, the phagocytosis of SPIO was shown to be mediated by scavenger receptors[107] and dependent on macrophage activation status.[108] The passive accumulation of SPIO in plaque macrophages of mice and human have been demonstrated *in vivo.*[109, 110] However, the rapid clearance of SPIO from the circulation limits their diffusion in atherosclerotic plaques, making them less favorable for atheroma imaging.[98]

#### 1.4.2.3 MPIO

MPIO, such as commercially available Dynabeads, are large iron oxide particles, conveying a high payload of iron that is many orders of magnitude greater than USPIO.[111] The effects of MPIO on local magnetic field homogeneity, and therefore detectable contrast effect, have reached a distance 50 times the physical diameter of the microparticle, known as the contrast "blooming effect".[112] The substantial contrast effects of MPIO render them detectable at the single-particle level under optimal conditions.[112] Being readily endocytosed by macrophages, MPIO have been utilised for cellular MRI, such as tracking graft rejection.[113] However, the use of non-targeted MPIO is only suitable for cells that readily phagocytose the particles. For direct reporting of specific molecular events, we require more sensitive imaging at a

molecular rather than a cellular level that mandates the use of a specific targeting system.

For molecular imaging of endovascular targets, MPIO possess a number of positive attributes. Firstly, the potent 'blooming effect' of MPIO greatly enhances their sensitivity to achieve *in vivo* detection of low-abundance endothelial molecular targets.[91] Secondly, the large size of these particles prevents them from translocating across the endothelium or nonspecific uptake by endothelial cells[85, 106] and therefore retains specificity for molecular targets expressed on the vascular endothelium. Thirdly, unbound MPIO have a rapid blood clearance with a blood half-life less than 2 minutes in rats, thus minimising background contrast, enhancing signal-to-noise ratio and plaque visualisation.[114] Lastly, MPIO possess manipulable surface chemistries that permit targeting molecules to be covalently bound to the particle surface.[85] MPIO are therefore well suited to evaluate the expression of adhesion molecules on activated endothelial cells in atherosclerosis.

## 1.5 TARGETED MPIO

The use of targeted MPIO may be better than nuclear imaging modalities, such as PET and SPECT because it does not involve the use of a radioisotope; this implies the contrast agent has fewer risks to patients in terms of radiation hazard, and fewer logistic problems arising from the short shelf life of radioisotope. In comparison with ultrasound-based imaging, where targeted contrast agents are also available, MRI provides superior spatial resolution, tissue penetration depth and soft tissue contrast, as well as definition of detailed anatomy.

To achieve targeted molecular MR imaging, purpose built contrast agents are required to target the molecules or metabolic processes of interest, such as endothelial adhesion molecules in atherosclerosis, with high binding affinity and specificity. Target specificity of contrast agents can be customised through conjugation of a variety of targeting ligands, such as monoclonal antibodies, antibody fragments (Fab), peptides or sugars, to functional groups on the surface of microparticles.[91, 115]

MPIO are commercially available with different reactive surface groups including p-toluene sulphydryl (tosyl) group, amine and carboxylic acid groups.[85] Functionalised MPIO therefore provide a manipulable platform that can be adapted for molecular imaging of a wide selection of endovascular molecular targets in atherosclerosis.

# 1.6 ENDOTHELIAL ADHESION MOLECULES: POTENTIAL TARGETS FOR IMAGING WITH MPIO

As discussed in section 1.1, intraplaque inflammation drives the progression and destabilisation of atherosclerotic lesions, converting chronic stable asymptomatic lesions into acute lesions with ensuing clinical sequelae. One of the earliest events in atherosclerotic plaque progression is the over-expression of adhesion molecules on the activated endothelium, such as VCAM-1, E-selectin (CD62E), and P-selectin (CD62P), all of which play vital roles in the tightly regulated inflammatory process. The 'adhesion dynamic modelling' predicts the interplay between rolling and firm adhesion by these two molecular systems to produce synergistic effect on leukocyte:endothelial binding.[116, 117] The major steps in leukocyte recruitment into vascular tissues are as follows: (1) initial selectin-dependent tethering and rolling, (2) triggering of adhesion via chemokines and their receptors or through selectin binding to P-selectin glycoprotein ligand-1 (PSGL-1),[118, 119] (3) integrin-dependent adhesion and adhesion strengthening by integrin clustering, (4) transmigration across endothelium.[120-122]

These endothelial markers are differentially expressed and reflect disease progression, and thus offer potential targets for imaging probes and therapeutic intervention in cardiovascular diseases.

### 1.6.1 E-selectin

The selectins are a family of cell-surface transmembrane glycoproteins that bind sialylated and fucosylated carbohydrate ligands.[123] They mediate initial leukocyte capture from circulation to the endothelium and promote tethering and rolling due to the rapid on/off interactions with their ligands.[124]

E-selectin is an endothelial-specific protein that is not constitutively expressed under non-inflamed conditions, but is synthesized in response to stimuli by inflammatory cytokines such as such as TNFα, IL-1α,[125] or platelet factor 4 (PF4), a platelet-specific chemokine released on platelet activation.[126] The cognate ligands for E-selectin are sialylated carbohydrates containing the sialyl Lewis x structure.[85] E-selectin is also found on human atherosclerosis-prone endothelial cells and on the surface of fibrous and lipid-containing human plaques.[127] In the mouse model, genetic deficiency of E-selectin leads to reduction in the lesion size.[128] The strongest effects in the inhibition of atherosclerosis have been demonstrated in mice with combined deficiency of E and P-selectins, showing 80% and 40% protection in the early and advanced stages of the disease respectively.[129]

### 1.6.2 P-selectin

P-selectin is stored in Weibel-Palade bodies of endothelial cells and in intracellular α-granules of platelets, and upon stimulation is rapidly translocated to the plasma membrane where it serves as a leukocyte receptor.[130] P-selectin binds P-selectin glycoprotein ligand-1 (PSGL-1) that

mediates the rolling of leukocyte along the endothelium.[131] P-selectin is found on the atherosclerotic endothelium of active plaques but not on the non-inflamed endothelium.[132] In P-selectin low density lipoprotein receptor double knockout mice, reduction in lesion sizes was shown throughout their life compared to the controls, suggesting a crucial role for this molecule in early and advanced atherosclerotic disease.[129] Dual-targeted MPIO have also been used for MRI of P-selectin and VCAM-1 in a mouse model of atherosclerosis.[133]

### 1.6.3 VCAM-1

VCAM-1 is an immunoglobulin superfamily glycoprotein (100 to 110 kDa) expressed on activated endothelial cells, macrophages and SMC.[134] VCAM-1 expression is up-regulated only on activated endothelium in response to stimuli by inflammatory cytokines such as TNFα, IL-1 or angiotensin II via the nuclear factor-kappa B (NF-κB) pathway,[135,136] but not on resting endothelial cells. VCAM-1 interacts with integrin α4β1, also known as very late antigen (VLA-4), expressed on leukocytes and mediates firm adhesion of mononuclear cells to activated endothelium.[137-139] Its role in the inflammatory initiation of atherosclerosis is well established, and is an attractive biomarker for targeted imaging.[133, 140-142] Antibody-bound MPIO allow MRI detection of VCAM-1 up-regulation in diverse models of clinically important vascular pathologies including acute vascular inflammation,[141] ischemia-reperfusion injury,[143] atherosclerosis,[133] and ischemic stroke.[144]

The strict temporal and spatial regulation of these inducible endothelial adhesion molecules, i.e. VCAM-1, E and P-selectin, their critical functions in atherosclerosis and their immediate accessibility via the circulation make them ideal targets for functional molecular imaging and targeted therapeutics.[85]

## 1.7 PURPOSE AND HYPOTHESIS

The purpose of this work is to develop and utilise novel *in vivo* MRI methodologies to assess inflammation in atherosclerotic plaques. This thesis describes the development of antibody-conjugated iron oxide particles targeted against endothelial adhesion molecules in order to act as a contrast agent for MR imaging of inflammation in atherosclerosis. This technique is utilised in both human atherosclerotic tissue and an apolipoprotein E-deficient (ApoE-/-) mouse model. We hypothesised that antibody-conjugated iron oxide particles would enable MR imaging of inflammation via binding to endothelial adhesion molecules in atherosclerosis in both human atherosclerotic tissue and an ApoE-/- mouse model.

This study is comprised of four main experimental stages, namely (1) *in vitro* cell culture stage, (2) *ex vivo* human carotid plaque stage, and both (3) *ex vivo in situ* and (4) *in vivo* ApoE-/- mouse stages. In the initial *in vitro* feasibility study, a cellular model of endothelial inflammation induced with TNFα was established, followed by MRI detection of activated endothelial cells using anti-E-selectin antibody and anti-VCAM-1 antibody conjugated SPIO with confirmatory immunocytochemistry. This study has been completed as part of a research project for an MSc in Surgical Science at Imperial College London. The results then informed the next stage of the work, namely to detect and characterise E-selectin and VCAM-1 on human carotid plaques using antibody-conjugated SPIO and immunohistochemistry. We furthermore sought

to differentiate biological plaque behaviour based on the MRI scans using these probes. The *ex vivo in situ* stage consisted of MRI detection of atherosclerotic lesions in the aortic root of ApoE-/- mice using a modified dual-targeted MPIO against VCAM-1 and P rather than E-selectin. The final *in vivo* stage involved detection of atherosclerotic lesions in the aortic root and aortic arch of ApoE-/- mice by *in vivo* MRI using dual-targeted MPIO against VCAM-1 and P-selectin. Following this, an animal model (ApoE-/- mouse) with focal atherosclerotic lesions in carotid arteries was developed by means of peri-arterial collar placement to allow *in vivo* molecular MRI using these probes.

## 1.8 OBJECTIVES SUMMARY

The objectives are listed as follows:

***In vitro* stage**

- Establish a cellular model of endothelial inflammation induced with TNFα
- Detect and characterise E-selectin and VCAM-1 on activated endothelial cells using antibody-conjugated SPIO and immunocytochemistry

***Ex vivo* stage**

- Detect and characterise E-selectin and VCAM-1 on human carotid plaques using antibody-conjugated SPIO and immunohistochemistry
- Determine whether it is possible to differentiate symptomatic carotid plaques from asymptomatic ones, and assess the heterogeneity within the asymptomatic plaque population, based on the degree of inflammation using these probes
- Evaluate the relationship between histological expression of VCAM-1, E-selectin and macrophage with MR contrast effect in the human carotid plaques

***Ex vivo in situ* stage**

- Detect atherosclerotic lesions in the aortic root of ApoE-/-mice by *ex vivo in situ* MRI following *in vivo* administration of dual-targeted MPIO against VCAM-1 and P-selectin

***In vivo* stage (mouse aortic root and aortic arch)**

- Detect atherosclerotic lesions in the aortic root and aortic arch of ApoE-/- mice by *in vivo* MRI using dual-targeted MPIO against VCAM-1 and P-selectin
- Determine whether MR contrast effect induced by dual-targeted MPIO can quantitatively track with the degree of inflammation (i.e. macrophage burden) within the lesions in aortic root
- Evaluate the extent to which dual-targeted MPIO bind to different types of cells (i.e. endothelial cell, macrophage and smooth muscle cell) in aortic root atherosclerotic lesions by immunohistochemistry
- Determine the binding patterns of dual-targeted MPIO in regions of the aortic arch that are susceptible to the development of atherosclerotic lesions by *in vivo* MRI and histology

***In vivo* stage (mouse carotid artery)**

- Develop an animal model (ApoE-/- mouse) with focal atherosclerotic lesions in carotid arteries by means of peri-arterial collar placement
- Detect the induced plaque lesions in carotid arteries of ApoE-/- mice by *in vivo* MRI using dual-targeted MPIO against VCAM-1 and P-selectin

- Determine whether it is possible to discriminate between the high-risk lesions with a vulnerable plaque phenotype from the stable ones based on the degree of inflammation using these MRI probes

# CHAPTER 2:

# *In Vitro* Endothelial Cell Stage

## 2.1 INTRODUCTION

The pilot *in vitro* feasibility study in MSc is summarised in this chapter. This work is an exploratory qualitative study aimed at visualising and characterising the degree of inflammation on endothelial cells using targeted SPIO as an MRI probe. We hypothesised that antibody-conjugated SPIO against E-selectin and VCAM-1 would enable MR imaging of inflamed endothelial cells.

## 2.2 MATERIALS AND METHODS

This section is a summary of the methodology in the *in vitro* cell culture stage, which has been completed as part of a research project for an MSc in Surgical Science at Imperial College London. For full details of methodology, please refer to Appendix A.

### 2.2.1 Induction of Inflammation on Endothelial Cells by TNFα

Bovine aortic endothelial cells (bAEC) (Lonza Wokingham Ltd., UK) were incubated with 1, 10 and 50 ng/ml recombinant rat TNFα (PeproTech Ltd., London, UK) for 4, 24, and 48 hours at 37°C to induce endothelial E-selectin and VCAM-1 expression.

### 2.2.2 Detection and Characterisation of Inflammatory Markers on Endothelial Cells by Immunocytochemistry

Following 20 minutes' incubation in 10% rabbit serum to block non-specific staining, goat anti-bovine primary antibodies against VCAM-1 and E-selectin (dilution 1:200, Santa Cruz Biotechnology, CA, US) were used to detect the inflammatory markers on bAEC. Secondary fluoresceinisothiocyanate (FITC) conjugated rabbit anti-goat polyclonal antibody (dilution 1:200, Autogen Bioclear UK Ltd., UK) was used to allow detection of inflammatory markers by fluorescence microscopy (Leica DMIRE2 inverted microscope, Leica Microsystems Limited, UK) (Figure 2.1).

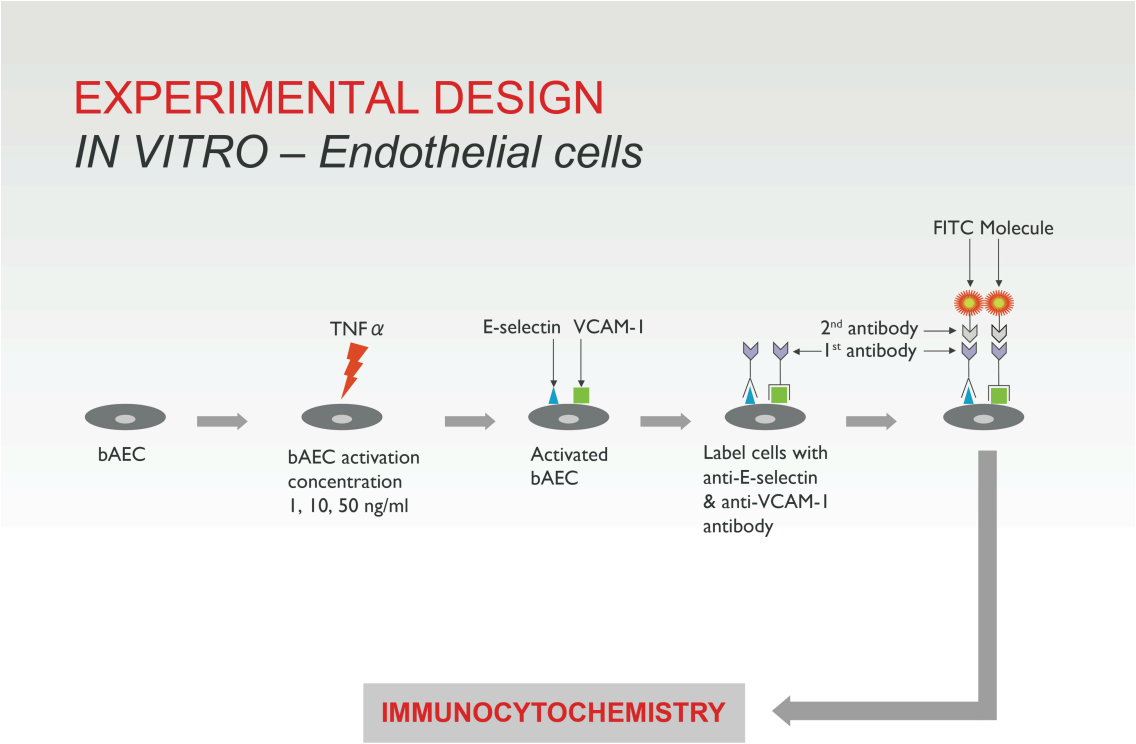



**Fig. 2.1 Experimental design of *in vitro* endothelial cells stage.** bAEC were incubated with 1, 10 and 50 ng/ml TNFα to induce endothelial E-selectin and VCAM-1 expression. These inflammatory markers on activated endothelial cells were detected and characterised by immunocytochemistry.

### 2.2.3 Detection, Characterisation and Imaging of Inflammatory Markers on Endothelial Cells by Biotinylated Antibody-Conjugated Streptavidin Microbeads

The final phase of this work involved MRI detection and characterisation of E-selectin and VCAM-1 on activated bAEC by antibody-conjugated SPIO. Streptavidin microbeads (Miltenyi Biotec Ltd, Surrey, UK) were the magnetic beads (50nm diameter SPIO) conjugated to streptavidin. E-selectin and VCAM-1 expressed on the activated bAEC were detected by biotinylated anti-E-selectin and anti-VCAM-1 mouse monoclonal immunoglobulin G (IgG) (Santa Cruz Biotechnology, CA, US) respectively, which were in turn bound

to the high-affinity streptavidin microbeads. Therefore, streptavidin microbeads were used for magnetic labelling of the activated endothelial cells, thereby making these cells 'MR visible' (Figure 2.2).

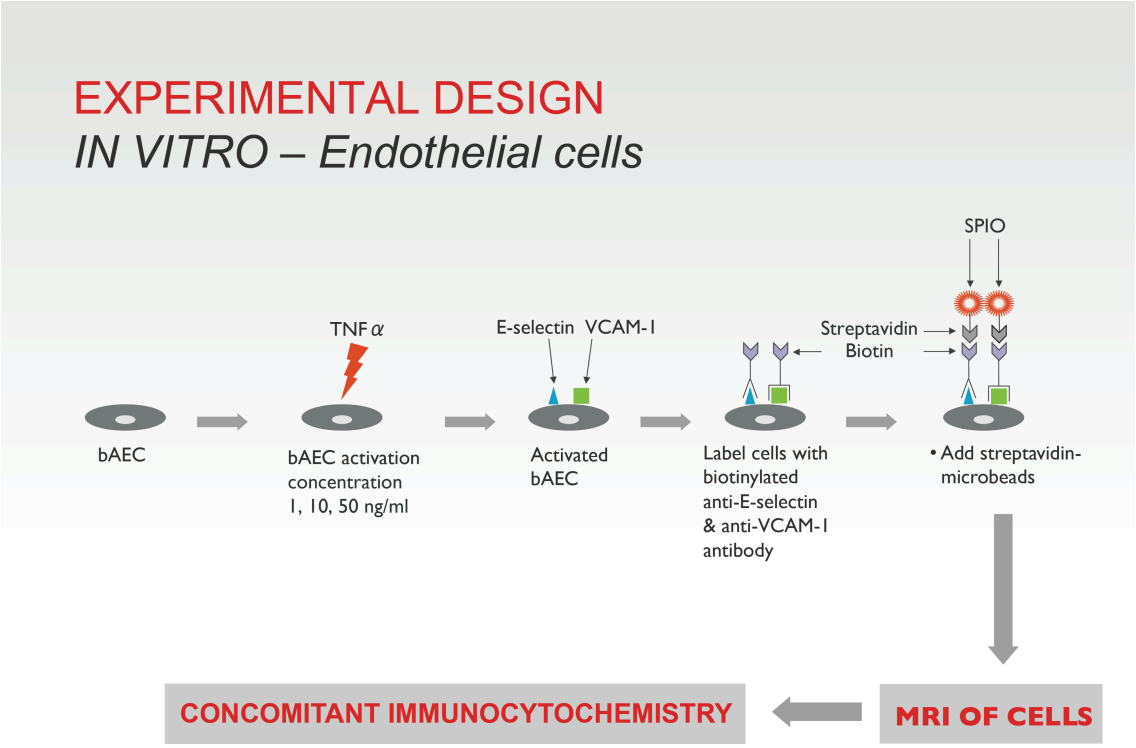



**Fig. 2.2 Experimental design of *in vitro* endothelial cell stage.** bAEC were stimulated by TNFα of different concentration (1,10 and 50ng/ml) to induce endothelial E-selectin and VCAM-1 expression. These inflammatory markers on activated endothelial cells were detected by biotinylated antibodies, which were in turn bound to the streptavidin microbeads, thereby making these cells 'MR visible'. Concomitant immunocytochemistry was performed.

## 2.2.4 Activated Endothelial Cells Labelled with Biotinylated Anti-E-selectin and Anti-VCAM-1 Antibody

Activated bAEC incubated with TNFα of different concentrations (1ng/ml, 10ng/ml and 50ng/ml) together with two negative controls were prepared:

Control 1: Unactivated cells only (cells without any TNFα treatment)

Control 2: Unactivated cells with subsequent addition of biotinylated antibodies and streptavidin microbeads to assess any non-specific binding by the antibodies and non-specific labelling by the microbeads.

The cells were washed twice by centrifugation and labelled at room temperature for 20 minutes with biotinylated anti-E-selectin and anti-VCAM-1 mouse monoclonal IgG at a concentration of 10μg/ml diluted in 10% rabbit serum for labelling $10^6$ cells. Concomitant immunocytochemistry was performed to correlate MRI data.

### 2.2.5 Activated Endothelial Cells Labelled with Streptavidin Microbeads

Following incubation, the cells were washed twice to remove unbound biotinylated antibodies with 2ml of labelling buffer composed of phosphate buffered saline (PBS X1), supplemented with 2mM ethylenediaminetetraacetic acid (EDTA), and centrifuged. The buffer was kept at 4°C throughout the experiment to prevent capping of antibodies on the cell surface and non-specific cell labelling. The endothelial cell pellet was re-suspended in 90μl of labelling buffer per $10^6$ cells and 10μl of streptavidin microbeads per $10^6$ cells. The cells were then incubated at 4°C for 15 minutes and washed to remove unbound streptavidin microbeads. The cells were re-suspended in 50μl of PBS for cell phantom MRI.

### 2.2.6 Cell Phantom MRI

The re-suspended activated bAEC stimulated by TNFα of different concentration (1ng/ml, 10ng/ml and 50ng/ml) and the 4 controls (unactivated cells with biotinylated antibodies and microbeads incubated, unactivated cells, PBS and streptavidin microbeads) were embedded in 2% agarose (Sigma-Aldrich, Dorset, UK). MRI of a cell phantom was performed using a 9.4 Tesla, horizontal bore scanner (Varian Inc., Palo Alto, CA, USA) running VnmrJ 2.3A software. The sample was placed in a quadrature birdcage coil (40mm internal diameter). T2 spin echo sequence was used with the following parameters: Repetition time (TR): 3500 ms; Echo time (TE): 40 ms; FOV 40x40 mm; Matrix 256x256; Average: 40; Thickness 0.5mm; Number of slices: 30; plane: axial; Flip angle: 90°. The MR images were analysed by ImageJ software (National Institutes of Health, http://rsb.info.nih.gov/ij/index.html). The signal-to-noise ratio for each sample was calculated to allow comparison between the samples.

# 2.3 RESULTS

## 2.3.1 Immunocytochemistry of bAEC

Expression of E-selectin and VCAM-1 were detected, as shown by the FITC signal, on bAEC activated at all concentrations of TNFα and incubation periods. By contrast, no expression of E-selectin or VCAM-1 was detected on the quiescent control cells. The following staining patterns were observed: within the same incubation period, the level of expression of both E-selectin and VCAM-1 were dose-dependent, in that greater expression on the cells was observed at higher concentrations of TNFα. The expression on bAEC activated by 50ng/ml TNFα was observed to be the greatest amongst the three concentrations used, followed by 10ng/ml, and finally the least with 1ng/ml TNFα (Figure 2.3). Within the same concentration of TNFα, E-selectin expression on activated bAEC was maximal at 4 hours after stimulation by TNFα, but declined after 24 hours and 48 hours, whilst VCAM-1 expression was maximal at 48 hours post stimulation, followed by 24 hours and the least at 4 hours.

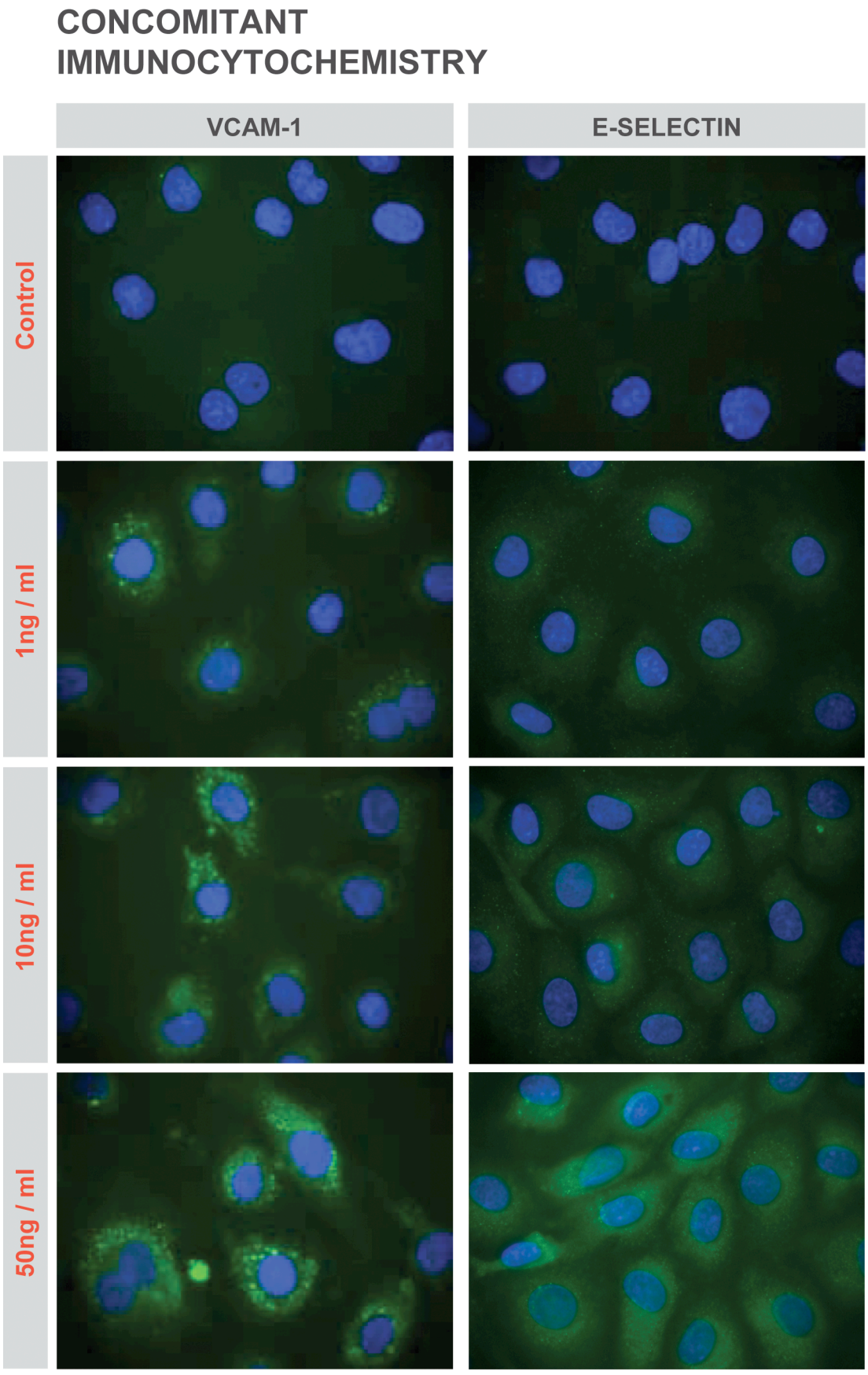



**Fig. 2.3 Immunocytochemistry for VCAM-1 and E-selectin on quiescent control bAEC (without TNFα stimulation) and activated bAEC by different concentrations of TNFα (1, 10 and 50ng/ml).** The level of expression of both VCAM-1 and E-selectin on activated bAEC were dose-dependent, i.e.

greatest level of expression on cells activated by 50ng/ml, followed by 10ng/ml, and finally the least with 1ng/ml TNFα. No expression of VCAM-1 or E-selectin was detected on the quiescent control cells. Green= FITC signal for VCAM-1 and E-selectin expression. Blue= DAPI staining for cell nuclei. Magnification x100.

### 2.3.2 MRI of Cell Phantom

The transaxial view of cell phantom MRI is illustrated in Figure 2.4. The streptavidin microbeads control were detected as signal void (hypointense signal) on the MR image using T2 spin echo sequence, and hence appeared to be darkest. Consistent with the immunocytochemistry results, activated bAEC stimulated by higher concentration of TNFα were observed to produce greater signal void, and appeared darker in the MR image. The bAEC stimulated by 50ng/ml TNFα were observed to be the darkest amongst the three concentrations used, followed by 10ng/ml, and finally the least with 1ng/ml TNFα. To quantify these observations, the mean signal-to-noise ratio (S/N) for each sample in 5 consecutive MR image slices was measured. The results are outlined in Figure 2.5. Consistent with the MR observations, the activated cells stimulated by higher concentration of TNFα produced a lower S/N and appeared to be darker. For further details on signal-to-noise ratio (S/N) calculated by Image J, please refer to Appendix B.

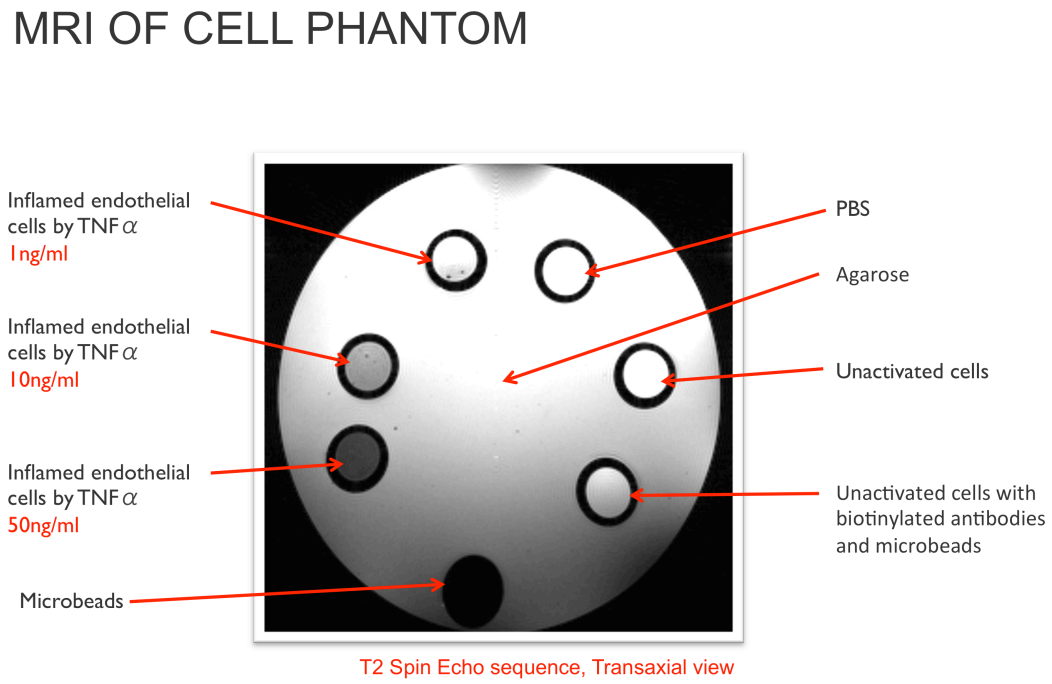



**Fig. 2.4 The transaxial view of MR image of cell phantom.** The streptavidin microbeads, positive control, were detected as signal void on the MR image using T2 spin echo sequence, and appeared to be the darkest amongst all the samples. The activated bAEC stimulated by higher concentration of TNFα were observed to produce greater signal void, and appeared darker on the MR image. The bAEC stimulated by 50ng/ml TNFα were observed to be the darkest amongst the three concentrations used, followed by 10ng/ml, and finally the least with 1ng/ml TNFα. By contrast, the negative controls: 1) PBS, 2) unactivated bAEC, and 3) unactivated bAEC added with biotinylated antibodies and microbeads were observed to produce minimal signal void, and appeared to be bright on the MR image.

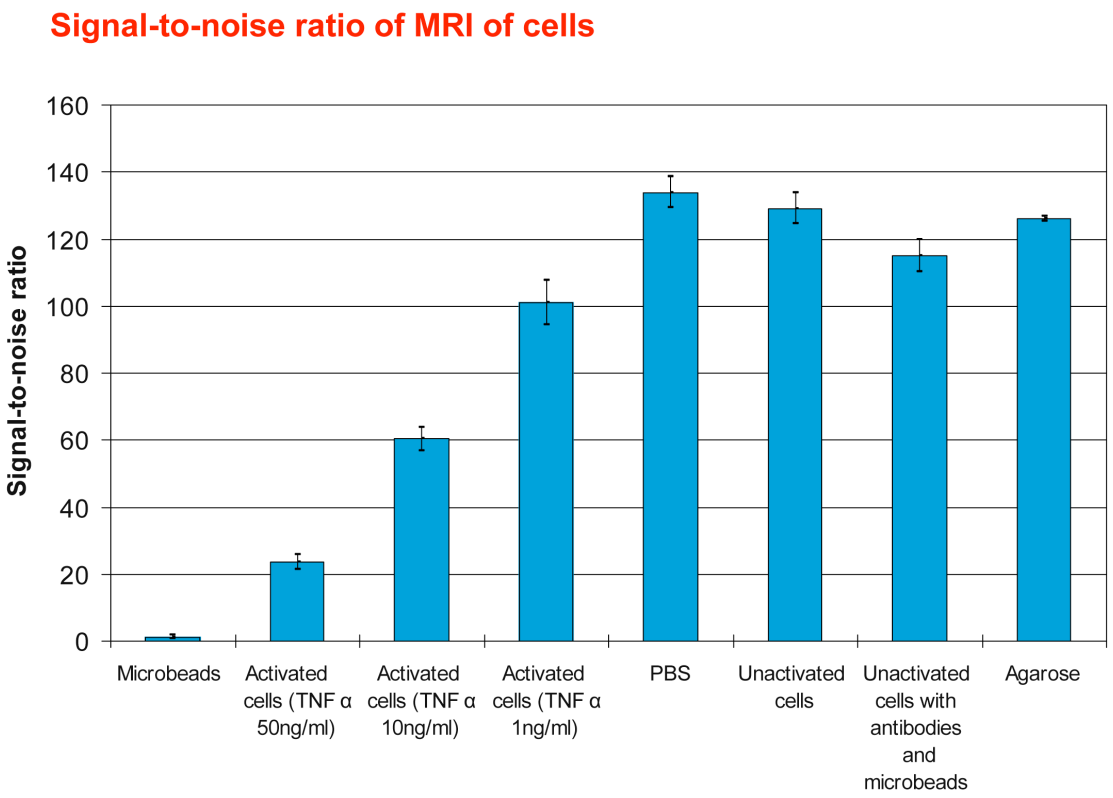



**Fig. 2.5 Signal-to-noise ratio of cell phantom MRI.** The S/N in streptavidin microbeads, positive control, was the smallest amongst all the samples. The activated cells stimulated by higher concentration of TNFα produced a lower S/N. By contrast, the negative controls: 1) PBS, 2) unactivated bAEC, and 3) unactivated bAEC added with biotinylated antibodies and microbeads produced high S/N.

## 2.4 DISCUSSION

We have established an *in vitro* model to detect and characterise inflamed endothelial cells by immunocytochemistry and MRI. This was supported by previous studies which have shown the up-regulation of E-selectin expression on endothelial activation in conditions such as atherosclerosis,[127] rheumatoid arthritis[145] and inflammatory bowel disease.[146] By using E-selectin conjugated USPIO, Reynolds *et al* [147] demonstrated that E-selectin expression on activated vascular endothelium in the inflamed mouse ear could be directly imaged by non-invasive *in vivo* MRI.

The role of VCAM-1 in the inflammatory initiation of atherosclerosis is well established in animal models.[139] Decreased VCAM-1 expression in experimental atherosclerosis appeared after treatment with either HMG- CoA reductase inhibitors[148] or angiotensin receptor blockers.[149] Moreover, it was suggested that the increased level of VCAM-1 expression appeared to be correlated with the extent of exposure to the atherosclerotic risk factors.[134] McAteer *et al* [133] demonstrated a dose dependent effect on the *in vitro* binding of anti-VCAM-1 MPIO to TNFα-stimulated endothelial cells. Consistent with this, we observed that activated cells stimulated by higher dose of TNFα produced greater signal void and appeared darker in the MR images. Higher dose of TNFα induced a greater level of E-selectin and VCAM-1 expression on the activated bAEC. Hence, greater amount of

antibody-conjugated microbeads were bound to these cells, producing a greater signal loss in T2 spin echo sequence and lower S/N.

## 2.5 CONCLUSION

We have established a robust *in vitro* model of vascular inflammation using bAEC induced with TNFα. We have successfully detected and characterised the degree of inflammation of endothelial cells by immunocytochemistry and MRI, which forms the basis for the next stages of this translational study to detect vascular inflammation in atherosclerosis.

# CHAPTER 3:

# *Ex Vivo* Human Carotid Plaque Stage

# 3.1 INTRODUCTION

To image vascular endothelial cell activation with MRI, we previously developed prototypic biotinylated antibody-conjugated streptavidin microbeads, which were essentially 50nm diameter streptavidin superparamagnetic particles of iron oxide (SPIO) conjugated to biotinylated antibodies against VCAM-1 and E-selectin as described in the previous chapter. This approach proved promising in the pilot *in vitro* feasibility study, in which the degree of inflammation on endothelial cells was characterised using the targeted SPIO as a molecular MRI probe. The next step was to determine whether this molecular MRI methodology could be successfully utilised to study human plaque tissue.

In this chapter, we describe the detection and characterisation of E-selectin and VCAM-1 on explanted human carotid plaques using antibody-conjugated SPIO and immunohistochemistry. The extent to which antibody-conjugated SPIO-induced MR signal tracks endothelial activation across a range of atherosclerotic lesions complexities in human by *ex vivo* MRI is evaluated. We hypothesised that symptomatic carotid plaques could be discriminated from asymptomatic ones predicated on the degree of inflammation detected, and additionally sought to determine whether heterogeneity within the asymptomatic plaque population based on the degree of inflammation could be detected using these MRI probes.

# 3.2 MATERIALS AND METHODS

## 3.2.1 Study Population

Atherosclerotic plaques were collected from 20 consecutive patients (n=10 from symptomatic patients, n=10 from asymptomatic patients) undergoing carotid endarterectomy (CEA) for extracranial high-grade internal carotid artery (ICA) stenosis (>70% luminal narrowing). Using NASCET criteria, "symptomatic" patients were defined as those who had a history of recent (less than 121 days before enlistment) occurrence of transient retinal or cerebral symptoms or ischaemic stroke attributable to the high-grade ICA lesion.[150] "Asymptomatic" patients were defined as those who had a history of no or only remote (more than 120 days) ischaemic symptoms. The symptomatic group had presented with cerebrovascular TIAs (n=8) or ischaemic stroke (n=2) within the preceding 4 months. All other specimens were collected from 10 clinically asymptomatic patients (with no history of ischaemic symptoms) exhibiting progressive ipsilateral ICA stenosis of >70% on serial ultrasound duplex. The degree of ICA stenosis was established in two consecutive ultrasound duplex before surgery in all cases. The degree of luminal stenosis was additionally confirmed by either computed tomography angiography (CTA) or magnetic resonance angiography (MRA). Preoperatively all patients underwent neurological evaluation. Macroscopically normal specimens adjacent to endarterectomised plaques were harvested from patients (n=2) who underwent femoral endarterectomy and served as

controls for MRI and histology. The study was approved by the local ethics committee, and written informed consent was obtained from all patients.

### 3.2.2 Tissue Collection

All patients underwent CEA in the regional vascular unit in St Mary's Hospital, Imperial College Healthcare NHS Trust, UK. The mean duration of patients undergoing CEA after symptom onset was 17 days (SD=16.4). At operation the carotid artery bifurcation was endarterectomised with an aim to remove the whole plaque intact (Figure 3.1). The excised plaque sample consisted of intima and inner medial layers of the artery. Thereafter the plaque was rinsed with PBS and cut into 5 sections, each of which was further subdivided into 2 smaller adjacent sections (Figure 3.2). Great care was taken to prevent plaque disintegration during division of the unfixed specimens. The orientation and sequence of the sections were marked and recorded. One adjacent section was fixed in 4% paraformaldehyde (PFA) at 4°C for MRI detection and characterisation of inflammatory markers (see section 3.2.3 and 3.2.4), whilst the other adjacent section was fixed in formalin and embedded in paraffin blocks for immunohistochemistry (see section 3.2.5). Concomitant immunohistochemistry was performed to correlate MRI data.

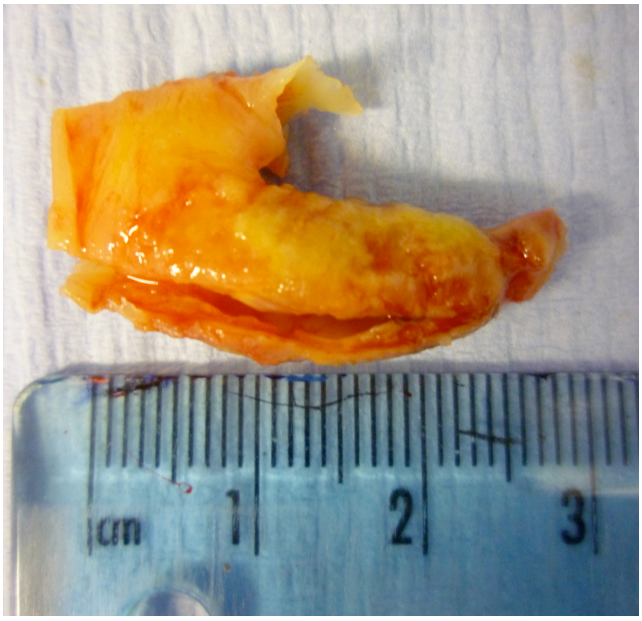



**Fig. 3.1 Carotid endarterectomy specimen.** At CEA operation, the carotid artery bifurcation was endarterectomised with an aim to remove the whole plaque intact.

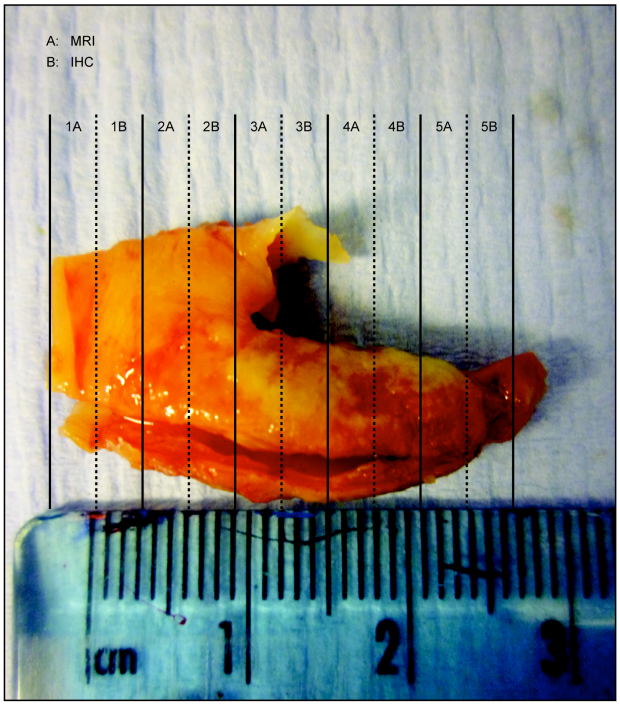



**Fig. 3.2 Carotid endarterectomy specimen cut into sections.** The plaque was cut into 5 sections, each of which was further subdivided into 2 smaller adjacent sections. One adjacent section was used for MRI detection and characterisation of inflammatory markers, whilst the other adjacent section was used for immunohistochemistry.

### 3.2.3 Detection, Characterisation and Imaging of Inflammatory Markers on Human Carotid Plaques by Biotinylated Antibody-Conjugated Streptavidin Microbeads

The principle was similar to that described in the *in vitro* stage in section 2.2. Following fixation in 4% PFA, plaque sections were rinsed in PBS. They were incubated with 2% horse serum at room temperature for 1 hour to block non-specific binding of antibodies. Plaque sections were then incubated with biotinylated mouse anti-human E-selectin monoclonal antibody (dilution: 10µg/ml, R&D Systems, Abingdon, UK) and biotinylated mouse anti-human VCAM-1 monoclonal antibody (dilution: 10µg/ml, GenWay Biotech, San Diego, USA) for 20 minutes at room temperature. Plaque sections were washed twice to remove unbound biotinylated antibodies by incubating with labelling buffer composed of PBS, supplemented with 2mM EDTA at 4°C for 10 minutes. The plaques were incubated in streptavidin microbeads (Miltenyi Biotec Ltd, Surrey, UK) diluted in labelling buffer (dilution 1:10) at 4°C for 15 minutes and washed to remove unbound streptavidin microbeads (Figure 3.3).

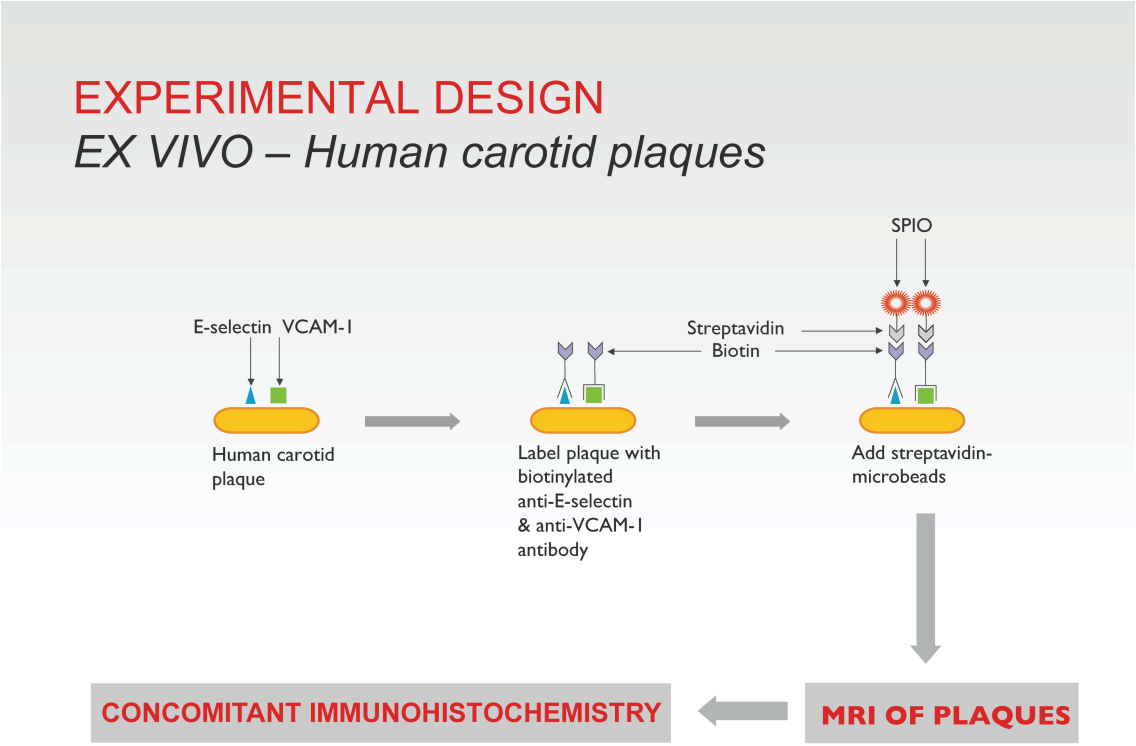



**Fig. 3.3 Experimental design of *ex vivo* human plaque stage.** The inflammatory markers on human carotid plaque were detected by biotinylated antibodies, which were in turn bound to the streptavidin microbeads, thereby making these plaques 'MR visible'. Concomitant immunohistochemistry was performed.

### 3.2.4 *Ex Vivo* MRI of Human Carotid Plaques

The carotid plaque from each patient was divided into 5 smaller sections giving symptomatic (n=10, 50 sections), asymptomatic (n=10, 50 sections), control femoral artery sections (n=2, 10 sections), together with 3 controls (symptomatic carotid plaque incubated with biotinylated non-immune IgG antibodies and microbeads, symptomatic carotid plaque, and streptavidin microbeads). All were embedded in 2% agarose (Sigma-Aldrich, Dorset, UK) (Figure 3.4).

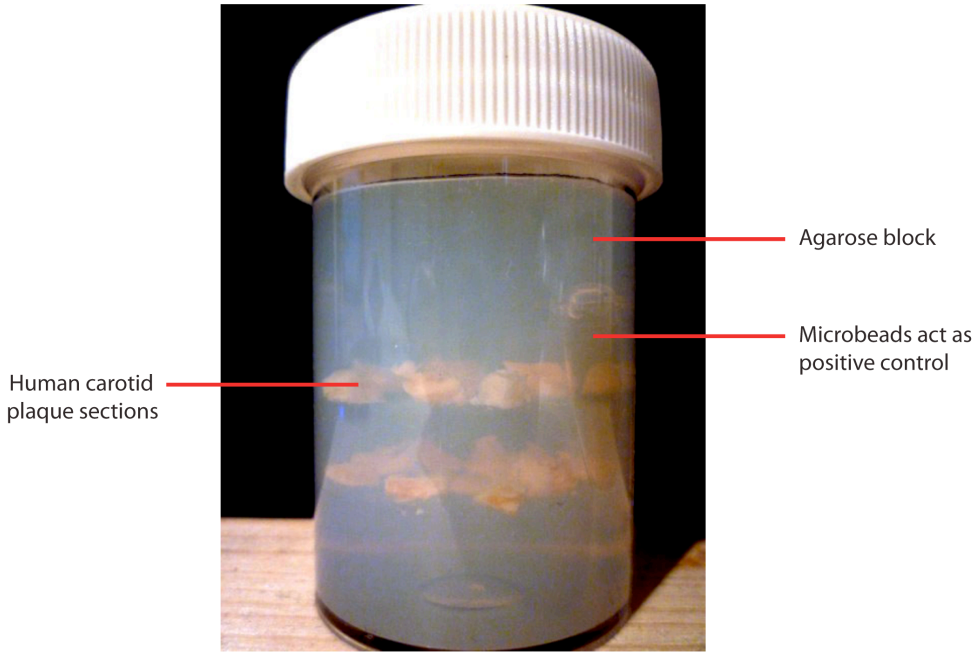



**Fig. 3.4 Human carotid plaque sections embedded in agarose block.** A tube of microbeads was also embedded in the agarose block to act as positive control.

*Ex vivo* MRI of human carotid plaques was performed using a 9.4 Tesla, horizontal bore scanner (Varian Inc., Palo Alto, CA, USA) running VnmrJ 2.3A software. The sample was placed in a quadrature birdcage coil (40mm internal diameter). T2 spin echo sequence was used with the following parameters: TR: 4500 ms; 16 echo times (TE): 5.344ms, 10.688ms, 16.032ms, 21.376ms, 26.72ms, 32.064ms, 37.408ms, 42.752ms, 48.096ms, 53.44ms, 58.784ms, 64.128ms, 69.472ms, 74.816ms, 80.16ms, 85.504ms; FOV 40x40 mm; Matrix 256x256; Average: 4; Thickness 0.5mm; Number of slices: 30; plane: axial; Flip angle: 90/180°.

### 3.2.4.1 Quantitative MR image analysis

MR images were analysed by ImageJ 1.43r software (National Institutes of Health, http://rsb.info.nih.gov/ij/index.html). The contours of each plaque section on the MR image were delineated manually and independently by two observers and defined as the region of interest (ROI). The signal within the ROI (plaque signal) was measured using ImageJ 1.43r software. The contrast effect in each plaque section was quantified by $T_2$ value, which was calculated using GraphPad Prism® 5 software (GraphPad software Inc., San Diego, USA).

***Intra-observer and inter-observer agreement***

The contours of all plaque sections on the MR images in every subject were delineated manually by one observer. Additionally, intra-observer agreement was assessed. The same manual delineation, plaque signal measurement and $T_2$ calculation procedures in every plaque sections were performed a second time by the same observer. To reduce recall bias, the second procedure took place at least 1 month after the first procedure. Moreover, inter-observer agreement was tested. The manual delineation, plaque signal measurement and $T_2$ calculation procedures on the MR images of all subjects were performed by another observer. The studies were presented in a random order.

## 3.2.5 Immunohistochemistry

### 3.2.5.1 Fixation and paraffin embedding of tissue

***Tissue fixation***

The freshly dissected carotid endarterectomy specimens were rinsed with PBS and cut transversely into small sections 3mm thick. The orientation and sequence of sections were marked and recorded prior to placement in tissue cassettes. Plaque sections were immediately fixed in 10% neutral buffered formalin (NBF) at room temperature for 24 hours before being rinsed with running tap water for 1 hour. Formalin was handled in a fume hood as it is a suspect carcinogen and can cause eye, skin and respiratory tract irritation. Acidic decalcification of plaque tissues was avoided as the acid reagents can cause progressive hydrolytic loss of ferric ions from tissue and may lead to false negative result in Perls' Prussian blue staining.[151]

***Paraffin embedding***

Plaque sections were dehydrated through a series of increasing alcohol concentrations. Sections were transferred sequentially to 70%, 80%, 95% and 100% alcohol for 2 hours each. They were then placed in a second 100% alcohol for 2 hours to ensure all water was removed. Sections were cleared through 2 changes of Xylene for 1 hour each. They were then immersed in 3 changes of paraffin at 56-58°C (the melting temperature of paraffin) for 1 hour each. Plaque tissues were properly orientated prior to embedment in paraffin blocks.

### 3.2.5.2 Preparation of paraffin sections for immunohistochemistry

***Tissue sectioning***

Paraffin-embedded tissue blocks were sectioned at 4μm thickness on a microtome. The sectioned paraffin slices were allowed to float on a 40°C water bath containing distilled water. Sections were mounted from warm water onto a silane coated slide (Sigma-Aldrich, Dorset, UK). The orientation and sequence of sections were recorded. Slides were allowed to dry overnight and store at room temperature until ready for use.

***Deparaffinization and rehydration of tissue slide***

Prior to deparaffinization, slides were placed in an oven at 60°C for 10 minutes to melt the paraffin. Sections were deparaffinized in 2 changes of Xylene for 5 minutes each. Sections were then rehydrated through 3 changes of 100% alcohol, 2 changes of 95% alcohol and 2 changes of 70% alcohol for 3 minutes each. Slides were rinsed in running distilled water for 5 minutes. Sections were incubated in 0.3% $H_2O_2$ solution in methanol at room temperature for 10 minutes to block endogenous peroxidase activity. Sections were rinsed through 2 changes of PBS for 5 minutes each.

***Antigen retrieval***

Serial histology sections underwent immunostaining for VCAM-1, E-selectin, CD68 (macrophages) and CD31 (endothelial cells). The presence of intralesional iron, indicative of past intraplaque haemorrhage, was visualised

using Perls' Prussian blue iron stain. One section per each antibody was stained with the peroxidase method.

Sections underwent heat-induced antigen retrieval in either citrate buffer (E-selectin, CD68 and CD31) or EDTA buffer (VCAM-1) to expose antibody epitopes. For anti-E-selectin, CD68 and CD31 immunostaining, antigen retrieval using 10mM sodium citrate buffer (pH6) was performed – the former E-selectin for 20 minutes and the latter two for 30 minutes in a microwave. For anti-VCAM-1 staining, antigen retrieval using 1mM EDTA buffer (pH8) for 20 minutes in a microwave was required. Sections were washed in 4 changes of distilled water and 2 changes of PBS for 5 minutes each.

#### 3.2.5.3 Immunohistochemical staining of paraffin embedded tissues

***E-selectin, VCAM-1, CD68 and CD31***

All incubations were performed in a humidified chamber and sections were not allowed to dry out. As controls for positive staining, paraffin embedded human atherosclerotic plaque sections were stained in parallel experiments for E-selectin, VCAM-1, CD68 and CD31.[122,127,152] For negative controls, one section on each slide was incubated with non-immune mouse IgG (Vector Laboratories, Peterborough, UK) of equivalent dilutions of the respective primary antibodies to determine staining specificity (Figure 3.5).

Sections were incubated with 2% horse serum (VECTASTAIN® ABC Kit, Vector Laboratories, Peterborough, UK) at room temperature for 1 hour to block non-specific binding of antibodies and thus reduce background staining.

Sections were then incubated at 4°C overnight with the respective primary mouse monoclonal anti-human antibodies listed in Table 3.1. Sections were rinsed in 3 changes of washing buffer (0.1% Triton X-100 in PBS) for 5 minutes each between antibody applications to remove unbound and non-specific binding of antibodies. Primary antibodies were detected by incubating sections with biotinylated horse anti-mouse secondary antibodies (VECTASTAIN® ABC Kit, Vector Laboratories, Peterborough, UK) for 1 hour at room temperature. Secondary antibodies were detected using the avidin-biotin-complex (ABC) reagent (VECTASTAIN® Elite® ABC Kit, Vector Laboratories, Peterborough, UK) for 30 minutes at room temperature. The ABC system was visualised by the development of the 3,3'-diaminobenzidine (DAB) substrate (DAB peroxidase substrate kit, Vector Laboratories, Peterborough, UK) prepared according to the manufacturer's instructions. Following development of brown reaction product, sections were rinsed in running tap water for 5 minutes to stop the reaction. Sections were counterstained with Harris Haematoxylin for 1 minute. Slides were rinsed in running tape water then distilled water for 5 minutes each.

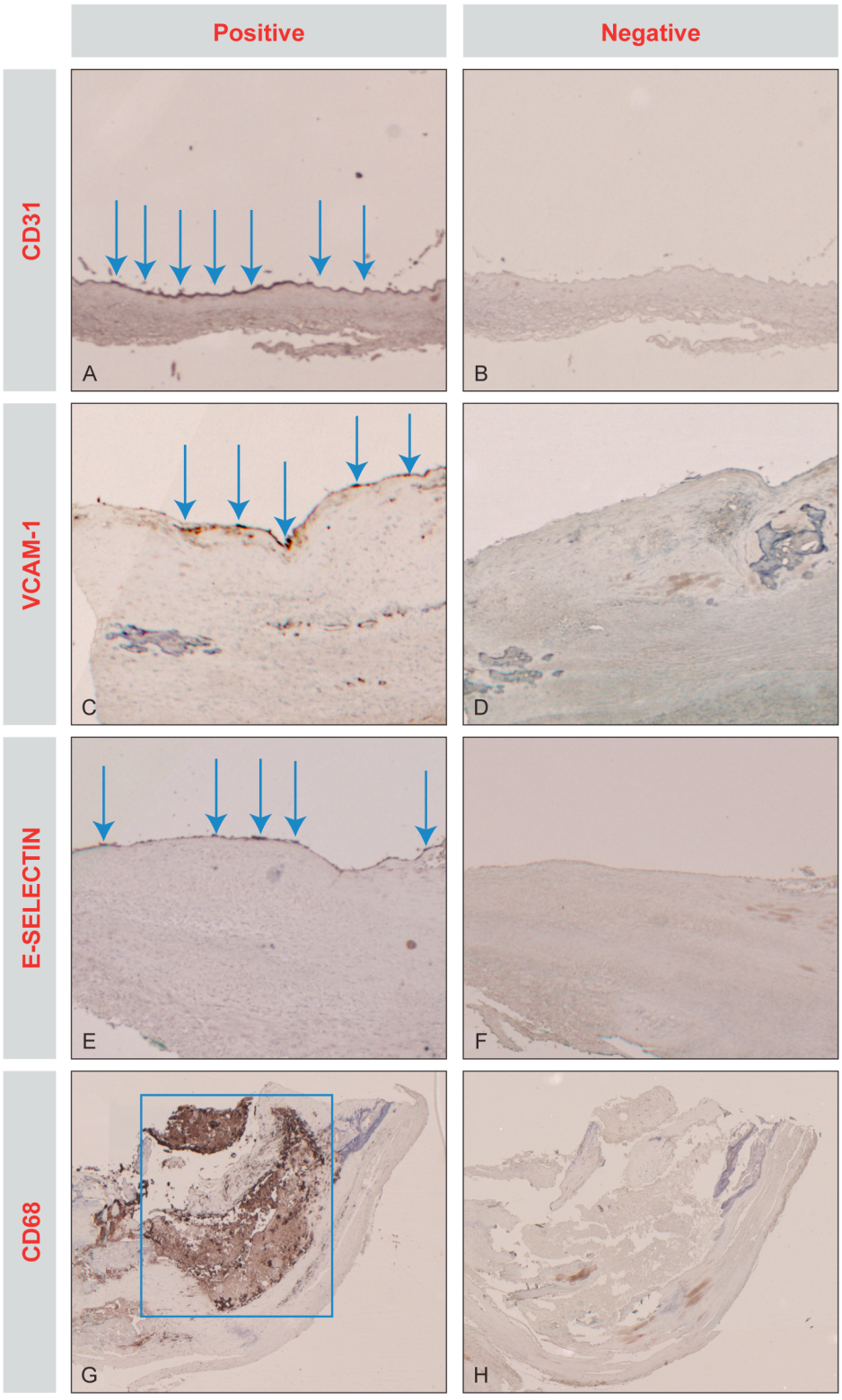



**Fig. 3.5 Representative images of human atherosclerotic plaque sections of positive and negative antibody control for CD31, VCAM-1, E-selectin and CD68 staining.**

Panel A (positive control) shows CD31 immunoreactivity (brown stain) in human atherosclerotic plaque. Blue arrows indicate endothelial cells exhibiting specific CD31 immunoreactivity in human atherosclerotic plaque. Panel B (negative control) shows no CD31 immunoreactivity in matching non-immune IgG controls. Original magnification x4

Panel C (positive control) shows VCAM-1 immunoreactivity (brown stain) in human atherosclerotic plaque (blue arrows). Panel D (negative control) shows no VCAM-1 immunoreactivity in matching non-immune IgG controls. Original magnification x4

Panel E (positive control) shows E-selectin immunoreactivity (brown stain) in human atherosclerotic plaque (blue arrows). Panel F (negative control) shows no E-selectin immunoreactivity in matching non-immune IgG controls. Original magnification x4

Panel G (positive control) shows CD68 immunoreactivity (brown stain) in human atherosclerotic plaque. Blue box indicates a group of CD68 immunoreactive cells (putatively macrophages) in the intima of atherosclerotic plaque. Panel H (negative control) shows no CD68 immunoreactivity in matching non-immune IgG controls. Original magnification x4

| Specificity/Target | Name | Concentration | Product number | Supplier |
|---|---|---|---|---|
| VCAM-1 | Mouse monoclonal anti-human VCAM-1 antibody | Pre-diluted concentration: 28.5µg/ml | Ab74514 | Abcam |
| E-selectin (CD62E) | Mouse monoclonal anti-human E-selectin antibody | 1:100 | Ab8165 | Abcam |
| Macrophages | Mouse monoclonal anti-human CD68 antibody | 1:50 | M0876 | Dako |
| Endothelial cells | Mouse monoclonal anti-human CD31 antibody | 1:100 | NCL-CD31-1A10 | Novocastra |

**Table 3.1. Primary antibodies used in immunohistochemical staining of paraffin embedded human carotid plaque sections.**
Abcam (Cambridge, UK); Dako (Ely, UK); Novocastra (Leica Microsystems Ltd., Milton Keynes, UK).

### *Perls' Prussian Blue*

Sections were deparaffinized with Xylene, rehydrated through graded alcohol concentrations and rinsed in distilled water as described in Section 3.2.5.2. Sections were immersed in equal parts mixture of 2% hydrochloric acid and 2% potassium ferrocyanide for 15 minutes at room temperature. Sections were washed in 3 changes of distilled water for 5 minutes each between each step.

Sections were counterstained with 0.2% saffranin in 1% acetic acid for 1 minute. As controls for positive staining, paraffin embedded spleen sections were stained in parallel experiments.

***Dehydration and mounting slides***

Sections were dehydrated through 4 changes of 70%, 90%, 100% and 100% alcohol and cleared through 2 changes of Xylene for 10 minutes each. Finally, sections were mounted with coverslips using DPX mounting medium (Leica Microsystems Ltd., Milton Keynes, UK).

### 3.2.5.4 Microscopy and quantification of immunostaining

Wide-field microscopy was performed with a Zeiss Axiovert 200 inverted microscope. The area of positive staining of VCAM-1, E-selectin, CD68 (macrophages), CD31 (endothelial cells) and Perls' stain (intralesional iron) in each plaque section was objectively quantified using Volocity® 5.5 image analysis software (PerkinElmer, Massachusetts, USA) (Figure 3.6). The stained area of Perls' (iron) and CD68 (macrophages) was quantified as a percentage of the total lesion area.[152] CD31 is commonly used to demonstrate the presence of endothelial cells. Hence the area of CD31 expression was considered as a total area of intact endothelium. Quantitative stereological analysis of VCAM-1 and E-selectin endothelial expression was related to CD31 staining in endothelium and calculated as

**VCAM-1/E-selectin expression on endothelial cells (%) = [Area (x) / Area (CD31)] x 100%**

where area (x) is the area of VCAM-1 or E-selectin expression in the endothelium and area (CD31) is the area of CD31 expression in the endothelium.[153]

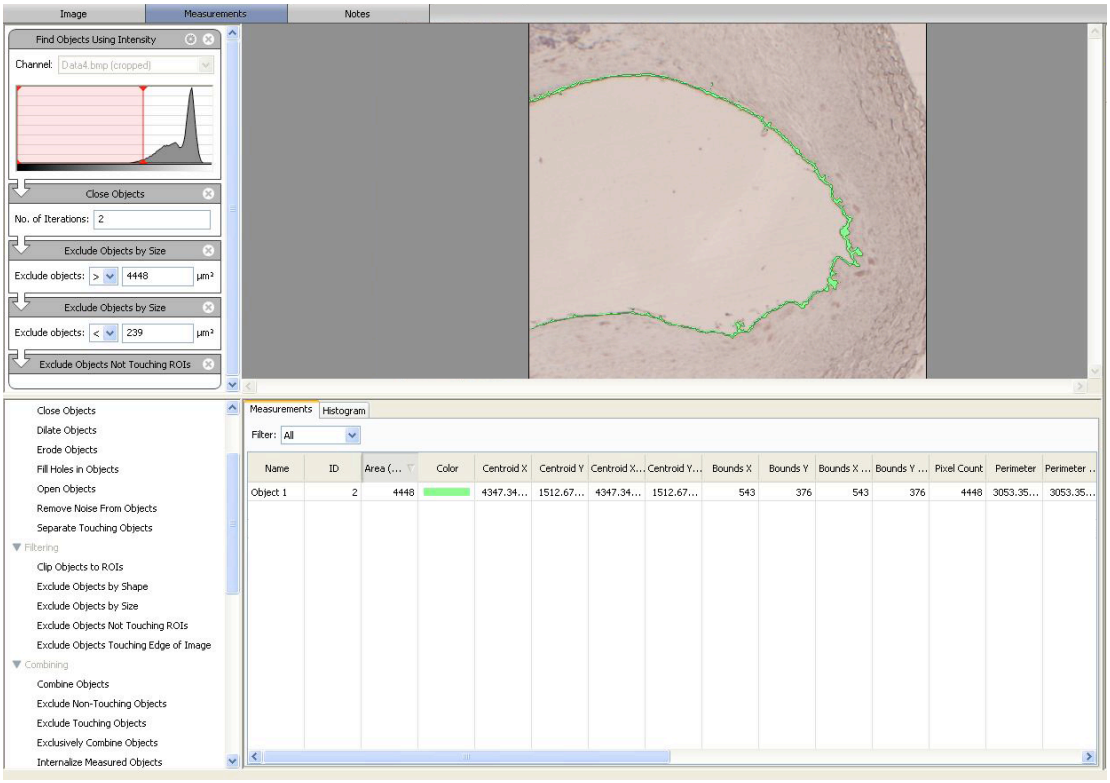



**Fig. 3.6 Objective quantification of immunostaining.** The stained area of CD31 (endothelial cells) in the human carotid plaque was selected (in green) and objectively quantified using Volocity® 5.5 image analysis software.

### 3.2.6 Statistical Methods

To assess differences in categorical variables in patient clinical characteristics, Fisher's exact test (two-tailed) was used. The relationship between the mean macrophage content and MR contrast effect quantified by mean $1/T_2$ of the whole plaque per patient was assessed by Spearman's correlation. Further, the strength of the relationship between histological marker data (expression of VCAM-1, E-selectin, CD68 and Perls' iron stain) and MR image data ($1/T_2$) in each of the five carotid plaque sections per patient was assessed by using correlation and regression analysis. Since data was collected on five sections per patient, repeated measures regression model were fitted by using MR image data as response variables and histological marker data as predictor variables, taking the symptom status of patient into account. In this model, sections were repeated measures for each patient and patient was taken as a random factor. The overall regression model significance was assessed by F test and the significance of the regression model parameter estimates were tested using t test. Repeated measures analysis of variance (ANOVA) was performed using general linear model (GLM) function in Statistical Analysis System (SAS) 9.1 software (SAS Institute, Inc, NC). A value of $P< 0.05$ was considered statistically significant. Intra-observer and inter-observer variability in $T_2$ values were analysed using Bland-Altman plot.

# 3.3 RESULTS

## 3.3.1 Baseline Demographics

Baseline demographics and clinical risk factors were similar in both symptomatic and asymptomatic patient groups (Table 3.2). Although more symptomatic patients were taking clopidogrel (4 of 10 vs. 0 of 10), the difference was not statistically significant.

| Variable | Symptomatic | Asymptomatic | P |
|---|---|---|---|
| Median age (range) | 73 (67-76) | 72 (66-77) | 0.7039** |
| Gender, Male/Female | 7/3 | 6/4 | 1.0000 |
| TIA, No. | 8 | 0 | 0.0007* |
| Stroke, No. | 2 | 0 | 0.4737 |
| Ischaemic heart disease, No | 4 | 5 | 1.0000 |
| Diabetes mellitus, No. | 2 | 3 | 1.0000 |
| Hypertension, No. | 7 | 7 | 1.0000 |
| Hypercholesterolaemia, No. | 7 | 8 | 1.0000 |
| Smoking, No. | 4 | 6 | 0.6563 |
| Medications: Statin, No. | 6 | 8 | 0.6285 |
| Medications: Antihypertensives, No. | 7 | 7 | 1.0000 |
| Medications: Aspirin, No. | 5 | 7 | 0.6499 |
| Medications:Clopidogrel, No. | 4 | 0 | 0.0867 |
| Medications: NSAIDs, No. | 2 | 1 | 1.0000 |

NSAIDs, Non-steroidal anti-inflammatory drugs; TIA, transient ischemic attack. *None of these characteristics differ significantly other than that for TIA, as determined by the Fisher Exact test. **No significant difference in age was found between the two patient groups, as determined by the Mann-Whitney U test.

**Table 3.2 Patient clinical characteristics.**

### 3.3.2 Immunohistochemistry

Representative histology images of human carotid plaque and control femoral artery tissue (i.e. macroscopically normal specimen adjacent to femoral endarterectomy plaque) are shown in Figure 3.7.

### 3.3.3 Intra-observer and Inter-observer Variability in Quantification of SPIO-induced Contrast Effect

The Bland-Altman plot was used to assess the intra-observer and inter-observer variability in quantification of SPIO-induced contrast effect on plaque sections ($T_2$ value). The Bland-Altman plot in Figure 3.8 demonstrated that the differences in $T_2$ values of plaque sections measured by the same observer at two different time points (one month interval) were within the 95% limits of agreement (mean difference ± 1.96 x standard deviation of the difference). Therefore, there was no significant intra-observer variability in the measurement of $T_2$ values in the plaque sections.

The Bland-Altman plot in Figure 3.9 showed that the differences in $T_2$ values of plaque sections independently measured by two observers were within the 95% limits of agreement. Therefore, there was no significant inter-observer variability in the measurement of $T_2$ values in the plaque sections.

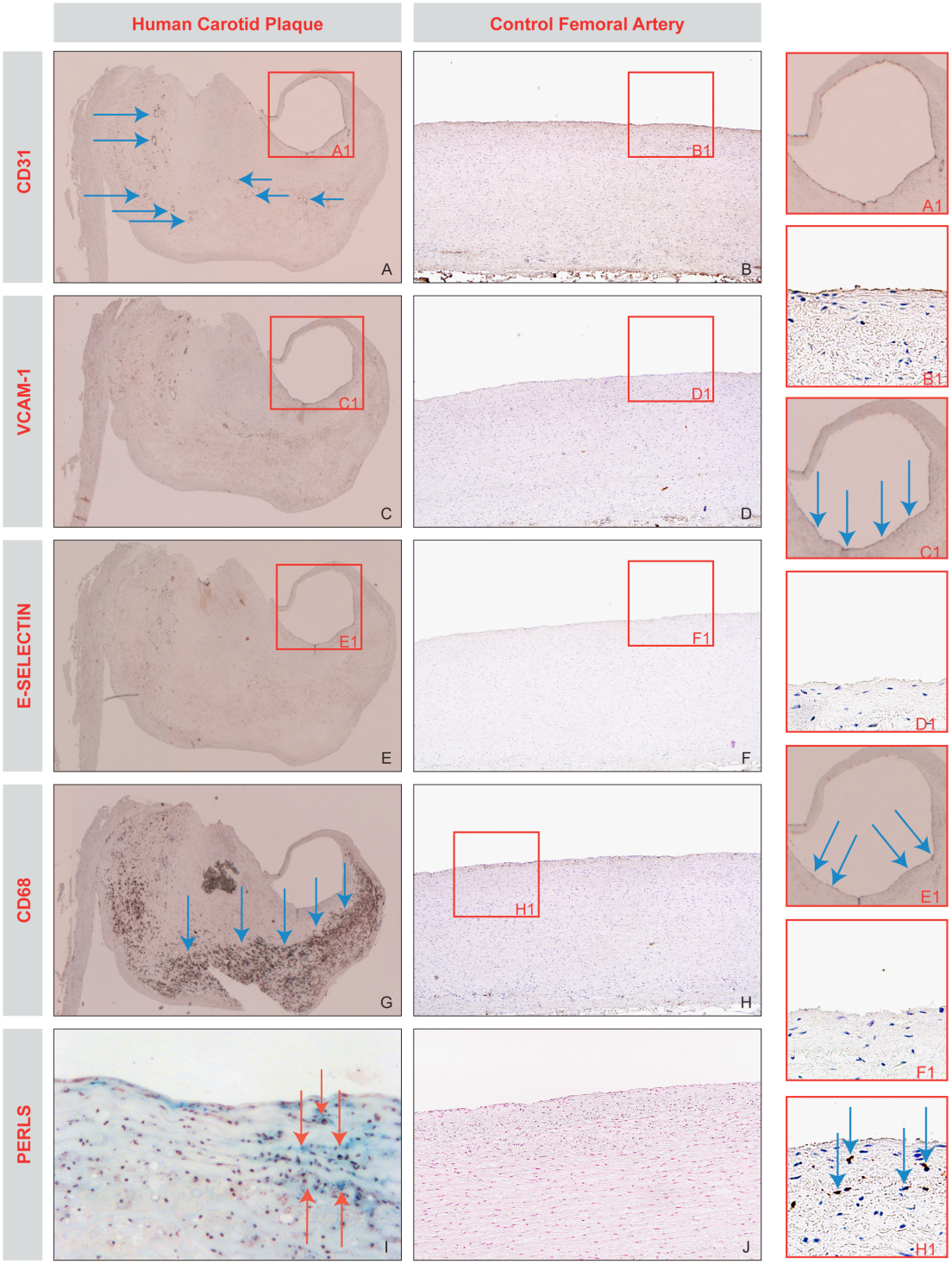



**Fig. 3.7 Representative histology images of human carotid plaque and control femoral artery.**

Panel A shows CD31 immunoreactivity (brown stain) in human carotid plaque. Red box (A1) indicates endothelial cells exhibiting specific CD31 immunoreactivity in the lumen of carotid plaque. Blue arrows indicate neovessels within plaque, which are identified by the presence of circular structures lined with cells staining positive for CD31. Panel B shows CD31 immunoreactivity (brown stain) in control femoral artery. Red box (B1) indicates endothelial cells exhibiting specific CD31 immunoreactivity in the control femoral artery. Original magnification x4

Panel C shows VCAM-1 immunoreactivity (brown stain) in human carotid plaque. Blue arrows in red box (C1) indicate endothelial cells exhibiting specific VCAM-1 immunoreactivity in human carotid plaque. Panel D (red box D1) shows no specific VCAM-1 immunoreactivity in control femoral artery. Original magnification x4

Panel E shows E-selectin immunoreactivity (brown stain) in human carotid plaque. Blue arrows in red box (E1) indicate endothelial cells exhibiting specific E-selectin immunoreactivity in human carotid plaque. Panel F (red box F1) shows no specific E-selectin immunoreactivity in control femoral artery. Original magnification x4

Panel G shows CD68 immunoreactivity (brown stain) in human carotid plaque. Blue arrows indicate an abundant amount of CD68 immunoreactive cells (putatively macrophages) in the intima of atherosclerotic plaque. Panel H (red box H1) shows small amount of CD68 immunoreactivity (blue arrows) in control femoral artery. Original magnification x4

The effect of intralesional iron content, indicative of past intraplaque haemorrhage, as visualised by the blue Perls' stain in human carotid plaque is shown in Panel I (red arrows). Panel J shows no Perls' stain for iron, suggesting no haemorrhage within the control femoral artery section. Original magnification x10

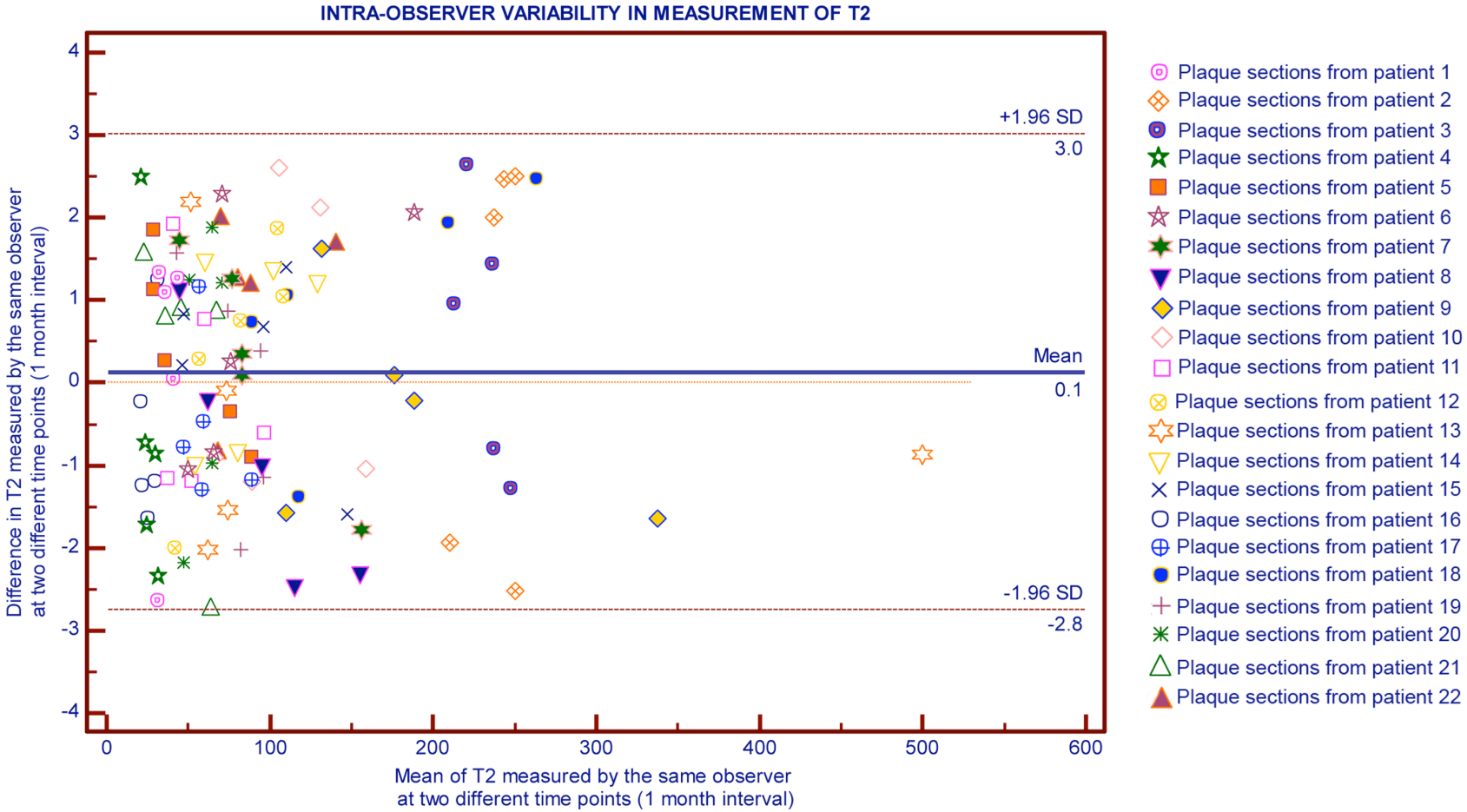



**Fig 3.8. The Bland-Altman plot for intra-observer variability.** The plot demonstrated that the differences in $T_2$ values of plaque sections measured by the same observer at two different time points (one month interval) were within the 95% limits of agreement (mean difference ± 1.96 x standard deviation of the difference).

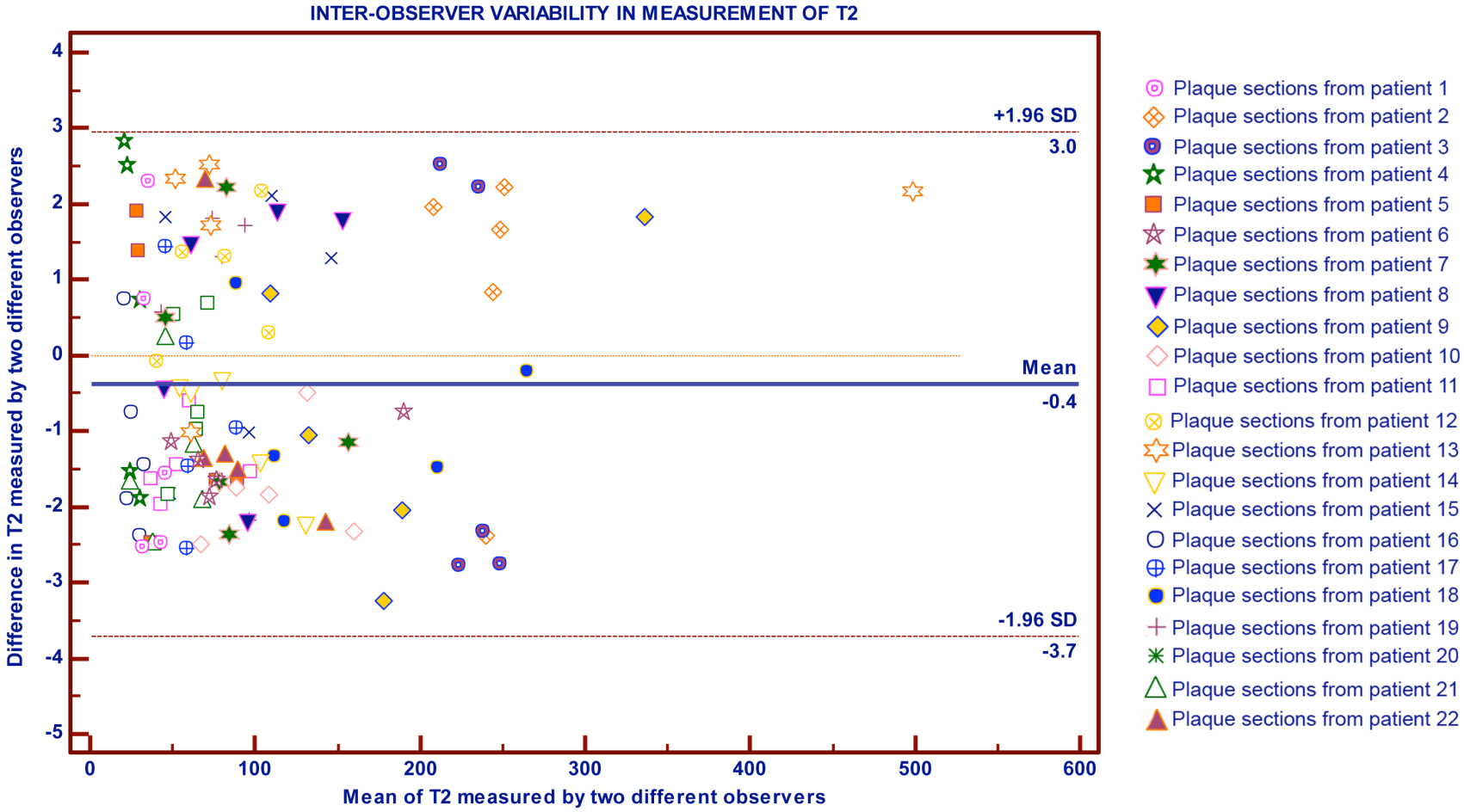



**Fig 3.9. The Bland-Altman plot for inter-observer variability.** The plot demonstrated the differences in $T_2$ values of plaque sections independently measured by two observers were within the 95% limits of agreement. (mean difference ± 1.96 x standard deviation of the difference).

### 3.3.4 Relationship between Mean Macrophage Content and Mean 1/ $T_2$ of Whole Plaque

This study showed that the degree of inflammation associated with human atherosclerotic plaques could be imaged using dual-antibody conjugated SPIO by *ex vivo* MRI. Figure 3.10 demonstrates a spectrum of MR images ranging from phenotypically symptomatic inflamed plaques, appearing darkest, followed by the asymptomatic plaques, to control femoral artery and negative controls (symptomatic plaque only and symptomatic plaque with IgG and microbeads), appearing brightest. Macrophage content in plaque was used as an index of plaque inflammation. Plaque was defined as inflamed if there was greater than 5% of macrophage staining in the total lesion area. Importantly, it was possible to observe a degree of heterogeneity in the asymptomatic plaque population based on the varying degree of inflammation, with inflamed plaques appearing darker than non-inflamed ones. Consistent with the MR images, the concomitant immunohistochemistry for CD68 (macrophages) was observed to be the most abundant on phenotypically symptomatic inflamed plaques, followed by the inflamed asymptomatic ones, then the non-inflamed asymptomatic ones and the least for the control femoral artery sections.

To quantify these observations, the mean 1/ $T_2$ value of whole plaque was calculated. Figure 3.11 demonstrates that the mean macrophage content (index of plaque inflammation) is significantly correlated with the mean 1/ $T_2$ (MR contrast effect) of the whole plaque per patient ($r=0.64$, $P<0.001$). Consistent with the MRI results, the symptomatic plaques (in red) with the greater level of inflammation produced a higher 1/ $T_2$ value and

appeared darker; followed by the inflamed asymptomatic plaques (in orange), then the non-inflamed plaques (in yellow).

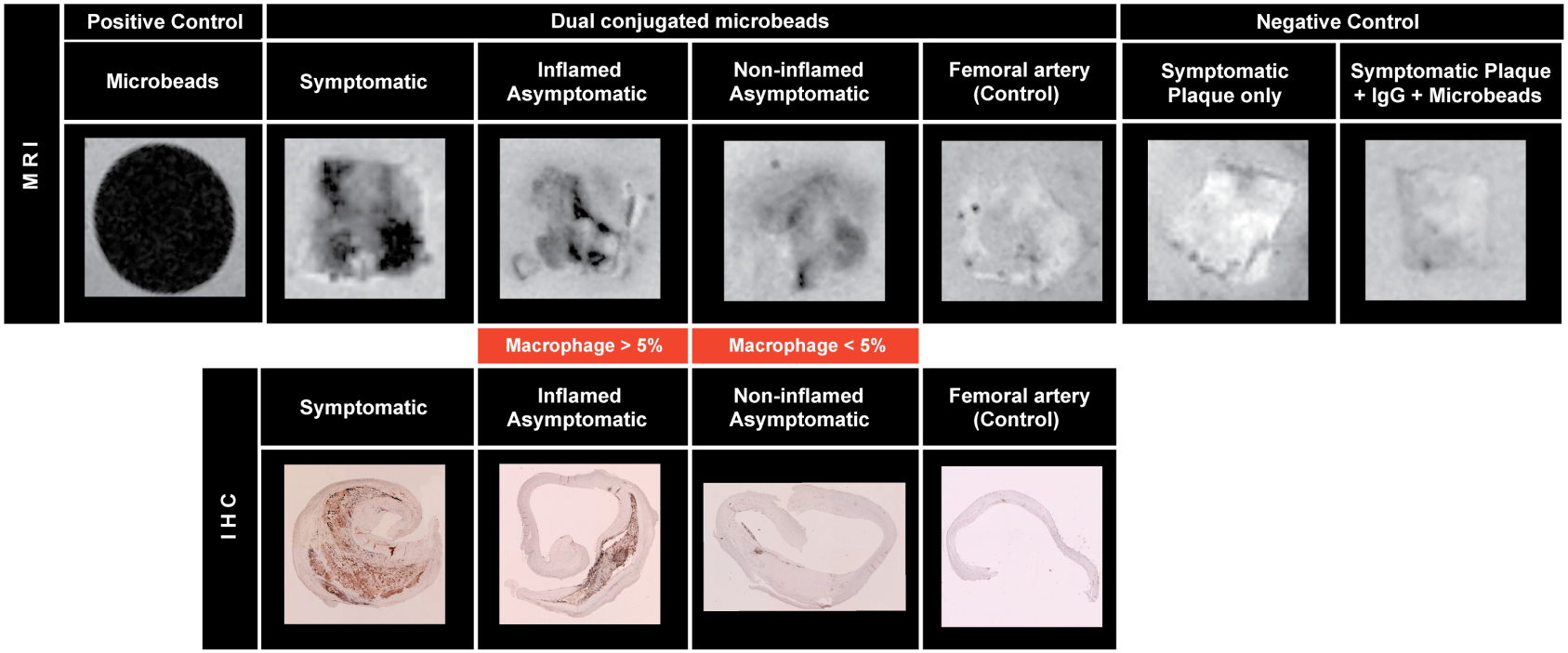



**Fig. 3.10 Spectrum of MR images and histological images of phenotypically symptomatic plaques, asymptomatic plaques and control femoral artery.**

The spectrum of MR images in the upper row range from phenotypically symptomatic inflamed plaques, appearing darkest, followed by the asymptomatic plaques, to control femoral artery and negative controls (symptomatic plaque only and symptomatic plaque with IgG and microbeads), appearing brightest. Importantly, a degree of heterogeneity in the asymptomatic plaque population is detected, with inflamed plaques appearing darker than non-inflamed ones.

Consistent with the MR images, the concomitant immunohistochemistry for CD68 (macrophages as indicated by brown stain) in the lower row is observed to be the most abundant on phenotypically symptomatic inflamed plaques, followed by the inflamed asymptomatic ones, then the non-inflamed asymptomatic ones and the least for the control femoral artery sections.

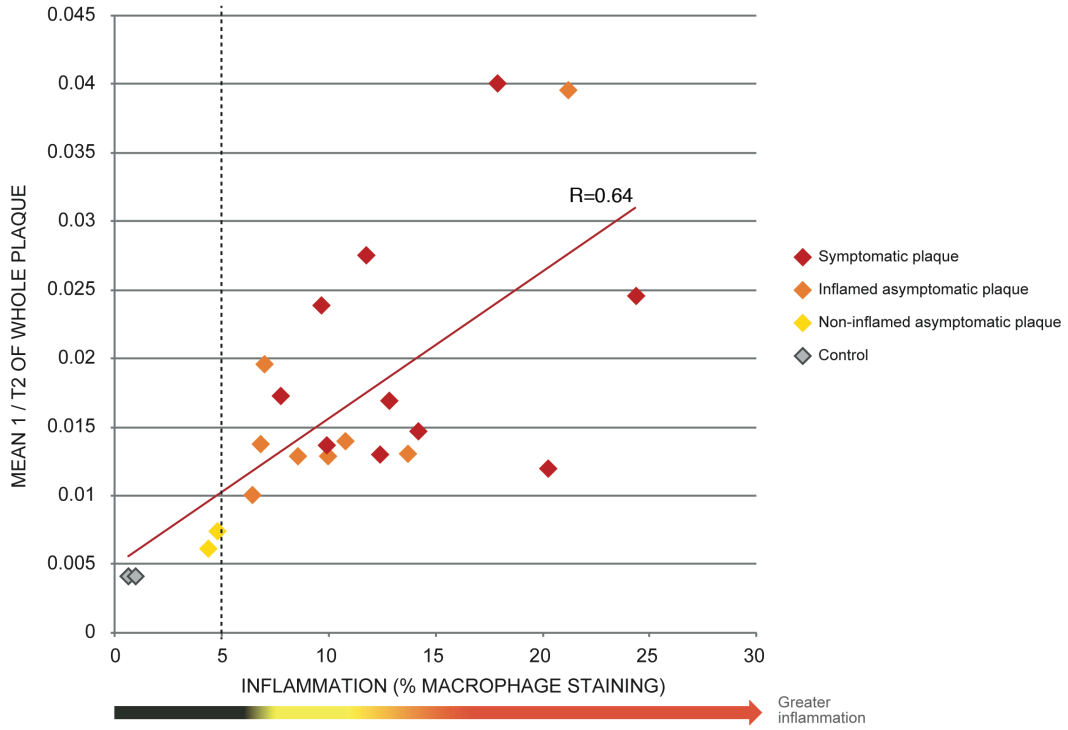



**Fig. 3.11 The relationship between intraplaque inflammation and MR contrast effect.** The mean macrophage content (index of plaque inflammation) is significantly correlated with the mean 1/ $T_2$ (MR contrast effect) of the whole plaque per patient (r=0.64, P<0.001). Consistent with the MRI results, the symptomatic plaques (in red) with the greater level of inflammation produce a higher 1/ $T_2$ value and appear darker; followed by the inflamed asymptomatic plaques (in orange), then the non-inflamed plaques (in yellow).

### 3.3.5 Relationship between Expression of Histological Markers (VCAM-1, E-selectin, CD68 and Perls' iron stain) and 1/ $T_2$

Taking the symptom status of each patient into account, the strength of the relationship between histological marker data (expression of VCAM-1, E-selectin, CD68 and Perls' iron stain) and MR contrast effect (1/ $T_2$) in each of the five carotid plaque sections per patient was assessed. The fitted regression model with endothelial expression of VCAM-1 in carotid plaque sections as predictors and 1/ $T_2$ as response variable controlling for symptom status of patient reported $R^2$ = 0.79. This indicates that 79% of the variation in

1/ $T_2$ is fitted by the endothelial VCAM-1 expression in carotid plaque sections. Further, the overall regression model was found to be statistically significant ($F(9, 90) = 37.93$, $p<0.01$). T test demonstrated that the estimated regression model parameter for endothelial VCAM-1 expression was found to be statistically significant ($b = 0.00224$, $t(1) = 7.317$, $p <0.001$). Therefore we can conclude that endothelial VCAM-1 expression in carotid plaque sections and $1/T_2$ is significantly strongly correlated. Similarly, endothelial expression of E-selectin in carotid plaque sections and $1/T_2$ was also significantly strongly correlated [$R^2 = 0.82$, ($F(9, 90) = 46.71$, $p<0.01$), ($b = 0.00339$, $t(1) = 7.48$, $p <0.001$)]. In comparison, CD68 expression in carotid plaque sections and $1/T_2$ was statistically significant, yet moderately correlated [$R^2 = 0.5687$, ($F(4, 105) = 34.61$, $p<0.001$), ($b = 0.001$, $t(1) = 5.13$, $p <0.0001$)]. The effect of intralesional iron content, indicative of past intraplaque haemorrhage, as visualised by Perls' stain in carotid plaque sections on $1/T_2$ was not statistically significant [($F(1, 104) = 2.02$, $p =0.158$), ($b = 0.0069$, $t(1) = 1.42$, $p=0.158$)].

### 3.3.6 Synergistic Relationship of E-selectin and VCAM-1 Expression on $1/T_2$

Repeated measures ANOVA was performed to test the significance of the effect of VCAM-1 and E-selectin endothelial expression and their interaction on $1/T_2$ in each of the five carotid plaque sections per patient. VCAM-1 expression and E-selectin expression explained 94.08% of the variation in $1/T_2$ in carotid plaque sections ($R^2 = 0.9408$) and was statistically significant [($F(1, 103) = 272.64$, $p <0.001$), ($b =-0.00015$, $t(1) = -8.96$, $p<0.01$)]. Compared to using E-

selectin or VCAM-1 expression alone, there was an increase of 12% and 15% respectively in the explanatory power by using E-selectin and VCAM-1 expression together. Therefore we conclude that there is a significant synergistic relationship between VCAM-1 and E-selectin endothelial expression on $1/T_2$.

## 3.4 DISCUSSION

We have differentiated the symptomatic plaques from the asymptomatic ones, and more importantly, the high risk inflamed plaques from the non-inflamed ones within the asymptomatic plaque population by *ex vivo* MRI. This study showed that the mean $1/T_2$ value of the whole plaque was significantly correlated with plaque inflammation (plaque macrophage content). Supported by previous postmortem and atherectomy studies, increased expression of VCAM-1, E-selectin, and P-selectin was known to correlate with a high density of macrophages and T lymphocytes in the inflamed coronary and carotid plaques.[154,155] This data suggested that higher levels of VCAM-1 and E-selectin endothelial expression from the inflamed plaques resulted in greater binding of antibody-conjugated microbeads to the endothelial cells, producing a greater signal loss in T2 spin echo sequence and greater $1/T_2$ value.

This was confirmed by further analysis using repeated measures modeling to assess the strength of the relationship between histological marker data and MR contrast effect in each of the five carotid plaque sections per patient. As previously described by Tang et al[82], compared to the simple paired analysis, this complex statistical model was designed specifically to be a more robust treatment of the data. The whole plaque has signal change assessed in five smaller plaque sections so as to minimise the chance of a focal signal loss being “lost” in a mean signal change for the whole plaque. However, each of these plaque sections cannot be considered as an entirely independent

observation, and to some extent the signal in one section will affect the signal in its adjacent section. Hence, if these data were treated as independent observations, the number of degrees of freedom of any statistical test would be erroneously high, resulting in an erroneously low p-value. In an attempt to minimise potential statistical error, a complex repeated measures modeling was used to model true variances in section data and bring the degrees of freedom back to the correct level.

In this model, a stronger correlation between endothelial expression of VCAM-1 and E-selectin with $1/T_2$ ($R^2$ = 0.79, P<0.01 and $R^2$ = 0.82, P<0.01 respectively) was demonstrated than that of CD68 with $1/T_2$ ($R^2$ = 0.57, P<0.001), suggesting that the antibody-conjugated iron particles predominantly targeting activated endothelial cells rather than macrophages. The dual-targeted SPIO-induced MR signal not only tracked closely with endothelial activation (i.e. endothelial expression of VCAM-1 and E-selectin), but unsurprisingly also reflected the macrophage burden within plaque lesion, suggesting that the degree of inflammation and endothelial activation correlated with the number of plaque based macrophages. The results were consistent with the role of increased endothelial expression of adhesion molecules in promoting monocyte recruitment into vascular tissues.[127,156,157] While the initial monocyte rolling along the activated endothelium were mediated by E-selectin and P-selectin,[127,157] firm adhesion of monocytes was mediated by the engagement of integrin α4β1, also known as very late antigen (VLA-4), with endothelial VCAM-1, preceding their transmigration to the lesion.[158,159] This was further supported by previous studies, which showed

that the increased expression of VCAM-1, E -selectin, and P-selectin was associated with heavy infiltration of macrophages and T lymphocytes within the intima of the inflamed coronary and carotid plaques.[154,155] The present results affirm that the MRI combined with dual-targeted SPIO approach can potentially offer a novel imaging tool for quantitative assessment of inflammation across a range of atherosclerotic lesions complexities in human in the future.

Furthermore, this study has utilised selectin-mediated monocyte rolling and VCAM-1 mediated firm adhesion mechanism to develop the antibody-conjugated SPIO. This work demonstrated a significant synergistic relationship between VCAM-1 and E-selectin endothelial expression on $1/T_2$ value, supporting a synergistically augmented binding of dual antibody-conjugated iron particles to atherosclerosis, as compared to either in isolation. Consistent with this, previous studies have also captured the *in vivo* dynamics of leukocyte binding to endothelium to develop a dual antibody-conjugated MPIO against P-selectin and VCAM-1,[133] which showed synergistically enhanced binding to atherosclerosis in a mouse model, as compared to either P-selectin or VCAM-1 alone.[133] Although this is an *ex vivo* work, it is the first study to demonstrate the synergistically augmented binding effect of the dual-antibody conjugated iron particles on human atherosclerotic plaques.

## Limitations and future work

The very high binding affinity of biotin with streptavidin has led to the use of this binding complex in a wide variety of *in vitro* and *in vivo* applications.[160]

However, the significant level of endogenous biotin present in serum[161] and the slow dissociation of the biotin-streptavidin complex[162] can pose a potential limitation of the translation of biotinylated antibody-conjugated streptavidin microbeads in clinical diagnostic and therapeutic applications. Moreover, the size of the SPIO (microbeads) was 50 nm in diameter. Compared to MPIO, SPIO can only convey a relatively small payload of iron, limiting its effect on local magnetic field homogeneity, and therefore compromising the contrast sensitivity. The substantial contrast effect and sensitivity of the dual antibody-conjugated SPIO demonstrated in this *ex vivo* study could be undermined when being translated to the *in vivo* condition. Furthermore, the small particle size permits SPIO to enter atherosclerotic plaques, potentially compromising the specificity of these particles for molecular targets expressed on vascular endothelium. However, the short incubation period of SPIO with plaque sections limits their passive diffusion into plaques. This was supported by the minimal signal loss on the negative control – symptomatic plaque incubated with non-immune IgG and microbeads, suggesting that non-specific binding or diffusion of SPIO to plaque sections was minimal (Figure 3.10).

In the following stages of animal work, large iron oxide particles, MPIO, will be used to enhance their sensitivity to achieve *in vivo* detection of low-abundance endothelial molecular targets. In addition, the streptavidin-biotin link between the biotinylated primary antibody and streptavidin microbeads will be replaced by a direct conjugation of antibodies to the iron oxide particles, moving a step closer to a practical clinical application.

## 3.5 CONCLUSION

Using the dual-antibody conjugated SPIO, we have imaged the degree of inflammation associated with human atherosclerotic plaques by *ex vivo* MRI. More importantly, we have identified the potentially high-risk inflamed plaques from the non-inflamed ones within the asymptomatic plaque population. The dual-targeted SPIO-induced MR signal not only tracked closely with endothelial activation (i.e. endothelial expression of VCAM-1 and E-selectin), but also reflected the macrophage burden within plaque lesions, offering a potential imaging tool for quantitative MRI of inflammatory activity in atherosclerosis. Moreover, this study has demonstrated the synergistically augmented binding effect of the dual- antibody conjugated SPIO on human atherosclerotic plaques. These functional molecular MRI probes potentially provide clinicians with a novel imaging tool for *in vivo* characterisation of atherosclerosis at a molecular level, thereby permitting more accurate risk stratification in carotid artery disease and optimising resource allocation to target the high-risk cohorts in the future.

# CHAPTER 4:

# *Ex Vivo In Situ* ApoE-/- Mouse Model Stage

# 4.1 INTRODUCTION

Understanding of the monocyte-endothelial binding mechanism forms the basis of the design of molecular imaging probes that can directly report arterial endothelial activation of atherosclerosis *in vivo*.[115] To image vascular endothelial cell activation with MRI, we have previously described selectin-mediated monocyte rolling and VCAM-1-mediated firm adhesion mechanism to develop the prototypic biotinylated antibody-conjugated streptavidin microbeads. Although this approach proved promising in feasibility experiments demonstrated by *ex vivo* MRI of explanted human carotid plaques, retention of SPIO (streptavidin microbeads) could be potentially insufficient at acceptable iron doses for reliable detection by *in vivo* molecular MRI. To overcome this limitation, we have developed a second generation of iron oxide particles – the dual antibody-conjugated MPIO against VCAM-1 and P-selectin. This new version of iron oxide particles has been improved in three ways: Firstly, the streptavidin-biotin link between the biotinylated primary antibody and streptavidin microbeads was replaced by a direct conjugation of antibodies to the iron oxide particles. Secondly, the size of MPIO (1μm diameter) is much greater than that of microbeads (50nm diameter). Thirdly, we took the opportunity to alter one of the target ligands in the manufacture of this larger MPIO, conjugating P rather than E selectin. The rationale behind these modifications will be discussed in details in section 4.4.

## ApoE-/- mice as atherosclerotic model

The animal models of hyperlipidaemia and atherosclerosis in apolipoprotein E-deficient (ApoE-/-) mice and low-density lipoprotein receptor-deficient (LDLR-/-) mice have been widely used.[163-165] Apolipoprotein E (ApoE) plays a pivotal role in lipoprotein trafficking. ApoE is a constituent of chylomicrons, very low density lipoprotein (VLDL), and high density lipoprotein (HDL) and acts as a ligand for the receptor-mediated clearance of these particles.[166] The absence of ApoE has multiple effects on lipid metabolism and transport. In normal mice, the profile of cholesterol-containing plasma lipoproteins includes an abundance of HDL and only trace amounts of LDL. In contrast, ApoE-/- mice have the reverse distribution: 80% of serum cholesterol is sequestered in LDL, while HDL-cholesterol is half the normal level. In addition, total cholesterol levels in plasma of ApoE-/- mice are up to five times that of normal mice. They develop atherosclerotic lesions spontaneously, even when fed a normal chow diet. The lesions resemble human lesions and progress over time from an initial fatty streak to a complex lesion with a fibrous cap,[167, 168] and lesion development can be accelerated by a high-fat, high-cholesterol diet.[169]

In contrast, mice lacking the LDL receptor (LDLR) gene have less severe disease, with a modest 2 times normal plasma cholesterol level when fed on a normal chow diet, and develop atherosclerosis only slowly.[170] However, they exhibit massive elevations in plasma cholesterol and rapidly develop atherosclerotic lesions when fed on a high-fat, high-cholesterol diet.[171] There is less published data on the kinetics of lesion development in LDLR-/- mice than in ApoE-/- mice.[164] Nevertheless, the lesions that develop in ApoE-/- and

LDLR-/- mice are generally the same, with the plaques developing in a time-dependent fashion, starting from the proximal aorta and spreading toward the distal aorta, and particularly involving areas where blood flow is disturbed.[164] These atherogenic mouse models have been viewed as very effective and practical models for the study of atherosclerosis for the following reasons: the availability of genetically defined inbred and mutant strains and the well-established means of using these strains to manipulate the mouse genome, the general advantages of mice, such as their small size, short generation time, and relative ease of care, and finally, the predictable development of plaques in these mutants has been well documented. Table 4.1 shows the scaling of lesions based on the American Heart Association (AHA)-defined stages of human atherosclerosis (stages I to VI) [172-175] and time frame for development in both ApoE-/- and LDLR-/- mice.[176] This allows researchers to reliably plan to have a specific stage of lesion form within a well-defined time frame. In our study, ApoE-/- mice were chosen over LDLR-/- mice because 1) more advanced lesions developed within a shorter time frame in ApoE-/- mice;[176] and 2) there were relatively more published studies on the kinetics of lesion development in ApoE-/- mice.[164]

| | Atherosclerotic Lesion Stage Obtained in the Ascending Aorta | | | | | |
|---|---|---|---|---|---|---|
| Mouse Model (Diet) | I | II | III | IV | V | VI |
| *apoe-/-* ( standard diet) | 1-2 months | 4-5 months | 7-9 months | 8-11 months | 10> months | N/A |
| *apoe-/-* ( Western diet) | 4-6 weeks | 8-10 weeks | 12-14 weeks | 14-16 weeks | 18-20 weeks | N/A |
| *ldlr-/-* ( standard diet) | 6-7 months | 9-10 months | 12> months | N/A | N/A | N/A |
| *ldlr-/-* ( Western diet) | 4-6 weeks | 6-12 weeks | 16-20 weeks | 24> weeks | N/A | N/A |

**Table 4.1. Lesion stage and time frame for development in both ApoE-/- and LDLR-/- Mice.[176]**

In the *ex vivo in situ* ApoE-/- mouse model stage, we aim at detection of atherosclerotic lesions in the aortic roots of ApoE-/-mice by *ex vivo in situ* MRI following *in vivo* administration of MPIO targeted against both VCAM-1 and P-selectin.

# 4.2 MATERIALS AND METHODS

## 4.2.1 Dual Antibody Conjugation to MPIO

Dual antibody conjugation to MPIO was previously described.[133] MPIO (1$\mu$m diameter; Dynabeads® MyOne™; Invitrogen, Paisley, UK) with p-toluenesulphonyl (tosyl) reactive surface groups were used for antibody conjugation. These tosyl groups react covalently with primary amino and sulfydryl groups predominantly in the Fc-region of antibodies, favoring optimal orientation. To prepare dual-targeted MPIO, purified monoclonal rat anti-mouse antibodies for VCAM-1 (CD106; clone MVCAM A; AbD Serotec, Kidlington, UK) and P-selectin (CD62P; clone RB40.34; BD Biosciences, Oxford, UK), were covalently conjugated to MPIO, by incubation at 37°C for 20 hours, with constant rotation ($10^7$ MPIO per 2.5 $\mu$g of each antibody). Control MPIO, incubated with purified monoclonal rat anti-mouse antibodies for IgG-1 (clone Lo-DNP-1; AbD Serotec, Kidlington, UK) ($10^7$ MPIO per 5 $\mu$g antibody), were prepared in the same way. MPIO were then washed twice in PBS containing 0.1% bovine serum albumin (BSA) at 4°C and incubated with tris buffer (0.1 mol/L, 0.1% BSA, pH 7.4) for 4 hours at 37°C, to block remaining active tosyl sites. MPIO were rinsed in PBS (0.1% BSA) at 4°C for 5 minutes and stored at $4x10^8$ MPIO per mL PBS (0.1% BSA) at 4°C.

### 4.2.2 *In Vivo* Systemic Administration of Dual-Targeted MPIO

Experiments were performed in accordance with UK Scientific Procedures Act (1986) and local ethical approval. Six 70-week-old homozygous ApoE-/- mice were bred and housed under specific pathogen-free conditions with standard 12-hour light/cycles and controlled temperature and humidity. Weaning of mice occurred at 3 weeks of age onto a standard mouse chow diet (Lillico, Surrey, UK) until the day of scanning. The mouse was weighed. Dual antibody-conjugated MPIO (n=4 mice) or control IgG-1-MPIO (n=2 mice) (5mg iron per kg body weight in 150µl PBS) was injected *in vivo* via tail vein and allowed to circulate for 30 minutes. (Figure 4.1)

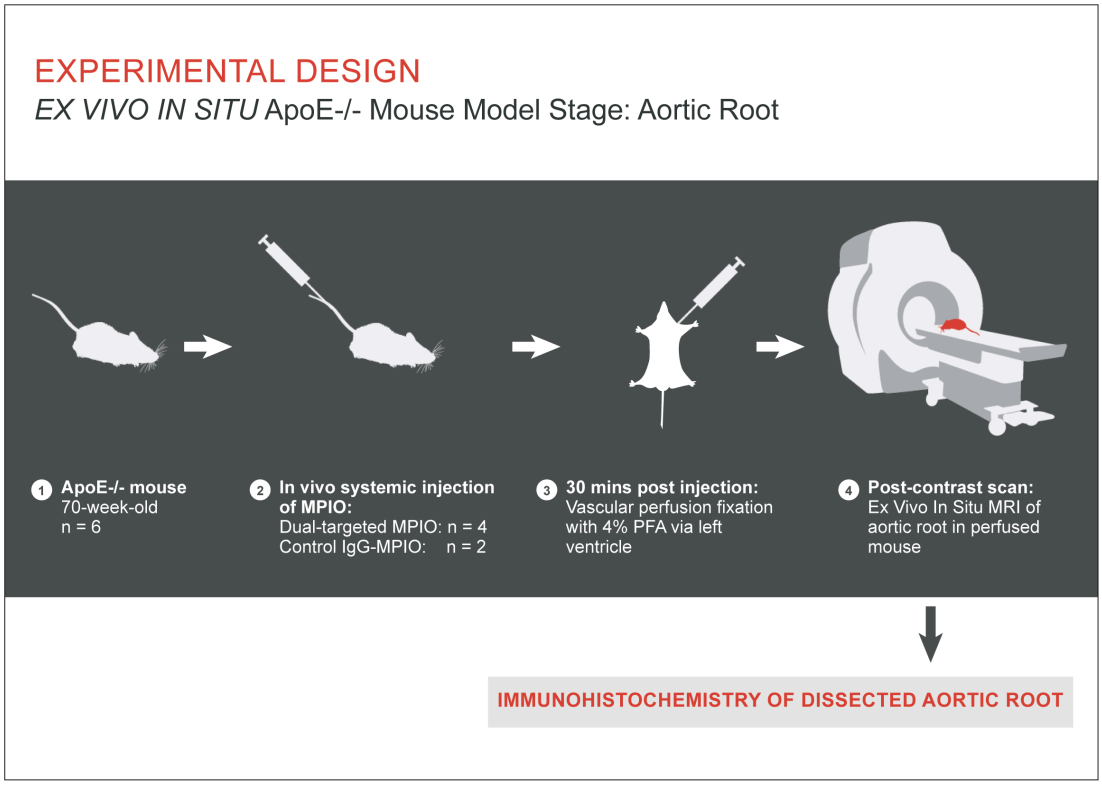



**Fig. 4.1 Experimental design of *ex vivo in situ* ApoE-/- mouse model stage.** Six 70-week-old ApoE-/- mice underwent *in vivo* systemic injection of MPIO (dual-targeted MPIO group: n=4; control IgG-MPIO group: n=2). 30 minutes after *in vivo* administration of iron particles, ApoE-/- mice underwent vascular perfusion fixation followed by *ex vivo in situ* MRI of the aortic root. The heart and aortic root were subsequently removed en bloc for immunohistochemistry.

### 4.2.3 Vascular Perfusion Fixation of ApoE-/- Mice

**Anaesthesia**

30 minutes after *in vivo* administration of iron particles, ApoE-/- mice were anaesthetised by pentobarbital (100mg/kg body weight) via intraperitoneal injection. The mouse was assessed to ensure anaesthesia had occurred, indicated by the absence of withdrawal reflex response to paw or tail pinching.

**Perfusion**

Perfusion procedures were performed in a chemical fume hood. Once the mouse was anaesthetized, it was placed in supine position with each limb taped down to the operating table. The withdrawal reflex was checked once more to ensure adequate depth of anaesthesia. The animal had to be unresponsive prior to perfusion procedures. A midline skin incision from thoracic inlet to pelvis was made. Blunt dissection was performed to expose the thoracic and peritoneal membrane surfaces. The peritoneal membrane was cut just below the xiphoid process to expose the diaphragm and visceral organs. The thoracic cavity was accessed by cutting the diaphragm along its length. The xiphoid process was grasped with forceps and a midline incision through the sternum was made. Caution was taken to avoid inadvertent laceration to the lungs, heart or major vasculature. A retractor was used to hold the edges of sternum apart to expose the heart. The heart was held steady with forceps while it was beating. The right atrium was lacerated with scissors to allow perfusate to exit the circulation. A 25 gauge needle

connected to a butterfly catheter was carefully inserted into the apex of left ventricle. Caution was taken to avoid extending the needle too far in to puncture the interventricular wall. The position of needle was secured by clamping in place at the point of entry. 10 to 20ml of 0.9% saline solution was injected slowly and steadily at a rate of 20ml/minute. The liver was observed to blanch as blood was replaced with saline solution. When the fluid exiting the mouse was clear of blood, paraformaldehyde (PFA) perfusion of the arterial tree was commenced after carefully changing out the syringes without dislodging the 25 gauge needle from the left ventricle. 10 to 20ml of freshly made 4% PFA in PBS was injected slowly and steadily at a rate of 5ml/minute. Spontaneous movement of the tail and paws resulting from aldehyde-crosslinking of nerves and muscle as well as blanching of the liver and mesenteric blood vessels were observed. At the completion of perfusion, the whole animal was stiff and the 25 gauge needle from the left ventricle was removed.

### 4.2.4 Ex Vivo In Situ MRI

The perfused mouse was placed in a custom-made cradle. *Ex vivo in situ* MRI of the aortic root was performed with a 9.4T horizontal bore scanner (Varian Inc., Palo Alto, CA, USA) using a 100 Gauss quadrature radiofrequency coil (internal diameter 33mm, RAPID biomedical GmbH, Germany). A T2*-weighted 3-dimensional gradient echo sequence was used (TR: 40.00 ms; TE: 4.71 ms; FOV 25 x 25 x 25 mm; matrix size 256x256x128; average: 2; flip angle: 20°). The heart and aortic root were subsequently removed en bloc with

orientation marked, formalin fixed and embedded in paraffin blocks as described in section 3.2.5.1. Sequential tissue sectioning commenced in the mouse heart until the aortic root containing semilunar valves together with the aorta appeared. From this point on, serial aortic root cross-sections were cut at 4µm thickness on a microtome and mounted onto silane coated slides. The orientation and sequence of sections were recorded. Serial histology sections of aortic roots underwent Haematoxylin and Eosin (H&E) and Perls' Prussian blue stain as described in section 3.2.5.3. Perls' Prussian blue stain was used as a surrogate marker to confirm the presence of MPIO binding to the atherosclerotic plaques in the aortic root. As controls for positive staining, paraffin embedded spleen sections were stained in parallel experiments. Wide-field microscopy was performed with a Zeiss Axiovert 200 inverted microscope.

## 4.3 RESULTS

### *In Vivo* Dual-Targeted MPIO Binding to Atherosclerosis and *Ex Vivo In Situ* MRI

To determine whether dual-targeted MPIO can bind to atherosclerosis under *in vivo* flow condition, *ex vivo in situ* MRI of aortic root was performed at 30 minutes after *in vivo* administration of MPIO. Representative MR images of the aortic root post-injection of either dual-targeted MPIO or negative control IgG-MPIO are shown in Figure 4.2. In the dual-targeted MPIO group, MRI detected highly conspicuous areas of hypointensity signal on the luminal side of the aortic root, in areas overlying atherosclerotic plaques in all 4 mice. (Figure 4.2 A) Contrast effects were confined to areas of the aortic root affected by atherosclerosis, but not to atherosclerosis-spared regions, as confirmed by the matching histological sections. The dark hypointensity effect was due to the presence of MPIO-labelled cells, which was confirmed by Perls' stain for iron on the surface, predominantly the shoulder region, of the atherosclerotic lesions in the aortic root (Figure 4.2 B,C). In the control IgG-1-MPIO group, however, no discrete hypointensity signal area was detected on the luminal side of the aortic root in all 2 mice (Figure 4.2 D). This was supported by minimal binding of the non-specific IgG-MPIO in the aortic root lesions, which was confirmed by the minimal amount of Perls' stain in the matching histological sections (Figure 4.2 E, F).

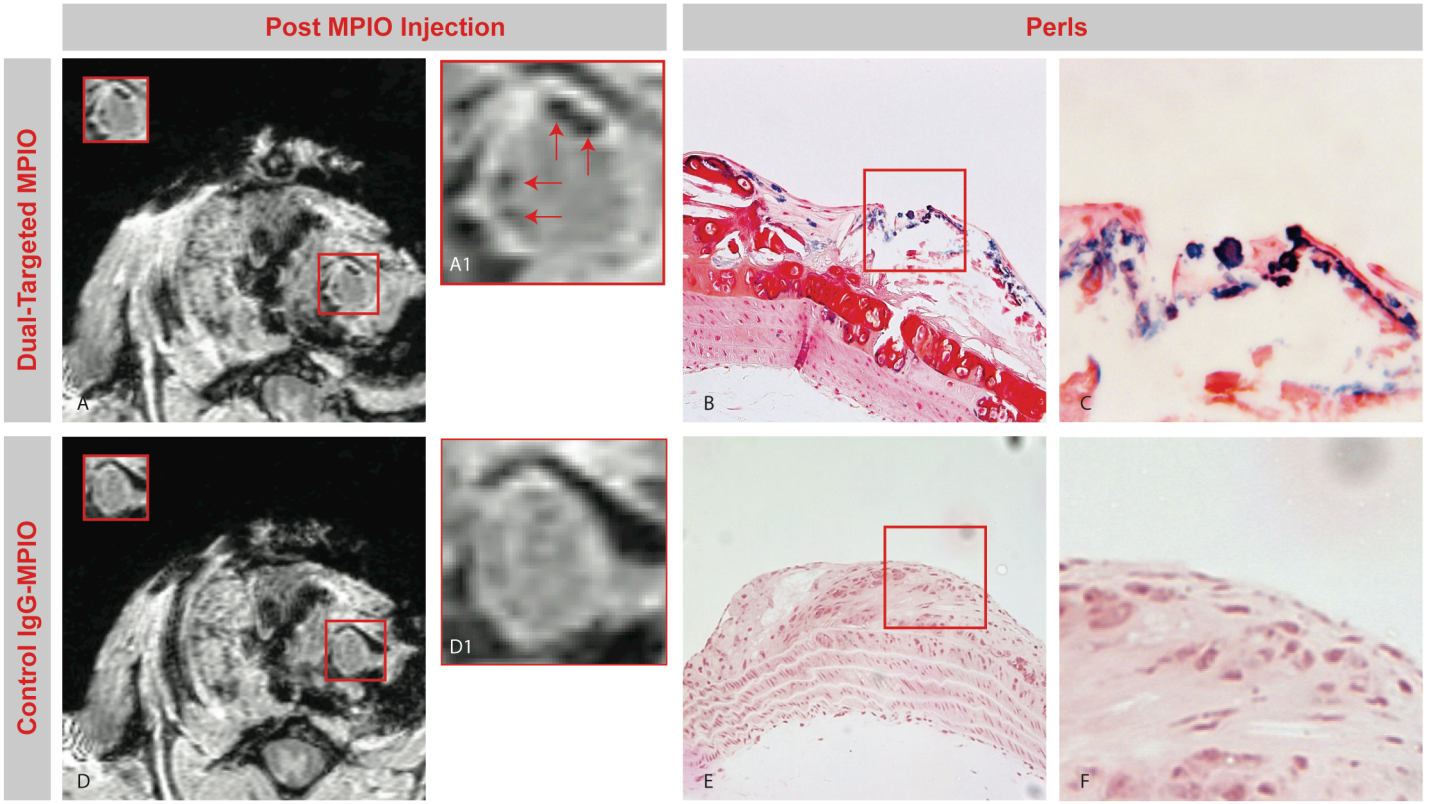



**Fig. 4.2 *Ex vivo in situ* MRI of aortic root at 30 minutes post-injection of either dual-targeted MPIO or negative control IgG-MPIO.** Panel A showed that discrete circular hypointensity signal areas were detected on the luminal side of the aortic root, in areas overlying atherosclerotic plaques, by high-resolution *ex vivo in situ* MRI. Panel A1 showed the magnified view of aortic root in red box. Red arrows indicated discrete circular hypointensity signal areas detected on the luminal side of the aortic root. The hypointensity effect was due to the presence of MPIO-labelled cells, which was confirmed by Perls' stain for iron on the surface, predominantly the shoulder region, of the atherosclerotic lesions in the aortic root (Panel B Magnification: x20, Panel C Magnification: x40). By contrast, no discrete hypointensity signal area was detected on the luminal side of the aortic root in the control IgG-MPIO group in Panel D. Panel D1 showed the magnified view of aortic root in red box. This was confirmed by minimal amount of Perls' stain on the aortic root lesions in the matching sections (Panel E Magnification: x20, Panel F Magnification: x40).

## 4.4 DISCUSSION

The animal work was performed using a newer iteration of the original SPIO used in the cell and plaque stage. We felt the dual-targeted MPIO was an improved version of the antibody-conjugated streptavidin microbeads because of three significant revisions: 1) Direct conjugation of antibodies to iron oxide particles replacing the streptavidin-biotin link between the biotinylated primary antibody and streptavidin microbeads; 2) MPIO (Dynabeads) replacing the SPIO (streptavidin microbeads); 3) MPIO conjugating P rather than E selectin. The rationale behind these modifications were as follows:

***1) Direct conjugation of antibodies to iron oxide particles***

The streptavidin-biotin link between the biotinylated primary antibody and streptavidin microbeads, which was not applicable to human, was replaced by a direct conjugation of antibodies to the iron oxide particles, moving the complex a step closer to a clinical application.

***2) MPIO replacing the SPIO***

Compared with nanoscale particles, MPIO possess a number of positive attributes that are well suited for molecular imaging of endovascular targets in atherosclerosis. 1) Increased sensitivity. The size of MPIO (1 μm diameter) is much greater than that of microbeads (50nm diameter). MPIO convey a high payload of iron (0.1–1.6 pg iron/MPIO particle), that is many orders of magnitude greater than the nanoscale particles.[111] As a result, the potent

contrast “blooming effect” of MPIO render them readily detectable at the single-particle level,[112] greatly enhancing their sensitivity to achieve *in vivo* detection of low-abundance endothelial molecular targets.[91] 2) Increased specificity to endovascular targets. The large size and incompressible nature of MPIO prevent the particles from translocating across the endothelium or undesirable passive accumulation, thereby retaining specificity for molecular targets expressed on the vascular endothelium.[85] 3) Increased binding efficiency. The increased surface area of MPIO enables greater loading capacity of antibodies to these particles, thereby increasing the binding efficiency of targeted MPIO to the endothelium.[177] 4) Fast blood clearance. Unbound MPIO are cleared swiftly from the circulation with a blood half-life less than 2 minutes in rats, resulting in rapid blood signal intensity recovery, minimising background contrast, enhancing target-to-background ratio and plaque visualisation.[114] 5) Manipulable surface chemistry. MPIO possess manipulable surface chemistries that permit targeting molecules to be covalently bound to the particle surface.[85] In summary, the size and physical properties of MPIO contribute to contrast sensitivity as well as efficient binding and blood clearance characteristics, while the conjugation of monoclonal antibodies to MPIO confers target specificity and binding affinity for relatively low-abundance vascular targets.

***3) MPIO conjugating P rather than E-selectin***

We took the opportunity to alter one of the target ligands in the manufacture of this larger MPIO, conjugating P rather than E-selectin. Current literature suggests that P as opposed to E-selectin plays a more important role in mouse

atherosclerosis. P-selectin expression increases with age and is a more specific marker for atherosclerotic lesion progression than E-selectin.[178] P-selectin expression in Apo E-/- mouse aorta is significantly upregulated (14 fold) compared to wild type mice, whilst there is only a non-significant tendency to increased induction of E-selectin in Apo E-/- versus wild type mouse aorta.[178] P-selectin deficient (P-/-) ApoE-/- mice are known to develop substantially smaller aortic lesions compared to Apo E-/- P+/+ mice,[179] but E-selectin nulls show smaller effects in lesion size.[128] Furthermore, P-selectin is an attractive target for acute inflammation imaging, since the synthesized protein is stored within the Weibel-Palade bodies of endothelial cells and upon stimulation is rapidly transported to the plasma membrane within minutes where it serves as a leukocyte receptor on cell surface.[130]

This preliminary study established the feasibility of detection of atherosclerotic lesions in the aortic roots of ApoE-/-mice by *ex vivo in situ* MRI following *in vivo* administration of dual-targeted MPIO against VCAM-1 and P-selectin. The study also demonstrated the swift binding of dual-targeted MPIO to the atherosclerotic plaques as early as 30 minutes under *in vivo* condition. Moreover, substantial 'target-to-background' contrast effect was observed in the dual-targeted MPIO group. The 'blooming effect' caused by the magnetic field distortion of MPIO was detected as discrete circular hypointensity signal areas on the luminal side of the aortic root, in areas overlying atherosclerotic plaques, confirmed by the presence of Perls' stain on the aortic root lesions in the matching sections. In contrast, no discrete low signal area was detected in the control IgG-1-MPIO group, which was confirmed by minimal Perls' stain on

the aortic root lesions. This study revealed two important attributes of dual-targeted MPIO for imaging acute plaque inflammation — high 'target-to-background' contrast effect and rapid binding efficiency under *in vivo* conditions. These attributes, however, remain to be validated in the *in vivo* MRI studies of a larger sample size. Furthermore, Perls' stain was observed to be on the surface, in particular the shoulder region, of the lesion, suggesting that the dual antibody-conjugated MPIO predominantly targeted at the surface of lesion. However, the types of cells at which the dual antibody-conjugated MPIO targeted also remain to be confirmed in the next stage of *in vivo* studies.

In accordance with previous studies,[133,180] the aortic root was chosen to be imaged in the transaxial plane in this work for the following reasons: the atherosclerotic lesions in ApoE-/- mice develop in a time-dependent fashion, starting early from the aortic root and spreading distally towards the aorta,[164] and progress in a reasonably predictable fashion.[167,181] Secondly, the aortic valve position in relation to the heart chambers provides an important fiducial reference to align both the imaging plane and circumferential orientation with the matching histological section for comparative analysis.

The dose of MPIO administered in our study was 5mg iron per kg body weight, which was slightly higher than that used clinically for non-targeted iron contrast agents in human oncological imaging (2.6 mg/kg),[182] but significantly lower than some USPIO doses used experimentally for imaging larger animal models such as rabbits (11–56 mg/kg).[183,184] In this preliminary study, a relatively high dose was used to see if the signal attenuation was feasible for

detection of atherosclerotic lesions. Although no ill effect was observed in the mice following MPIO administration before being sacrificed, further optimisation of the dose of MPIO is warranted in future studies.

## 4.5 CONCLUSION

This study demonstrated the feasibility of detection of atherosclerotic lesions in the aortic roots of four ApoE-/-mice by *ex vivo in situ* MRI following *in vivo* administration of dual-targeted MPIO against VCAM-1 and P-selectin. The high 'target-to-background' contrast effect combined with the swift binding efficiency of dual-targeted MPIO revealed in this study are the important attributes for imaging acute thrombo-embolic events. These attributes will be validated in the next stage, namely *in vivo* MRI of live anaesthetised mice with a larger sample size.

# CHAPTER 5:

# *In Vivo* ApoE-/- Mouse Model Stage: Aortic Root and Aortic Arch

# 5.1 INTRODUCTION

Atherosclerosis is a progressive inflammatory disease characterised by a tightly regulated series of cellular and molecular events from early inflammatory lesions ("fatty streaks"), comprised of monocyte-derived macrophages and T lymphocytes, to the development of advanced plaque, and eventually rupture and thrombosis.[3,4] Macrophages play a vital role in promoting fibrous cap degradation, plaque destabilisation with ensuing thrombotic complications in atherosclerosis.[185-187] Conversely, dietary cholesterol lowering and statin treatment have been associated with decreased inflammation, reduced endothelial activation and diminished monocyte/macrophage infiltration in plaque lesions. [188,189] Accumulating evidence shows that the lesion macrophage population is dynamic and engages in constant influx and excursion.[190] Despite the critical role played by macrophages, there remains a dramatic need for real time quantification and *'in vivo* microscopy' reporting the underlying dynamic macrophage burden in atherosclerotic lesions.

Monocyte recruitment into vascular tissues is mediated by the over-expression of adhesion molecules, such as vascular cell adhesion molecule-1 (VCAM-1; CD106) and P-selectin (CD62P), on the activated endothelium.[127,156,157] The interplay between rolling and firm adhesion by these two molecule systems was shown to produce synergistic effect on monocyte-endothelial binding.[116,117] Based on the monocyte-endothelial binding mechanism, we

have synthesised a dual targeting strategy directing at both cell adhesion molecules and selectins on the activated endothelium, which was shown to be more effective than either alone in the *ex vivo* human carotid plaque stage. Further, these molecular imaging probes were shown to directly report the arterial endothelial activation reflecting greater macrophage burden in more inflamed explanted human carotid plaques by *ex vivo* MRI. Based on this prototypic dual targeting strategy, we then developed a new version of dual-ligand MPIO against VCAM-1 and P-selectin and demonstrated its feasibility in *ex vivo in situ* MRI of atherosclerotic lesions in aortic roots of ApoE-/- mice following *in vivo* administration of MPIO. Accordingly, we translated this MRI combined with dual-targeted MPIO approach to the *in vivo* ApoE-/- mouse stage.

In this stage, we aim to detect atherosclerotic lesions in the aortic roots of ApoE−/− mice by *in vivo* MRI using dual-targeted MPIO against VCAM-1 and P-selectin. We evaluate the extent to which dual-targeted MPIO bind to activated endothelium and reflect macrophage content in aortic root atherosclerotic lesions in ApoE-/- mice by *in vivo* MRI and immnunohistochemistry. We further determine the binding patterns of dual-targeted MPIO in regions of the aortic arch that are susceptible to the development of atherosclerotic lesions by *in vivo* MRI and histology.

## 5.2 MATERIALS AND METHODS

### 5.2.1 *In Vivo* MRI of Aortic Root and Aortic Arch

Experiments were performed in accordance with UK Scientific Procedures Act (1986) and local ethical approval. Eleven 70-week-old homozygous ApoE-/- mice were bred and housed under specific pathogen-free conditions with standard 12- hour light cycle and controlled temperature and humidity. Weaning of mice occurred at 3 weeks of age onto a standard mouse chow diet (Lillico, Surrey, UK) until the day of scanning. The mice were weighed. ApoE-/- mice were anaesthetised with 3% isofluorane in medical oxygen (1.2 litre/minute) and maintained with 1-2% isoflurane during the MRI experiment. The tail vein was cannulated for systemic injection of MPIO. The mouse was placed in a custom-made cradle. Body temperature was monitored using a rectal probe and maintained at 37°C by circulating warm air system. Respiratory rate and heart rate were monitored with a balloon sensor and ECG trigger leads respectively throughout. *In vivo* MRI was performed with a 9.4T horizontal-bore scanner (Varian Inc., Palo Alto, CA, USA) running VnmrJ 2.3A software. A baseline pre-contrast *in vivo* imaging of the aortic root was performed using a 100 Gauss quadrature radiofrequency coil (internal diameter 33mm, RAPID biomedical GmbH, Germany). MRI acquisition was both cardiac and respiratory gated to eliminate any movement artifacts as a result of heartbeat and respiration. A T2*-weighted fast low angle shot (FLASH) sequence was used with the following parameters: TR: 22.2 ms; TE:

1.27 ms; FOV 25.6 x 25.6 mm; acquisition matrix: 256x256; average: 8; slice thickness: 0.5 mm; plane: axial; flip angle: 25°. Dual antibody or IgG-1 conjugation to MPIO was previously described in section 4.2.1. The same iron particles used in the *ex vivo in situ* stage were also used in this study. Dual antibody-conjugated MPIO (n=8 mice) or control IgG-1-MPIO (n=3 mice) (5mg iron per kg body weight in 150µl PBS) was injected *in vivo* via the tail vein. Post-contrast *in vivo* MRI using the same parameters was performed from 20 minutes up to 2 hours after MPIO injection to visualise the aortic root (Figure 5.1).

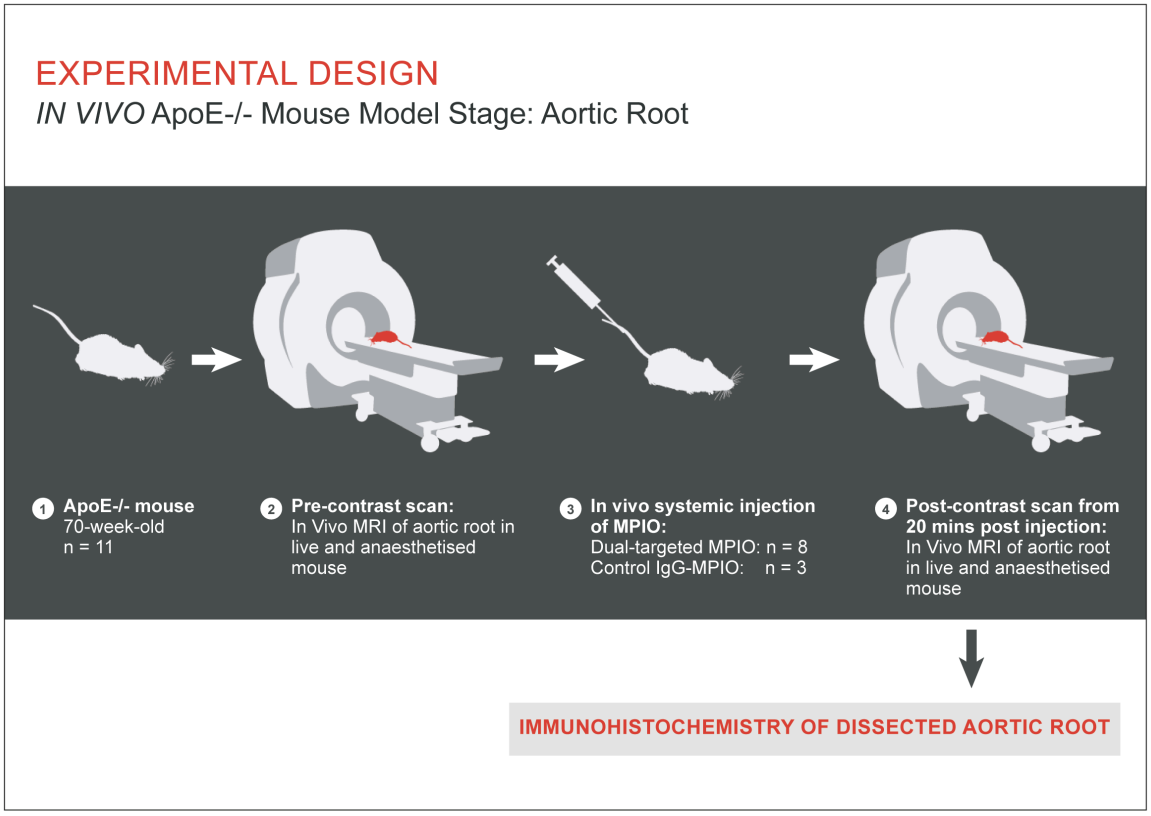



**Fig. 5.1 Experimental design of in vivo ApoE-/- mouse model stage.** Eleven 70-week-old ApoE-/- mice underwent pre-contrast scan of aortic root followed by in vivo systemic injection of MPIO (dual-targeted MPIO group: n=8; control IgG-MPIO group: n=3). 20 minutes after in vivo administration of iron particles, the live and anaesthetised ApoE-/- mouse underwent in vivo MRI of the aortic root. The heart and aortic root were subsequently removed en bloc for immunohistochemistry.

6 of these 11 mice (dual-targeted MPIO group: n=4 mice; control IgG-1 MPIO group: n=2 mice) underwent further imaging of aortic arch using another T2*-weighted FLASH sequence with the following parameters: TR: 78.00 ms; TE: 1.54 ms; FOV: 25.6 x 25.6 mm; acquisition matrix: 256x256; average: 10; slice thickness: 0.5 mm; plane: coronal; flip angle: 25°. This sequence was used in both baseline pre-contrast and post-contrast imaging of aortic arch. Moreover, in order to eliminate the signal void and effect of air on MR image, the same T2*-weighted FLASH sequence with optimised frequency offset was also used in the post-contrast imaging of the aortic arch. (Figure 5.2)

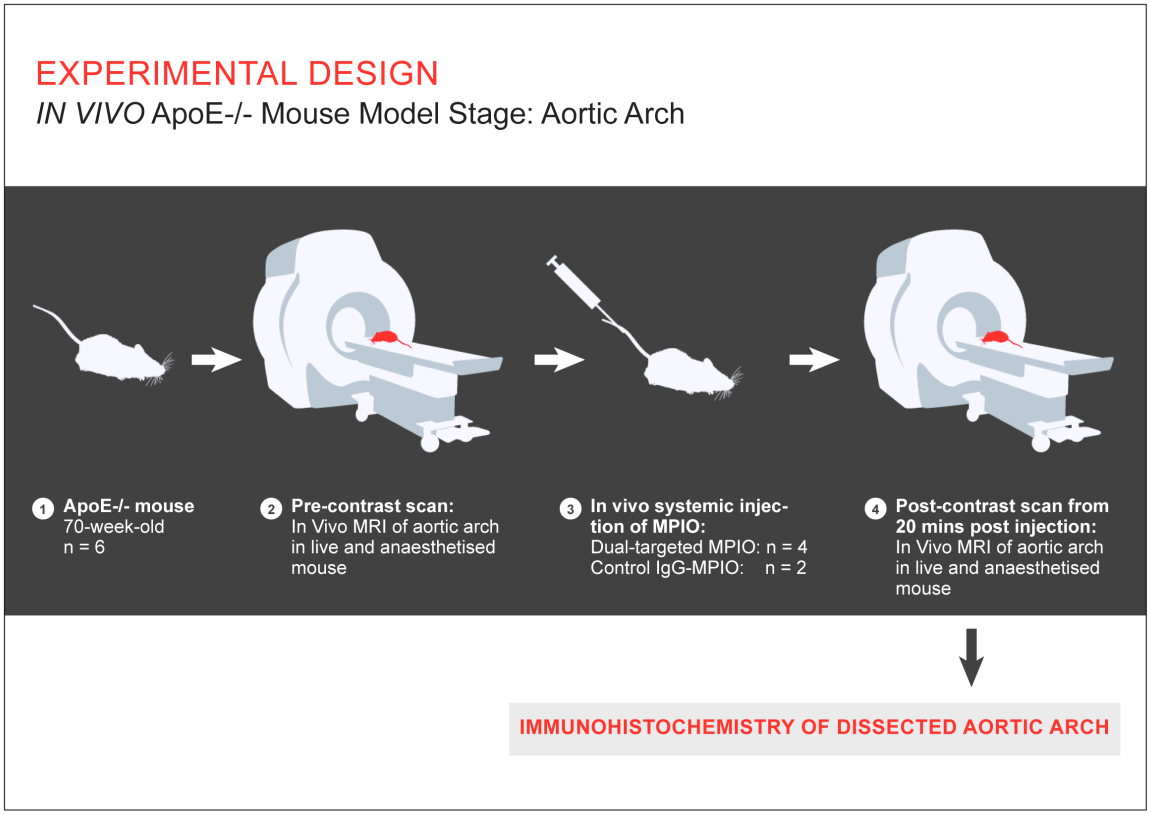



**Fig. 5.2 Experimental design of *in vivo* ApoE-/- mouse model stage.** Six 70-week-old ApoE-/- mice underwent pre-contrast scan of aortic arch followed by *in vivo* systemic injection of MPIO (dual-targeted MPIO group: n=4; control IgG-MPIO group: n=2). 20 minutes after *in vivo* administration of iron particles, the live and anaesthetised ApoE-/- mouse underwent *in vivo* MRI of the aortic arch. Both T2*-weighted FLASH sequence with and without optimised frequency offset were used in the post-contrast scan. The heart and aortic arch were subsequently removed en bloc for immunohistochemistry.

## 5.2.2 Analysis of MR Imaging of the Aortic Root

### 5.2.2.1 Qualitative MR Image Analysis

The MR images were assigned a numerical code at the time of data acquisition and subsequently analysed in batches to minimise bias. The MR images were analysed by ImageJ 1.43r software (National Institute of Health, USA. http://rsb.info.nih.gov/ij). Using the base of the aortic valve as a reference marker, post-contrast slices were precisely anatomically matched to the slices obtained on the pre-contrast baseline scan. All pre-contrast and post-contrast images were viewed at 300% magnification. Images were regarded as acceptable for analysis if the entire border of the vessel wall of the aortic root was visible and the lumen free of flow artifacts. Subsequently, images were manually segmented into quadrants using predefined rules and therefore less susceptible to intra-observer and inter-observer errors. This involved constructing an imaginary set of perpendicular axes with their intersection at the center of the vessel lumen. This approach was applied to both pre-contrast and post-contrast images. Then each pair of matched quadrants (Quadrants 1-4 in Figure 5.3) was independently viewed by two observers. The presence of MPIO-induced signal effect within the plaque was confirmed by noting whether the matched post-contrast image contained a new region(s) of hypointense signal within the vessel wall (plaque). The presence or absence and the location (quadrant) of signal change were recorded.

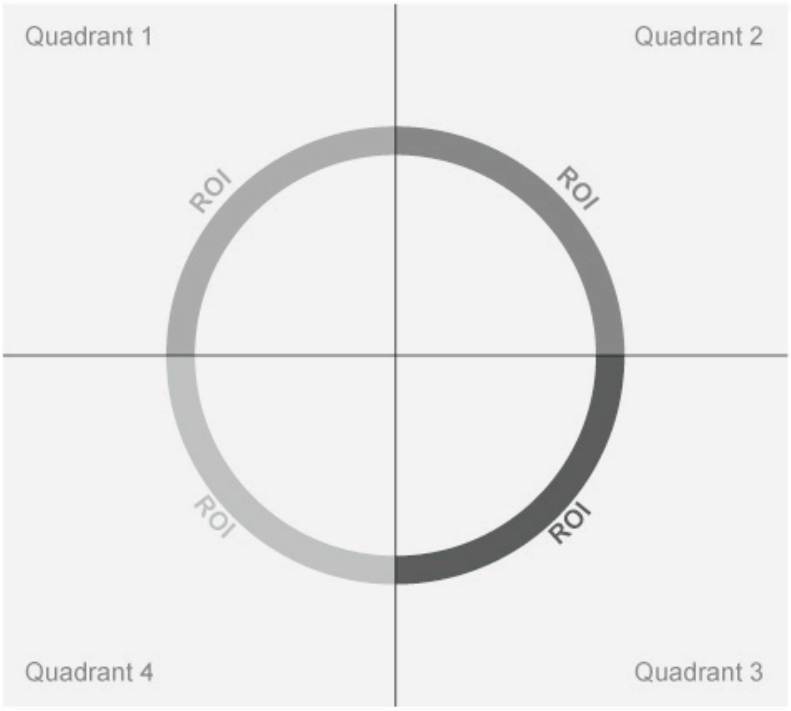



**Fig. 5.3 MR image analysis.** The vessel wall of the aortic root was divided into 4 quadrants. Each quadrant of vessel wall was defined as region of interest (ROI).

### *Intra-observer and inter-observer agreement*

One observer analysed all pre-contrast and post-contrast images in every subject. Additionally, intra-observer agreement was assessed. All images of 11 subjects were read a second time by the same observer. To reduce recall bias, the second reading took place at least 1 month after the first reading. Inter-observer agreement was also tested. All pre-contrast and post-contrast images of 11 subjects were independently read by another observer. The studies were presented in a random order. The presence or absence and the location (quadrant) of signal change were recorded.

### 5.2.2.2 Quantitative MR Image Analysis

On each quadrant, the inner and outer contours of the aortic wall were delineated manually and independently by two observers and defined as the region of interest (ROI) (Figure 5.4). The signal within the ROI (plaque signal) and that of a similar sized ROI in the background noise were measured using ImageJ 1.43r software (National Institute of Health, USA. http://rsb.info.nih.gov/ij). The signal-to-noise ratio (SNR) for each quadrant of the aortic vessel wall (ROI) was calculated as below.

SNR of each quadrant = (Signal within ROI) / (Signal in background noise)

The same quantification method was repeated in 3 consecutive slices of image. Following this, the mean of the SNR in each quadrant of all 3 consecutive slices was calculated.

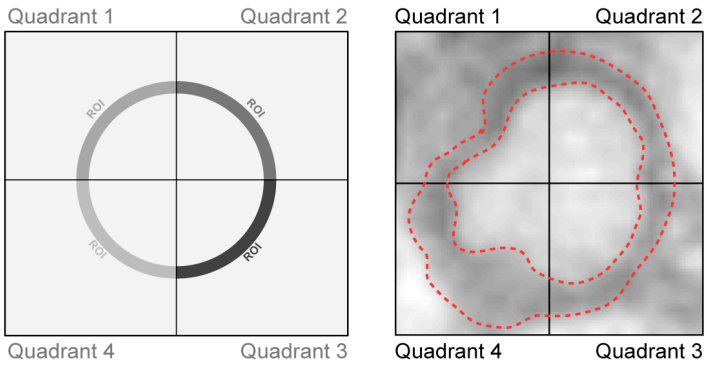



**Fig. 5.4 Quantitative MR image analysis.** The inner and outer contours of the aortic wall were delineated manually. The vessel wall of the aortic root was divided into 4 quadrants, each of which was defined as region of interest (ROI).

### *Intra-observer and inter-observer agreement*

The inner and outer contours of aortic wall in all pre-contrast and post-contrast image quadrants of every subject were delineated manually by one observer. Additionally, intra-observer agreement was assessed. The same manual

delineation and SNR measurement procedures of all image quadrants of 11 subjects were performed a second time by the same observer. To reduce recall bias, the second procedure took place at least 1 month after the first procedure. Inter-observer agreement was also tested. The manual delineation and SNR measurement of all pre-contrast and post-contrast image quadrants of 11 subjects were performed by another observer. The studies were presented in a random order.

### 5.2.3 Histological Staining of Aortic Root and Aortic Arch

ApoE-/- mice were terminally anesthetised by isofluorane inhalation at the end of the scanning session. The chest cavity was exposed and while the heart was beating, the arterial tree was perfusion fixed via the left ventricle with 4% paraformaldehyde (PFA) as previously described in section 4.2.3. The heart together with aortic root and arch were subsequently removed en bloc with orientation marked, formalin fixed and embedded in paraffin blocks as described in section 3.2.5.1.

4-μm-thick sections were cut from the paraffin-embedded blocks, beginning at the apex of the heart until the aortic root containing semilunar valves together with the aorta appeared. The sections were collected starting from the base of the aortic valve and moving in cephalic direction towards the commissural level in this stack of sections. To match the 3 levels of the corresponding MR slices with slice thickness of 0.5mm, sections were chosen at three levels, i.e. the base of aortic valve with three semilunar leaflets, which was defined as the reference level, 0.5mm and 1mm from this reference level in cephalic direction

as shown in Figure 5.5. Serial tissue sectioning continued into aortic arch in the 6 mice which underwent further imaging of aortic arch. The orientation and sequence of sections were recorded. To determine the distribution and localisation of MPIO, serial histology sections of aortic root and arch underwent Perls' staining (iron), and immunostaining for endothelial cells (CD31), macrophages (Mac-3), and smooth muscle cells [α smooth muscle actin (αSMA)], with one antibody per section. Endothelial activation was determined by immunostaining for VCAM-1 in aortic root sections in each mouse. Perls' Prussian blue staining was previously described in section 3.2.5.3.

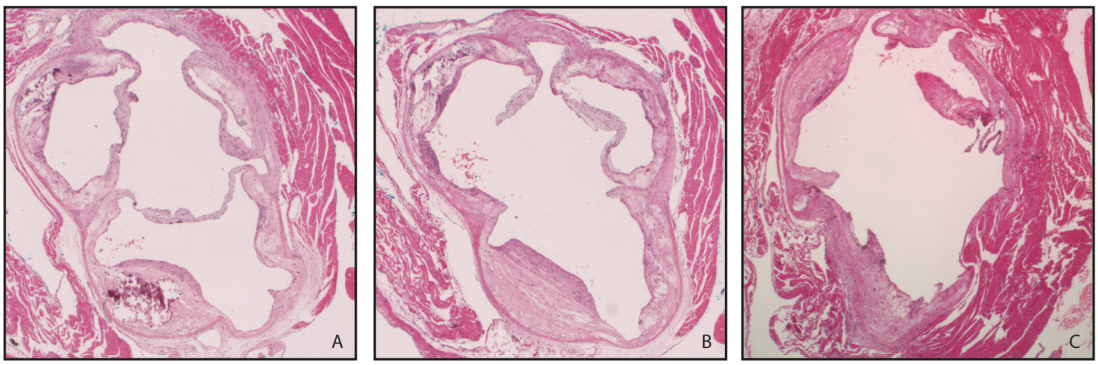



**Fig. 5.5. Histological cross-sections of the aortic root showing three levels of cutting of the aortic valve**.

The sections were collected starting from the base of the aortic valve and moving in cephalic direction towards the commissural level in this stack of sections. Three levels of sections were chosen and they are (A) the base of aortic valve with three semilunar leaflets, which was defined as the reference level, (B) 500 μm and (C) 1mm from the reference level in cephalic direction. Original magnification x4.

### 5.2.3.1 CD31

Serial sections of aortic roots and arches were de-paraffinised and rehydrated as described in section 3.2.5.2. Sections underwent antigen retrieval to expose antibody epitopes using 10μg/ml proteinase K in PBS for 30 minutes at room temperature. Sections were blocked with a casein based serum-free blocking

agent (Dako, Ely, UK) for 30 minutes at room temperature to prevent non-specific binding of antibodies and thus reduce background staining. Sections were then incubated with rat monoclonal anti-mouse CD31 antibodies (dilution 1:25 in blocking solution, Abcam, Cambridge, UK, product number Ab56299) for 16 hours at 4°C. Sections were rinsed in PBS-Tween20 (0.1%) three times, 5 minutes each, between antibody applications to remove unbound and non-specific binding of antibodies. Primary antibodies were detected by incubating sections with ImmPRESS anti-rat Ig (mouse adsorbed) peroxidase polymer detection kit (Vector Laboratories, Peterborough, UK, product number MP-7444) for 30 minutes at room temperature. The peroxidase micropolymer system was visualised by the development of the 3,3'-diaminobenzidine (DAB) substrate (DAB peroxidase substrate kit, Vector Laboratories, Peterborough, UK) prepared according to the manufacturer's instructions. Following development of brown reaction product, sections were rinsed in running tap water for 5 minutes to stop the reaction. Sections were counterstained with Harris Haematoxylin for 1 minute. Slides were rinsed in running tape water then distilled water for 5 minutes each. Sections were dehydrated through 4 changes of 70%, 90%, 100% and 100% alcohol and cleared through 2 changes of Xylene for 10 minutes each. Finally, sections were mounted with coverslips using DPX mounting medium (Leica Microsystems Ltd., Milton Keynes, UK).

As controls for positive staining, paraffin embedded mouse artery sections were stained in parallel experiments for the CD31. For negative controls, one section on each slide was incubated with the rat isotype-matched non-immune

IgG2a (dilution 1:50, Abcam, Cambridge, UK, product number Ab18450) (Figure 5.6).

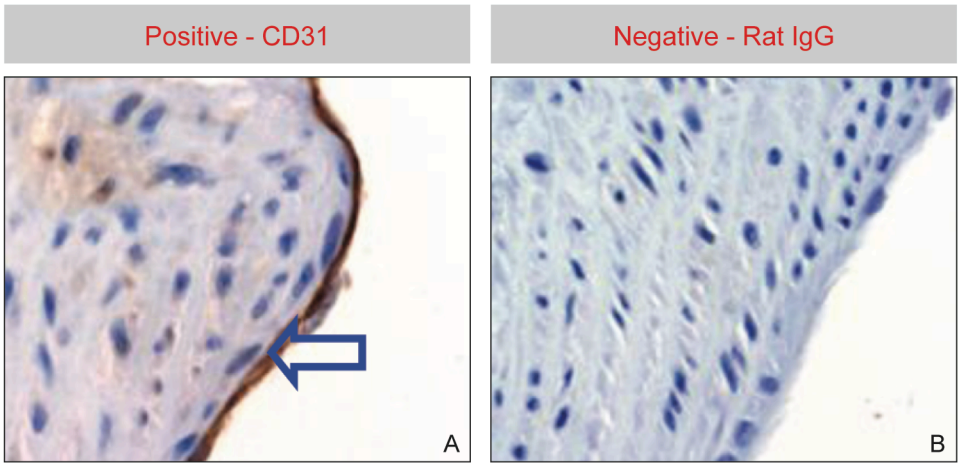



**Fig 5.6. Representative images of mouse artery sections of positive and negative antibody control for CD31 staining.**

Panel A (positive control) shows CD31 immunoreactivity in mouse artery. Blue arrow indicates endothelial cells exhibiting specific CD31 immunoreactivity in mouse artery. Panel B (negative control) shows no CD31 immunoreactivity in matching non-immune IgG controls. Original magnification x20.

### 5.2.3.2 VCAM-1

Endothelial activation was determined by immunostaining for VCAM-1 in aortic root sections in each mouse. Sections of aortic roots were de-paraffinised and rehydrated as described in section 3.2.5.2. Sections underwent heat-induced antigen retrieval to expose antibody epitopes using 10mM sodium citrate buffer (pH6) for 10 minutes in a microwave. Sections were blocked with a casein based serum-free blocking agent (Dako, Ely, UK) for 30 minutes at room temperature to prevent non-specific binding of antibodies and thus reduce background staining. Sections were then incubated with a primary VCAM-1 goat polyclonal antibody with cross-reactivity for mouse (dilution 1:100, Santa Cruz Biotechnology Inc., USA, product number sc1504) for 16 hours at 4°C.

Sections were rinsed in PBS-Tween20 (0.1%) three times, 5 minutes each, between antibody applications to remove unbound and non-specific binding of antibodies. Primary antibodies were detected by incubating sections with biotinylated horse anti-goat secondary antibodies (VECTASTAIN® ABC Kit, Vector Laboratories, Peterborough, UK) for 1 hour at room temperature. Secondary antibodies were detected using the avidin-biotin-complex (ABC) reagent (VECTASTAIN® Elite® ABC Kit, Vector Laboratories, Peterborough, UK) for 30 minutes at room temperature. The ABC system was visualised by the development of the 3,3'-diaminobenzidine (DAB) substrate (DAB peroxidase substrate kit, Vector Laboratories, Peterborough, UK) prepared according to the manufacturer's instructions. Following development of brown reaction product, sections were rinsed in running tap water for 5 minutes to stop the reaction. Sections were counterstained, dehydrated, cleared and mounted with coverslips as described in section 5.2.3.1.

As controls for positive staining, paraffin embedded mouse vasculature sections were stained in parallel experiments for the VCAM-1. For negative controls, one section on each slide was incubated with the goat non-immune IgG (dilution 1:200, Santa Cruz Biotechnology Inc., USA, product number sc2028). (Figure 5.7)

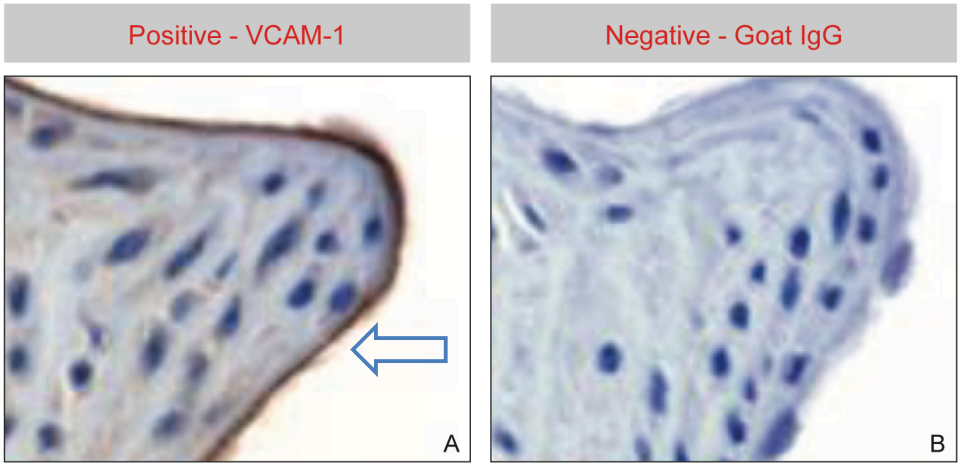



**Fig 5.7. Representative images of mouse artery sections of positive and negative antibody control for VCAM-1 staining.**

Panel A (positive control) shows VCAM-1 immunoreactivity in mouse artery. Blue arrow indicates endothelial cells exhibiting specific VCAM-1 immunoreactivity in mouse artery. Panel B (negative control) shows no VCAM-1 immunoreactivity in matching non-immune IgG controls. Original magnification x20.

### 5.2.3.3 Mac-3

Serial sections of aortic roots and arches were de-paraffinised and rehydrated as described in section 3.2.5.2. Sections underwent heat-induced antigen retrieval to expose antibody epitopes using 10mM sodium citrate buffer (pH6) for 8 minutes in a microwave. Sections were blocked with a casein based serum-free blocking agent (Dako, Ely, UK) for 30 minutes at room temperature to prevent non-specific binding of antibodies and thus reduce background staining. Sections were then incubated with rat monoclonal anti-mouse Mac3 antibodies (dilution 1:50, BD Biosciences, Oxford, UK, product number 550292) for 2 hours at room temperature. Sections were rinsed in PBS-Tween20 (0.1%) three times, 5 minutes each, between antibody applications to remove unbound and non-specific binding of antibodies. Primary antibodies were detected using biotinylated rabbit anti-rat secondary antibodies (dilution: 1:250, Vector Laboratories, Peterborough, UK, product number BA-4000) for 1 hour at room temperature. Secondary antibodies were detected using the

VECTASTAIN alkaline phosphatase (AP)-Avidin and Biotinylated enzyme macromolecular Complex (ABC) system (Vector Laboratories, Peterborough, UK, product number AK-5000) according to the manufacturer's instructions. The ABC-AP system was visualised by the development of the Vector Red alkaline phosphatase substrate (Vector Laboratories, Peterborough, UK, product number SK-5100) prepared in 100mM Tris-HCl (pH 8.2) according to the manufacturer's instructions. Levamisole solution (Vector Laboratories, Peterborough, UK, product number SP-5000) was used in conjunction with the alkaline phosphatase substrate solution according to the manufacturer's instructions to inhibit endogenous alkaline phosphatase. Following development of red reaction product, sections were rinsed in running tap water for 5 minutes to stop the reaction. Sections were counterstained, dehydrated, cleared and mounted with coverslips as described in section 5.2.3.1.

As controls for positive staining, paraffin embedded mouse artery sections were stained in parallel experiments for the Mac-3. For negative controls, one section on each slide was incubated with the rat non-immune $IgG_K$ (dilution 1:800, BD Biosciences, Oxford, UK, product number 559072). (Figure 5.8)

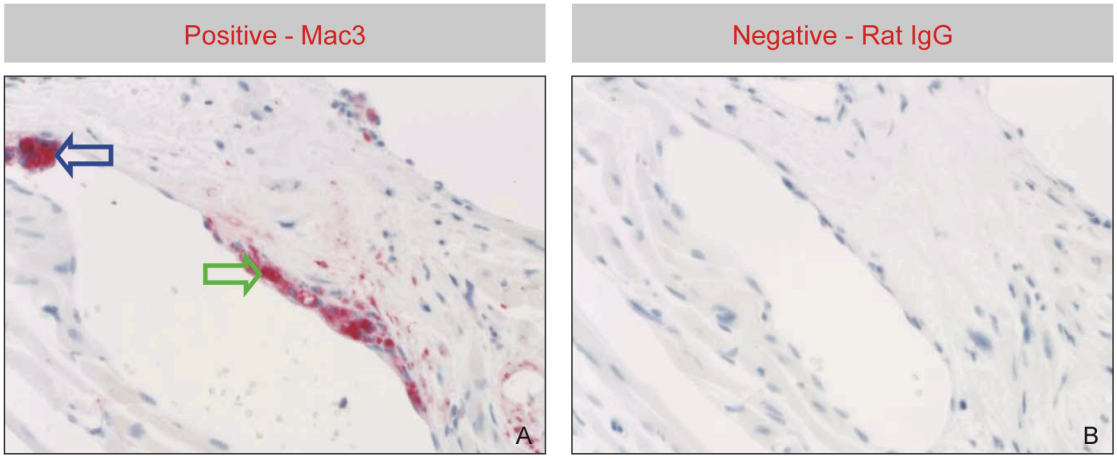



**Fig 5.8 Representative images of mouse artery sections of positive and negative antibody control for Mac-3 staining.**

Panel A (positive control) shows Mac-3 immunoreactivity in mouse vasculature. Blue and green arrows indicate a group of Mac-3 immunoreactive cells (putatively macrophages) inside the mouse artery exhibiting specific Mac-3 immunoreactivity in mouse artery. Panel B (negative control) shows no Mac-3 immunoreactivity in matching non-immune IgG controls. Original magnification x20.

### 5.2.3.4 αSMA

Serial sections of aortic roots and arches were de-paraffinised and rehydrated as described in section 3.2.5.2. Sections underwent heat-induced antigen retrieval to expose antibody epitopes using 10mM sodium citrate buffer (pH6) for 10 minutes in a microwave. Sections were blocked with a casein based serum-free blocking agent (Dako, Ely, UK) for 30 minutes at room temperature to prevent non-specific binding of antibodies and thus reduce background staining. Sections were then incubated with rabbit monoclonal anti-mouse αSMA antibodies (dilution 1:1000, Abcam, Cambridge, UK, product number Ab32575) for 16 hours at 4°C. Sections were rinsed in PBS-Tween20 (0.1%) three times, 5 minutes each, between antibody applications to remove unbound and non-specific binding of antibodies. Primary antibodies were detected by incubating sections with ImmPRESS anti-rabbit Ig (peroxidase) polymer detection kit (Vector Laboratories, Peterborough, UK, product number

MP-7401) for 30 minutes at room temperature. The peroxidase micropolymer system was visualised by the development of the 3,3'-diaminobenzidine (DAB) substrate (DAB peroxidase substrate kit, Vector Laboratories, Peterborough, UK) prepared according to the manufacturer's instructions. Following development of brown reaction product, sections were rinsed in running tap water for 5 minutes to stop the reaction. Sections were counterstained, dehydrated, cleared and mounted with coverslips as described in section 5.2.3.1.

As controls for positive staining, paraffin embedded mouse vasculature sections were stained in parallel experiments for the αSMA. For negative controls, one section on each slide was incubated with the rabbit non-immune IgG (dilution 1:7000, Abcam, Cambridge, UK, product number Ab27478) (Figure 5.9).

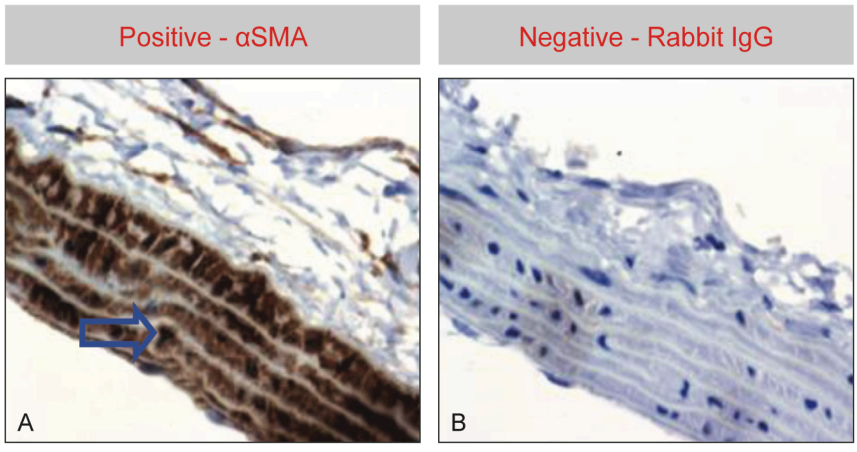



**Fig 5.9 Representative images of mouse artery sections of positive and negative antibody control for αSMA staining.**

Panel A (positive control) shows αSMA immunoreactivity in mouse vasculature. Blue arrow indicates smooth muscle cells exhibiting specific αSMA immunoreactivity in mouse artery. Panel B (negative control) shows no αSMA immunoreactivity in matching non-immune IgG controls. Original magnification x20.

## 5.2.4 Analysis Of Histological Staining Of Aortic Root

### 5.2.4.1 Qualitative Histological Image Analysis

Wide-field microscopy was performed with a Zeiss Axiovert 200 inverted microscope. The histological images were assigned a numerical code at the time of microscopy and subsequently analysed in batches to minimise bias. The marked aortic root sections were orientated and manually co-registered according to corresponding MR images for comparative analysis. Subsequently, the histological images of aortic root were manually segmented into quadrants using predefined rules and therefore less susceptible to intra-observer and inter-observer errors. This involved constructing an imaginary set of perpendicular axes with their inter-section at the center of the vessel lumen. Then each quadrant of the three histological images per subject was independently viewed by two observers. Perls' Prussian Blue stain was used as a surrogate marker to confirm the presence of MPIO binding to the atherosclerotic plaques in the aortic root. The presence or absence of Perls' stain within each quadrant were recorded. Based on histological classification of atherosclerotic lesions by the American Heart Association (AHA), advanced lesion was used as an umbrella term for all lesions that disrupt intimal structure, i.e. all lesions following type III.[175] 'Atherosclerotic lesions were classified as advanced when accumulations of lipid, cells, and matrix components are associated with structural disorganisation, repair, and thickening of the intima, as well as deformity of the arterial wall.' [175] The presence or absence of advanced atherosclerotic lesion within each quadrant was recorded. MPIO particles were considered to have colocalised with a

particular cell type (endothelial cell, macrophage, smooth muscle cell) if both the typical blue appearance of the Perls' stain and the brown appearance of the antibody revealing chromogen were present in the adjacent serial section.

***Intra-observer and inter-observer agreement***

One observer analysed all histological images in every subject. Additionally, intra-observer agreement was assessed. All images of 11 subjects were read a second time by the same observer. To reduce recall bias, the second reading took place at least 1 month after the first reading. Inter-observer agreement was also tested. All histological images of 11 subjects were independently read by another observer. The studies were presented in a random order. The presence or absence of advanced atherosclerotic lesion and Perls' stain within each quadrant were recorded.

### 5.2.4.2 Quantitative Histological Image Analysis

The area of staining of CD31 (endothelial cells), Mac-3 (macrophages), αSMA (smooth muscle cells) and Perls' (iron) in each quadrant was objectively quantified using Volocity® 5.5 image analysis software (PerkinElmer, Massachusetts, USA). Specific analysis criteria including colour threshold were established. The subsequent analysis of all images in single batch by Volocity software allowed histological staining quantified in a standardised and objective way, eliminating intra-observer and inter-observer errors. The stained area of CD31 (endothelial cells), Mac-3 (macrophages), αSMA (smooth muscle cells) and Perls' (iron) were quantified as a percentage of the total

lesion area. The same quantification method was repeated in all three histological images per subject. Following this, the mean of the percentage of stained area in each quadrant of all 3 histological images was calculated.

## 5.2.5 Statistical Analysis

### 5.2.5.1 Qualitative Analysis of MR Image and Histological Staining of the Aortic Root

For each combination of slices and quadrants, agreement between location of signal loss on MR image and location of Perls' positive cells on the matched histological section was measured by computing Cohen's kappa. Fisher's exact test (two-tailed) was also conducted to test the association between the location of MR signal effect and the location of Perls' positive cells on the matched histological section. The intra-observer and inter-observer agreement on the presence or absence of 1) advanced atherosclerotic lesions and 2) Perls' stain on histological images, as well as 3) signal loss on MR images were measured by computing Cohen's Kappa. Fisher's exact test (two-tailed) was also conducted to test the significance of the intra-observer and inter-observer agreement for each combination of slices and quadrants.

### 5.2.5.2 Quantitative Analysis of MR Image of the Aortic Root

The magnitude of change in the mean SNR between the pre and post-contrast image quadrant, induced by MPIO, was quantified as the percentage change in SNR within the defined ROI. Repeated measures ANOVA was performed to

test the significance of difference between pre-contrast and post-contrast SNR measurements as well as the difference in percentage change of mean SNR between dual-targeted MPIO group and control IgG-MPIO group. The pre-contrast and post-contrast groups were taken as within subjects' effect and contrast groups (i.e. dual-targeted MPIO group and control IgG-MPIO group) were taken as between subjects' effect, controlling for effect of repeated measurements on quadrants within the same subject. Furthermore, repeated measures ANOVA was also performed to test the significance of difference between pre-contrast and post-contrast SNR measurements in dual-targeted MPIO group and control IgG-MPIO group separately. F test was used to assess the significance of difference between pre-contrast and post-contrast SNR measurements as well as the difference in percentage change of mean SNR between dual-targeted MPIO group and control IgG-MPIO group. Repeated measures ANOVA was performed using GLM function in SAS 9.1 software (SAS Institute, Inc, NC). A value of $P< 0.05$ was considered statistically significant. Intra-observer and inter-observer variability in measurement of percentage change of SNR in aortic vessel wall were analysed using Bland-Altman plot.

#### 5.2.5.3 Comparative Analyses between MR Image and Histology

Generalised estimating equations (GEE) were fitted with exchangeable correlation matrix and robust standard errors were estimated. Quadrant was taken as within subject variable and each mouse was taken as between subject variable. The amount of staining of Perls', CD31, Mac3 and αSMA on histological sections of aortic root as well as contrast group were included as

predictor variables and percentage change in SNR between the respective pre-contrast and post-contrast image quadrant was included as the response variable.

#### 5.2.5.4 Quantitative Analysis of Histology of the Aortic Root

GEE were fitted with exchangeable correlation matrix and robust standard errors were estimated. Quadrant was taken as within subject variable and each mouse was taken between subject variable. The amount of staining of CD31, Mac3 and αSMA, as well as contrast group were included as predictor variables and the amount of Perls' staining was included as the response variable. All statistical analysis was performed using SAS 9.1 software (SAS Institute, Inc, NC). A value of $P < 0.05$ was considered statistically significant.

# 5.3 RESULTS

## 5.3.1 Qualitative Analysis of MR Image and Histological Staining of the Aortic Root

### 5.3.1.1 Detection of MPIO-Induced Signal Effect in the Aortic Root

To determine whether dual-targeted MPIO can detect atherosclerosis, serial *in vivo* MRI of aortic root was performed from 20 minutes post-injection of MPIO up to 2 hours. Representative MR images of aortic root pre- and post-injection of either dual-targeted MPIO or negative control IgG-MPIO are shown in Figure 5.10. Following administration of dual-targeted MPIO, new areas of hypointensity signal were mostly visualised as diffuse, extending between the peri-luminal and peri-adventitial regions of aortic root in the post-contrast image (Figure 5.10 B). The dark hypointensity effect was due to the presence of MPIO-labelled cells, which was confirmed by Perls' stain for iron on the aortic root lesions in the matching histological sections (Figure 5.10 D). Dual-targeted MPIO were confined to regions of the aortic root affected by atherosclerosis but not to lesion-free areas, as confirmed by histology (Figure 5.10 D). In the control IgG-MPIO group, however, negligible degree of homogeneous hypointensity was observed in the post-contrast image of aortic root (Figure 5.10 F). This was supported by minimal binding of the non-specific IgG-MPIO in the aortic root lesions which was confirmed by the negligible amount of Perls' stain in the matching sections (Figure 5.10 H). Consistent with the *ex vivo in situ* results in section 4.3, *in vivo* MRI detected contrast

effect in the dual-targeted MPIO group from 30 to 45 minutes post-contrast injection, and persisted for the entire 2-hour imaging period.

Supporting these observations, the number of post-contrast image quadrants of aortic roots being deemed positive for hypointensity signal was compared between dual-targeted MPIO group and control IgG-MPIO group. The presence of advanced atherosclerotic lesions in aortic roots was confirmed by histology in all mice. There were 12 matched pre- and post-contrast MR image quadrant pairs generated from each mouse, i.e. 3 images per mouse and 4 quadrants per image. Comparison between the pre- and post-contrast image quadrant pairs in each mouse resulted in 5 to 12 (41.7% -100%) post-contrast image quadrants being deemed positive for hypointensity signal in the dual-targeted MPIO group, whereas only 1 to 3 (8.3% -25%) quadrants in the control IgG-MPIO group (Figure 5.11).

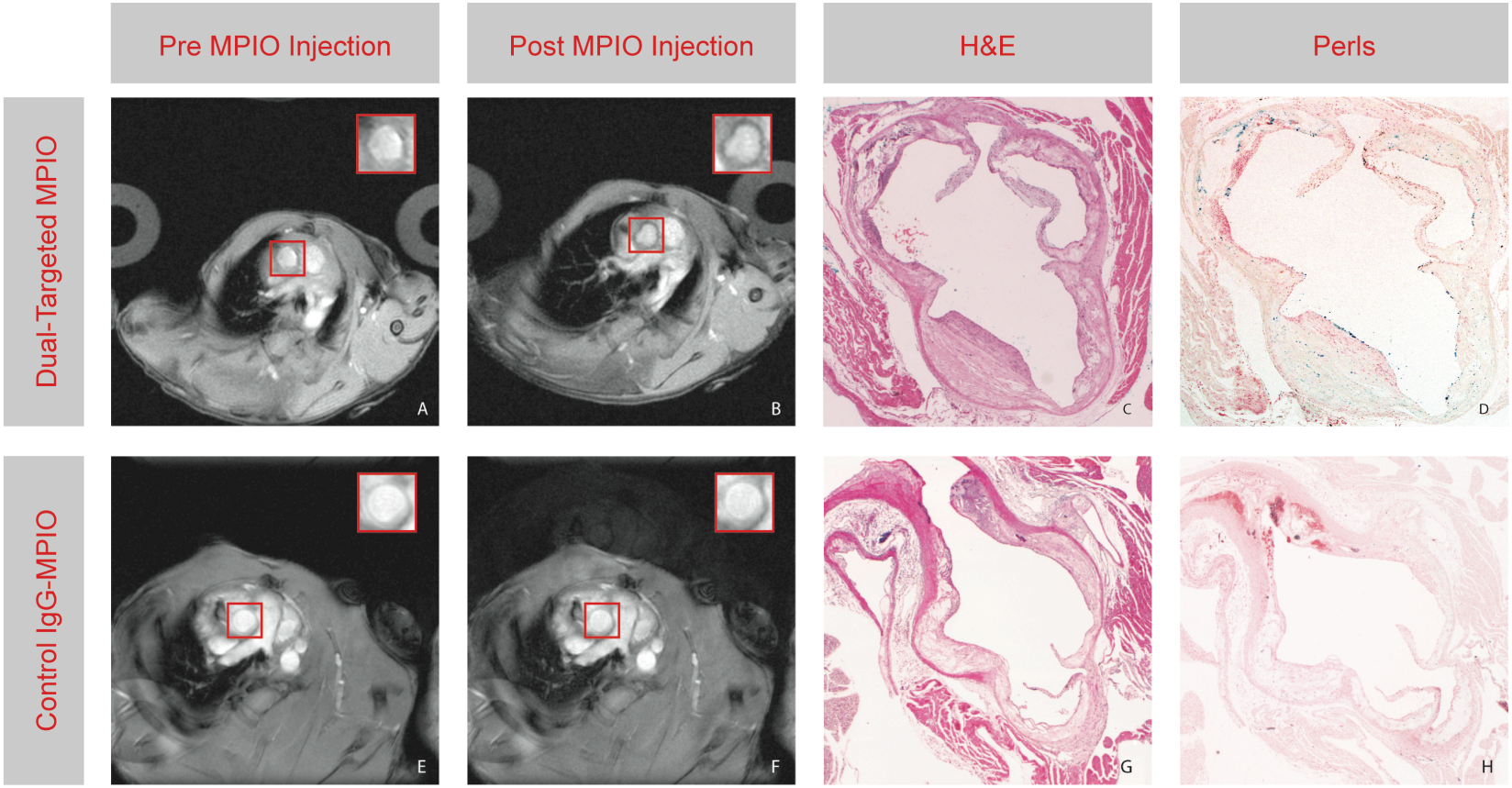



**Fig. 5.10. Representative MR and histological images of the aortic root.**
Panel A showed no hypointensity signal detected on aortic root (red box) before contrast injection in the dual-targeted MPIO group. Panel B showed the MR image of aortic root at 120 minutes post-contrast injection. New area of hypointensity in aortic root (red box) was observed to be diffused, extending between the peri-luminal and peri-adventitial regions. The hypointensity signal was due to the presence of MPIO which was confirmed by Perls' stain on the aortic root lesions in the matching section in panel D (Magnification x4). The presence of advanced atherosclerotic lesions in the aortic root was confirmed by H&E in the matching section in panel C (Magnification x4). Panel E showed a representative MR image of aortic root before contrast injection in the control IgG-MPIO group. Panel F showed the MR image of aortic root at 120 minutes post-contrast injection. The signal effect in control IgG-MPIO group was observed to have negligible degree of homogeneous hypointensity, which was confirmed by minimal amount of Perls' stain on the aortic root lesions in the matching section in panel H (Magnification x4). The presence of advanced atherosclerotic lesions in the aortic root was confirmed by H&E in the matching section in panel G (Magnification x4).

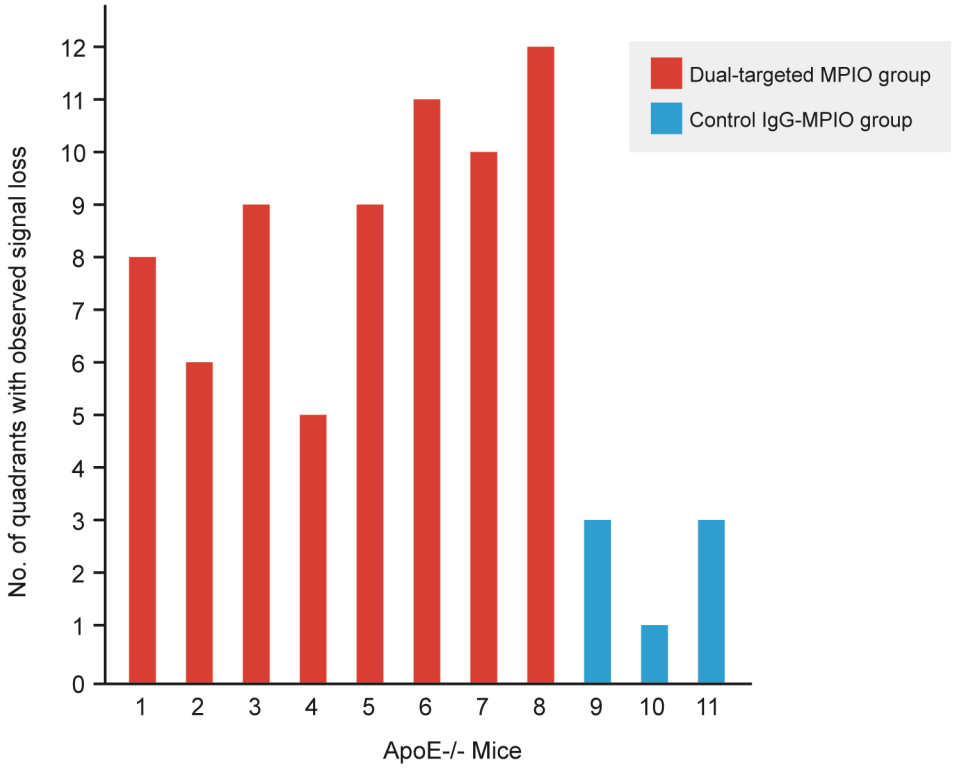



**Fig. 5.11. Bar chart comparing detection of hypointensity signal effect in the aortic root between dual-targeted MPIO group and control IgG-MPIO group**. Hypointensity signal was observed in 5 to 12 (out of 12) post-contrast image quadrants per mouse in the dual-targeted MPIO group (red bars), whereas only 1 to 3 (out of 12) quadrants in the control IgG-MPIO group (blue bars).

### 5.3.1.2 Agreement between Location of MR Signal Loss and Location of MPIO-labeled Cells

To determine whether MR signal loss was attributable to the presence of MPIO-labelel cells, agreement between location of signal loss on MR image and location of Perls' positive cells on the matched histological section was measured. There were 33 matched MR and histology image pairs generated following the coregistration process from 11 mice for comparative analysis, 3 image pairs from each mouse. With each image divided into 4 quadrants, there were a total of 132 matched MR and histology image quadrant pairs generated. After review of the coregistered MRI-histology image quadrant

pairs, Kappa coefficients of location of signal loss on MR images and location of Perls' positive cells on matched histological images for each combination of slices and quadrants were reported in Table 5.1. Kappa coefficients reported were high (i.e. >0.74) and statistically significant in 9 out of 12 combination of slices and quadrants. Therefore we conclude that strong agreement was present between the location of MPIO-labeled cells seen with Perls' staining and the location of hypointensity signal detected by MRI.

| | Slice 1 | Slice 2 | Slice 3 |
|---|---|---|---|
| Quadrant 1 | 0.792* | 0.542 | 0.744* |
| Quadrant 2 | 0.267 | 0.621 | 0.792* |
| Quadrant 3 | 1.000* | 1.000* | 0.814* |
| Quadrant 4 | 0.792* | 0.792* | 0.814* |

**Table 5.1.** Kappa Coefficient Estimates of Location of MR Signal Effect and Location of Iron-Positive Cells on Histology. *p value of Fisher's exact test < .05 (significant at 0.05 level)

#### 5.3.1.3 Intra-observer and Inter-observer Agreement on MR Signal Loss

Kappa coefficients of intra-observer agreement on the presence of signal loss on MR images for each combination of slices and quadrants were reported in Table 5.2. Kappa coefficients reported were excellent (i.e. >0.79) and statistically significant in 9 out of 12 combination of slices and quadrants. Therefore we conclude that there was strong intra-observer agreement on the presence of signal loss on MR images.

| | Slice 1 | Slice 2 | Slice 3 |
|---|---|---|---|
| Quadrant 1 | 1.000* | 1.000* | 0.621 |
| Quadrant 2 | 0.820* | 0.792* | 0.792* |
| Quadrant 3 | 1.000* | 0.607 | 0.814* |
| Quadrant 4 | 0.645 | 0.814* | 0.820* |

**Table 5.2.** Kappa Coefficient Estimates of intra-observer agreement on signal loss in each combination of slices and quadrants of MR images. *p value of Fisher's exact test < .05 (significant at 0.05 level)

Kappa coefficients of inter-observer agreement on the presence of signal loss on MR images for each combination of slices and quadrants were reported in the Table 5.3. Kappa coefficients reported were excellent (i.e. >0.79) and statistically significant in 9 out of 12 combination of slices and quadrants. There was strong inter-observer agreement on the presence of signal loss on MR images.

| | Slice 1 | Slice 2 | Slice 3 |
|---|---|---|---|
| Quadrant 1 | 1.000* | 0.792* | 0.560 |
| Quadrant 2 | 0.633 | 1.000* | 0.792* |
| Quadrant 3 | 0.814* | 0.814* | 0.814* |
| Quadrant 4 | 1.000* | 0.607 | 0.814* |

**Table 5.3.** Kappa Coefficient Estimates of inter-observer agreement on signal loss in each combination of slices and quadrants of MR images. *p value of Fisher's exact test < .05 (significant at 0.05 level)

### 5.3.1.4 Intra-observer and Inter-observer Agreement on the Presence of Perls' Stain

Kappa coefficients of intra-observer agreement on the presence of Perls' stain on histological images for each combination of slices and quadrants were reported in Table 5.4. Kappa coefficients reported were excellent (i.e. >0.79) and statistically significant in 9 out of 12 combination of slices and quadrants. There was strong intra-observer agreement on the presence of Perls' stain on histological images.

| | Slice 1 | Slice 2 | Slice 3 |
|---|---|---|---|
| Quadrant 1 | 0.792* | 1.000* | 1.000* |
| Quadrant 2 | 0.820* | 0.645 | 0.607 |
| Quadrant 3 | 1.000* | 0.814* | 1.000* |
| Quadrant 4 | 0.792* | 0.542 | 0.814* |

**Table 5.4.** Kappa Coefficient Estimates of intra-observer agreement on the presence of Perls' stain in each combination of slices and quadrants of histological images. *p value of Fisher's exact test < .05 (significant at 0.05 level)

Kappa coefficients of inter-observer agreement on the presence of Perls' stain on histological images for each combination of slices and quadrants were reported in Table 5.5. Kappa coefficients reported were excellent (i.e. >0.79) and statistically significant in 10 out of 12 combination of slices and quadrants. There was an excellent inter-observer agreement on the presence of Perls' stain on histological images.

| | Slice 1 | Slice 2 | Slice 3 |
|---|---|---|---|
| Quadrant 1 | 0.792* | 1.000* | 0.792* |
| Quadrant 2 | 1.000* | 0.820* | 0.814* |
| Quadrant 3 | 0.633 | 0.814* | 1.000* |
| Quadrant 4 | 0.792* | 0.792* | 0.607 |

**Table 5.5.** Kappa Coefficient Estimates of inter-observer agreement on the presence of Perls' stain in each combination of slices and quadrants of histological images. *p value of Fisher's exact test < .05 (significant at 0.05 level).

#### 5.3.1.5 Intra-observer and Inter-observer Agreement on the Presence of Advanced Atherosclerotic Disease

Kappa coefficients of intra-observer agreement on the presence of advanced atherosclerotic disease on histological images for each combination of slices and quadrants were reported in Table 5.6. Kappa coefficients reported were excellent (i.e. 1.000) and statistically significant in 9 out of 12 combination of slices and quadrants. There was excellent intra-observer agreement on the presence of advanced atherosclerotic disease on histological images.

| | Slice 1 | Slice 2 | Slice 3 |
|---|---|---|---|
| Quadrant 1 | 1.000* | 1.000* | 0.621 |
| Quadrant 2 | 1.000* | 1.000* | 1.000* |
| Quadrant 3 | 0.621 | 0.621 | 1.000* |
| Quadrant 4 | 1.000* | 1.000* | 1.000* |

**Table 5.6.** Kappa Coefficient Estimates of intra-observer agreement on the presence of atherosclerotic disease in each combination of slices and quadrants of histological images. *p value of Fisher's exact test < .05 (significant at 0.05 level).

Kappa coefficients of inter-observer agreement on the presence of advanced atherosclerotic disease on histological images for each combination of slices and quadrants were reported in Table 5.7. Kappa coefficients reported were excellent (i.e. >0.79) and statistically significant in 10 out of 12 combination of slices and quadrants. There was excellent inter-observer agreement on the presence of atherosclerotic disease on histological images.

| | Slice 1 | Slice 2 | Slice 3 |
|---|---|---|---|
| Quadrant 1 | 1.000* | 1.000* | 1.000* |
| Quadrant 2 | 1.000* | 0.792* | 1.000* |
| Quadrant 3 | 1.000* | 1.000* | 0.792* |
| Quadrant 4 | -0.100 | 0.621 | 1.000* |

**Table 5.7.** Kappa Coefficient Estimates of inter-observer agreement on the presence of atherosclerotic disease in each combination of slices and quadrants of histological images. *p value of Fisher's exact test < .05 (significant at 0.05 level).

## 5.3.2 Quantitative Analysis of MR Images and Histology of the Aortic Root

### 5.3.2.1 Quantification of MPIO-Induced Signal Effect in Aortic Root

The MPIO-induced signal effect in the aortic root was quantified by the magnitude of reduction in SNR between the pre- and post-contrast images. The magnitude of MPIO-induced reduction in SNR was compared between dual-targeted MPIO group and control IgG-MPIO group. There was a significant difference between pre-contrast SNR and post-contrast SNR (Wilk's

lamda = 0.391, F (1, 42) = 65.409, P <0.001). The interaction effect of pre-contrast and post-contrast group and contrast types (i.e. dual-targeted MPIO and control IgG-MPIO) was also significant (Wilk's lamda = 0.552, F (1, 42) = 34.076, P<0.001). Furthermore, repeated measures ANOVA was performed separately for dual-targeted MPIO and control IgG-MPIO group. In the dual-targeted MPIO group there was a reduction in the mean SNR of 7.563 (23.1% reduction in SNR) between pre-contrast and post-contrast groups. This reduction in SNR was statistically significant (Wilk's lamda = 0.189, F (1, 31) = 132.847, P <0.001). Although there was negligible homogeneous hypointensity of the aortic wall observable in the control IgG-MPIO group, there was a small but statistically significant reduction in the mean SNR of 1.222 (3.8% reduction in SNR) between pre-contrast and post-contrast groups (Wilk's lamda = 0.231, F (1, 11) = 36.647, P <0.001). (Figure 5.12)

To summarise, the reduction in mean SNR between pre-contrast and post-contrast image quadrants was statistically significant in both dual-targeted MPIO group and control IgG-MPIO group. However, the magnitude of MPIO-induced reduction in SNR was significantly greater in dual-targeted MPIO group than in control IgG-MPIO group (23.1% vs. 3.8%).

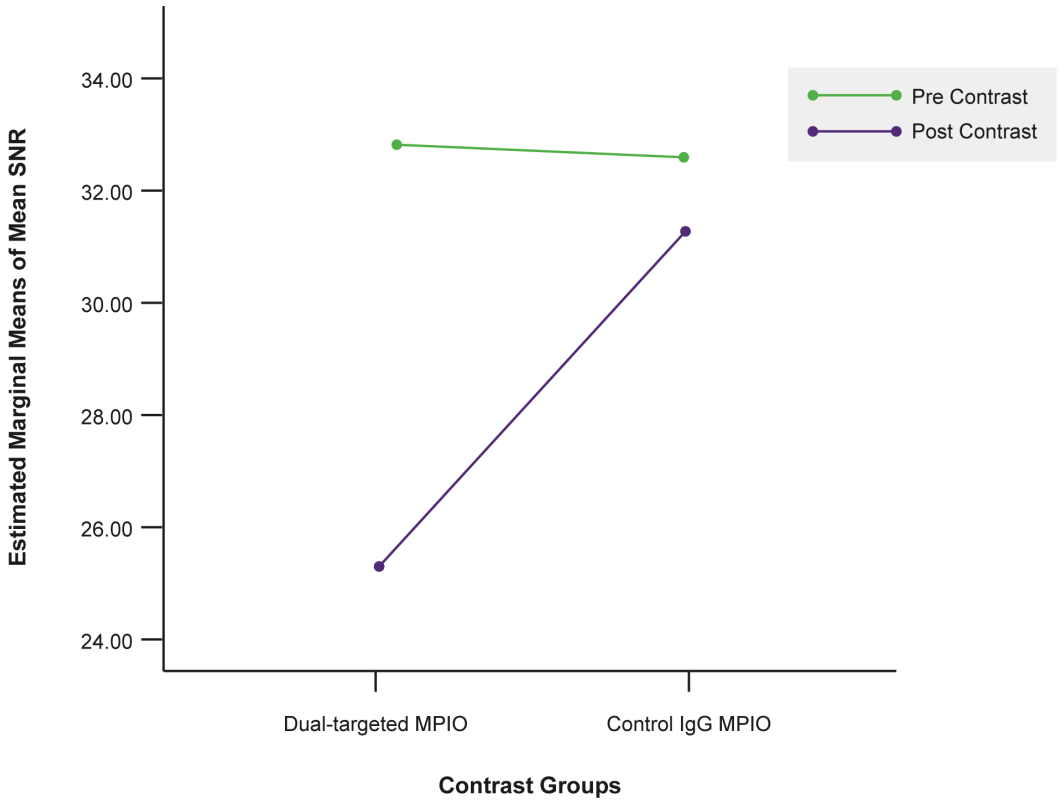



**Fig. 5.12. The profile plot of pre-contrast and post-contrast SNR comparison in dual-targeted MPIO group and control IgG-MPIO group**. There was 23.1% reduction in mean SNR in dual-targeted MPIO group, but only 3.8% reduction in mean SNR in control IgG-MPIO group.

### *Intra-observer and inter-observer variability*

The Bland-Altman plot in Figure 5.13 demonstrated that all the differences in % change of SNR measured by the same observer at two different time points (one month interval) were within the 95% limits of agreement (mean difference ± 1.96 x standard deviation of the difference). Therefore, there was no significant intra-observer variability in the measurement of % change of SNR in aortic vessel wall.

The Bland-Altman plot in Figure 5.14 showed that all the differences in % change of SNR measured by two observers were within the 95% limits of

agreement. Therefore, there was no significant inter-observer variability in the measurement of % change of SNR in aortic vessel wall.

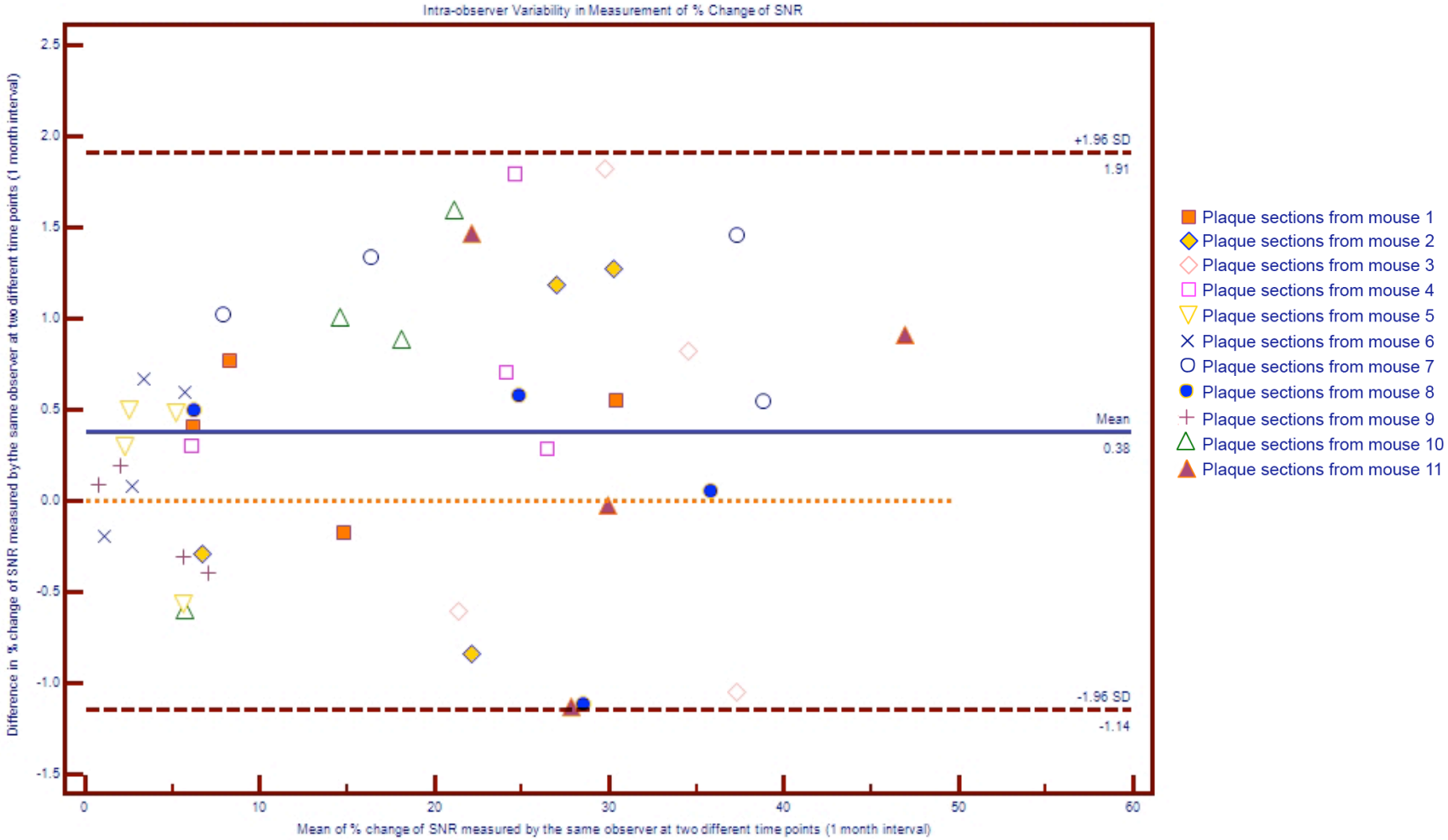



**Fig 5.13. The Bland-Altman plot for intra-observer variability.** The plot demonstrates that all the differences in % change of SNR measured by the same observer at two different time points (one month interval) are within the 95% limits of agreement (mean difference ± 1.96 x standard deviation of the difference).

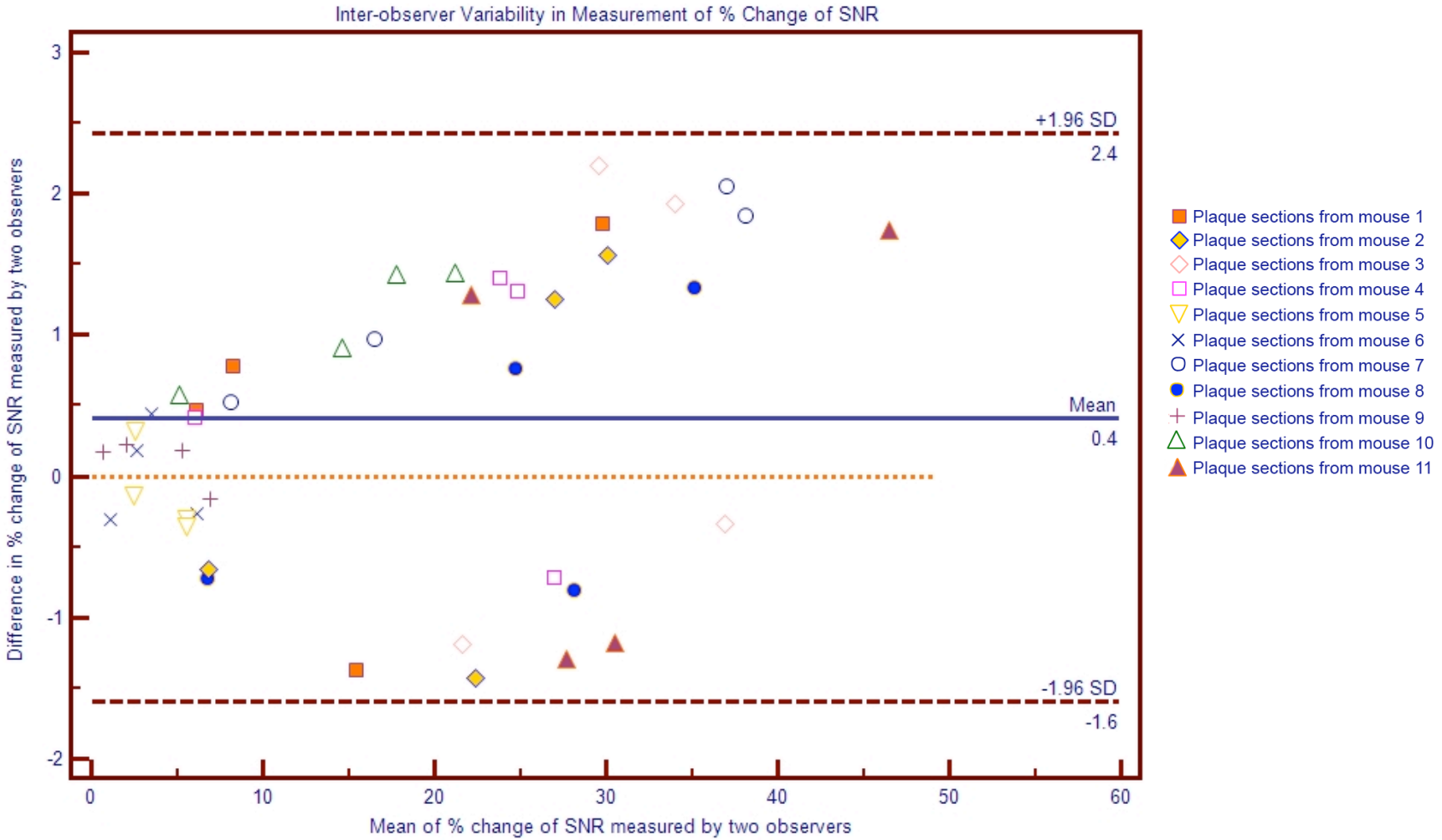



**Fig 5.14. The Bland-Altman plot for inter-observer variability.** The plot demonstrates that all the differences in % change of SNR measured by two observers are within the 95% limits of agreement (mean difference ± 1.96 x standard deviation of the difference).

### 5.3.2.2 Comparative Analyses Between MR and Histology

***Relationship of MPIO-labeled cell, endothelial cell, macrophage and smooth muscle cell content with the magnitude of reduction in SNR***

The extent to which dual-targeted MPIO induced MR contrast effect tracked the MPIO-labeled cell, endothelial cell, macrophage and smooth muscle cell content within plaque lesions was assessed. The relationship of different types of cell content with the magnitude of reduction in SNR in plaque lesion was quantitatively evaluated. The amount of Perls' staining for iron on aortic root sections was significantly positively related to the magnitude of reduction in SNR between the respective pre-contrast and post-contrast MR image quadrants in both groups ($\beta = 4.503$, $\chi2\ (1) = 40.840$, $p < 0.001$). The amount of CD31 staining for endothelial cells and Mac3 staining for macrophages were significantly positively related to the magnitude of reduction in SNR in the respective MR image quadrants in the dual-targeted MPIO group [CD31: ($\beta = 4.766$, $\chi2\ (1) = 5.983$, $p = 0.014$); Mac3: ($\beta = 0.383$, $\chi2\ (1) = 6.859$, $p = 0.009$)]. However, the amount of αSMA staining for smooth muscle cells on aortic root sections was not significantly related to the magnitude of reduction in SNR in the respective MR image quadrants in the dual-targeted MPIO group ($\beta = -0.049$, $\chi2\ (1) = 0.152$, $p = 0.697$). By contrast, the amount of all different types of cell content, i.e. endothelial cells, macrophages and smooth muscle cells, on aortic root sections were not significantly related to the magnitude of reduction in SNR in the respective MR images in the control IgG-MPIO group. Furthermore, controlling for the effect of these predictors (the different types of cell content), the magnitude of reduction in SNR was significantly greater in the

dual-targeted MPIO group than in control IgG-MPIO group ($\beta = 9.602$, $\chi 2$ (1) = 13.013, $p = <0.001$).

The GEE model was fitted again by dropping the insignificant predictor (amount of αSMA staining). The result of this analysis also reported that the amount of staining of Perls' for iron, CD31 for endothelial cells and Mac3 for macrophages on aortic root sections were significantly positively related to the magnitude of reduction in SNR in the respective MR image quadrants in the dual-targeted MPIO group. Standardised parameter estimate for Perls' staining for iron was 0.534 and that for CD31 staining for endothelial cells and Mac3 staining for macrophages were 0.218 and 0.143 respectively. Therefore the effect of MPIO-labeled cell content on the magnitude of reduction in SNR was relatively stronger compared to the effect of endothelial cell content and macrophage burden in the plaque lesion while the effect of endothelial cell content was stronger than that of macrophage burden in the dual-targeted MPIO group.

The results suggested that the dual-targeted MPIO induced MR contrast effect closely reflected the MPIO-labeled cell content within plaques. Moreover, this induced MR signal also tracked with the endothelial cell content and macrophage burden within plaque lesions, but not the smooth muscle cell content. By contrast, the control IgG-MPIO induced MR signal did not reflect or track all different types of cell content, i.e. endothelial cells, macrophages or smooth muscle cells, within plaque lesions. This suggested that the very small but statistically significant contrast effect (3.8% reduction in SNR) in the control

IgG-MPIO group (section 5.3.2.1) was unlikely due to MPIO binding to a specific cell type within plaque lesions; rather, it was likely due to small amount of non-specific MPIO retention within the plaques.

## 5.3.3 Histological Analysis Of the Aortic Root

### 5.3.3.1 Qualitative Histological Image Analysis

***Colocalisation of MPIO***

To investigate which types of cells colocalise with MPIO within the lesion, serial histological sections of Perls' staining for iron and immunostaining for different cell types, i.e. endothelial cells, macrophages and smooth muscle cells, were examined. In the dual-targeted MPIO group, the majority of the focal or multi-focal Perls' staining was observed to localise in the surface or peri-luminal region of the plaques with small amount of diffused Perls' staining sporadically distributed in the deep portions of the intima close to the lipid core (Figure 5.15 A, B and C). Serial sections stained for endothelial cells revealed that majority of Perls' staining colocalised to endothelial cells. Serial sections stained for macrophages showed that there was sparse, but definite, Perls' staining colocalised to macrophages in subendothelial fibrous cap region and within the intima close to the necrotic lipid core. However, frequently there were locations within plaque sections where there were abundant macrophages, but where Perls' staining was scarce. Serial sections stained for smooth muscle cells revealed minimal colocalisation of Perls' staining to this cell type (Figure 5.15). To summarise, serial sections of Perls' staining and immunostaining for different cell types revealed that there was good degree of

colocalisation of the Perls stain with endothelial cells, and sparse, but definite, colocalisation with macrophages, but minimal colocalisation with smooth muscle cells. However, the relationship between the content of different cell types and the amount of MPIO retention within plaque lesion remains to be quantitatively validated in section 5.3.3.2.

In the control IgG-MPIO group, only a minority of plaques was shown to have small amount of Perls' staining sparingly distributed in a diffuse pattern in the deep portions of the intima. Serial sections stained for endothelial cells and smooth muscle cells revealed an absence of these cell types in these locations. Plaque sections stained for macrophages showed that small amount of Perls staining sparsely colocalised to macrophages within the intima close to the lipid core (Figure 5.15).

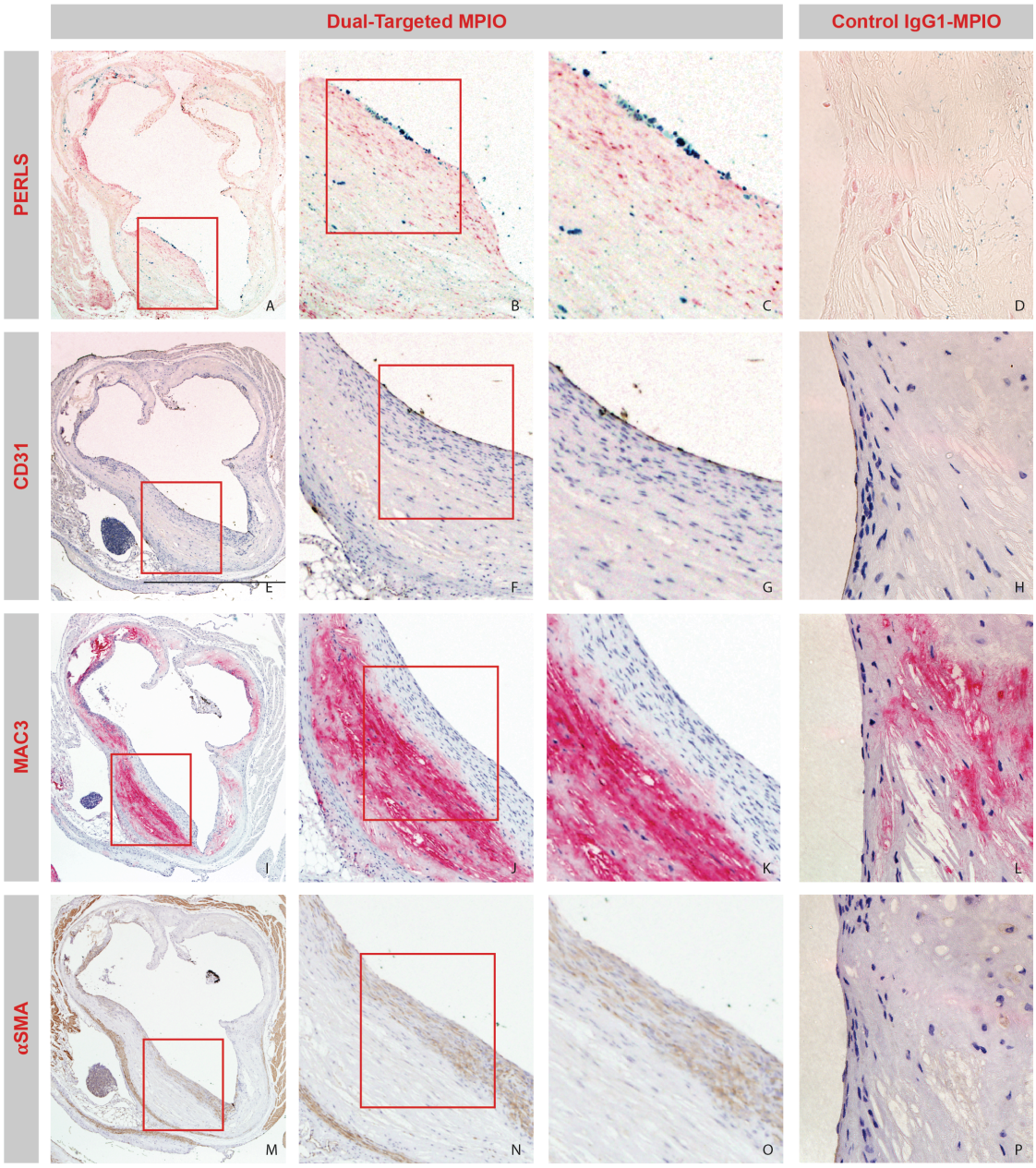



**Fig. 5.15. Representative serial histological images of aortic root.**

Panel A, B and C showed Perls' staining for iron particles in aortic root sections from the dual-targeted MPIO group. Multifocal Perls' staining was seen to localise in the surface or peri-luminal region of the plaques with small amount of diffuse Perls' staining sporadically distributed in the deep portions of the intima close to the lipid core.

Panel D showed Perls' staining in aortic root sections from the control IgG-MPIO group. Perls staining was seen to sparingly distribute in a diffuse pattern in the intima.

Panel E, F and G showed CD31 staining for endothelial cells in the serial aortic root sections from the dual-targeted MPIO group. Endothelial cells were seen to colocalise to Perls' staining in panel A, B and C.

Panel H showed CD31 staining in serial aortic root sections from the control IgG-MPIO group.

Endothelial cells were not observed to colocalise to Perls' staining in panel D.

Panel I, J and K showed Mac3 staining for macrophages in the serial aortic root sections from the dual-targeted MPIO group. Perls' staining in Panel A, B and C was seen to have sparse, but definite, colocalisation to macrophages in subendothelial fibrous cap region and within the intima close to the necrotic lipid core in panel I. However, frequently there were locations within plaque sections, where there were abundant macrophages (panel K, red marquee in panel I and J), but where Perls' staining was relatively scarce (panel C, red marquee in panel A, B).

Panel L showed Mac3 staining for macrophages in serial aortic root sections from the control IgG-MPIO group. Small amount of Perls' staining in Panel D was seen to sparsely colocalise to macrophages within the intima in panel L.

Panel M, N and O showed αSMA staining for smooth muscle cells in serial aortic root sections from the dual-targeted MPIO group. Minimal amount of smooth muscle cells in panel M, N and O was seen to colocalise to Perls' staining in panel A, B and C.

Panel P showed αSMA staining in serial aortic root sections from the control IgG-MPIO group. Smooth muscle cells were not observed to colocalise to Perls' staining in panel D.

Original magnification x4 in panel A, E, I and M; Original magnification x10 in the remaining panels.

At higher magnification, dual-targeted MPIO were observed to colocalise only at endothelial cells overlying atherosclerotic lesions, with no MPIO bound to lesion-free endothelium, whereas no accumulation of control IgG-MPIO in these cells was observed. A few iron particles were observed to sparsely colocalise with macrophages within the intima close to the lipid core of the plaques in both groups. Minimal amount of iron particles were observed to colocalise with smooth muscles cells of the plaques in both groups (Figure 5.16). Immunohistochemistry for VCAM-1 and endothelial cells on serial sections confirmed endothelial activation on atherosclerotic lesions (Figure 5.17).

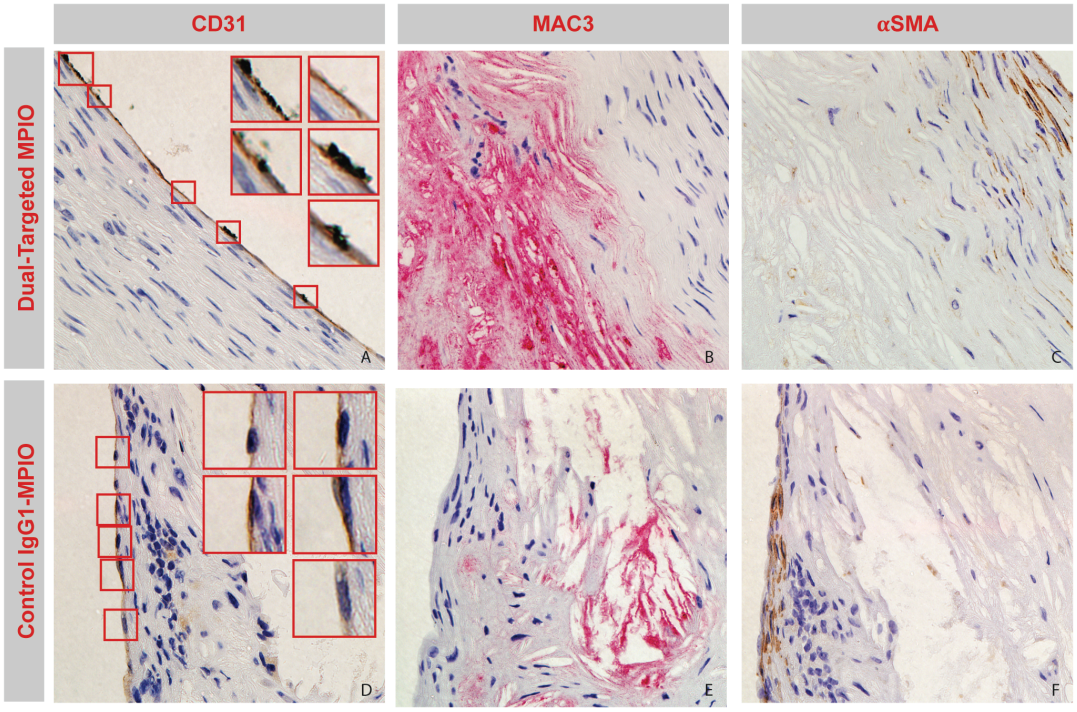



**Fig. 5.16. Representative serial histological images of aortic root in the dual-targeted MPIO group and control IgG-MPIO group.** Dual-targeted MPIO (red marquee in panel A) were observed to colocalise at endothelial cells of the aortic root plaque lesions. Minimal dual-targeted MPIO were observed to sparsely colocalise with macrophages within the intima. No dual-targeted MPIO were observed to colocalise with smooth muscles cells of the plaques in panel C. No iron particles were observed to colocalise at endothelial cells (panel D), macrophages (panel E) and smooth muscle cells (panel F) of the aortic root plaque lesions in the control IgG-MPIO group. Original magnification x40.

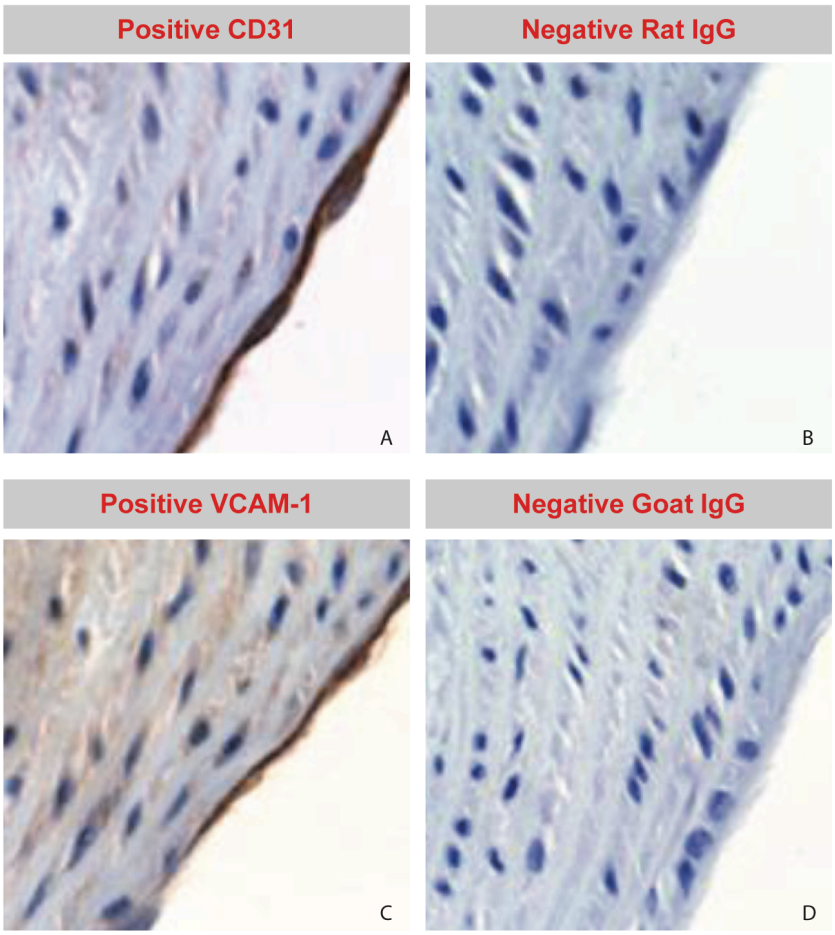



**Fig. 5.17. Representative serial histological images of aortic root atherosclerotic lesion of positive and negative antibody control for CD31 and VCAM-1 staining.** Panel A (positive control) shows endothelial cells exhibiting specific CD31 immunoreactivity in aortic root lesion. Panel B (negative control) shows no CD31 immunoreactivity in matching non-immune IgG controls. Adjacent section in panel C shows VCAM-1 immunoreactivity on endothelial cells overlying the aortic root lesion. Panel D (negative control) shows no VCAM-1 immunoreactivity in matching non-immune IgG controls. Original magnification x20.

### 5.3.3.2 Quantitative Histological Image Analysis

***Relationship of endothelial cell, macrophage and smooth muscle cell content with amount of MPIO retention***

The relationship of endothelial cell, macrophage and smooth muscle cell content with the amount of MPIO retention within the plaque lesion was evaluated quantitatively. The amount of CD31 staining for endothelial cells on

aortic root sections was significantly positively related to the amount of Perls' staining for iron on the same section quadrants in the dual-targeted MPIO group (β = 1.243, χ2 (1) = 12.752, p = <0.001). However, the amount of Mac3 staining for macrophages and αSMA staining for smooth muscle cells on the section quadrants were not significantly related to that of Perls' staining for iron on the same section quadrants in the dual-targeted MPIO group [Mac3: (β = 0.002, χ2 (1) = 0.006, p = 0.938); αSMA: (β = -0.004, χ2 (1) = 0.015, p = 0.912)]. In the control IgG-MPIO group, by contrast, all different types of cell contents, i.e. endothelial cells, macrophages and smooth muscle cells, were not significantly related to that of Perls' staining for iron on the same sections of plaque lesion**.** Furthermore, controlling for the effect of these predictors, the amount of MPIO retention within the plaque lesion was significantly greater in the dual-targeted MPIO group than control IgG-MPIO group (β = 2.162, χ2 (1) = 171.345, p = <0.001).

The GEE model was fitted again by dropping insignificant predictors (Mac3 and αSMA staining). The result of this analysis also reported that the amount of CD31 staining for endothelial cells content was significantly positively related to the amount of MPIO retention within the same section quadrants of the plaque lesion in the dual-targeted MPIO group (standardised β=0.488, χ2 (1) = 19.694, p = <0.001).

### 5.3.4 *In Vivo* MRI of Aortic Arch

To determine whether dual-targeted MPIO can detect atherosclerosis, *in vivo* MRI of aortic arch was performed at 30 minutes post-injection of MPIO. Representative MR images of aortic arch pre- and post-injection of either dual-targeted MPIO or negative control IgG-MPIO are shown in Figure 5.18. In the baseline pre-contrast *in vivo* imaging, no discrete low signal area was detected on the luminal side of the aortic arch (Figure 5.18 A). At 30 minutes post-injection of dual-targeted MPIO, a new discrete area of hypointensity signal was observed on the luminal side of the lesser curvature of aortic arch (Figure 5.18 B). The hypointensity signal effect was due to the presence of MPIO-labeled cells, which was confirmed by Perls' stain for iron on the atherosclerotic lesions on the lesser curvature of aortic arch (Figure 5.18 D). By contrast, following injection of control IgG-MPIO, no new area of hypointensity was observed in the post-contrast image of aortic arch (Figure 5.18 F), which was confirmed by the absence of Perls' stain on the plaque lesion in the lesser curvature of aortic arch (Figure 5.18 H).

Further, a T2*-weighted FLASH sequence with optimised frequency offset was used as an adjunct to detect and characterise atherosclerotic plaques by dual-targeted MPIO. In contrast to the MPIO-induced hypointensity (dark signal) in T2*-weighted FLASH sequence (Figure 5.19 B), the MPIO-induced signal effect on the luminal side of the lesser curvature of aortic arch was observed as hyperintensity (bright signal) in this T2*-weighted FLASH sequence with

optimised frequency offset (Figure 5.19 C). The overlay image in Figure 5.19 D revealed the new area of hypointensity in Figure 5.19 B coincide with the area of hyperintensity in the lesser curvature of aortic arch. Both of the MPIO-induced hypointensity and hyperintensity signal effects were confirmed by the presence of Perls' stain on the atherosclerotic lesions in the lesser curvature of aortic arch (Figure 5.19 E).

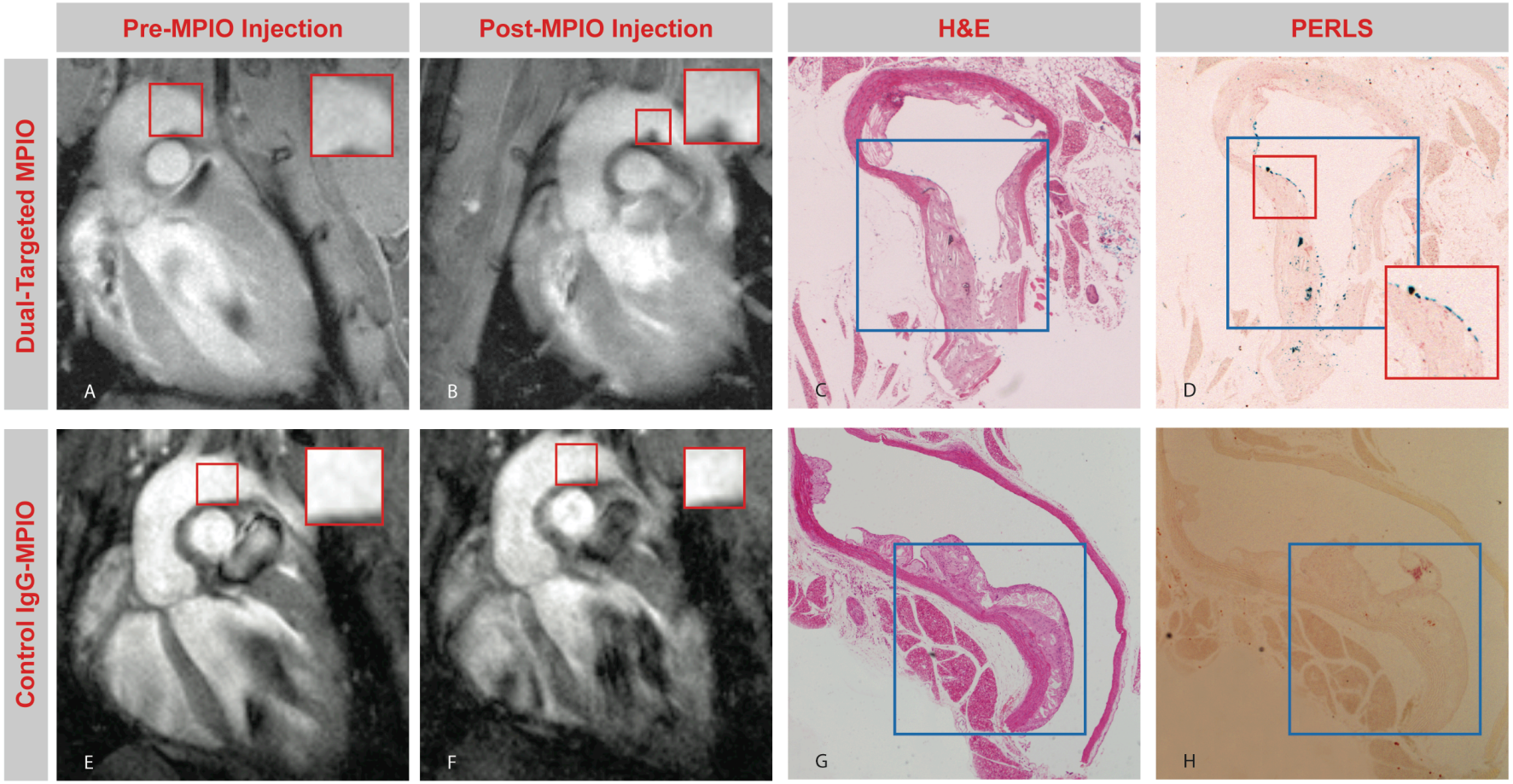



**Fig. 5.18. Representative MR and histological images of aortic arch.**

Panel A showed no discrete hypointensity detected on the luminal side of the aortic arch before contrast injection in the dual-targeted MPIO group. At 30 minutes post-contrast administration, a new discrete area of hypointensity was observed on the luminal side of the lesser curvature (red box) of aortic arch in panel B. The H&E in panel C confirmed the presence of advanced atherosclerotic lesions, predominantly in the lesser curvature (blue box) of the aortic arch. The MPIO-induced signal effect was confirmed by the presence of Perls' stain predominantly on the atherosclerotic lesions in the lesser curvature (blue box) of aortic arch in panel D. Panel E showed a representative MR image of aortic arch before contrast injection in the control IgG-MPIO group. Panel F showed the MR image of aortic arch at 30 minutes post-contrast injection. No discrete hypointensity area was observed on the luminal side of the lesser curvature (red box) of aortic arch in panel F. The H&E in panel G confirmed the presence of advanced atherosclerotic lesions in the lesser curvature (blue box) of aortic arch. The absence of MPIO-induced signal effect was confirmed by the absence

of Perls' stain on the atherosclerotic lesions in the lesser curvature (blue box) of aortic arch in panel H. Original magnification x10.

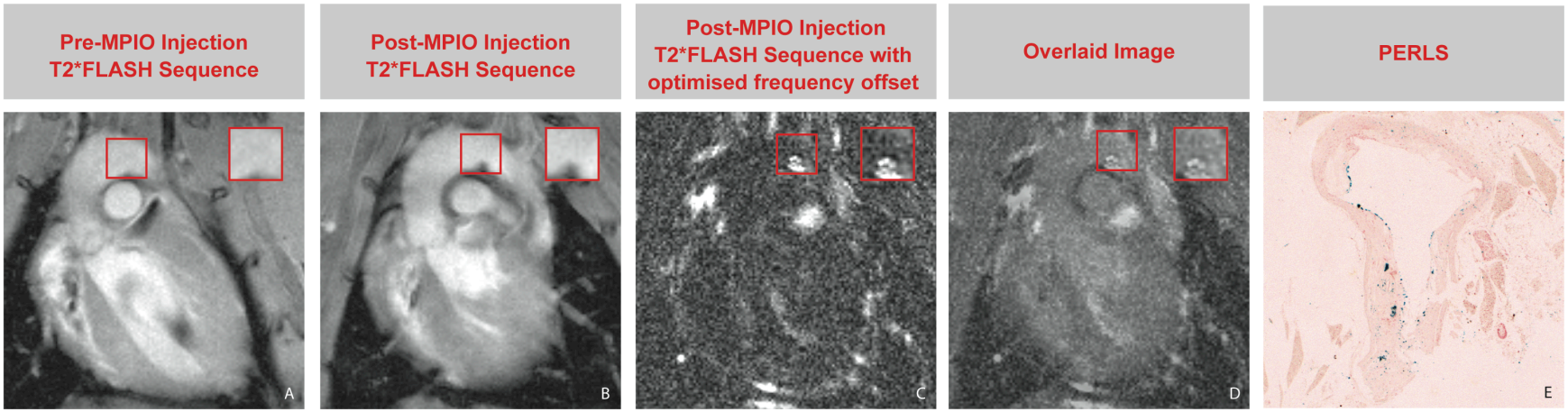



**Fig. 5.19. Representative MR images of aortic arch.**

Panel A showed no discrete hypointensity detected on the luminal side of the aortic arch before contrast injection in the dual-targeted MPIO group. 30 minutes post-contrast administration, a new discrete area of MPIO-induced hypointensity was detected on the luminal side of the lesser curvature of aortic arch using T2*-weighted FLASH sequence in panel B. On the contrary, the MPIO-induced signal effect on the luminal side of the lesser curvature of aortic arch was detected as hyperintensity (bright signal) in the T2*-weighted FLASH sequence with optimised frequency offset in panel C. The overlay image in panel D revealed the new area of hypointensity in panel B coincide with the area of hyperintensity in the lesser curvature of aortic arch in panel C. Both of the MPIO-induced hypointensity and hyperintensity signal effects were confirmed by the presence of Perls' stain on the atherosclerotic lesions in the lesser curvature of aortic arch in panel E.

## 5.4 DISCUSSION

Quantitative reporting of local plaque inflammatory status is a prime objective in the diagnosis and characterisation of atherosclerotic disease. Quantitative molecular imaging enhances the diagnostic utility of MRI as it potentially allows the severity of disease to be determined and response to therapeutic interventions monitored. It is becoming increasingly important because drugs directly targeting inflammatory pathways are in development for the treatment of high-risk patients with atherosclerosis.[191] The vascular endothelium is an important regulatory interface that controls leukocyte recruitment into sites of inflammation, mediated by the over-expression of adhesion molecules, and hence serving an important target for imaging probes and therapeutic intervention in cardiovascular diseases.[157,192] In this study, we demonstrate non-invasive *in vivo* molecular MRI of atherosclerotic lesions in aortic root and aortic arch in ApoE−/− mice using dual-targeted MPIO against VCAM-1 and P-selectin. These particles swiftly achieve steady state binding at target sites and provide evident 'target-to-background' and quantifiable contrast effects. Moreover, the MR contrast effects generated by dual-ligand MPIO binding tracked quantitatively with macrophage burden within the lesion. However, our histological results showed that the dual-ligand MPIO selectively binds to endothelial cells, with minimal binding to macrophages within the plaque. We further demonstrated the preferential binding of dual-targeted MPIO in atherosclerosis-susceptible lesser curvature of the aortic arch compared with the atherosclerosis-resistant greater curvature of the aortic arch by *in vivo* MRI with confirmatory histology.

### 5.4.1 *In Vivo* Imaging of Atherosclerosis in Mice Using Dual-Targeted MPIO

Molecular imaging strategies benefit from swift binding and maintenance of steady state at target, with rapid clearance of unbound contrast from the blood pool, to achieve high 'target-to-background' contrast effect. To determine whether dual-targeted MPIO can detect atherosclerosis *in vivo*, serial MRI scans of the aortic root was performed from 20 minutes post-injection of MPIO up to 2 hours. The MRI showed new areas of dark signal after dual-ligand MPIO injection, with minimal MR signal effects observed in pre-contrast images and in aortic root images of mice injected with control IgG-MPIO. Perls' stain confirmed the dark signal was due to the presence of MPIO-labelled cells on the aortic root lesions. Further, the amount of MPIO-labeled cells in aortic root lesions was shown to be significantly positively correlated with the magnitude of MR contrast effect. We feel that it is important to compare post-contrast with corresponding pre-contrast images to differentiate signal reductions attributable to MPIO uptake from other effects. For example, plaque calcification, haemorrhage, cell necrosis, and tissue-interface inhomogeneity can also have strong susceptibility effects, and therefore cause signal loss, which in turn leads to misinterpretation of the MRI results. However, in contrast to signal loss attributable to MPIO uptake, these tissues or artifacts would have already caused signal loss in the pre-contrast images. The *in vivo* detection of atherosclerotic lesions by dual-targeted MPIO was further supported by the findings as follows: Firstly, significantly higher number of post-contrast image quadrants of aortic roots was observed to have dark signal in the dual-targeted MPIO group than in control IgG-MPIO group. Secondly, the magnitude of

MPIO-induced SNR reduction in dual-targeted MPIO group was significantly greater than that in control IgG-MPIO group, reflecting the fact that plaque lesions were preferentially targeted by dual-ligand MPIO, but not non-specific IgG-MPIO, as confirmed by histology. These results affirm the ability of dual-targeted MPIO to detect atherosclerotic lesions with in live ApoE-/- mice by *in vivo* MRI with evident 'target-to-background' contrast effect, which is an important attribute of clinical contrast agent in imaging acute plaque based events.

Previous pre-clinical and clinical studies demonstrated the use of USPIO as a passive contrast agent to identify plaque macrophages as surrogate markers of plaque inflammation for assessment of atherosclerosis in patients and animal models.[193-195] USPIO can potentially be used in the clinical setting to differentiate between high- and low-risk plaques for risk stratification because USPIOs predominantly accumulate in macrophages within ruptured and rupture-prone lesions.[196] While being a positive attribute for macrophage imaging, the prolonged blood half-life poses two major drawbacks in targeted contrast agents including the high background contrast for an extended period, and the extensive delay after USPIO injection before imaging.[105] The long delay between the USPIO administration and the imaging window restricts widespread clinical use, particularly in the acute setting, of these agents. The recommended interval in the majority of animal models and human studies was 5 to 7 days,[195,197] and 24 to 36 hours respectively,[105] although the recently emerged P904-USPIO has shortened this interval to 24 hours in animal model due to faster blood clearance of these particles.[198] Moreover, accumulating

evidence shows that the lesion macrophage population is not static, but is involved in ongoing influx and excursion.[190] The dynamic macrophage population in plaque lesions together with the extensive delay in imaging begs the question: In the event of acute thrombo-embolism such as stroke or myocardial infarction, is the signal detected due to the after-effect of the event rather than the plaque instability that provokes rupture and symptoms? Furthermore, because USPIO can be taken up non-specifically and can extravasate passively,[106] particularly in the sites of inflammation with enhanced vascular permeability, there is potential to compromise the specificity of molecular targeting.

Compared with nanoscale particles, ligand-conjugated MPIO are potentially better suited for imaging acute clinical events. VCAM-1 conjugated MPIOs have been widely used to image acute inflammatory processes not only in the context of atherosclerosis,[133,199] but also in acute brain inflammation[141] and acute vascular syndromes such as ischaemia-reperfusion injury.[143] Building on these previous approaches,[133,141,143,199] our study demonstrates that dual-targeted MPIO binding was rapid and specifically to the endothelium overlying atherosclerotic lesions in aortic root and aortic arch under *in vivo* conditions, showing contrast effect from 30 to 45 minutes, and persisted for the entire 2-hour imaging period. MPIO offer distinct advantages over nanoscale particles: 1) MPIO convey a great payload of iron and, hence sensitivity is high and contrast effect is potent.[112] 2) Unbound MPIO are cleared swiftly from circulation so background blood phase contrast is minimal, enhancing target-to-background ratio and plaque visualisation. [114] 3) The large size and

incompressible nature of MPIO prevent the particles from translocating across the endothelium or undesirable passive accumulation, thereby retaining specificity for molecular targets expressed on the vascular endothelium.[85] 4) Unlike contrast agents that need to be concentrated within cells or to permeate tissue beyond the vasculature, the dual-antibody conjugated MPIO against VCAM-1 and P-selectin are designed to mimic the binding of peripheral blood leukocytes to the activated vascular endothelium, which is a rapid process, occurring within minutes.[199] 5) The increased surface area of MPIO enables greater loading capacity of antibodies to these particles, thereby increasing the binding efficiency of targeted MPIO to the endothelium.[140,177] The potent contrast sensitivity, rapid binding and clearance kinetics of dual-ligand MPIO, coupled with the immediate accessibility to endothelial molecular markers (circumventing the need to permeate the plaque), distinguish targeted MPIO as a valuable molecular imaging platform in the context of imaging acute clinical events.

The temporal change in the signal effect on MRI in our study indicated that a practical imaging time frame for atherosclerosis, which lies between 30 minutes to 2 hours post-injection. However, the optimal time window remains to be further validated by serial imaging studies with larger sample size. The time window should be long enough to allow specific binding of the dual-targeted MPIO at sites of lesion under *in vivo* flow condition, but short enough to exclude non-specific uptake of these particles, in particular, by macrophages.

### 5.4.2 Dual-targeted MPIO Selectively Bind to Atherosclerosis-Susceptible Sites

Predisposition to atherosclerosis is uneven in the proximal aorta with endothelial activation in the atherosclerosis-prone lesser curvature and is relatively sparing in the atherosclerosis-resistant greater curvature of the arch.[199] The endothelial cells in regions of low shear stress, such as the lesser curvature of aortic arch, display irregular shape, disorganised alignment, as well as over-expression of cell adhesion molecules. By contrast, regions of high shear stress, such as the greater curvature of aortic arch, display endothelial cells of normal shape and alignment with minimal expression of cell adhesion molecules.[199] In our study, MRI demonstrated a new discrete area of dark signal on the luminal side of the lesser curvature of aortic arch after dual-ligand MPIO injection, with minimal MR signal effects observed in pre-contrast images and in aortic arch images of mice injected with control IgG-MPIO. This was further validated by using the same T2*-weighted FLASH sequence but with optimised frequency offset in the post-contrast imaging to eliminate the possible effect of air on MR image. Confirmed by histology, dual-targeted MPIO were selectively retained in the atherosclerosis-susceptible lesser curvature of the aortic arch compared with the atherosclerosis-resistant greater curvature of the arch. This is consistent with earlier studies, which showed dual-ligand MPIO or microbubbles targeted to either P-selectin or VCAM-1 preferentially bind to atherosclerosis-susceptible regions in the aortic arch, with similar upregulation in endothelial P-selectin and VCAM-1 expression in atherosclerotic lesions.[199,200] In doing so, dual-targeted MPIO can potentially

be used to correlate spatially with vascular inflammation in atherosclerosis in the future.

### 5.4.3 Dual-Targeted MPIO Bind to Activated Endothelial Cells Overlying Atherosclerotic Lesions

To test the cellular specificity of dual-targeted MPIO binding, the quantitative relationship of endothelial cell, macrophage and smooth muscle cell content with the amount of MPIO retention within the plaque lesion was evaluated. Our study reported that only the endothelial cell content, but neither macrophage nor smooth muscle cell content, was significantly positively related to the amount of dual-targeted MPIO within the aortic root lesions. The results suggested that dual-targeted MPIO predominantly bind to endothelial cells, with minimal binding to macrophages and smooth muscle cells. Supporting this, histology confirmed that dual-targeted MPIO localised only to endothelium overlying atherosclerotic lesions, with no MPIO bound to lesion-free endothelium. Only few or minimal iron particles were observed to sparsely colocalise with macrophages or smooth muscle cells within the lesion respectively. Immunohistochemistry for VCAM-1 and endothelial cells on serial sections confirmed endothelial activation overlying atherosclerotic lesions. This agrees with reports that VCAM-1 is most strongly upregulated in vascular endothelium overlying plaque.[201] Demonstration of the presence of adhesion molecules on plaque endothelial cells did not by itself prove that these molecules were targeted by the dual-ligand MPIO, but it could, at the very least, be regarded as a marker of ‘activation’ of endothelial cells overlying the plaque lesion. In the presence of endothelial activation on plaque lesions, only

dual-targeted MPIO, but not non-specific IgG-MPIO, selectively targeted at endothelial cells, putatively suggesting that dual-targeted MPIO selectively bound to activated endothelial cells overlying atherosclerotic lesions. The present results are consistent with previous flow cytometry study of cellular suspensions from digested aortas, which showed fluorescently labeled dual-ligand MPIO bound specifically to activated endothelial cells, and were not taken up by macrophages or other cell types.[199]

### 5.4.4 Dual-targeted MPIO induced MR Contrast Effect Tracks Quantitatively with Lesion Macrophage Burden

The role of plaque macrophage burden and activity in the onset of plaque instability and acute thrombotic complications of atherosclerosis has been established.[14] Recent studies have linked clinical evidence, macrophage biology, and molecular imaging research to explore the feasibility of visualising macrophage burden or activation in cardiovascular diseases.[183,193,196,202,203] Monocytes were shown to be actively recruited in a progressive manner that was proportional to the severity of atherosclerotic disease.[204] Clinical evidence established that lowering of cholesterol level reduced acute coronary events.[205,206] Preclinical studies further showed that dietary cholesterol lowering and statin treatment limited inflammation, reduced endothelial activation and diminished monocyte/macrophage infiltration in arteries.[188,189,207,208,209] Therefore, non-invasive monitoring of plaque macrophage burden or activity should help identify patients with subclinical inflamed lesions and provide novel and important insights into preventive cardiovascular medicine. Our study demonstrated the correlation between the MR contrast effect induced by endothelial-bound dual-ligand MPIO and lesion macrophage content. This is consistent with regulation of monocyte influx at the vascular endothelium interface, with overall lesion macrophage burden reflecting the net effects of recruitment versus efflux, apoptosis, and necrosis.[190] The results affirm that an *in vivo* MRI approach combined with dual-targeted MPIO can quantitatively track the macrophage burden within the atherosclerotic lesions. Previous studies have shown that quantification of lesion macrophage burden by USPIO-induced signal change was difficult due

to a non-linear relationship between signal loss on T2*-weighted imaging and overall macrophage burden.[210] The clustering of USPIO in tissues can lead to additional T2* shortening and the 'blooming effect',[211] where protons some distance away from the iron particles are dephased, resulting in disproportionately enhanced hypointensity signal. Moreover, USPIO can be taken up non-specifically and can extravasate passively,[106] particularly in the sites of inflammation with enhanced vascular permeability, that has the potential to confound quantitative reporting of the actual lesion macrophage burden. By contrast, MPIO can provide potent contrast sensitivity, and, because of their uniform size and composition, offering an opportunity for quantitative reporting.[143] Furthermore, the binding of dual-ligand MPIO is directly dependent on its interaction with the immediate accessible targets, i.e. adhesion molecules on the endothelium, without any intervening processes, such as vessel permeability, tissue diffusion or cell membrane transporter function, that have the potential to confound quantitative reporting of the molecular target.[143] Therefore, using dual-targeted MPIO, MRI can be used to attain quantitative reporting of local inflammatory status that is commonly only achievable with nuclear imaging techniques, such as positron emission tomography. This imaging approach, when translated to clinical setting, presents a favorable method for screening and monitoring arteries in patients because of its non-invasive nature and the absence of iodine-based contrast or radioactive agents. Moreover, dual-ligand MPIO may provide a novel functional imaging probe to gauge plaque macrophage burden, which is a well-validated indicator of local inflammatory status. This could have a number of important clinical implications, including the assessment of the inflammatory

burden, rather than the mere anatomy, of atherosclerotic plaques in individual patients before clinical complications occur, thereby contributing a personalised approach to the management of atherosclerotic disease. The risk stratification offered by this imaging strategy helps identify the high-risk asymptomatic patients, hence optimising resource allocation to target the appropriate cohorts. Further, dual-targeted MPIO provide a useful molecular imaging platform to dissect the role of vascular inflammation in clinical outcomes. The non-invasive monitoring of the changes in plaque macrophage burden during therapeutic interventions will likely to provide new insights into preventive cardiovascular medicine and offer potent tools for choosing doses and evaluating efficacy in pilot clinical trials on novel anti-inflammatory or lipid lowering therapies. Finally, the developed dual-targeted MPIO probes could be used potentially as a scaffold for further development of novel targeted therapeutics, which shuttle therapeutic drugs to the site of inflammation in a targeted fashion, increasing the efficacy-to-toxicity ratio.

The PET tracer 18F-fluorodeoxyglucose (FDG) has been extensively evaluated for measuring intraplaque inflammation in atherosclerotic lesions, with success in identifying acute lesions[87] and in monitoring response to therapy.[87,212] Despite ample evidence, concerns have been raised about specificity of this tracer for imaging inflammatory cells as FDG is taken up by any metabolically active tissue.[69] Moreover, a recent *in vitro* study suggests that this technique may be sensitive to hypoxia in plaque macrophages rather than quantifying inflammation per se.[213] As a result, considerable effort has been recently directed towards the development of novel 'radio-ligands' to

enhance the diagnostic performance of detection of vulnerable plaques.[70,71,72] Despite this, the drawbacks of nuclear imaging modalities, including its limited spatial resolution, logistics of isotope provision, substantial radiation exposure and expense, limit its widespread clinical use.

### 5.4.5 Statistics

Repeated measures modeling was used to assess the strength of the relationship between the different types of cell content in plaque and the magnitude of MPIO-induced reduction in SNR in each of the four quadrants per mouse. As previously described by Tang et al[82], compared to the simple paired analysis, this complex statistical model was designed specifically to be a more robust treatment of the data for the reasons as follows: Each slice has signal change assessed in four quadrants so as to minimise the chance of a focal signal loss being "lost" in a mean signal change for the whole slice. However, each of these quadrants cannot be regarded as an entirely independent observation and to some extent the signal in one quadrant will affect the signal in its adjacent quadrant. Hence, if these data were treated as independent observations, the number of degrees of freedom of any statistical test would be erroneously high, resulting in an erroneously low p-value. In an attempt to minimise potential statistical error, a complex repeated measures modeling was used to model true variances in quadrant data and bring the degrees of freedom back to the correct level.

### 5.4.6 Limitations

One of the limitations of devising a model to look for relationship between MPIO-induced MR contrast effect and the different types of cell content in the plaque is that although T2* weighted imaging does allow visualisation of the effect of MPIO, there has been much debate in the literature as how to best quantify the MPIO-induced dark signal within the plaque. Ruehm et al.[183] and Trivedi et al.[193] used manually delineated regions of interest (ROI) and calculated the normalised signal change between pre- and post-USPIO images. The signal was normalised to the signal in the adjacent sternocleidomastoid muscle and any ROI delineated that showed an actual normalised signal reduction were interpreted as USPIO uptake. However, this demonstrated only a moderate correlation with macrophages staining positively for USPIO on Perls' staining. The main advantage of this ROI approach originates from its concentration on the magnetic susceptibility artifacts or signal voids itself.[82] However, SNR measurements are performed only in specific regions of the vessel wall selected by the observer, hence the technique does not provide a mean intensity of the entire vessel wall nor does it allow an estimate of the ROI spatial extension. This technique has an inherent problem of subjective bias and observer error which potentially compromise its accuracy in quantification of signal effect and inflammatory burden. [82]

In view of this, a recently emerged approach was adopted in this study. This technique involved dividing the vessel wall in each slice into quadrants by constructing perpendiculars to the horizontal axis across the image.[210] This

technique has the advantage that data points contributed by the whole vessel and every quadrant that has plaque rather than the biased predefined ROI. Thus, a quadrant showing signal loss, once normalised to background noise, was taken to represent MPIO uptake in that quadrant.[82] Furthermore, there was no significant intra-observer and inter-observer variability in the measurement of MPIO-induced reduction in SNR using this quadrant approach shown in this study. Whilst minimising operator bias, this technique has a number of restrictions associated with it. Small focal areas of hypointensity signal can still be lost in a quadrant if the area of region is too large, or when regions of signal enhancement are found around it, limiting the sensitivity of the analysis. On the contrary, if the region-size is too small, the region-to-region variability in SNR measurement will increase.[82] Furthermore, the SNR measurement in the quadrant generally represents the mean density of accumulated iron oxide particles rather than the detailed distribution of iron-labelled cells. Although the relationship between MPIO-induced MR contrast effect and the different types of cell content in the plaque was demonstrated in this study, T2-mapping might be able to offer an alternative way to quantify iron oxide-labelled cells.

The aortic root lesions were detectable with evident 'target-to-background' contrast effect by *in vivo* MRI using dual-targeted MPIO. However, the difference in quantification methods adopted by previous studies made it difficult to compare the magnitude of iron particles-induced MR contrast effect in our study with those in previous ones.[105,193,199] Further optimisation in SNR is warranted in future studies.

## 5.5 CONCLUSIONS

We have developed a dual-targeted contrast agent, for in vivo molecular MRI, that rapidly binds to vascular endothelium overlying atherosclerotic lesions in aortic root and aortic arch. Although predominantly bound to endothelium, the accumulation of MPIO contrast agent quantitatively tracked with macrophage content within the lesions. We further demonstrated the preferential binding of dual-targeted MPIO in atherosclerosis-prone regions of the aortic arch compared with the atherosclerosis-resistant areas of the aortic arch. The *in vivo* MRI combined with dual-targeted MPIO approach provides significant advantages: (1) swift binding and maintenance of steady state at target sites; (2) evident 'target-to-background' and quantifiable contrast effects; (3) quantitative tracking of macrophage burden with atherosclerotic lesions. This molecular imaging strategy will potentially allow real time *'in vivo* microscopy' reporting the underlying inflammatory process in vulnerable plaques and could have a number of important clinical implications in the future, including (1) assessment of the inflammatory burden of atherosclerotic plaques in individual patients, thereby contributing a personalised approach to the management of atherosclerotic disease; (2) identification of the high risk patients with subclinical inflamed lesions, hence optimising resource allocation to target the appropriate cohorts; (3) non-invasive monitoring of response to treatment; (4) evaluation of efficacy in pilot clinical trials on novel therapies; (5) potent platform for development of targeted drug delivery.

# CHAPTER 6:

# *In Vivo* ApoE-/- Mouse Model Stage: Carotid Artery

# 6.1 INTRODUCTION

The non-uniform distribution of atherosclerotic lesions in the arterial system is closely linked to local hemodynamic factors.[214] Shear stress, measured in N/m2 or Pascal (Pa), is the tangential stress due to the friction or drag force of the flowing blood on the endothelial surface of the arterial wall.[215] Shear stress is thought to play a vital role in the development of endothelial dysfunction and atherosclerosis. This concept is based on the observation that low shear stress (<1.5 N/m2 in humans) in the inner curvatures of coronary arteries, or oscillatory shear stress (i.e. displaying directional change and boundary layer separation) near arterial bifurcations or branch ostia are closely associated with atheroma formation. [216-218] By contrast, straight arterial segments with laminar flow in human have shear stress levels of 1.5 N/m2 or greater and this appears to be atheroprotective.[216-218] The relationship between shear stress and atherosclerosis is largely based on observational studies in human and large animals.[216,219,220] The role of altered shear stress in causing changes in gene expression was confirmed by *in vitro* experiments studying endothelial cells in flow chambers under well-controlled shear stress conditions.[221,222] In order to investigate the direct casual relationship between alterations in shear stress and atherosclerosis, recent studies have developed a perivascular shear stress modifier (referred to as a cuff) that can induce changes in shear stress patterns *in vivo* in different segments of a straight vessel and in a defined manner. [223,224]

Placement of the cuff around the common carotid artery creates lowered shear

stress upstream from the cuff, increased shear stress within the cuff, and oscillatory (i.e. bidirectional, with vortices) shear stress downstream from the cuff, confirmed by the Doppler measurements.[223] Furthermore, it was shown that lowered shear stress induced the development of larger lesions with vulnerable plaque phenotype, whereas vortices with oscillatory shear stress induced the growth of stable lesions.[224]

Previously, we have developed the dual-targeted contrast agent for *in vivo* molecular MRI — it not only rapidly binds to vascular endothelium overlying atherosclerotic lesions in the aortic root and aortic arch, but also quantitatively tracks the macrophage burden within atherosclerotic lesions. We further demonstrated the preferential binding of dual-targeted MPIO in atherosclerosis-prone regions - the inner curvature, of the aortic arch - where shear stress is relatively low, compared with the atherosclerosis-resistant greater curvature. This chapter describes the use of *in vivo* molecular MRI to image vulnerable plaque lesions in the carotid arteries of apolipoprotein E–deficient (ApoE-/-) mice. In this experiment, we first utilised the cuff model to induce *in vivo* alterations of shear stress patterns in the common carotid artery in a defined manner in order to develop atherosclerotic lesions of different plaque phenotypes along the artery (i.e. vulnerable plaques in low shear stress region and stable lesions in oscillatory shear stress region) in ApoE-/- mice. Following this, we sought to detect and characterise these cuff-induced plaques using dual-targeted MPIO against VCAM-1 and P-selectin and immunohistochemistry. An important aim was to determine whether we could discriminate between high-risk lesions with a vulnerable plaque phenotype

from the stable ones based on the degree of inflammation using these MRI probes.

## 6.2 MATERIALS AND METHODS

### 6.2.1 The Shear Stress Modifying Cuff

The shear stress modifying cuff in this study was kindly provided by the Cytokine Biology of Atherosclerosis Group at the Kennedy Institute of Rheumatology, Imperial College London. The cuff was initially designed by Cheng *et al*. based on calculated fluid dynamics.[223] The cuff is made of thermoplastic polyetherketone and consists of two longitudinal halves of a cylinder with a conical inner lumen, with the largest inner diameter of 500μm at upstream end and gradually declines to the smallest inner diameter of 250μm at downstream tapered end. (Figure 6.1) This tapering induces a gradual increase in shear stress within the cuff (high shear stress region). Moreover, the constrictive stenosis reduces the blood flow, resulting in a low shear stress region upstream from the cuff. Therefore, the cone shaped inner lumen is imperative for creating defined regions of low (upstream), high (within the cuff) and oscillatory shear stress (downstream) within the common carotid artery.[223] (Figure 6.2) The outer surface of the half shells have a groove running perpendicular to the inner lumen, guiding placement of the suture binding the two half shells together to form a complete functional cuff.[225] (Figure 6.1) The cuff half shells were stored in 70% ethanol before use.

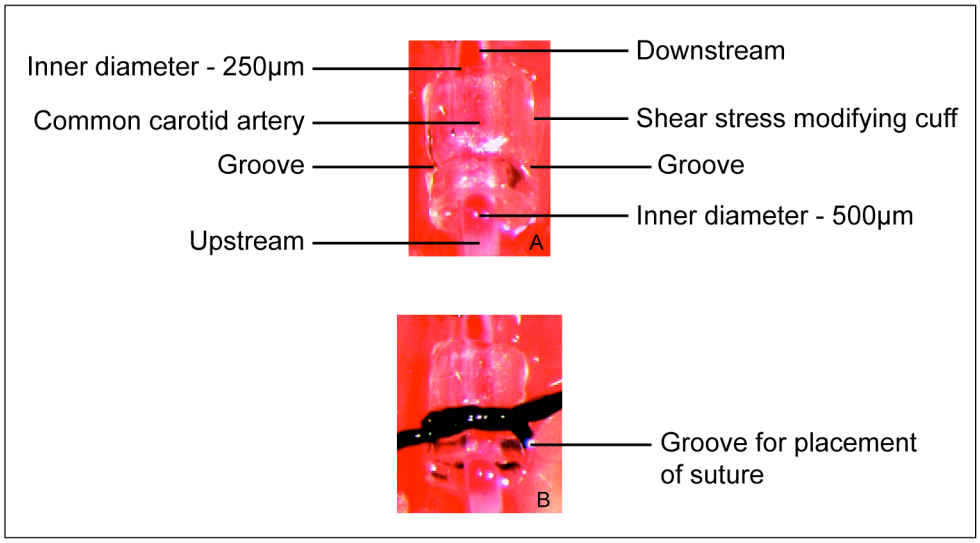



**Fig. 6.1. The shear stress modifying cuff around the common carotid artery.**
A. The shear stress modifying cuff has a conical inner lumen with the largest inner diameter of 500µm at upstream end and the smallest inner diameter of 250µm at downstream tapered end.
B. The outer surface of the cuff has a groove running perpendicular to the inner lumen, guiding placement of the suture binding the two half shells together to form a complete functional cuff.

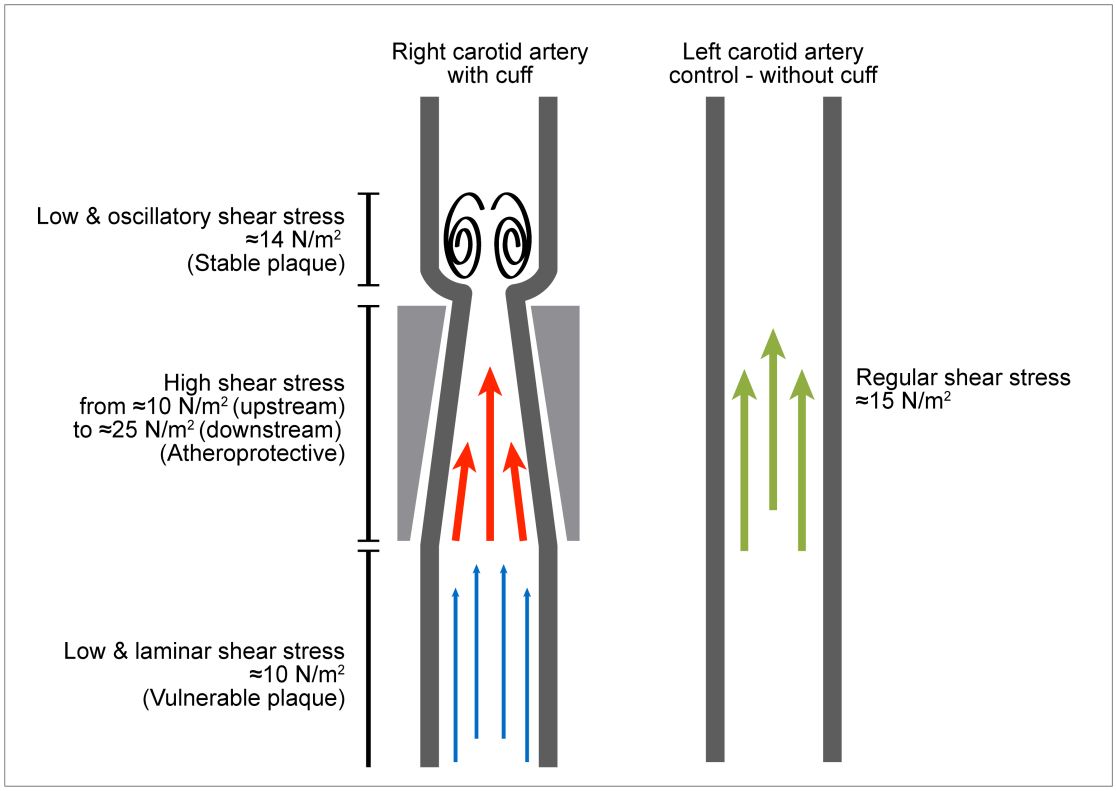



**Fig. 6.2. Regions of different flow dynamics and shear stress.**
Implantation of the cuff with cone shaped inner lumen induces changes in flow dynamics, thereby creating defined regions of low (upstream), high (within the cuff) and oscillatory shear stress (downstream) within the common carotid artery. The local values for shear stress in different regions are based on Doppler measurements.[224] The image was adapted from Kuhlmann MT, Cuhlmann S, Hoppe I, Krams R, Evans PC, Strijkers GJ, Nicolay K, Hermann S, Schäfers M. Implantation of a carotid cuff for triggering shear-stress induced atherosclerosis in mice. J Vis Exp. 2012;(59):e3308.[225]

### 6.2.2 Implantation of Carotid Cuff

Experiments were performed in accordance with UK Scientific Procedures Act (1986) and local ethical approval. The experimental design is illustrated in Figure 6.3. Twelve homozygous ApoE-/- mice were bred and housed under specific pathogen-free conditions with standard 12-hour light/cycles and controlled temperature and humidity. Weaning of mice occurred at 3 weeks of age onto a standard mouse chow diet (Lillico, Surrey, UK). At 18 weeks of age, the mice were put on high fat diet (Lillico, Surrey, UK) 2 weeks prior to cuff implantation until the day of scanning. At week 20, surgical implantation of the shear stress modifying cuff was performed on the right common carotid artery while the left common carotid artery was left untreated as a control. The cuff implantation procedure was previously described[223-225] and illustrated in Figure 6.4. The procedure was performed under a surgical microscope and in sterile conditions, where a surgical gown, mask and cap as well as sterile gloves were worn, and the instruments were sterilised for 30 seconds in a bead instrument steriliser. The mouse was anaesthetised with 3% isoflurane in medical oxygen (1.2 litre/minute) and maintained with 2% isoflurane supplied via a small rodent mask during the surgical procedure. The mouse was assessed to ensure anaesthesia had occurred, indicated by the absence of withdrawal reflex response to paw pinching. The mouse was placed in supine position and the forelimbs and hind limbs were taped down on a heated surgical plate. The hair between mandible and sternum was shaved off. The surgical field was disinfected with Betadine. A 5mm midline incision of skin and underlying neck fascia from manubrium extending in cephalic direction was made using sharp small scissors. The right parotid gland was retracted and a

surgical spreader was inserted to expose surgical field. Blunt dissection was performed to expose the carotid triangle, which was bounded posteriorly by sternocleidomastoid muscle, inferiorly by the superior belly of omohyoid muscle and superiorly by the posterior belly of digastric muscle. The pulsating right common carotid artery was identified within the carotid triangle deep to sternocleidomastoid muscle. Using fine curved forceps, the right common carotid artery was dissected by carefully removing the surrounding carotid sheath. To completely expose the common carotid artery, it was carefully separated from the vagus nerve and the internal jugular vein. Caution was taken not to damage the vagus nerve and the internal jugular vein, both of which are closely running along with the carotid artery within the carotid sheath. In order to isolate the carotid artery, two slings of 6-0 silk sutures were put underneath the artery prior to collar placement. The tip of the forceps was carefully put underneath the carotid artery and the forceps was opened to thread a piece of 6-0 silk suture under the carotid and form a loop. Between the loop and the carotid one cuff half shell was placed beneath the artery. The side with the narrowest lumen of the cuff pointed to downstream direction. The second cuff half shell was placed within the loop on top of the artery. The suture loop was gently tightened to bind the two cuff half shells together to form a complete functional shear stress modifier around the right common carotid artery. In order to induce different types of shear stress in the defined regions of carotid artery, it is essential that the suture is running exactly within the preformed groove on the outer surface of the cuff to ensure its precise fitting around the artery. The right parotid gland was moved back to its original position. The skin was closed using 6-0 prolene suture. A single dose of 5

mg/kg Carprofen was injected subcutaneously to provide prophylactic pain relief. The mouse was subsequently placed in a warming chamber until it recovered from anaesthesia.

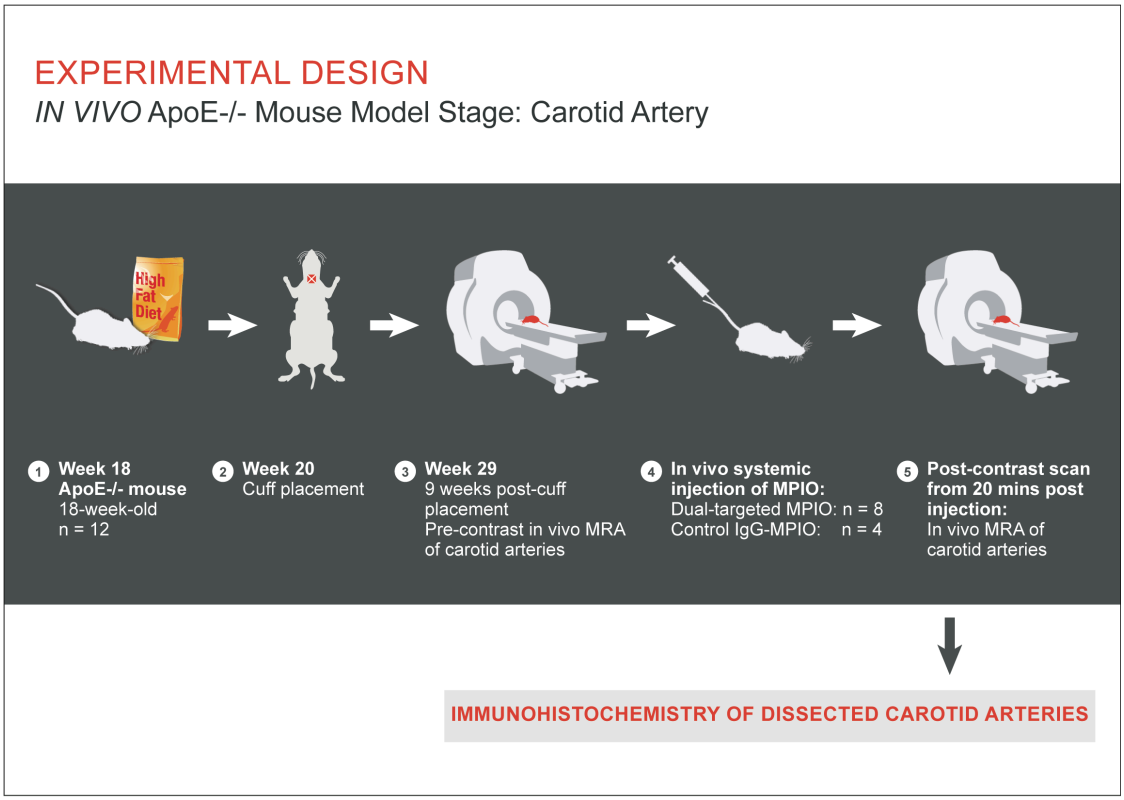



**Fig. 6.3. Experimental design of *in vivo* ApoE-/- mouse model stage.**
At 18 weeks of age, twelve ApoE-/- mice were put on high fat diet. At week 20, surgical implantation of the shear stress modifying cuff was performed on the right common carotid artery while the left common carotid artery was left untreated as a control. At 29 weeks of age, i.e. 9 weeks post-collar placement, the mouse underwent pre-contrast *in vivo* MRI of carotid artery followed by *in vivo* systemic injection of MPIO (dual-targeted MPIO group: n=8; control IgG-MPIO group: n=4). 20 minutes after *in vivo* administration of iron particles, the mouse underwent post-contrast *in vivo* MRI of the carotid artery. At the end of scanning session, the mouse was terminally anesthetised by isofluorane inhalation. The arterial tree was perfusion fixed via the left ventricle with 4% paraformaldehyde. The carotid cuff was explanted from right common carotid artery. Both carotid arteries were subsequently removed for immunohistochemistry.

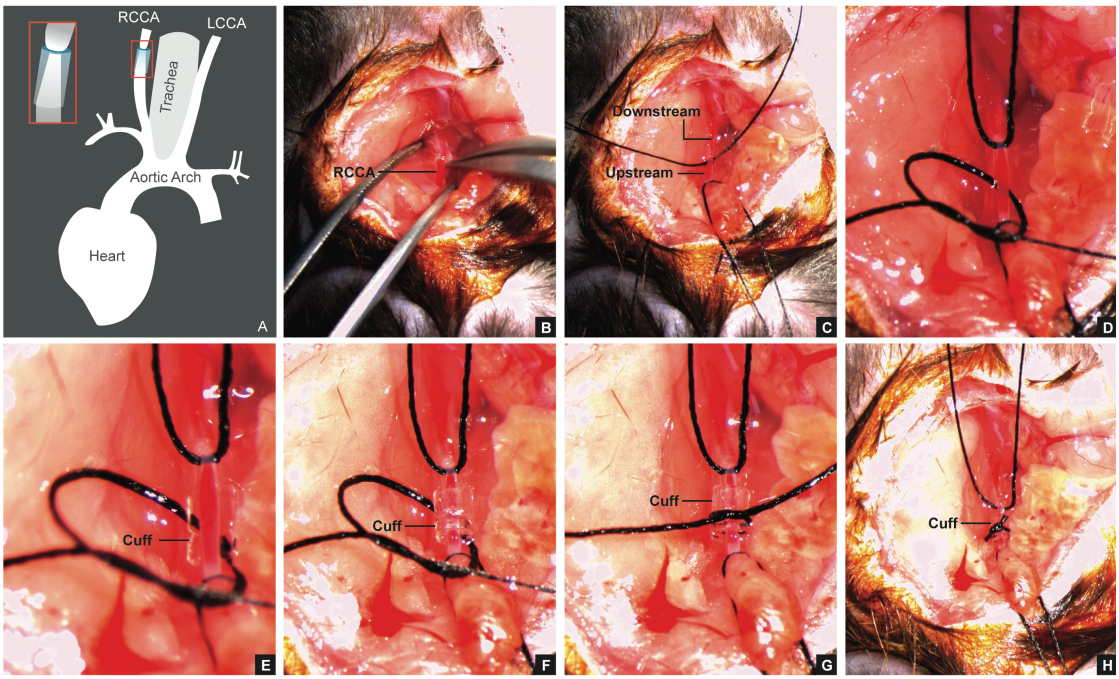



**Figure 6.4. Surgical implantation of shear stress modifier cuff around the right common carotid artery.**

A. Schematic diagram of the implanted cuff. The cuff is placed around the right common carotid artery (RCCA) and the contralateral side [left common carotid artery (LCCA)] serves as a control.
B. The right common carotid artery is identified. Using fine curved forceps, the right common carotid artery is dissected by carefully removing the surrounding connective tissue.
C. In order to isolate the carotid artery, two slings of 6-0 silk sutures are put underneath the artery prior to collar placement.
D. Between the two slings, a loop is formed around the carotid artery prior to collar placement.
E. Between the loop and the carotid, one cuff half shell is placed beneath the artery. The side with the narrowest lumen of the cuff points to downstream direction.
F. The second cuff half shell is placed within the loop on top of the artery.
G. & H. The suture loop is gently tightened to bind the two cuff half shells together to form a complete functional shear stress modifier around the right common carotid artery.

*Figure 6.4A was adapted from Kuhlmann MT et al. Implantation of a carotid cuff for triggering shear-stress induced atherosclerosis in mice. J Vis Exp. 2012;13(59):e3308.* [225]
*Photos courtesy of Mr. Michael Goddard from Cytokine Biology of Atherosclerosis Group at the Kennedy Institute of Rheumatology, Imperial College London.*

### 6.2.3 *In Vivo* MRI

At 29 weeks of age, i.e. 9 weeks post-collar placement, the ApoE-/- mouse underwent *in vivo* MRI of both carotid arteries. The mouse was weighed and subsequently anaesthetised with 3% isofluorane in medical oxygen (1.2 litre/minute) and maintained with 1-2% isoflurane during the MRI experiment. The tail vein was cannulated for systemic injection of MPIO. The mouse was placed in a custom-made cradle. Body temperature was monitored

using a rectal probe and maintained at 37°C by circulating warm air system. Respiratory rate and heart rate were monitored with a balloon sensor and ECG trigger leads respectively throughout. *In vivo* MRI was performed with a 9.4T horizontal-bore scanner (Varian Inc., Palo Alto, CA, USA) running VnmrJ 2.3A software. A baseline pre-contrast *in vivo* imaging of the carotid arteries was performed using a 100 Gauss quadrature radiofrequency coil (internal diameter 33mm, RAPID biomedical GmbH, Germany). MRI acquisition was both cardiac and respiratory gated to eliminate any movement artifacts as a result of heartbeat and respiration. A T2*-weighted 3-dimensional time of flight (TOF) angiography sequence was used with the following parameters: TR: 30.0 ms; TE: 1.20 ms; FOV 18x18x18 mm; acquisition matrix: 256x256x256; average: 2; slab thickness: 18mm; flip angle: 45°. Dual antibody or IgG-1 conjugation to MPIO was previously described in section 4.2.1. The same iron particles used in *ex vivo in situ* and *in vivo* imaging of aortic root described in the last two chapters were also used in this study. Dual antibody-conjugated MPIO (n=8 mice) or control IgG-1-MPIO (n=4 mice) (5mg iron per kg body weight in 150µl PBS) was injected *in vivo* via tail vein. Post-contrast *in vivo* MRI using the same parameters was performed from 20 minutes up to 2 hours after MPIO injection to visualise atherosclerosis of the carotid arteries.

### 6.2.4 Explantation of Carotid Cuff and Carotid Arteries

ApoE-/- mouse was terminally anesthetised by isofluorane inhalation at the end of the scanning session. The chest cavity was exposed and while the heart was beating, the arterial tree was perfusion fixed via the left ventricle with 4% paraformaldehyde (PFA) as previously described in section 4.2.3. The right

common carotid artery was exposed, the connecting suture was cut and the two cuff half shells of the cuff were removed. The whole length of both common carotid arteries were dissected out carefully. The orientation of both carotid arteries was marked. They were formalin fixed and embedded in paraffin blocks as described in section 3.2.5.1.

### 6.2.5 Histological Staining of Carotid Arteries

Serial 4-μm-thick sections were cut from the paraffin-embedded blocks, beginning at the proximal end of carotid arteries in a cephalic direction. The sections were collected at the three defined regions of low (upstream), high (within the cuff) and oscillatory shear stress (downstream) within the common carotid artery. The orientation and sequence of sections were recorded. To determine the distribution and localisation of MPIO, serial histology sections of carotid artery underwent staining for iron (Perls') and collagen (Picrosirius Red), and immunostaining for endothelial cells (CD31), macrophages (Mac-3), and smooth muscle cells [α smooth muscle actin (αSMA)], with one antibody per section. Perls' staining was used as a surrogate marker to confirm the presence of MPIO binding to the atherosclerotic plaques in the carotid artery and was previously described in section 3.2.5.3. Immunostaining for endothelial cells (CD31), macrophages (Mac-3), and smooth muscle cells (αSMA) were previously described in section 5.2.3.1, section 5.2.3.3 and section 5.2.3.4. Microscopy was performed with a Zeiss Axiovert 200 inverted microscope.

#### 6.2.5.1 Picrosirius Red

Sections were de-paraffinised and rehydrated in descending series of ethanols followed by distilled water as described in section 3.2.5.2. Sections were counterstained with Harris Haematoxylin for 2 minutes. Sections were rinsed in running tape water then distilled water for 5 minutes each. Picrosirius red stain kit (Polysciences inc., Germany, product number 24901) was used to stain collagen according to the manufacturer's instructions. Sections were placed in Solution A (0.2% phosphomolybdic acid hydrate) for 2 minutes then rinsed in water for 3 minutes. Sections were placed in Solution B (1.3% 2,4,6-Trinitrophenol and 0.4% direct red 80) for 110 minutes, Solution C (0.4% hydrogen chloride) for 2 minutes and then in 70% ethanol for 45 seconds. Sections were then dehydrated in an ascending series of ethanols (90-95-100%), cleared in three changes of xylene and mounted with coverslips.

# 6.3 RESULTS

## 6.3.1 *In Vivo* Detection of Vulnerable Plaque Lesions in Mouse Carotid Arteries using Dual-Targeted MPIO

To determine whether dual-targeted MPIO can detect vulnerable plaque lesions, serial *in vivo* MRA of carotid arteries was performed from 20 minutes post-injection of MPIO up to 2 hours. Representative MR images of carotid arteries pre- and post-injection of either dual-targeted MPIO or negative control IgG-MPIO were shown in Figure 6.5 and Figure 6.6 respectively. In the dual-targeted MPIO group, no discrete dark signal was seen on the luminal side in all regions of both right and left common carotid arteries in the pre-contrast images of all three planes, i.e. sagittal, coronal and axial. (Figure 6.5 A, C, E, G) Following administration of dual-targeted MPIO, new areas of discrete hypointensity signal were detected on the luminal side in the low shear stress region (upstream or proximal to the cuff) of the right common carotid artery in the post-contrast images of all three planes (Figure 6.5 B, F, H). The hypointensity signal was due to the presence of MPIO-labelled cells, which was confirmed by Perls' stain for iron predominantly binding on the surface of the vulnerable plaque lesions in the low and laminar shear stress region of the right common carotid artery in the matching histological sections (Figure 6.7 B). By contrast, no discrete dark signal was seen on the luminal side in the 1) high shear stress region (within the cuff) or 2) oscillatory shear stress region (downstream or distal to the cuff) of the right common carotid artery, and 3) throughout the left common carotid artery in the post-contrast images of all

three planes (Figure 6.5 D, F, H). The absence of dark signal in oscillatory shear stress region of the right common carotid artery was confirmed by the absence of Perls' stain for iron in the lesions of relatively stable phenotype in the region (Figure 6.7 N). No hypointensity signal was observed in 1) high shear stress region in the right common carotid artery or 2) throughout the left common carotid artery, which was supported by the absence of Perls' stain for iron in these atherosclerosis-spared regions in the matching histological sections (Figure 6.7 H, T).

In the control IgG-1-MPIO group, no discrete dark signal was observed on the luminal side in all regions, i.e. the low and laminar shear stress region, high shear stress region and oscillatory shear stress region, of both right and left common carotid arteries in both pre-contrast (Figure 6.6 A, C, E, G) and post-contrast (Figure 6.6 B, D, F, H) images of all three planes, i.e. sagittal, coronal and axial. The absence of dark signal in the post-contrast images of both carotid arteries was confirmed by the absence of Perls' stain for non-specific IgG-MPIO binding in these regions in the matching histological sections (Figure 6.8 B, H, N, T). Consistent with the *in vivo* findings of aortic root imaging in section 5.3.1.1, *in vivo* MRI detected contrast effect in the carotid arteries of dual-targeted MPIO group from 30 to 45 minutes post-contrast injection, and persisted for the entire 2-hour imaging period. No ill effect or symptom was observed following cuff placement and administration of iron particles until terminal anaesthesia at the end of the scanning session.

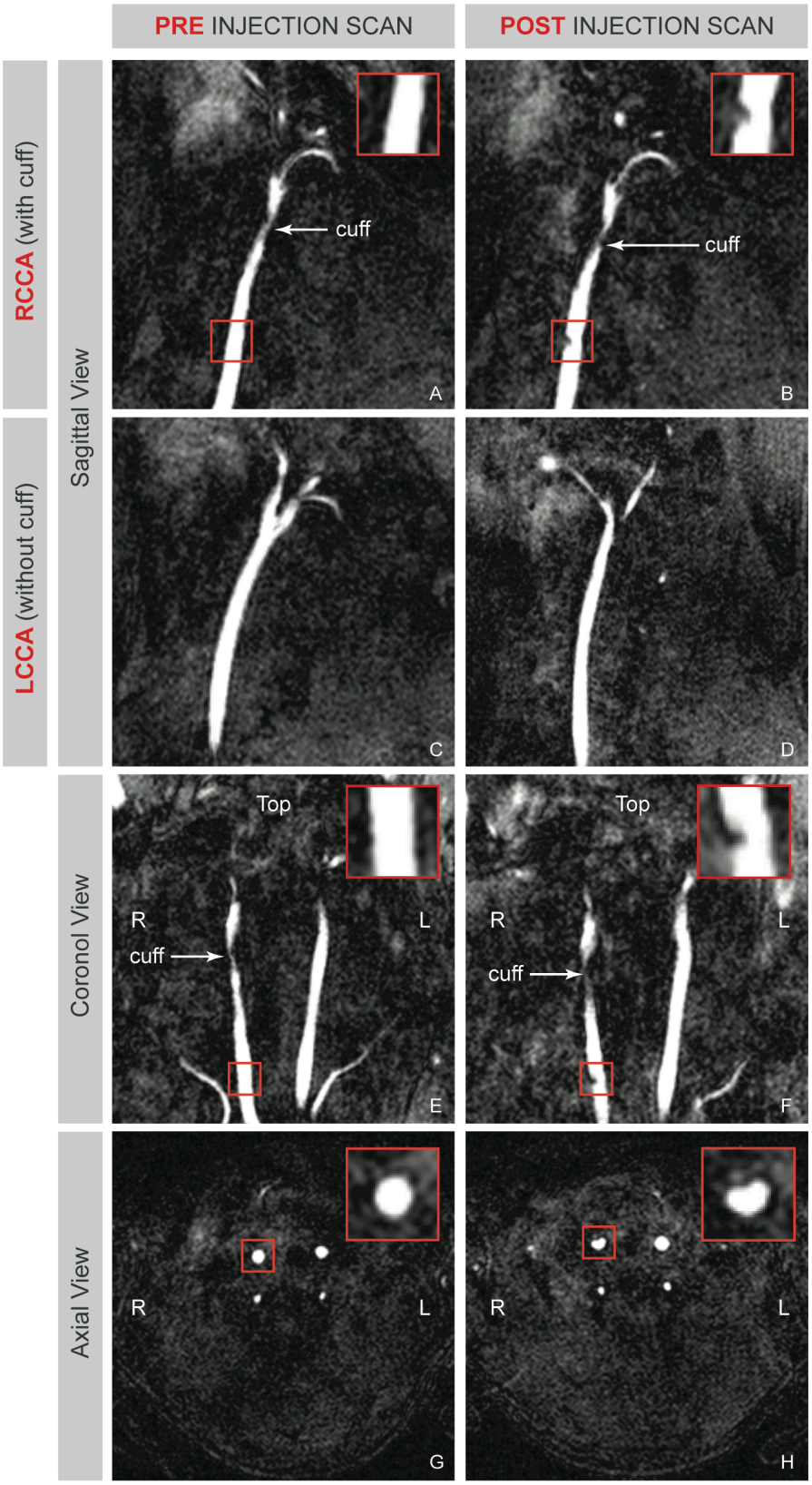



**Fig. 6.5 Representative images of *in vivo* MRA of carotid arteries in dual-targeted MPIO group.** No discrete dark signal was observed on the luminal side in all regions of both right and left common carotid arteries in the pre-contrast images of all three planes, i.e. sagittal (Panel A and C), coronal (Panel E) and axial (Panel G). Panel B, D, F and H showed the MRA images of carotid arteries at 30 minutes after administration of dual-targeted MPIO. New areas of discrete hypointensity signal were detected on

the luminal side in the low and laminar shear stress region (upstream or proximal to the cuff highlighted in red box) of the right common carotid artery in the post-contrast images of all three planes, i.e. sagittal (Panel B), coronal (Panel F) and axial (Panel H). By contrast, no discrete dark signal was seen on the luminal side in the 1) high shear stress region (within the cuff) or 2) oscillatory shear stress region (downstream or distal to the cuff) of the right common carotid artery, and 3) throughout the left common carotid artery in the post-contrast images of all three planes (Panel B, D, F and H).

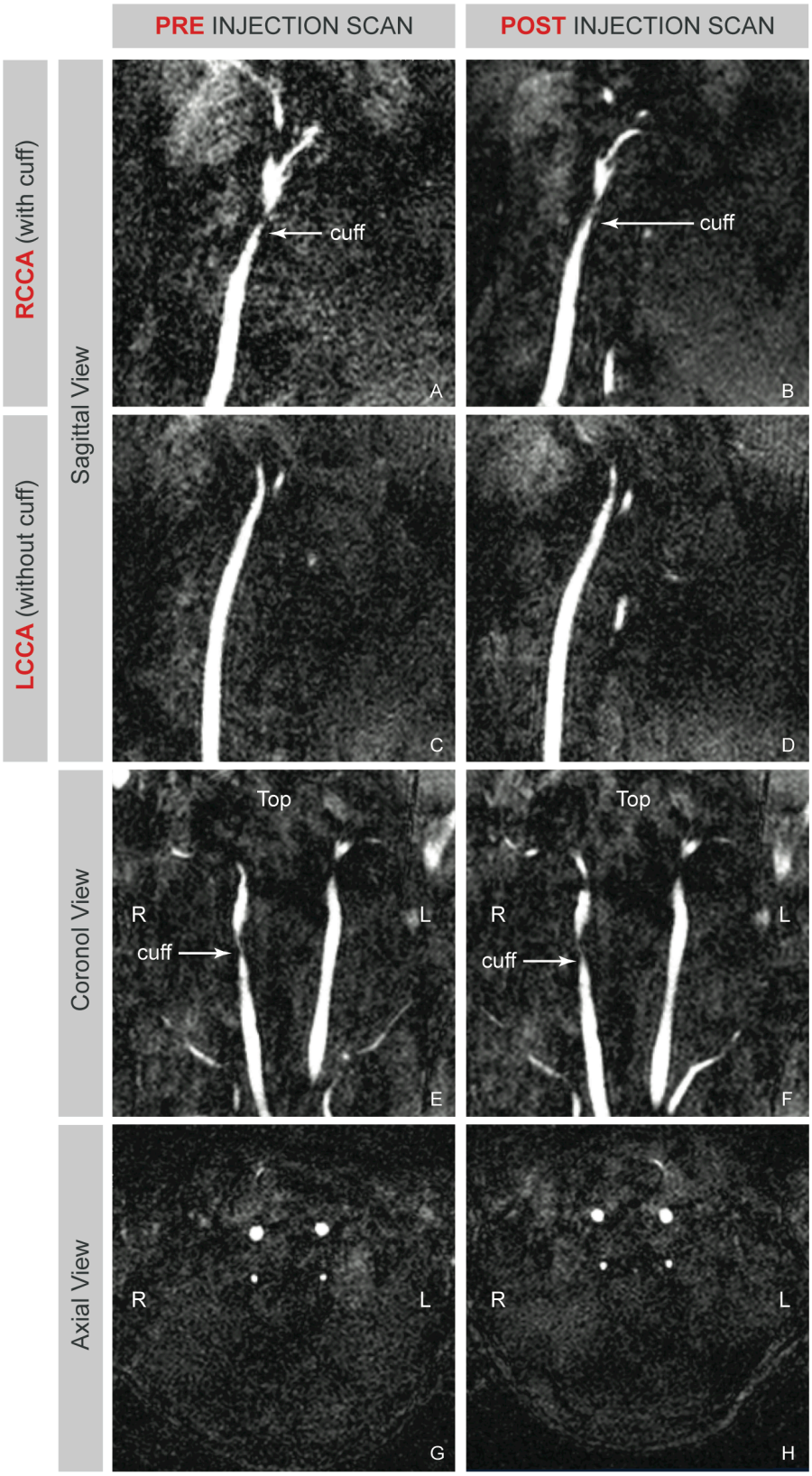



**Fig. 6.6 Representative images of *in vivo* MRA of carotid arteries in control IgG-MPIO group.** No discrete dark signal was observed on the luminal side in all regions of both right and left common carotid arteries in the pre-contrast images of all three planes, i.e. sagittal (Panel A and C), coronal (Panel E) and axial (Panel G). Panel B, D, F and H showed the MRA images of carotid arteries at 30 minutes after administration of control IgG-MPIO. No new area of discrete hypointensity signal was detected on

the luminal side in the low and laminar shear stress region (upstream or proximal to the cuff) of the right common carotid artery in the post-contrast images of all three planes, i.e. sagittal (Panel B), coronal (Panel F) and axial (Panel H). Moreover, no discrete dark signal was detected on the luminal side in the 1) high shear stress region (within the cuff) or 2) oscillatory shear stress region (downstream or distal to the cuff) of the right common carotid artery, and 3) throughout the left common carotid artery in the post-contrast images of all three planes (Panel B, D, F and H).

## 6.3.2 Histological Analysis

### 6.3.2.1 Low Shear Stress and Oscillatory Shear Stress Both Induce Atherosclerotic Plaque Formation, Whereas High Shear Stress Protects Against Atherosclerosis

To determine whether different lesion phenotypes could be discriminated using dual-targeted MPIO, ApoE**-/-** mice were fed a high fat diet and underwent surgical implantation of cuff around the right common carotid artery 9 weeks prior to MR scanning and humanely killed for histological analysis. Representative histological images displaying carotid artery morphology after 9 weeks of cuff placement in the low, high and oscillatory shear stress regions, as well as in the contralateral non-treated carotid artery (undisturbed shear stress) of either dual-targeted MPIO or negative control IgG-MPIO group were shown in Figure 6.7 and Figure 6.8 respectively. Histological analysis confirmed that all animals developed lesions in the right common carotid arteries under low and oscillatory shear stress at 9 weeks post-cuff placement (Figure 6.7 and 6.8). However, the lesions have a strikingly different morphology. In the low shear stress regions, the lesions were observed to be considerably more extensive than those in the oscillatory shear stress regions. Moreover, outward vascular remodeling was present in the low shear stress

region, whereas no significant remodeling was observed in the oscillatory shear stress region. By contrast, no atherosclerotic lesion was present in the high shear stress region of right common carotid artery and under undisturbed shear stress in the non-treated left common carotid artery. The appearance of the vessel wall in the high shear stress region is very similar to that of the undisturbed, control region.

#### 6.3.2.2 Low Shear Stress Induces Formation of Lesions With Vulnerable Plaque Phenotype, Whereas Oscillatory Shear Stress Induces Development of Stable Lesions

We further examined the effect of low shear stress and oscillatory shear stress on carotid plaque composition. CD31 staining confirmed the presence of endothelium in all regions, i.e. low, high, oscillatory and undisturbed shear stress regions (Panel C, I, O, and U in Figure 6.7 and 6.8). The macrophage content was observed to be significantly higher in the lesions located in the low shear stress regions than in those in the oscillatory shear stress regions (Panel D and P in Figure 6.7 and 6.8). Further analysis of lesion components revealed that low shear stress lesions contained only thin layers of smooth muscle cells and collagen in the cap of the lesion (Panel E and F in Figure 6.7 and 6.8), whereas in the oscillatory shear stress lesions, smooth muscle cells and collagen were observed to be uniformly distributed in the intima (Panel Q and R in Figure 6.7 and 6.8). The results suggested that low shear stress induced formation of lesions with vulnerable plaque phenotype, whereas oscillatory shear stress induced development of lesions with a relatively stable phenotype.

#### 6.3.2.3 Dual-targeted MPIO Selectively Bind to Lesions With Vulnerable Plaque Phenotype but Not to Stable Lesions

In the dual-targeted MPIO group, Perls' stain for iron was present predominantly on the surface of the lesions with a vulnerable phenotype in the low shear stress region of the right common carotid artery (Panel B in Figure 6.7). No Perls' stain was observed in the lesions of relatively stable phenotype in the oscillatory shear stress region (Panel N in Figure 6.7). Absence of Perls' stain was confirmed in the atherosclerosis-spared areas in the high shear stress region in the right common carotid artery and undisturbed shear stress region in the control left common carotid artery (Panel H and T in Figure 6.7). The results suggested that dual-targeted MPIO selectively bound not only to lesions, but also specifically bound to lesions with vulnerable plaque phenotype, and not to lesions with relatively stable phenotype. Moreover, the results confirmed that the discrete dark signal detected on the post-contrast MRA in the low shear stress region (proximal to cuff placement) on the right common carotid artery (Figure 6.5) was attributable to the dual-conjugated MPIO targeting at the vulnerable plaque lesions in that region. Furthermore, the absence of Perls' stain for iron in the histological sections concurred with the absence of discrete dark signal in the matching post-contrast MRA in the following regions: 1) the lesions of relatively stable phenotype in the oscillatory shear stress region (Panel M to R in Figure 6.7), 2) the atherosclerosis-spared areas in the high shear stress region in the right common carotid artery (Panel G to L in Figure 6.7), and 3) atherosclerosis-spared areas in the undisturbed shear stress region in the control left common carotid artery (Panel S to X in

Figure 6.7).

In the control IgG-MPIO group, no Perls' stain was observed in all regions: 1) the lesions with vulnerable plaque phenotype in the low shear stress region (Panel A to F in Figure 6.8), 2) the lesions of relatively stable phenotype in the oscillatory shear stress region (Panel M to R in Figure 6.8), 3) the atherosclerosis-spared areas in the high shear stress region in the right common carotid artery (Panel G to L in Figure 6.8), and 4) the atherosclerosis-spared areas in the undisturbed shear stress region in the control left common carotid artery (Panel S to X in Figure 6.8). The results confirmed that there were no non-specific IgG-MPIO binding in all regions, which was consistent with the absence of discrete dark signal throughout right and left common carotid arteries in the matching post-contrast MRA (Figure 6.6).




**Fig. 6.7 Representative histological images of carotid arteries of ApoE double knockout mouse in dual-targeted group under high fat diet 9 weeks after implantation of cuff.**

Panel A-F: The low shear stress (upstream of the cuff) induced development of lesion with vulnerable plaque phenotype characterised by: 1) outward vascular remodeling as shown by H&E stained cross-section in Panel A; 2) high macrophage content (Panel D) surrounded by 3) thin layers of smooth muscle cells (Panel E) and collagen (Panel F) in the cap of the lesion. Perls' stain was present predominantly on the surface of the vulnerable plaque lesions. However, small amount of Perls' stain was also observed to

sporadically distribute within the intima close to the necrotic lipid core of the plaques. (Panel B)

Panel M-R: The oscillatory shear stress (downstream of the cuff) induced development of lesion with relatively stable phenotype characterised by: 1) a thick, fibrous cap (Panel R) heavily infiltrated with vascular smooth muscle cells (Panel Q) covering the lesion with relatively smaller amount of macrophages (Panel P) and lipids than the vulnerable plaque lesions in the low shear stress region. Negligible amount of Perls' stain was present within the intima of the stable lesion (Panel N). No Perls' stain was observed to be present on the surface of the stable lesion.

Panel G-L: The high shear stress (within the cuff) protected the carotid artery against atherosclerosis. No atherosclerotic lesion or macrophages was present in the vessel wall as shown in Panel G and J respectively. Normal lining of endothelial cells, smooth muscle cells and collagen in the vessel wall were shown in Panel I, K and L. No Perls' stain was present within the vessel wall (Panel H).

Panel S-X: No atherosclerotic lesion was present in the undisturbed shear stress region of the non-treated control left common carotid artery. No macrophages was present in the vessel wall as shown in Panel V. Normal lining of endothelial cells, smooth muscle cells and collagen in the vessel wall were shown in Panel U, W and X. No Perls' stain was present within the vessel wall (Panel T). The vessel wall under undisturbed shear stress conditions shared similar appearance to that under high shear stress.

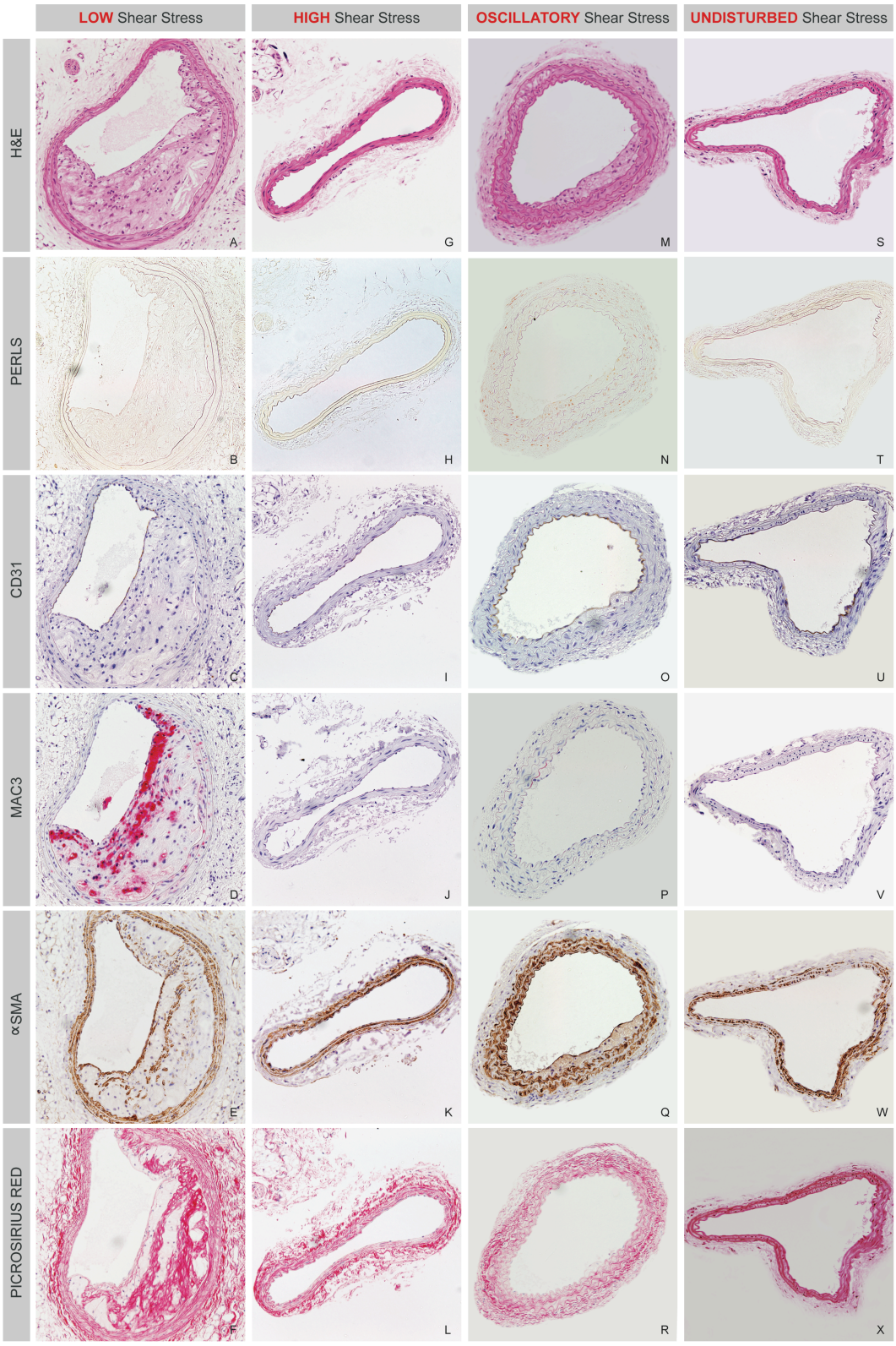



**Fig. 6.8 Representative histological images of carotid arteries of ApoE double knockout mouse in control IgG-MPIO group under high fat diet 9 weeks after implantation of cuff.**

Panel A-F: The low shear stress (upstream of the cuff) induced development of lesion with vulnerable plaque phenotype characterised by: 1) significant outward vascular remodeling as shown by H&E stained cross-section in Panel A; 2) high macrophage content (Panel D) surrounded by 3) thin layers of smooth muscle cells (Panel E) and collagen (Panel F) in the cap of the lesion. No Perls' stain was present on the surface or within the intima of the vulnerable plaque lesion (Panel B).

Panel M-R: The oscillatory shear stress (downstream of the cuff) induced development of lesion with relatively stable phenotype characterised by: 1) a thick, fibrous cap (Panel R) infiltrated with vascular smooth muscle cells (Panel Q) covering the lesion with little macrophages (Panel P) and lipids. No Perls' stain was present on the surface or within the intima of the stable lesion (Panel N).

Panel G-L: The high shear stress (within the cuff) protected the carotid artery against atherosclerosis. No atherosclerotic lesion or macrophages was present in the vessel wall as shown in Panel G and J respectively. Normal lining of endothelial cells, smooth muscle cells and collagen in the vessel wall were shown in Panel I, K and L. No Perls' stain was present within the vessel wall (Panel H).

Panel S-X: No atherosclerotic lesion was present in the undisturbed shear stress region of the non-treated control left common carotid artery. No macrophages was present in the vessel wall as shown in Panel V. Normal lining of endothelial cells, smooth muscle cells and collagen in the vessel wall were shown in Panel U, W and X. No Perls' stain was present within the vessel wall (Panel T). The vessel wall under undisturbed shear stress conditions shared a similar appearance to that under high shear stress.

#### 6.3.2.4 Dual-targeted MPIO Selectively Bind to Endothelium Overlying Lesions With Vulnerable Plaque Phenotype

Representative histological images displaying carotid artery morphology after 9 weeks of cuff placement in the low shear stress region in the dual-targeted MPIO group were shown in Figure 6.9. The lesions induced by low shear stress demonstrated a vulnerable plaque phenotype, which was characterised by 1) high macrophage content (Panel D in Figure 6.9), 2) large lipid core surrounded by 3) thin layers of smooth muscle cells (Panel E in Figure 6.9) and 4) collagen in the cap of the lesion (Panel F in Figure 6.9). At higher magnification, Perls' stain was observed to be present predominantly on the surface of the lesions with vulnerable plaque phenotype (Panel B in Figure 6.9). However, small amount of Perls' stain was also observed to sporadically distribute within the intima close to the necrotic lipid core of the plaques. Consistent with the presence of Perls' stain on the lesion surface, dual-

targeted MPIO was observed to colocalise along the endothelium overlying the vulnerable plaque lesions (Panel C and C1 to C6 in Figure 6.9). No iron particles were seen to colocalise with macrophages, smooth muscle cells or collagen in the lesion (Panel D, E and F in Figure 6.9).

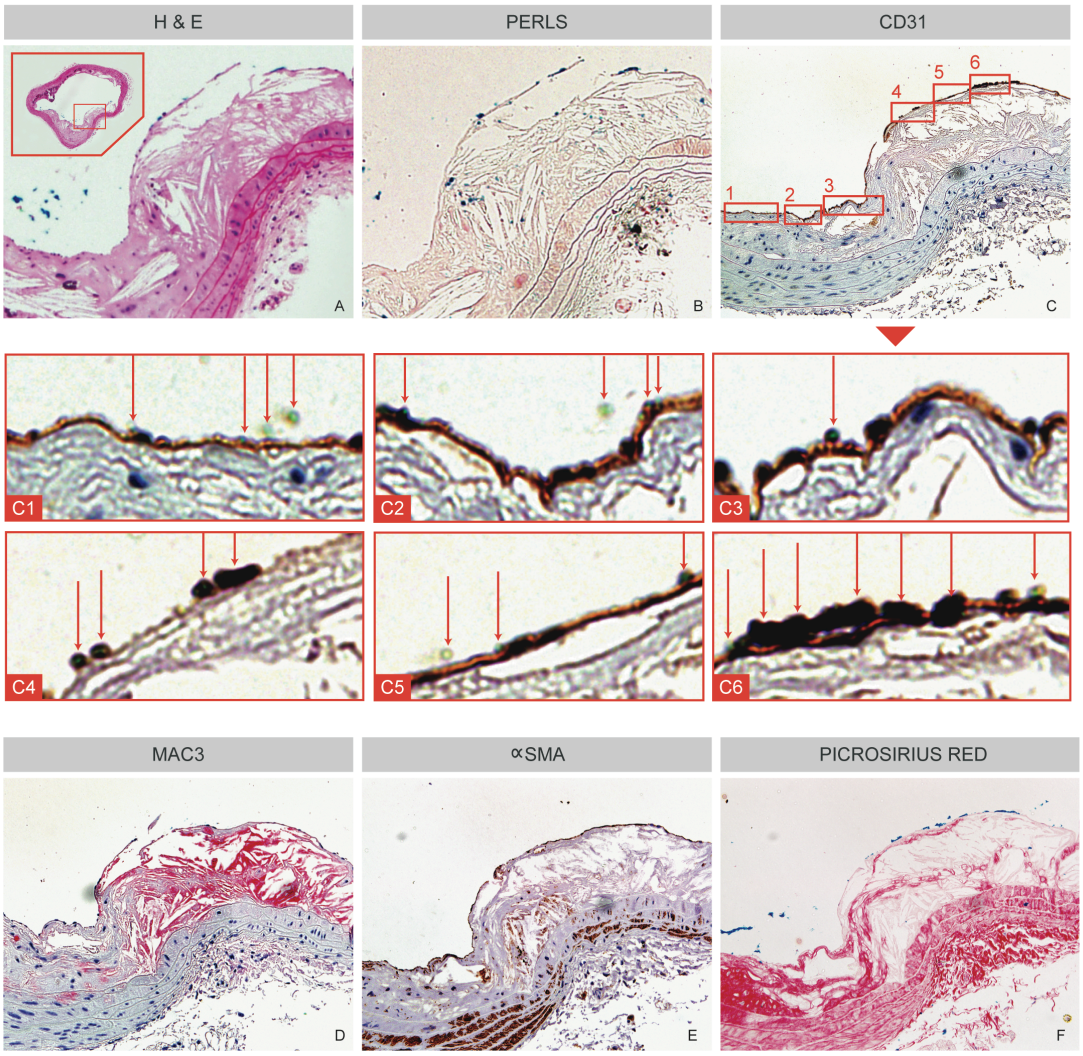



**Fig. 6.9 Representative histological images at higher magnification of carotid arteries of ApoE double knockout mouse in dual-targeted group 9 weeks after implantation of cuff.**

The low shear stress (upstream of the cuff) induced development of lesion with vulnerable plaque phenotype characterised by: 1) outward vascular remodeling as shown by H&E stained cross-section in Panel A; 2) high macrophage content (Panel D) surrounded by 3) thin layers of smooth muscle cells (Panel E) and collagen (Panel F) in the cap of the lesion. Perls' stain was present predominantly on the surface of the vulnerable plaque lesions. However, small amount of Perls' stain was also observed to sporadically distribute within the intima close to the necrotic lipid core of the plaques. (Panel B) Red arrows in Panel C and C1 to C6 indicated the dual-targeted MPIO appearing as green or brown spheres colocalising along the endothelium overlying the vulnerable plaque lesions. No iron particles were seen

to colocalise with macrophages, smooth muscle cells or collagen in the lesion (Panel D, E and F).

Representative histological images displaying carotid artery morphology after 9 weeks of cuff placement in the oscillatory shear stress region in the dual-targeted MPIO group were shown in Figure 6.10. The lesions induced by oscillatory shear stress demonstrated a stable plaque phenotype, which was characterised by a thick, fibrous cap (Panel F in Figure 6.10) heavily infiltrated with vascular smooth muscle cells (Panel E in Figure 6.10) covering the lesion with relatively fewer macrophages (Panel D in Figure 6.10) and less lipids than the lesions in the low shear stress region. At higher magnification, only negligible amount of Perls' stain was present within the intima of the stable lesion (Panel B in Figure 6.10). No Perls' stain was observed to be present on the surface of the stable lesion. Consistent with this, no dual-targeted MPIO was observed to colocalise along the endothelium overlying the stable plaque lesion (Panel C in Figure 6.10). No iron particles were seen to colocalise with macrophages, smooth muscle cells or collagen in the plaque lesion (Panel D, E and F in Figure 6.10).

Representative histological images displaying carotid artery morphology after 9 weeks of cuff placement in the high shear stress region of the right common carotid artery and the undisturbed shear stress region of the non-treated left common carotid artery in the dual-targeted MPIO group were shown in Panel G to L in Figure 6.10 and Panel M to R in Figure 6.10 respectively. The appearance of the vessel wall in the high shear stress region was very similar to that of the undisturbed, control region; both were spared of atherosclerotic lesion development and infiltration of macrophages. At higher magnification,

no Perls' stain was observed to be present in the vessel wall in both regions (Panel H and N in Figure 6.10). Consistent with this, no dual-targeted MPIO was observed to colocalise along the endothelium of the vessel wall (Panel I and O in Figure 6.10). No iron particles were seen to colocalise with smooth muscle cells or collagen in the vessel wall (Panel K and L in Figure 6.10).

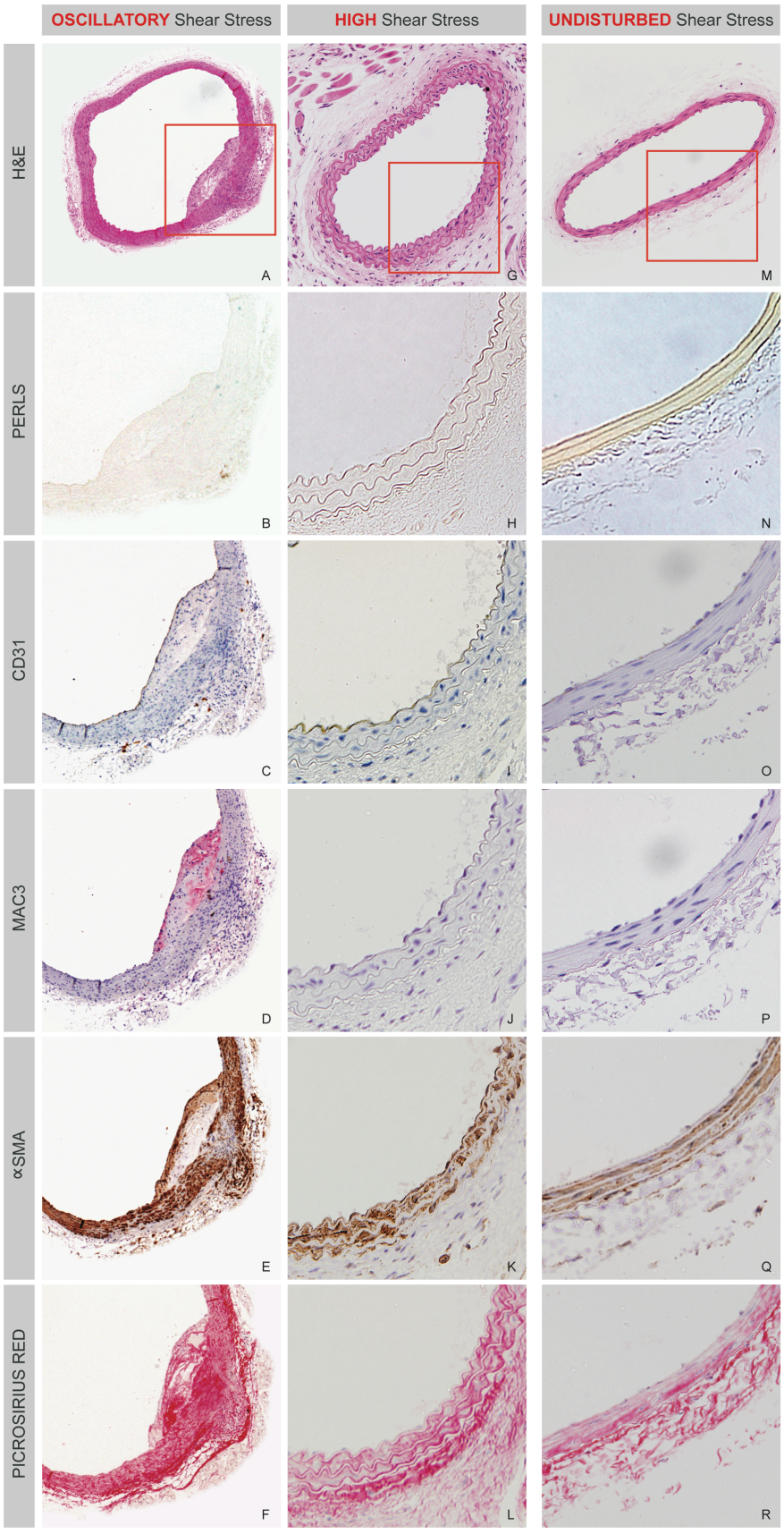



**Fig. 6.10 Representative histological images at higher magnification of carotid arteries of ApoE double knockout mouse in dual-targeted group 9 weeks after implantation of cuff.**

Panel A-F: The oscillatory shear stress (downstream of the cuff) induced development of lesion with relatively stable phenotype characterised by: 1) a thick, fibrous cap (Panel F) heavily infiltrated with vascular smooth muscle cells (Panel E) covering the lesion with relatively smaller amount of macrophages (Panel D) and lipids than the vulnerable plaque lesions in the low shear stress region. Negligible amount of Perls' stain was present within the intima of the stable lesion (Panel B). No Perls' stain was observed to be present on the surface of the stable lesion. No dual-targeted MPIO was observed to colocalise along the endothelium overlying the stable plaque lesion (Panel C) or with macrophages, smooth muscle cells or collagen in the plaque lesion (Panel D, E and F).

Panel G-L: The high shear stress (within the cuff) protected the carotid artery against atherosclerosis. No atherosclerotic lesion or macrophages was present in the vessel wall as shown in Panel G and J respectively. Normal lining of endothelial cells, smooth muscle cells and collagen in the vessel wall were shown in Panel I, K and L. No Perls' stain was present within the vessel wall (Panel H). No dual-targeted MPIO was observed to colocalise along the endothelium (Panel I) or with macrophages, smooth muscle cells or collagen in the vessel wall (Panel J, K and L).

Panel M-R: No atherosclerotic lesion was present in the undisturbed shear stress region of the non-treated control left common carotid artery. No macrophages was present in the vessel wall as shown in Panel P. Normal lining of endothelial cells, smooth muscle cells and collagen in the vessel wall were shown in Panel O, Q and R. No Perls' stain was present within the vessel wall (Panel N). The vessel wall under undisturbed shear stress conditions shared similar appearance to that under high shear stress. No dual-targeted MPIO was observed to colocalise along the endothelium (Panel O) or with macrophages, smooth muscle cells or collagen in the vessel wall (Panel P, Q and R).

Representative histological images displaying carotid artery morphology after 9 weeks of cuff placement in the low shear stress region in the control IgG-MPIO group were shown in Panel A to F in Figure 6.11. Similar to the lesions in the dual-targeted MPIO group, the plaques induced by low shear stress also demonstrated a vulnerable plaque phenotype with significant outward vascular remodeling, high macrophage content and large lipid core surrounded by thin layers of smooth muscle cells and collagen in the cap of the lesion. At higher magnification, however, no Perls' stain was observed to be present in the vulnerable plaque lesion (Panel B in Figure 6.11). Consistent with this, no non-specific IgG-MPIO binding was observed on endothelial cells, macrophages, smooth muscle cells or collagen in the plaque lesion (Panel C, D, E and F in Figure 6.11).

Representative histological images displaying carotid artery morphology after 9 weeks of cuff placement in the oscillatory and high shear stress region of the

right common carotid artery as well as the undisturbed shear stress region of the non-treated left common carotid artery in the control IgG-MPIO group were shown in Figure 6.11. Similar to the results in dual-targeted MPIO group, no Perls' stain was observed to be present in the stable lesions in oscillatory shear stress region or in atherosclerosis-spared areas in the high shear stress region and undisturbed shear stress region. Consistent with this, no non-specific IgG-MPIO binding was observed on endothelial cells, macrophages, smooth muscle cells or collagen in the vessel wall in all these regions (Figure 6.11).

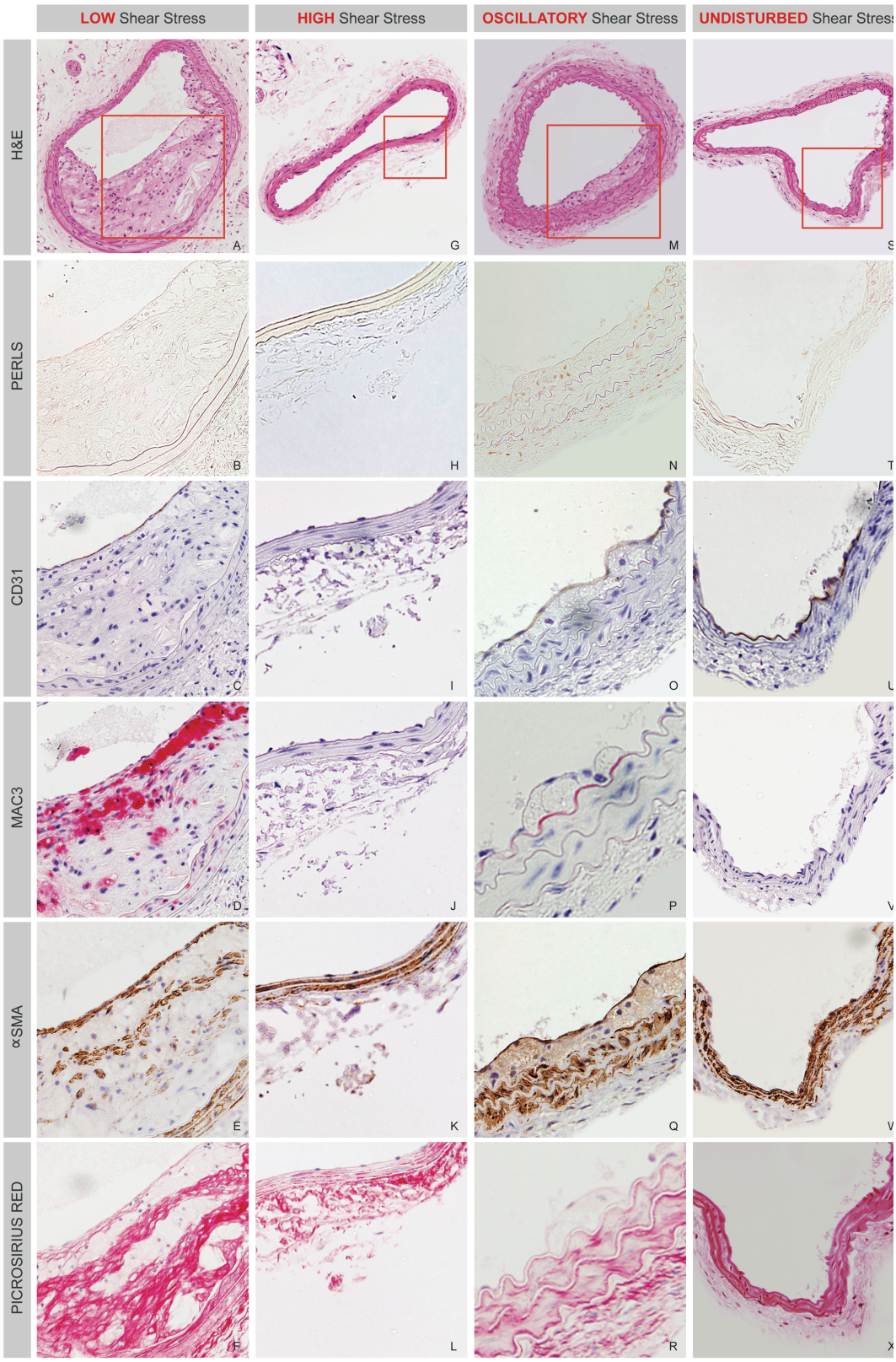



**Fig. 6.11 Representative histological images at higher magnification of carotid arteries of ApoE double knockout mouse in control IgG-MPIO group 9 weeks after implantation of cuff.**
Panel A-F: The low shear stress (upstream of the cuff) induced development of lesion with vulnerable plaque phenotype characterised by: 1) significant outward vascular remodeling as shown by H&E stained cross-section in Panel A; 2) high macrophage content (Panel D) surrounded by 3) thin layers of smooth muscle cells (Panel E) and collagen (Panel F) in the cap of the lesion. No Perls' stain was

present on the surface or within the intima of the vulnerable plaque lesion (Panel B). No control IgG-MPIO was observed to colocalise along the endothelium overlying the vulnerable plaque lesion (Panel C) or with macrophages, smooth muscle cells or collagen in the plaque lesion (Panel D, E and F).

Panel M-R: The oscillatory shear stress (downstream of the cuff) induced development of lesion with relatively stable phenotype characterised by: 1) a fibrous cap (Panel R) infiltrated with vascular smooth muscle cells (Panel Q) covering the lesion with little macrophages (Panel P) and lipids. No Perls' stain was present on the surface or within the intima of the stable lesion (Panel N). No control IgG-MPIO was observed to colocalise along the endothelium overlying the stable lesion (Panel O) or with macrophages, smooth muscle cells or collagen in the plaque lesion (Panel P, Q and R).

Panel G-L: The high shear stress (within the cuff) protected the carotid artery against atherosclerosis. No atherosclerotic lesion or macrophages was present in the vessel wall as shown in Panel G and J respectively. Normal lining of endothelial cells, smooth muscle cells and collagen in the vessel wall were shown in Panel I, K and L. No Perls' stain was present within the vessel wall (Panel H). No control IgG-MPIO was observed to colocalise along the endothelium (Panel I) or with macrophages, smooth muscle cells or collagen in the vessel wall (Panel J, K and L).

Panel S-X: No atherosclerotic lesion was present in the undisturbed shear stress region of the non-treated control left common carotid artery. No macrophages was present in the vessel wall as shown in Panel V. Normal lining of endothelial cells, smooth muscle cells and collagen in the vessel wall were shown in Panel U, W and X. No Perls' stain was present within the vessel wall (Panel T). The vessel wall under undisturbed shear stress shared similar appearance to that under high shear stress. Similarly, no control IgG-MPIO was observed to colocalise along the endothelium (Panel U) or with macrophages, smooth muscle cells or collagen in the vessel wall (Panel V, W and X).

## 6.4 DISCUSSION

While there is a worldwide consensus in the treatment of recently symptomatic patients with carotid atherosclerotic disease,[24,25] there is a lack of concordance regarding the optimal way of treating asymptomatic patients. It is largely accepted that the 'one size fits all' strategy of mass intervention in asymptomatic patients is both ineffective and unsustainable.[37,38,40] On the other hand, invasive intervention will undoubtedly confer benefit in a small cohort of high-risk asymptomatic patients.[28,29] This directs our goal to identify and treat this high-risk asymptomatic subgroup, rather than continuing with a policy of mass intervention that consumes vast amounts of resources but benefits very few patients in the long term.[33] To date, the degree of luminal stenosis alone as assessed by conventional angiographic techniques has not been effective in identifying high-risk asymptomatic subgroup patients.[33] This has directed the search for new adjunctive imaging strategies toward characterisation of vulnerable plaques to improve carotid disease evaluation.

In this study, we have provided evidence that alterations in shear stress patterns in a cuff model significantly influenced the initiation of atherosclerosis and induced the formation of atherosclerotic lesions of different plaque phenotypes along the carotid artery in ApoE-/- mice. We concluded that both low shear stress and oscillatory shear stress were pro-atherogenic, whereas high shear stress protected against atherosclerosis. This was supported by (1) well-developed lesions were present from week 9 post-cuff placement in all of

the cuff-treated animals under both low shear stress and oscillatory shear stress conditions; (2) lesions were absent in the straight vessel segments of the contralateral, non-treated carotid arteries; and (3) the area of increased shear stress in the carotid arteries treated with the cuff was spared from atherosclerotic lesion formation. Moreover, low shear stress induced formation of lesions with vulnerable plaque phenotype, whereas oscillatory shear stress induced the growth of stable lesions. Furthermore, we demonstrated detection and characterisation of high-risk vulnerable plaque lesions in the murine carotid artery by *in vivo* MRA using dual-targeted MPIO against VCAM-1 and P-selectin. This was further supported by histological results, which showed dual-targeted MPIO selectively bound to the endothelium overlying carotid lesions with vulnerable plaque phenotype but not to stable lesions. Although the relationship between shear stress pattern and atherosclerotic lesion development, composition and vulnerability have been well documented, to the best of our knowledge, this is the first study to use 1) the shear stress modifying cuff to generate both stable and rupture-prone lesions to allow targeted molecular imaging; 2) *in vivo* molecular MRI strategy to differentiate the heterogeneity (i.e. stable versus unstable lesions) within the asymptomatic plaque population and to identify the high-risk vulnerable plaque lesions in the murine carotid artery.

We chose to investigate the carotid territory due to the following reasons: Firstly, there were large variations in shear stress among different vascular beds (e.g. femoral, carotid, and coronary arteries) even within the same species and different vascular beds could respond to shear stress to different

extent.[226] The lesions were induced in the carotid artery instead of other vascular beds, moving a step closer to translating this *in vivo* imaging strategy to human application, particularly in patients with carotid atherosclerotic disease. Secondly, having detected and characterised the plaque lesions in the aortic root and arch by *in vivo* molecular MRI previously, we moved further to establish whether the resolution was sufficient to detect and characterise the atherosclerotic lesions with different plaque phenotypes in the carotid territory.

Earlier studies disclosed that the placement of a perivascular, non-constrictive cuff could induce intimal hyperplasia or atherosclerosis in the treated vessel region.[227] There were several factors that could trigger the development of atherosclerosis in these cuff models: 1) the cuff material; 2) the surgical procedure itself. A third factor worth highlighting was the location in which the cuffs were placed. In some studies, the device was placed in a superficial location around the femoral arteries, in which the movement of the hind limbs could result in reduced blood flow in the cuffed vessels, producing lowered shear stress therefore inducing atherosclerosis.[227] In this study, the cuff was placed around the carotid arteries, thus eliminating the possibility of eliciting such a response. Moreover, we had previous experience in placement of non-constrictive sham cuffs that did not trigger atherosclerosis in the upstream and downstream regions. Thus, the cuff material or surgical procedure per se did not induce a non-specific inflammatory response in the vessel wall that could have led to atherosclerotic disease. Furthermore, denudation or severe damage to the endothelium due to cuff placement could have also triggered a non-specific atherogenic response and compromised shear stress

responsiveness.[224] In the present study, however, CD31 staining revealed an almost intact endothelium in all shear stress regions examined after 9 weeks of cuff placement (Figure 6.7, 6.8). This concurred with previous studies which showed the endothelium was continuous after cuff placement.[223,224]

It is worth noting that low wall shear stress means relatively low, compared with the average shear stress in a straight vessel segment, like the non-treated control carotid artery. The stenosis of the cuff reduced the rate of blood flow, resulting in a lowered shear stress in the vessel upstream from the cuff. However, the absolute shear stress values in the low shear stress region in mice are higher than those in humans. Nonetheless, it does not necessarily imply that shear stress cannot be studied in mice. For example, cardiac function has been widely studied in genetically modified mouse models even though the heart rate of mice is much higher than that of humans. Moreover, both humans and mice share the same predilection sites for atherosclerosis attributable to local shear stress patterns.

In this study, no atherosclerotic lesions were present in either the non-treated undisturbed flow regions or the increased shear stress regions 9 weeks after cuff placement. The present results were consistent with the generally accepted notion that plaques do not develop under relatively high shear stress conditions.[228-230] In the undisturbed flow region or high shear stress region, endothelial cells express various athero-protective genes, and decrease several pro-atherogenic ones, leading to stability and quiescence.[231] Moreover, it has been suggested that a physiologic laminar shear stress or high shear

stress protected against atherogenesis via a tri-molecular complex expressed on endothelial cells.[232] Studies have also reported that other mechano-sensory receptors were able to convert mechanical forces into biochemical signals via inhibition of the cell cycle, suppression of prothrombotic tissue factor activity[233] as well as anti-inflammatory activation of endothelial cells.[234-238] The latter response was mediated by inhibition of c-Jun N-terminal kinase (JNK) and p38 mitogen-activated protein (MAP) kinase signaling[235,239] and alteration of NF-kB activity and function.[237,238,240] Therefore, a physiologic laminar shear stress or high shear stress protected arteries from atherosclerosis by regulating the activities of pro-inflammatory MAP kinase and NF-kB signalling pathways in endothelial cells.

Lesions with vulnerable plaque phenotype are characterised by relatively large amount of “destabilising” components (lipids and macrophages) and lower amount of “stabilising” components (vascular smooth muscle cells and collagen). Morphologically, large pools of destabilising components accumulate underneath a thin, fibrous cap, with little infiltration of vascular smooth muscle cells.[241,242] Shear stress could determine the vulnerability of the lesion by altering the gene expression of endothelial cells. In low shear stress region, the atheroprotective genes are suppressed, while the pro-atherogenic genes are over-expressed, thereby promoting atherogenesis. The local low shear stress stimulated the mechanoreceptors on the endothelial cell surface,[231,243,244] which in turn trigger a network of intracellular cascades, leading to the activation of transcription factors and subsequently phenotypic endothelial cell expression to an atherosclerotic state.[243,245-249] Through

activation of nuclear factor-**k**B, low shear stress induced higher levels of VCAM-1 and intercellular adhesion molecule-1 endothelial expression than did vortices with oscillatory shear stress; these molecules engaged integrins expression by activated leukocytes, reducing the rolling speed of inflammatory cells over the endothelium, thereby promoting transmigration of greater amount of circulating monocytes into the intima. [223,224,250-252] Once monocytes infiltrated beneath the endothelium, they differentiated to macrophages and ultimately developed into foam cells, sustaining the atherosclerosis progression.[4] Consistent with previous studies, we found that differences in infiltration capacity of monocytes induced by lowered and oscillatory shear stress could have resulted in the observed differences in macrophage content and lesion size in our study, i.e. compared with lesions induced by oscillatory shear stress, low shear stress lesions were larger in size with higher degree of inflammation indicated by the greater lesional macrophage content.

*In vivo* studies have revealed that low shear stress up-regulates the elastolytic activity of elastases (MMP-2, –9, –12, and cathepsins K, L, and S) and collagenases (MMP-1, –8, and –13), probably through nuclear factor-**k**B-dependent pathways. [224,253-256] Moreover, low shear stress lesions were shown to have greater MMP activity than the lesions in oscillatory shear stress regions.[224] Increased collagen breakdown in the low shear stress lesions by collagenase activity contributes to thinning of the fibrous cap, increasing its vulnerability to rupture. Elastases, on the other hand, break down elastin fibres in the internal elastic lamina, thereby promoting compensatory or even excessive wall expansion and accommodation of the enlarging plaque.[253,257-

[259] Moreover, fragmentation of the internal elastic lamina facilitates the migration of 1) macrophages from the intima to media, resulting in wall expansion; and 2) smooth muscle cells from the media to intima, accelerating plaque growth.[243] Low shear stress has also been shown to induce smooth muscle cell apoptosis, resulting in the relatively fewer vascular smooth muscle cells in the low shear stress lesions than in oscillatory shear stress lesions.[242] These animal studies clearly demonstrated that low shear stress induced the following responses on the plaque lesions: 1) Over-expression of endothelial adhesion molecules; 2) augmented inflammatory response with increased macrophage content; 3) degradation of extracellular matrix and internal elastic lamina; 4) growth in plaque size; 5) outward vascular remodeling; 6) decline in vascular smooth muscle cells; 7) thinning of the fibrous cap, all of which are critical steps in the development of a high-risk rupture-prone plaque.

Consistent with these previous studies, in our mouse carotid artery *in vivo* model, both low and oscillatory shear stress led to atherosclerotic plaque formation, but only low, non-oscillatory pattern was associated with the development of vulnerable plaque lesions with inflammatory changes and proclivity to rupture. Although the histological sections remained to be analysed quantitatively, compared with lesions in the oscillatory shear stress region, low shear stress lesions were observed to be 1) larger in size with outward vascular remodeling; 2) more inflamed with greater macrophage content; 3) had thinner fibrous caps containing less collagen and fewer vascular smooth muscle cells; all of which contribute to the characteristics of plaque vulnerability. By contrast, oscillatory shear stress induced the growth of

more stabilised plaques, morphologically characterised by a relatively thick, collagen-rich fibrous cap heavily infiltrated with vascular smooth muscle cells, which overlay relatively small amount of macrophages and lipid than the lesions in the lowered shear stress regions.

With the pro-atherogenic shear stress fields induced by the cuff, we have established an animal model in which both stable and unstable lesions can be studied in a single carotid artery. This animal model created an important opportunity to allow us to differentiate the high-risk vulnerable plaque lesions from the stable ones in the same carotid artery within the same animal at the same time and experimental settings using *in vivo* molecular MRI strategy. Our study revealed that dual-targeted MPIO binding was rapid and specific to the endothelium overlying vulnerable plaque lesions in carotid arteries under *in vivo* conditions, showing contrast effect from 30 to 45 minutes, and persisted for the entire 2-hour imaging period. The imaging window period for carotid atherosclerosis was consistent with that in the MRI of aortic root atherosclerosis. As discussed in section 5.4.1, MPIO offer distinct advantages over nanoscale particles: The strong contrast sensitivity, swift binding and clearance kinetics of dual-ligand MPIO, coupled with the immediate accessibility to endothelial molecular markers (circumventing the need to permeate the plaque), distinguish targeted MPIO as a potent functional MRI probes for real time *in vivo* characterisation of plaque vulnerability in the context of imaging acute thrombo-embolic events. The temporal change in the signal effect on MRI in our study indicated that a practical imaging time frame for atherosclerosis, which lies between 30 minutes to 2 hours post-

injection. However, the optimal time window remains to be further validated by serial imaging studies with larger sample size. Moreover, we have demonstrated MRI detection of new discrete areas of dark signal only in the low shear stress region of the cuff-treated carotid artery after dual-ligand MPIO injection. The new dark signal was due to the presence of dual-targeted MPIO-labelled cells, which was confirmed by Perls' stain for iron particles predominantly binding on the endothelium overlying the vulnerable plaque lesions in the low shear stress region of the cuff-treated carotid artery. By contrast, no discrete dark signal was observed in 1) pre-contrast images of both treated and non-treated carotid arteries; 2) high shear stress region or oscillatory shear stress region of the cuff-treated carotid artery as well as non-treated carotid artery in post-contrast images; 3) both pre-contrast and post-contrast carotid artery images of mice injected with control IgG-MPIO. The absence of dark signal in oscillatory shear stress region of the cuff-treated carotid artery was confirmed by the absence of dual-targeted MPIO in the lesions of relatively stable phenotype in the region. Similarly, the absence of dark signal in the non-treated control artery or high shear stress region of the cuff-treated carotid artery was also supported by the lack of dual-targeted MPIO in these atherosclerosis-spared regions. The absence of dark signal in the post-contrast carotid artery images of mice injected with control IgG-MPIO was confirmed by no non-specific IgG-MPIO binding in both stable or unstable lesions. Using dual-targeted MPIO, we have differentiated the high-risk unstable lesions from the stable ones and identified the high-risk vulnerable plaque lesions in murine carotid artery by *in vivo* MRA. Furthermore, the histological results confirmed dual-targeted MPIO selectively bound to the

endothelium overlying the more inflamed vulnerable plaque lesions with large macrophage burden but not to the stable lesions with relatively small macrophage content. This was consistent with earlier studies which showed low shear stress up-regulated endothelial expression of adhesion molecule than did vortices with oscillatory shear stress. [223,224,250-252] The increased endothelial adhesion molecule expression on the inflamed vulnerable plaques in low shear stress region resulted in greater binding of dual-targeted MPIO to the endothelium over these plaques, hence producing discrete areas of signal loss on MR images in T2*-weighted sequence. Although the macrophage burden and MR contrast effect remain to be analysed quantitatively, the present results are consistent with our previous findings in the aortic root stage, in which the endothelial-bound dual-targeted MPIO induced MR contrast effect quantitatively tracked with macrophage content within the lesions.

As previously discussed in section 5.4.1, USPIOs can potentially be used in clinical setting to *in vivo* differentiate between high- and low-risk plaques for risk stratification because USPIOs predominantly accumulate in the ruptured and rupture-prone lesions.[196] While being a positive attribute for macrophage imaging, the prolonged blood half-life led to an extensive delay between USPIO administration and imaging window.[105] This delay restricted the widespread clinical use of USPIO for real time *in vivo* characterisation of plaque vulnerability in the context of imaging acute thrombo-embolic events. Recently a similar study demonstrated that endothelial-bound dual-targeted MPIO quantitatively tracked the plaque inflammatory status, i.e. macrophage

content within lesions, in a mouse model by *in vivo* MRI.[199] However, the vascular bed imaged in this study was aortic root, which was by far greater in diameter than that of carotid artery. Other groups have used the cuff model to induce formation of both stable and vulnerable plaque lesions in murine carotid artery, thereby allowing quantification of flow velocities and wall shear stress at these lesion sites by *in vivo* MRI.[260] Building on these previous studies, we have utilised the shear stress modifying cuff model to generate both stable and rupture-prone lesions in murine carotid artery, thereby allowing the successful characterisation and identification of the high-risk vulnerable carotid plaques by *in vivo* MRA using dual-targeted MPIO.

Dual-ligand MPIO may provide a novel functional imaging probe to differentiate the high-risk unstable lesions from the stable ones and identify the rupture-prone plaque lesions by *in vivo* MRI. This *in vivo* MRI combined with dual-targeted MPIO approach could have a number of important clinical implications: the *in vivo* characterisation of plaque vulnerability based on the inflammatory burden will add further prognostic information to luminal stenosis alone in individual patients before clinical complications occur, thereby contributing a personalised approach to the management of carotid atherosclerotic disease. The risk stratification offered by this imaging strategy will identify the high-risk asymptomatic subgroup. Moreover, because of its non-invasive nature and the absence of iodine-based contrast or radioactive agents, this imaging approach presents a valuable tool for screening and monitoring the progression of atherosclerotic disease during therapeutic interventions, thereby evaluating the efficacy of pharmacological therapy.

Furthermore, the dual-targeted MPIO probes could potentially be further developed as a carrier for targeted drug delivery, which convey potent therapeutics to the precise sites of atherosclerotic plaques, in particular the vulnerable plaques, maximising the efficacy-to-toxicity ratio of the therapy.

## 6.5 CONCLUSIONS

Although the relationship between shear stress pattern and atherosclerotic lesion development, composition and vulnerability have been well documented, to the best of our knowledge, this is the first study to use the shear stress modifying cuff to generate both stable and rupture-prone lesions to allow *in vivo* targeted molecular MRI to differentiate the heterogeneity (i.e. stable versus unstable lesions) within the asymptomatic plaque population in the murine carotid artery. We conclude that both low shear stress and oscillatory shear stress were pro-atherogenic, whereas high shear stress protected against atherosclerosis. Moreover, low shear stress induced formation of lesions with vulnerable plaque phenotype, whereas oscillatory shear stress induced the growth of stable lesions.

Using dual-targeted MPIO, we have differentiated the high-risk unstable lesions from the stable ones and identified the high-risk vulnerable plaque lesions in murine carotid artery by *in vivo* MRA. We further confirmed dual-targeted MPIO selectively bound to the endothelium overlying the inflamed vulnerable carotid plaque lesions with large macrophage burden but not to the stable lesions with relatively small macrophage content. The *in vivo* MRI combined with dual-targeted MPIO approach will potentially allow real time *in vivo* characterisation of plaque vulnerability and could have a number of important clinical implications in the future, including (1) non-invasive screening and accurate risk stratification in individual patients, thereby contributing a personalised approach to the management of carotid

atherosclerotic disease; (2) identify and treat the high-risk asymptomatic subgroup with subclinical inflamed lesions, hence optimising resource allocation to target the appropriate cohorts; (3) non-invasive monitoring of response to treatment; (4) potent platform for development of carrier for targeted drug delivery.

# CHAPTER 7:

# Conclusion

# 7.1 CONCLUSION

In the initial *in vitro* feasibility study, we utilised selectin-mediated monocyte rolling and VCAM-1-mediated firm adhesion mechanism to develop the prototypic biotinylated antibody-conjugated streptavidin microbeads (SPIO) to image vascular endothelial cell activation with MRI. We have established a robust cellular model of endothelial inflammation induced with TNFα. Following this, we have demonstrated MRI detection and characterisation of the degree of endothelial inflammation using anti-E-selectin antibody and anti-VCAM-1 antibody conjugated SPIO with confirmatory immunocytochemistry. As part of a research project for an MSc at Imperial College London, this work forms the basis for the next stages of this translational study to detect vascular inflammation in atherosclerosis.

In the *ex vivo* stage, we are able to image the degree of inflammation associated with human carotid atherosclerotic plaques by *ex vivo* MRI using the dual antibody-conjugated SPIO against E-selectin and VCAM-1. More importantly, we are able to discriminate high-risk inflamed plaques from non-inflamed ones within the asymptomatic plaque population. These particles track not only the endothelial expression of VCAM-1 and E-selectin, but also macrophage burden in plaque lesions offering a potential imaging tool for quantitative MRI of inflammatory activity in atherosclerosis. Moreover, this study has demonstrated the synergistically augmented binding effect of the dual antibody conjugated SPIO on human atherosclerotic plaques. These functional molecular MRI probes potentially provide clinicians with a novel

imaging tool for *in vivo* characterisation of atherosclerosis at a molecular level in the future.

In the *ex vivo in situ* stage, we have developed a new improvised version of iron oxide particles – the dual antibody-conjugated MPIO against VCAM-1 and P-selectin. This study demonstrated the feasibility of detection of atherosclerotic lesions in the aortic roots of ApoE-/-mice by *ex vivo in situ* MRI following *in vivo* administration of dual-targeted MPIO against VCAM-1 and P-selectin.

In the *in vivo* mouse aortic root stage, we have demonstrated that the dual-targeted MPIO against VCAM-1 and P-selectin rapidly bind to vascular endothelium overlying atherosclerotic lesions in aortic root and aortic arch by *in vivo* MRI. Although predominantly bound to endothelium, the contrast effect induced by dual-targeted MPIO quantitatively tracked with macrophage content within the lesions. We further demonstrated the preferential binding of these iron particles in atherosclerosis-prone regions of the aortic arch compared with the atherosclerosis-resistant areas of the aortic arch. As a functional molecular MRI probe, dual-targeted MPIO provides significant advantages: (1) swift binding and maintenance of steady state at target sites; (2) evident ‘target-to-background’ and quantifiable contrast effects; (3) quantitative tracking of macrophage burden within atherosclerotic lesions. This molecular imaging strategy will potentially allow real time *'in vivo* microscopy' reporting the underlying inflammatory process in vulnerable plaques in the future.

In the final *in vivo* mouse carotid stage, although the relationship between shear stress pattern and atherosclerotic lesion development and vulnerability have been well documented, to the best of our knowledge, this is the first study to use the shear stress modifying cuff to generate both stable and rupture-prone lesions to allow *in vivo* targeted molecular MRI to differentiate plaque heterogeneity (i.e. stable versus unstable lesions) within the asymptomatic plaque population in the murine carotid artery. We conclude that both low shear stress and oscillatory shear stress are pro-atherogenic, whereas high shear stress protects against atherosclerosis. Moreover, low shear stress induces formation of lesions with a vulnerable plaque phenotype, whereas oscillatory shear stress induces the growth of stable lesions. Using dual-targeted MPIO, we have differentiated the high-risk unstable lesions from the stable ones and identified the high-risk vulnerable plaque lesions in murine carotid artery by *in vivo* MRA. We further confirmed dual-targeted MPIO selectively bound to the endothelium overlying the inflamed vulnerable carotid plaque lesions with large macrophage burden but not to the stable lesions with relatively small macrophage content. The *in vivo* MRI combined with dual-targeted MPIO approach will potentially allow real time *in vivo* characterisation of plaque vulnerability, leading to accurate risk stratification in individual patients, thereby contributing a personalised approach to the management of carotid atherosclerotic disease in the future.

## 7.2 LIMITATIONS

Although the *in vivo* MRI combined with targeted MPIO approach provides distinct advantages over other imaging modalities as outlined previously, there are nevertheless limitations: (1) The high cost of MRI scanners often makes them less accessible to patients; (2) MRI is highly motion sensitive; (3) The combination of being put in an enclosed space and loud noises during the imaging procedure can present challenges to patients who suffer from claustrophobia; (4) MRI is contra-indicated in patients with metallic implants, such as cardiac pacemakers, aneurysm clips, some coronary artery stents; (5) Although atherosclerotic lesions can be visualised in the mouse aortic root, aortic arch as well as the carotid artery at high field strengths (9.4T) in this study, effective resolution is likely to diminish at clinically relevant field strengths; (6) The large size and incompressible nature of MPIO prevent the particles from translocating across the endothelium to access targets within atherosclerotic plaque. However, this property is also advantageous since it evades undesirable passive accumulation, thereby retaining specificity for molecular targets expressed on the vascular endothelium; (7) Although no ill effect or complication was observed in the mice following MPIO administration in this study, the distribution, degradation, excretion and long term toxicity of the particles remain to be evaluated in the future. (8) Although *in vitro* study revealed no adverse effects of MPIO on function or iron homeostasis in human liver cells,[261] the MPIO that we used in this study are not suitable for human use due to their potential long-term toxicity. However, a range of

biodegradable MPIO with a coating of poly(lactide-co-glycolide) (PLGA) or cellulose (both FDA-approved polymers) have recently been developed. [262,263]

## 7.3 FUTURE WORK

While the current generation of commercially available MPIO have been proven as functional molecular MRI probes in murine atherosclerosis model[133,199], additional development is mandatory to advance the technology to clinical applications. Future work may focus on two areas; the development of non-toxic, biodegradable particles that is applicable to humans, and the use of non-immunogenic targeting systems, either through the use of humanised antibodies or cognate ligands, to minimise immunogenicity. Factors affecting MPIO binding efficiency, such as, target selection and density, size and shape of particle and local shear stress, should also be taken into consideration in the development of novel imaging contrasts. Moreover, the relatively large surface area and adaptable surface chemistry of MPIO open the possibility of drug incorporation into the particles, making them function as a carrier vehicle for targeted drug delivery as well as a targeted imaging contrast agent, serving a dual diagnostic and therapeutic capability.[85]

One of the biggest challenges in translating this molecular MRI strategy to clinical application is the lack of a robust preclinical model. The pharmaceutical industry and academic laboratories are currently using human cells growing in two dimensions, followed by animal work to mimic a three-dimensional model. Animal models have been instrumental in serving as a surrogate for patients in the evaluation of novel diagnostic agents and therapeutic drugs. Indeed, animal studies are a prerequisite to human clinical trials for approval of new

biomedical products. Although animal models will remain as a unique source of *in vivo* information and the irreplaceable link between *in vitro* studies and our patients, they do not always have a great human predictive value in clinical efficacy and safety. Differences in physiology and size, as well as variations in the homology of targets between animals and human, may lead to translational limitations. In fact, the literature is littered with examples of biomedical products that show good results in animal model but fail to provide similar efficacy or safety in humans at the late stages of clinical trial, costing tremendous amount of time and resources.[264] There is an increasing awareness that better models are needed earlier in the development process of biomedical products. Recently, researchers are actively exploring the potential of biofabrication technology, 3-dimensional (3D) bioprinting, to build functional human tissues. Bioprinting entails the printing and patterning in three dimensions of all the components that make up a tissue (cells and matrix materials) to generate structures analogous to tissues.[265] Early applications of bioprinted tissues are currently being used in academic research laboratories and pharmaceutical development for biomarker discovery, drug screening and toxicology testing.[265,266] The bioprinted tissue has tremendous potential in improving the predictiveness and bio-relevance of preclinical models, even more superior than animal models, because it is living human tissues that are 3D, architecturally correct and made entirely of living human cells.[267] In December 2010, Organovo, one of the pioneer bioprinting companies, created the first blood vessels to be bioprinted using cells cultured from a single person.[267] Capturing this novel bioprinting technology, the future direction of our study will be taken to a new level by inducing atherosclerotic plaque

lesions in a living bioprinted human blood vessel model to allow translation of the targeted molecular MRI strategy developed in this study to a 3D human disease model, moving a step closer to clinical application.

# REFERENCES

1. Cardiovascular diseases due to atherosclerosis. In: Global Atlas on Cardiovascular Disease Prevention and Control. Mendis S, Puska P, Norrving B (eds). World Health Organization, Geneva 2011: 2-56.

2. Libby P. Inflammation in atherosclerosis. Nature 2002: 420: 868-874.

3. Stoll G, Bendszus M. Inflammation and atherosclerosis: novel insights into plaque formation and destabilization. Stroke 2006: 37: 1923-1932.

4. Libby P, Ridker PM, Maseri A. Inflammation and atherosclerosis. Circulation 2002: 105: 1135–1143.

5. Ross R. Atherosclerois - an inflammatory disease. N Engl J Med 1999: 340: 115–126.

6. Verma S, Anderson TJ. Fundamentals of endothelial function for the clinical cardiologist. Circulation 2002: 105: 546–549.

7. Moncada S, Higgs A. The L-arginine-nitric oxide pathway. N Engl J Med 1993: 329: 2002–2012.

8. Szmitko PE et al. New markers of inflammation and endothelial cell activation: part I. Circulation 2003: 108: 1917-1923.

9. Cominacini L et al. The binding of oxidized low-density lipoprotein (ox-LDL) to ox-LDL receptor-1 in endothelial cells reduces the intracellular concentration of nitric oxide through an increased production of superoxide. J Biol Chem 2001: 276: 13750–13755.

10. Kranzhofer R et al. Angiotensin induces inflammatory activation of human vascular smooth muscle cells. Arterioscler Thromb Vasc Biol 1999: 19: 1623–1629.

11. Kunjathoor VV et al. Scavenger receptors class A-I/II and CD36 are the principal receptors responsible for the uptake of modified low density lipoprotein leading to lipid loading in macrophages. J Biol Chem 2002: 277: 49982–49988.

12. Hansson GK et al. Innate and adaptive immunity in the pathogenesis of atherosclerosis. Circ Res 2002: 91: 281–291.

13. Szmitko PE et al. Biomarkers of vascular disease linking inflammation to endothelial activation: part II. Circulation 2003: 108: 2041-2048.

14. de Boer OJ, van der Wal AC, Teeling P, Becker AE. Leucocyte recruitment in rupture prone regions of lipid-rich plaques: a prominent role for neovascularization? Cardiovasc Res. 1999;41:443–449.

15. Galis ZS, Khatri JJ. Matrix metalloproteinases in vascular remodeling and atherogenesis: the good, the bad, and the ugly. Circ Res 2002: 90: 251–262.

16. Papalambros E et al. Vascular endothelial growth factor and matrix metalloproteinase 9 expression in human carotid atherosclerotic plaques: relationship with plaque destabilization via neovascularization. Cerebrovasc Dis 2004: 18: 160–165.

17. Naylor AR, Gaines PA. Extracranial cerebrovascular disease. Beard JD and Gaines PA (Eds). Vascular and endovascular surgery. Elsevier Limited, 2007: 287-313.

18. Wolfe C. The burden of stroke. In Wolfe C, Rudd T, Beech R (Eds). Stroke services and research. The Stroke Association, 1996.

19. Adamson J, Beswick A, Ebrahim S. Is stroke the most common cause of disability? J Stroke Cerebrovasc Dis 2004: 13: 171-177.

20. Saka O, McGuire A, Wolfe C. Cost of stroke in the United Kingdom. Age Ageing 2009: 38: 27-32.

21. Donnan GA, Fisher M, Macleod M et al. Stroke. Lancet 2008: 371: 1612-1623.

22. Warlow C. Stroke. Lancet 2003: 362: 1211-1224.

23. Kolominsky-Rabas PL, Weber M, Gefeller O, Neundoerfer B, Heuschmann PU. Epidemiology of ischemic stroke subtypes according to toast criteria: Incidence, recurrence, and long-term survival in ischemic stroke subtypes: A population-based study. Stroke 2001: 32: 2735-2740.

24. European Carotid Surgery Trialists Collaborative Group. MRC European Carotid Surgery Trial: interim results for symptomatic patients with severe (70–99%) or with mild (0–29%) carotid stenosis. Lancet 1991: 337: 1235–1243.

25. North American Symptomatic Carotid Endarterectomy Trial Collaborators. Beneficial effect of carotid endarterectomy in symptomatic patients with high-grade stenosis. N Engl J Med 1991: 325: 445–453.

26. Halliday, A. et al. Prevention of disabling and fatal strokes by successful carotid endarterectomy in patients without recent neurological symptoms: randomised controlled trial. Lancet 2004: 363: 1491–1502.

27. Executive Committee for the Asymptomatic Carotid Atherosclerosis Study. Endarterectomy for asymptomatic carotid artery stenosis. JAMA 1995: 273: 1421–1428.

28. Goldstein, L. B. et al. Guidelines for primary prevention of stroke: a guideline for healthcare professionals from the American Heart Association/American Stroke Association. Stroke 2011: 42: 517–584.

29. Brott, T. G. et al. ASA/ACCF/AHA/AANN/AANS/ACR/ASNR/CNS/SAIP/SCAI/SIR/SNIS/SVM/SVS guideline on management of patients with extracranial carotid and vertebral artery disease: executive summary: a report of the American College of Cardiology Foundation/American Heart Association Task Force on Practice Guidelines, and the American Stroke Association, American Association of Neuroscience Nurses, American Association of Neurological Surgeons, American College of Radiology, American Society of Neuroradiology, Congress of Neurological Surgeons, Society of Atherosclerosis Imaging and Prevention, Society for Cardiovascular Angiography and Interventions, Society of Interventional Radiology, Society of NeuroInterventional Surgery, Society for Vascular Medicine, and Society for Vascular Surgery. Stroke 2011: 16: 35–77.

30. Schneider P. A. & Naylor, A. R. Trans-Atlantic debate. Asymptomatic carotid artery stenosis—medical therapy alone versus medical therapy plus carotid endarterectomy or stenting? Eur J Vasc Endovasc Surg 2010: 40: 274–281.

31. Schneider, P. Response to comment regarding trans-Atlantic debate: asymptomatic carotid artery stenosis. Eur J Vasc Endovasc Surg 2010: 40: 679.

32. Wholey, M. H., Barbato, J. E. & Al-Khoury, G. E. Treatment of asymptomatic carotid disease with stenting: pro. Sem Vasc Surg 2008: 21: 95–99.

33. Naylor, A. R. Time to rethink management strategies in asymptomatic carotid artery disease. Nat Rev Cardiol 2012: 9: 116–124.

34. Abbott, A. Asymptomatic carotid artery stenosis—It's time to stop operating. Nat Clin Pract Neurol 2008:4: 4–5.

35. Abbott, A. L. Medical (nonsurgical) intervention alone is now best for prevention of stroke associated with asymptomatic severe carotid stenosis: results of a systematic review and analysis. Stroke 2009: 40: e573–e583.

36. Barnett, H. J., Pelz, D. M. & Lownie, S. P. Reflections by contrarians on the post-CREST evaluation of carotid stenting for stroke prevention. Int J Stroke 2010: 5: 455–456.

37. Naylor, A. R., Gaines, P. A. & Rothwell, P. M. Who benefits most from intervention for asymptomatic carotid stenosis: patients or professionals? Eur J Vasc Endovasc Surg 2009: 37: 625–632.

38. Naylor AR, Gaines PA, Rothwell PM. Corrigendum to “Who benefits most from intervention for asymptomatic carotid stenosis: patients or professionals?” [Eur. J. Vasc. Endovasc. Surg. 37, 625–632 (2009).]. Eur J Vasc Endovasc Surg 2009: 38: 657.

39. Arazi, H. C. et al. Carotid endarterectomy in asymptomatic stenosis: a decision analysis. Clin Neurol Neurosurg 2008: 110: 472–479.

40. Whitty, C. J., Sudlow, C. L. & Warlow, C. P. Investigating individual subjects and screening populations for asymptomatic carotid stenosis can be harmful. J Neurol Neurosurg Psych 1998: 64: 619–623.

41. Kadoglou, N. P. et al. Intensive lipid-lowering therapy ameliorates novel calcification markers and GSM score in patients with carotid stenosis. Eur J Vasc Endovasc Surg 2008: 35: 661–668.

42. Amarenco P, Bogousslavsky J, Callahan A 3rd, Goldstein LB, Hennerici M, Rudolph AE, Sillesen H, Simunovic L, Szarek M, Welch KM, Zivin JA; Stroke Prevention by Aggressive Reduction in Cholesterol Levels (SPARCL) Investigators. High-dose atorvastatin after stroke or transient ischemic attack. N Engl J Med 2006:10: 355(6): 549-59.

43. Ward MR et al. Arterial remodeling: mechanisms and clinical implications. Circulation 2000: 102: 1186–1191.

44. Glagov S et al. Compensatory enlargement of human atherosclerotic coronary arteries. N Engl J Med 1987: 316: 1371–1375.

45. Benes V et al. Comparison between degree of carotid stenosis observed at angiography and in histological examination. Acta Neurochir (Wien) 2004: 146: 671– 677.

46. Nicolaides, A. N. et al. Severity of asymptomatic carotid stenosis and risk of ipsilateral hemispheric ischaemic events: results from the ACSRS study. Eur J Vasc Endovasc Surg 2005: 30: 275–284.

47. American Heart Association. Heart Disease & Stroke Statistics—2009 Update (American Heart Association, Dallas, TX, 2009).

48. Kakkos, S. K. et al. Silent embolic infarcts on computed tomography brain scans and risk of ipsilateral hemispheric events in patients with asymptomatic internal carotid artery stenosis. J Vasc Surg 2009: 49: 902–909.

49. Nicolaides, A. N. et al. Asymptomatic internal carotid artery stenosis and cerebrovascular risk stratification. J Vasc Surg 2010: 52: 1486–1496.

50. Griffin, M., Nicolaides, A. & Kyriacou, E. Normalisation of ultrasonic images of atherosclerotic plaques and reproducibility of gray scale median using dedicated software. Int Angiol 2007: 26: 372–377.

51. Geroulakos, G. et al. Characterization of symptomatic and asymptomatic carotid plaques using high-resolution, real-time ultrasonography. Br J Surg 1993: 80: 1274–1277.

52. Griffin, M. B. et al. Juxtaluminal hypoechoic area in ultrasonic images of carotid plaques and hemispheric symptoms. J Vasc Surg 2010: 54: 69–76.

53. Tegos, T. J. et al. Types of neurovascular symptoms and carotid plaque ultrasonic textural characteristics. J Ultrasound Med 2011: 20: 113–121.

54. Nicolaides, A. N. et al. Effect of image normalization on carotid plaque classification and the risk of ipsilateral hemispheric ischemic events: results from the Asymptomatic Carotid Stenosis and Risk of Stroke study. Vascular 2005: 13: 211–221.

55. Markus, H. S. et al. Asymptomatic embolisation for prediction of stroke in the Asymptomatic Carotid Emboli Study (ACES): a prospective observational study. Lancet Neurol 2010: 9: 663–671.

56. Spence, J. D. et al. Effects of intensive medical therapy on microemboli and cardiovascular risk in asymptomatic carotid stenosis. Arch Neurol 2010: 67, 180–186.

57. Spence, J. D., Tamayo, A., Lownie, S. P., Ng, W. P. & Ferguson, G. G. Absence of microemboli on transcranial Doppler identifies low-risk patients with asymptomatic carotid stenosis. Stroke 2005: 36: 2373–2378.

58. Coli S, Magnoni M, Sangiorgi G et al. Contrast-enhanced ultrasound imaging of intraplaque neovascularization in carotid arteries: correlation with histology and plaque echogenicity. J Am Coll Cardiol*:* 2008: 52(3): 223-230.

59. Shalhoub J, Monaco C, Owen DR et al. Late-Phase Contrast-Enhanced Ultrasound Reflects Biological Features of Instability in Human Carotid Atherosclerosis. Stroke 2011: 42(12): 3634-3636.

60. Hamilton AJ, Huang S-L, Warnick D, Rabbat M, Kane B, Nagaraj A, Klegerman M, McPherson DD. Intravascular ultrasound molecular imaging of atheroma components in vivo*1. J Am Coll Cardiol 2004: 43: 453– 460.

61. Lindner JR, Song J, Christiansen J, Klibanov AL, Xu F, Ley K. Ultrasound assessment of inflammation and renal tissue injury with microbubbles targeted to P-selectin. Circulation 2001:104: 2107–2112.

62. Demos SM, Alkan-Onyuksel H, Kane BJ, Ramani K, Nagaraj A, Greene R, Klegerman M, McPherson DD. In vivo targeting of acoustically reflective liposomes for intravascular and transvascular ultrasonic enhancement. J Am Coll Cardiol 1999: 33: 867– 875.

63. Javier M. Romero, Lukasz S et al. Arterial Wall Enhancement Overlying Carotid Plaque on CT Angiography Correlates With Symptoms in Patients With High Grade Stenosis. Stroke 2009: 40:1894-1896.

64. Fleiner M, Kummer M, Mirlacher M et al. Arterial neovascularization and inflammation in vulnerable patients: Early and late signs of symptomatic atherosclerosis. Circulation 2004: 110: 2843–285.

65. Kircher MF, Grimm J, Swirski FK et al. Noninvasive in vivo imaging of monocyte trafficking to atherosclerotic lesions. Circulation 2008: 117: 388 –395.

66. Davies JR, Rudd JH, Fryer TD, et al. Identification of culprit lesions after transient ischemic attack by combined 18F fluorodeoxyglucose positron-emission tomography and high-resolution magnetic resonance imaging. Stroke 2005: 36: 2642–47.

67. Rudd J, Warburton E, Fryer T et al. Imaging atherosclerotic plaque inflammation with [18F]-fluorodeoxyglucose positron emission tomography. Circulation 2002: 105: 2708 –2711.

68. Paulmier B, Duet M, Khayat R et al. Arterial wall uptake of fluorodeoxyglucose on PET imaging in stable cancer disease patients indicates higher risk for cardiovascular events. J Nucl Cardiol 2008: 15:209 –217.

69. Davies JR, Izquierdo-Garcia D, Rudd JH et al. FDG-PET can distinguish inflamed from non-inflamed plaque in an animal model of atherosclerosis. Int J Cardiovasc Imaging 2010: 26: 41–48.

70. Wagner S, Breyholz HJ, Faust A, et al. Molecular imaging of matrix metalloproteinases in vivo using small molecule inhibitors for SPECT and PET. Curr Med Chem 2006:13: 2819–38.

71. Laufer EM,Winkens HM, Corsten MF, et al. PET and SPECT imaging of apoptosis in vulnerable atherosclerotic plaques with radiolabeled Annexin A5. Q J Nucl Med Mol Imaging 2009: 53: 26–34.

72. Gaemperli O, Shalhoub J, Owen DR et al. Imaging intraplaque inflammation in carotid atherosclerosis with 11C-PK11195 positron emission tomography/computed tomography. Eur Heart J 2012: 33(15): 1902-10.

73. Saam, T. et al. Quantitative evaluation of carotid plaque composition by in vivo MRI. Arterioscler Thromb Vasc Biol 2005: 25: 234–239.

74. Saam, T. et al. Reader and platform reproducibility for quantitative assessment of carotid atherosclerotic plaque using 1.5T Siemens, Philips, and General Electric scanners. J Magn Reson Imaging 2007: 26: 344–352.

75. Hunter R. Underhill, Thomas S et al. MRI of carotid atherosclerosis: clinical implications and future directions. Nat Rev Cardiol 2010: 7: 165–173.

76. Takaya, N. et al. Association between carotid plaque characteristics and subsequent ischemic cerebrovascular events: a prospective assessment with MRI—initial results. Stroke 2006: 37: 818–823.

77. Altaf, N. *et al.* Detection of intraplaque hemorrhage by magnetic resonance imaging in symptomatic patients with mild to moderate carotid stenosis predicts recurrent neurological events. J Vasc Surg 2008: 47: 337–342.

78. Singh, N. *et al.* Moderate carotid artery stenosis: MR imaging-depicted intraplaque hemorrhage predicts risk of cerebrovascular ischemic events in asymptomatic men. Radiology 2009: 252: 502–508.

79. Redgrave JNE, Lovett JK, Gallagher PJ, Rothwell PM. Histological assessment of 526 symptomatic carotid plaques in relation to the nature and timing of ischemic symptoms: the Oxford plaque study. Circulation 2006: 113: 2320 –2328.

80. Li, Z. Y. *et al.* Structural analysis and magnetic resonance imaging predict plaque vulnerability: a study comparing symptomatic and asymptomatic individuals. J Vasc Surg 2007: 45: 768–775.

81. Tang D, Yang C, Zheng J et al. 3D MRI-based multicomponent FSI models for atherosclerotic plaques. Ann Biomed Eng 2004: 32: 947-60.

82. Tang TY, Howarth SP, Li ZY et al. Correlation of carotid atheromatous plaque inflammation with biomechanical stress: utility of USPIO enhanced MR imaging and finite element analysis. Atherosclerosis 2008:196: 879-87.

83. Mankoff DA. A definition of molecular imaging. J Nucl Med 2007;48, 18N, 21N.

84. Choudhury RP, Fuster V, Fayad ZA. Molecular, cellular and functional imaging of atherothrombosis. Nat Rev Drug Disc 2004: 3: 913–925.

85. Jefferson A, Wijesurendra RS, McAteer MA, Choudhury RP. Development and application of endothelium-targeted microparticles for molecular magnetic resonance imaging. Wiley Interdiscip Rev Nanomed Nanobiotechnol 2012: 4(3): 247-56.

86. Seeing is believing: Introduction to image contrast. In: MRI from Picture to Proton. Donald W. McRobbie, Elizabeth A. Moore, Martin J. Graves, Martin R. Prince (eds). Cambridge University Press 2006: 30-46.

87. James H.F. Rudd, Fabien Hyafil and Zahi A. Fayad. Inflammation Imaging in Atherosclerosis. Arterioscler Thromb Vasc Biol 2009: 29: 1009-1016.

88. Kerwin W, Hooker A, Spilker M, Vicini P, Ferguson M, Hatsukami T, Yuan C. Quantitative magnetic resonance imaging analysis of neovasculature volume in carotid atherosclerotic plaque. Circulation 2003: 107: 851–856.

89. Kerwin, W. S. et al. Inflammation in carotid atherosclerotic plaque: a dynamic contrast enhanced MR imaging study. Radiology 2006: 241: 459–468.

90. Kerwin, W. S., Oikawa, M., Yuan, C et al. MR imaging of adventitial vasa vasorum in carotid atherosclerosis. Magn Reson Med 2009: 59: 507–514.

91. Martina A. McAteer, Asim M. Akhtar, Constantin von zur Muhlen, Robin P. Choudhury. An approach to molecular imaging of atherosclerosis, thrombosis, and vascular inflammation using microparticles of iron oxide. Atherosclerosis 2010: 209: 18–27.

92. Briley-Saebo KC, Mulder WJ, Mani V, Hyafil F, Amirbekian V, Aguinaldo JG, Fisher EA, Fayad ZA. Magnetic resonance imaging of vulnerable atherosclerotic plaques: current imaging strategies and molecular imaging probes. J Magn Reson Imaging 2007: 26: 460–479.
93. Frias JC, Williams KJ, Fisher EA, Fayad ZA. Recombinant HDL-like nanoparticles: a specific contrast agent for MRI of atherosclerotic plaques. J Am Chem Soc 2004: 126: 16316-7.
94. Glickson JD, Lund-Katz S, Zhou R, et al. Lipoprotein nanoplatform for targeted delivery of diagnostic and therapeutic agents. Mol Imaging 2008: 7: 101–10.
95. Frias JC, Ma Y, Williams KJ, Fayad ZA, Fisher EA. Properties of a versatile nanoparticle platform contrast agent to image and characterize atherosclerotic plaques by magnetic resonance imaging. Nano Lett 2006: 6: 2220–4.
96. Corbin IR, Li H, Chen J, et al. Low-density lipoprotein nanoparticles as magnetic resonance imaging contrast agents. Neoplasia 2006: 8: 488–98.
97. Penfield JG, Reilly Jr RF. What nephrologists need to know about gadolinium. Nat Clin Pract Nephrol 2007: 3: 654–68.
98. Tang TY, Muller KH, Graves MJ, Li ZY, Walsh SR, Young V, Sadat U, Howarth SP, Gillard JH. Iron oxide particles for atheroma imaging. Arterioscler Thromb Vasc Biol 2009: 29(7): 1001-8.
99. London, E., The molecular formula and proposed structure of the iron-dextran complex, IMFERON. J Pharm Sci 2004: 93(7): 1838-46.
100. Pouliquen, D., et al., Iron oxide nanoparticles for use as an MRI contrast agent: pharmacokinetics and metabolism. Magn Reson Imaging 1991: 9(3): 275-83.
101. Eakins, M.N., et al., Physicochemical properties, pharmacokinetics, and biodistribution of gadoteridol injection in rats and dogs. Acad Radiol 1995: 2(7): 584-91.
102. Ayala, A., et al., Mechanism of splenic immunosuppression during sepsis: key role of Kupffer cell mediators. J Trauma 1997: 42(5): 882-8.
103. Contrast agent development. In: Design and Synthesis of Intracellular MR Contrast Agents. Jones W. PhD thesis Imperial College London 2007: 40-95.
104. Kooi ME, Cappendijk VC, Cleutjens KBJM, Kessels AGH, Kitslaar PJEHM, Borgers M, Frederik PM, Daemen MJAP, van Engelshoven JMA. Accumulation of ultrasmall

superparamagnetic particles of iron oxide in human atherosclerotic plaques can be detected by in vivo magnetic resonance imaging. Circulation. 2003;107:2453–2458.
105. Trivedi RA, U-King-Im J-M, Graves MJ, Cross JJ, Horsley J, Goddard MJ, Skepper JN, Quartey G, Warburton E, Joubert I, Wang L, Kirkpatrick PJ, Brown J, Gillard JH. In vivo detection of macrophages in human carotid atheroma: temporal dependence of ultrasmall superparamagnetic particles of iron oxide-enhanced MRI. Stroke. 2004;35:1631–1635.
106. Briley-Saebo K, BjA˜ çrnerud A, Grant D, Ahlstrom Hk, Berg T, Kindberg Gr. Hepatic cellular distribution and degradation of iron oxide nanoparticles following single intravenous injection in rats: implications for magnetic resonance imaging. Cell Tissue Res 2004: 316: 315-323.
107. Raynal I, Prigent P, Peyramaure S, Najid A, Rebuzzi C, Corot C. Macrophage endocytosis of superparamagnetic iron oxide nanoparticles: mechanisms and comparison of ferumoxides and ferumoxtran-10. Invest Radiol 2004: 39: 56–63.
108. von Zur Muhlen C, von Elverfeldt D, Bassler N, Neudorfer I, Steitz B, Petri-Fink A, Hofmann H, Bode C, Peter K. Superparamagnetic iron oxide binding and uptake as imaged by magnetic resonance is mediated by the integrin receptor Mac-1 (CD11b/CD18): implications on imaging of atherosclerotic plaques. Atherosclerosis 2007: 193: 102–111.
109. Litovsky S, Madjid M, Zarrabi A, Casscells SW, Willerson JT, Naghavi M. Superparamagnetic iron oxide-based method for quantifying recruitment of monocytes to mouse atherosclerotic lesions in vivo: enhancement by tissue necrosis factor-alpha, interleukin-1beta, and interferon-gamma. Circulation 2003:107: 1545–1549.
110. Kawahara I, Nakamoto M, Kitagawa N, Tsutsumi K, Nagata I, Morikawa M, Hayashi T. Potential of magnetic resonance plaque imaging using superparamagnetic particles of iron oxide for the detection of carotid plaque. Neurol Med Chir (Tokyo) 2008: 48:157–161.
111. Shapiro EM, Skrtic S, Koretsky AP. Sizing it up: cellular MRI using micron-sized iron oxide particles. Magn Reson Med 2005: 53: 329–38.
112. Shapiro EM, Skrtic S, Sharer K, et al. MRI detection of single particles for cellular imaging. Proc Natl Acad Sci USA 2004: 101: 10901–6.

113. Wu YL, Ye Q, Foley LM, Hitchens TK, Sato K,Williams JB, Ho C. In situ labeling of immune cells with iron oxide particles: an approach to detect organ rejection by cellular MRI. Proc Natl Acad Sci U S A 2006: 103: 1852–1857.

114. Ye Q, Wu YL, Foley LM, et al. Longitudinal tracking of recipient macrophages in a rat chronic cardiac allograft rejection model with noninvasive magnetic resonance imaging using micrometer-sized paramagnetic iron oxide particles. Circulation 2008: 118: 149–56.

115. Choudhury RP, Fisher EA. Molecular imaging in atherosclerosis, thrombosis, and vascular inflammation. Arterioscler Thromb Vasc Biol. 2009: 29(7): 983-91.

116. Bhatia SK, King MR, Hammer DA. The State Diagram for Cell Adhesion Mediated by Two Receptors. Biophys J. 2003;84:2671–2690.

117. Eniola AO, Willcox PJ, Hammer DA. Interplay between rolling and firm adhesion elucidated with a cell-free system engineered with two distinct receptor-ligand pairs. Biophys J. 2003;85:2720 –2731.

118. Hidalgo A, Peired AJ, Wild MK, Vestweber D, Frenette PS. Complete identification of E-selectin ligands on neutrophils reveals distinct functions of PSGL-1, ESL-1, and CD44. Immunity. 2007;26:477– 489.

119. Zarbock A, Lowell CA, Ley K. Spleen Tyrosine Kinase Syk Is Necessary for E-Selectin-Induced alpha(L)beta(2) Integrin-Mediated Rolling on Intercellular Adhesion Molecule-1. Immunity. 2007: 26:773–783.

120. Springer TA. Traffic signals for lymphocyte recirculation and leukocyte emigration: the multistep paradigm. Cell. 1994: 76: 301–314.

121. Ley K, Laudanna C, Cybulsky M, Nourshargh S. Getting to the site of inflammation: the leukocyte adhesion cascade updated. Nat Rev Immunol 2007: 7(9): 678-89.

122. Galkina E and Ley K. Vascular Adhesion Molecules in Atherosclerosis. Arterioscler Thromb Vasc Biol 2007: 27: 2292-2301.

123. Ley K. The role of selectins in inflammation and disease. Trends Mol Med 2003: 9: 263–268.

124. Mehta P, Cummings RD, McEver RP. Affinity and kinetic analysis of P-selectin binding to P-selectin glycoprotein ligand-1. J Biol Chem 1998, 273: 32506–32513.

125. Stocker CJ, Sugars KL, Harari OA, Landis RC, Morley BJ, Haskard DO. TNF-alpha, IL-4,

and IFN-gamma regulate differential expression of P and E-selectin expression by porcine aortic endothelial cells. J Immunol. 2000;164:3309 –3315.

126. Yu G, Rux AH, Ma P, Bdeir K, Sachais BS. Endothelial expression of E-selectin is induced by the platelet-specific chemokine platelet factor 4 through LRP in an NF-kappaB-dependent manner. Blood. 2005;105: 3545–3551.

127. Davies MJ, Gordon JL, Gearing AJ, Pigott R, Woolf N, Katz D, Kyriakopoulos A. The expression of the adhesion molecules ICAM-1, VCAM-1, PECAM, and E-selectin in human atherosclerosis. J Pathol. 1993;171:223–229.

128. Collins RG, Velji R, Guevara NV, Hicks MJ, Chan L, Beaudet AL. P-Selectin or intercellular adhesion molecule (ICAM)-1 deficiency substantially protects against atherosclerosis in apolipoprotein E-deficient mice. J Exp Med. 2000;191:189 –194.

129. Dong ZM, Chapman SM, Brown AA, Frenette PS, Hynes RO, Wagner DD. The combined role of P- and E-selectins in atherosclerosis. J Clin Invest. 1998;102:145–152.

130. Koedam JA, Cramer EM, Briend E, Furie B, Furie BC, Wagner DD. P-selectin, a granule membrane protein of platelets and endothelial cells, follows the regulated secretory pathway in AtT-20 cells. J Cell Biol 1992: 116: 617–625.

131. Norman KE, Moore KL, McEver RP, Ley K. Leukocyte rolling in vivo is mediated by P-selectin glycoprotein ligand-1. Blood 1995, 86:4417–4421.

132. Johnson-Tidey RR, McGregor JL, Taylor PR, Poston RN. Increase in the adhesion molecule P-selectin in endothelium overlying atherosclerotic plaques. Coexpression with intercellular adhesion molecule-1. Am J Pathol 1994: 144: 952–961.

133. McAteer MA et al. Magnetic resonance imaging of endothelial adhesion molecules in mouse atherosclerosis using dual-targeted microparticles of iron oxide. ArterioscIerThromb Vasc Biol 2008: 28(1): 77-83.

134. Iiyama K et al. Patterns of vascular cell adhesion molecule-1 and intercellular adhesion molecule-1 expression in rabbit and mouse atherosclerotic lesions and at sites predisposed to lesion formation. Circ Res 1999: 85: 199–207.

135. Osborn L,Hession C, Tizard R, Vassallo C, Luhowskyj S, Chi-Rosso G, Lobb R. Direct expression cloning of vascular cell adhesion molecule 1, a cytokine-induced endothelial protein that binds to lymphocytes. Cell 1989: 59: 1203–1211.

136. Pueyo ME, Gonzalez W, Nicoletti A, Savoie F, Arnal JF, Michel JB. Angiotensin II stimulates endothelial vascular cell adhesion molecule-1 via nuclear factor kappa B activation induced by intracellular oxidative stress. Arterioscler Thromb Vasc Biol 2000: 20: 645–651.
137. Elices MJ, Osborn L, Takada Y, Crouse C, Luhowskyj S, Hemler ME, Lobb RR. VCAM-1 on activated endothelium interacts with the leukocyte integrin VLA-4 at a site distinct from the VLA-4/fibronectin binding site. Cell 1990: 60:577–584.
138. Mazo IB, Gutierrez-Ramos JC, Frenette PS, Hynes RO, Wagner DD, von Andrian UH. Hematopoietic progenitor cell rolling in bone marrow microvessels: parallel contributions by endothelial selectins and vascular cell adhesion molecule 1. J ExpMed 1998: 188: 465–474.
139. Ramos CL, Huo Y, Jung U, Ghosh S, Manka DR, Sarembock IJ, Ley K. Direct demonstration of P-selectin- and VCAM-1-dependent mononuclear cell rolling in early atherosclerotic lesions of apolipoprotein E-deficient mice. Circ Res 1999, 84: 1237–1244.
140. Jefferson A, Wijesurendra RS, McAteer MA, Digby JE, Douglas G, Bannister T, Perez-Balderas F, Bagi Z, Lindsay AC, Choudhury RP. Molecular imaging with optical coherence tomography using ligand conjugated microparticles that detect activated endothelial cells: rational design through target quantification. Atherosclerosis 2011: 219: 579–587.
141. McAteer MA, SibsonNR, von Zur Muhlen C, Schneider JE, Lowe AS, Warrick N, Channon KM, Anthony DC, Choudhury RP. In vivo magnetic resonance imaging of acute brain inflammation using microparticles of iron oxide. Nat Med 2007: 13: 1253–1258.
142. Cybulsky MI, Iiyama K, Li H, Zhu S, Chen M, Iiyama M, Davis V,Gutierrez-Ramos JC, Connelly PW, Milstone DS. A major role for VCAM-1, but not ICAM-1, in early atherosclerosis. J Clin Invest 2001: 107: 1255–1262.
143. Akhtar AM, Schneider JE, Chapman SJ, Jefferson A, Digby JE, Mankia K, Chen Y, McAteer MA, Wood KJ, Choudhury RP. In vivo quantification of VCAM-1 expression in renal ischemia reperfusion injury using non-invasive magnetic resonance molecular imaging. PLoS One. 2010 Sep 21;5(9):e12800.
144. Hoyte LC, Brooks KJ, Nagel S, Akhtar A, Chen R, Mardiguian S, McAteer MA, Anthony DC, Choudhury RP, Buchan AM, Sibson NR. Molecular magnetic resonance imaging of acute vascular cell adhesion molecule-1 expression in a mouse model of cerebral ischemia. J Cereb Blood Flow Metab 2010: 30(6):1178-87.

145. Jamar F et al. Scintigraphy using a technetium 99m-labelled anti-E-selectin Fab fragment in rheumatoid arthritis. Rheumatol (Oxford) 2002;41: 53-61.

146. Bhatti M *et al*. Visualising E-selectin in the detection and evaluation of inflammatory bowel disease. *Gut* 1998: 43: 40–47.

147. Reynolds PR et al. Detection of vascular expression of e-selectin in vivo with MR Imaging. Radiology 2006: 241(2): 469-476.

148. Sukhova GK, Williams JK, Libby P. Statins reduce inflammation in atheroma of nonhuman primates independent of effects on serum cholesterol. *Arterioscler Thromb Vasc Biol* 2002: 22: 1452–1458.

149. Candido R *et al*. Irbesartan but not amlodipine suppresses diabetes associated atherosclerosis. *Circulation* 2004: 109: 1536 –1542.

150. North American Symptomatic Carotid Endarterectomy Trial (NASCET) Steering Committee. North American Symptomatic Carotid Endarterectomy Trial: methods, patient characteristics, and progress. Stroke. 1991; 22:711–720.

151. Stuart-Smith SE, Hughes DA, Bain BJ. Are routine iron stains on bone marrow trephine biopsy specimens necessary? J Clin Pathol. 2005; 58(3):269-72.

152. Jander S, Sitzer M, Schumann R, Schroeter M, Siebler M, Steinmetz H, Stoll G. Inflammation in high-grade carotid stenosis: a possible role for macrophages and T cells in plaque destabilization. Stroke. 1998;29(8):1625-30.

153. Nachtigal P, Jamborova G, Pospisilova N, Pospechova K, Solichova D, Zdansky P, Semecky V. Atorvastatin has distinct effects on endothelial markers in different mouse models of atherosclerosis. J Pharm Pharmaceut Sci. 2006;9(2):222-30.

154. Johnson-Tidey J, McGregor JL, Taylor PR, Poston RN. Increase in the adhesion molecule P-selectin in endothelium overlying atherosclerotic plaque. Am J Pathol. 1994;144:952–961.

155. O'Brien KD, McDonald TO, Chait AA, Allen MD, Alpers CE. Neovascular expression of E-selectin, intercellular adhesion molecule-1, and vascular cell adhesion molecule-1 in human atherosclerosis and their relation to intimal leukocyte content. Circulation. 1996;93:672– 682.

156. Nakashima Y, Raines EW, Plump AS, Breslow JL, Ross R. Upregulation of VCAM-1 and ICAM-1 at atherosclerosis-prone sites on the endothelium in the ApoE-deficient mouse.

Arterioscler Thromb Vasc Biol.1998;18:842–851.

157. Ramos CL, Huo Y, Jung U, Ghosh S, Manka DR, Sarembock IJ, Ley K. Direct demonstration of P-selectin- and VCAM-1-dependent mononuclear cell rolling in early atherosclerotic lesions of apolipoprotein E-deficient mice. Circ Res. 1999;84:1237–1244.

158. Huo Y, Hafezi-Moghadam A, Ley K. Role of vascular cell adhesion molecule-1 and fibronectin connecting segment-1 in monocyte rolling and adhesion on early atherosclerotic lesions. Circ Res. 2000;87:153–159.

159. May AE, Neumann FJ, Schomig A, Preissner KT. VLA-4 (alpha(4) beta(1)) engagement defines a novel activation pathway for beta(2) integrin-dependent leukocyte adhesion involving the urokinase receptor. Blood. 2000;96:506–513.

160. Wilchek M, and Bayer EA. Avidin-Biotin Technology. Methods Enzymology. 1990;184:746-784.

161. Baker, H. Assessment of Biotin Status: Clinical Implications. Ann. N. Y. Acad. Sci. 1985;447:129-132.

162. Hamblett KJ, Kegley BB, Hamlin DK, Chyan MK, Hyre DE, Press OW, Wilbur DS, Stayton PS. A streptavidin-biotin binding system that minimizes blocking by endogenous biotin. Bioconjug Chem. 2002;13(3):588-98.

163. Breslow JL. Transgenic mouse models of lipoprotein metabolism and atherosclerosis. Proc Natl Acad Sci USA 1993: 90: 8314-8318.

164. Knowles JW, Maeda N. Genetic modifiers of atherosclerosis in mice. Arterioscler Thromb Vasc Biol 2000: 20: 2336-2345.

165. de Winther MP, Hofker MH. New mouse models for lipoprotein metabolism and atherosclerosis. Curr Opin Lipidol 2002: 13: 191-197.

166. Mahley RW. Apolipoprotein E: cholesterol transport protein with expanding role in cell biology. Science. 1988: 240: 622-630.

167. Nakashima Y, Plump AS, Raines EW, Breslow JL, Ross R. ApoE- deficient mice develop lesions of all phases of atherosclerosis throughout the arterial tree. Arterioscler Thromb. 1994:14: 133-140.

168. Reddick RL, Zhang SH, Maeda N. Atherosclerosis in mice lacking ApoE: evaluation of lesional development and progression. Arterioscler Thromb. 1994: 14: 141-147.

169. Zhang SH, Reddick RL, Burkey B, Maeda N. Diet-induced atherosclerosis in mice heterozygous and homozygous for apolipoprotein E gene disruption. J Clin Invest. 1994: 94:937-945.

170. Merat S, Fruebis J, Sutphin M, Silvestre M, Reaven PD. Effect of aging on aortic expression of the vascular cell adhesion molecule-1 and atherosclerosis in murine models of atherosclerosis. J Gerontol A Biol Sci Med Sci. 2000: 55: B85–B94.

171. Ishibashi S, Goldstein JL, Brown MS, Herz J, Burns DK. Massive xanthomatosis and atherosclerosis in cholesterol-fed low density lipoprotein receptor-negative mice. J Clin Invest.1994: 93: 1885–1893.

172. Stary HC, Blankenhorn DH, Chandler AB, et al. A definition of the intima of human arteries and of its atherosclerosis-prone regions. A report from the Committee on Vascular Lesions of the Council on Arteriosclerosis, American Heart Association. Arterioscler Thromb 1992: 12: 120-134.

173. Stary HC, Blankenhorn DH, Chandler AB, et al. A definition of the intima of human arteries and of its atherosclerosis-prone regions. A report from the Committee on Vascular Lesions of the Council on Arteriosclerosis, American Heart Association. Circulation 1992: 85: 391-405.

174. Stary HC, Chandler AB, Dinsmore RE, et al. A definition of advanced types of atherosclerotic lesions and a histological classification of atherosclerosis. A report from the Committee on Vascular Lesions of the Council on Arteriosclerosis, American Heart Association. Arterioscler Thromb Vasc Biol 1995: 15: 1512-1531.

175. Stary HC, Chandler AB, Dinsmore RE, et al. A definition of advanced types of atherosclerotic lesions and a histological classification of atherosclerosis. A report from the Committee on Vascular Lesions of the Council on Arteriosclerosis, American Heart Association. Circulation 1995: 92: 1355-1374.

176. Whitman SC. A Practical Approach to Using Mice in Atherosclerosis Research. Clin Biochem Rev 2004: 25: 81-93.

177. Charoenphol P, Mocherla S, Bouis D, Namdee K, Pinsky DJ, Eniola-Adefeso O. Targeting therapeutics to the vascular wall in atherosclerosis-carrier size matters. Atherosclerosis 2011, 217:364–370.

178. Tom J.M. Molenaar, Jaap Twisk, Sonja A.M. de Haas, Niels Peterse, Bram J.C.P. Vogelaar, Steven H. van Leeuwen, Ingrid N. Michon, Theo J.C. van Berkel, Johan Kuiper, Erik A.L. Biessen. P-selectin as a candidate target in atherosclerosis. Biochemical Pharmacology 66 (2003) 859–866.

179. Zhao Ming Dong ; Allison A. Brown; Denisa D. Wagner. Prominent Role of P-Selectin in the Development of Advanced Atherosclerosis in ApoE-Deficient Mice. Circulation. 2000;101:2290-2295.

180. Nahrendorf M, Jaffer FA, Kelly KA, Sosnovik DE, Aikawa E, Libby P, Weissleder R. Noninvasive vascular cell adhesion molecule-1 imaging identifies inflammatory activation of cells in atherosclerosis. Circulation. 2006;114:1504–1511.

181. Paigen B, Morrow A, Holmes PA, Mitchell D, Williams RA. Quantitative assessment of atherosclerotic lesions in mice. Atherosclerosis.1987;68:231–240.

182. Will O, Purkayastha S, Chan C, Athanasiou T, Darzi AW, Gedroyc W, Tekkis PP. Diagnostic precision of nanoparticle-enhanced MRI for lymph-node metastases: a meta-analysis. Lancet Oncol. 2006;7:52–60.

183. Ruehm SG, Corot C, Vogt P, Kolb S, Debatin JF. Magnetic resonance imaging of atherosclerotic plaque with ultrasmall superparamagnetic particles of iron oxide in hyperlipidemic rabbits. Circulation. 2001;103:415–422.

184. Schmitz SA, Coupland SE, Gust R, Winterhalter S, Wagner S, Kresse M, Semmler W, Wolf KJ. Superparamagnetic iron oxide-enhanced MRI of atherosclerotic plaques in Watanabe hereditable hyperlipidemic rabbits. Invest Radiol. 2000;35:460–471.

185. Moreno PR, Falk E, Palacios IF, Newell JB, Fuster V, Fallon JT. Macrophage infiltration in acute coronary syndromes. Implications for plaque rupture. Circulation. 1994;90:775–778.

186. Moreno PR. Pathophysiology of plaque disruption and thrombosis in acute ischemic syndromes. J Stroke Cerebrovasc Dis. 2001;10(2 Pt 2):2–9.

187. Shah PK, Falk E, Badimon JJ, Fernandez-Ortiz A, Mailhac A, Villareal-Levy G, Fallon JT, Regnstrom J, Fuster V. Human monocyte-derived macrophages induce collagen breakdown in fibrous caps of atherosclerotic plaques. Potential role of matrix-degrading metalloproteinases and implications for plaque rupture. Circulation. 1995;92:1565–1569.

188. Aikawa M, Sugiyama S, Hill CC, Voglic SJ, Rabkin E, Fukumoto Y, Schoen FJ, Witztum

JL, Libby P. Lipid lowering reduces oxidative stress and endothelial cell activation in rabbit atheroma. Circulation. 2002;106:1390–1396.

189. Aikawa M, Rabkin E, Sugiyama S, Voglic SJ, Fukumoto Y, Furukawa Y, Shiomi M, Schoen FJ, Libby P. An HMG-CoA reductase inhibitor, cerivastatin, suppresses growth of macrophages expressing matrix metalloproteinases and tissue factor in vivo and in vitro. Circulation. 2001;103:276–283.

190. Ley K, Miller YI, Hedrick CC. Monocyte and macrophage dynamics during atherogenesis. Arterioscler Thromb Vasc Biol. 2011;31:1506–1516.

191. Sanz J, Fayad ZA. Imaging of atherosclerotic cardiovascular disease. Nature. 2008;451:953–957.

192. Dansky HM, Barlow CB, Lominska C, Sikes JL, Kao C, Weinsaft J, Cybulsky MI, Smith JD. Adhesion of monocytes to arterial endothelium and initiation of atherosclerosis are critically dependent on vascular cell adhesion molecule-1 gene dosage. Arterioscler Thromb Vasc Biol. 2001;21:1662–1667.

193. Trivedi RA, Mallawarachi C, U-King-Im JM, et al. Identifying inflamed carotid plaques using in vivo USPIO-enhanced MR imaging to label plaque macrophages. Arterioscler Thromb Vasc Biol 2006;26:1601–1606.

194. Tang, T. Y. et al. The ATHEROMA (Atorvastatin Therapy: Effects on Reduction of Macrophage Activity) Study. Evaluation using ultrasmall superparamagnetic iron oxide enhanced magnetic resonance imaging in carotid disease. J. Am. Coll. Cardiol. 53, 2039–2050 (2009).

195. Hyafil F, Laissy JP, Mazighi M, et al. Ferumoxtran-10-enhanced MRI of the hypercholesterolemic rabbit aorta: relationship between signal loss and macrophage infiltration. Arterioscler Thromb Vasc Biol 2006; 26:176–181.

196. Kooi ME, Cappendijk VC, Cleutjens KB, et al. Accumulation of ultrasmall superparamagnetic particles of iron oxide in human atherosclerotic plaques can be detected by in vivo magnetic resonance imaging. Circulation 2003;107:2453–2458.

197. Durand E, Raynaud JS, Bruneval P, et al. Magnetic resonance imaging of ruptured plaques in the rabbit with ultrasmall superparamagnetic particles of iron oxide. J Vasc Res 2007;44:119–128.

198. Monica Sigovan, Loic Boussel, Abdulrazzaq Sulaiman et al. Rapid-Clearance Iron Nanoparticles for Inflammation Imaging of Atherosclerotic Plaque: Initial Experience in Animal Model. Radiology 2009; 252: 401-409.

199. McAteer MA, Mankia K, Ruparelia N, Jefferson A, Nugent HB, Stork LA, Hagen R, Channon KM, Schneider JE, Choudhury RP. A leukocyte-mimetic magnetic resonance imaging contrast agent homes rapidly to activated endothelium and tracks with atherosclerotic lesion macrophage content. Arterioscler Thromb Vasc Biol. 2012; 32(6):1427-35.

200. Kaufmann BA, Carr CL, Belcik JT, Xie A, Yue Q, Chadderdon S, Caplan ES, Khangura J, Bullens S, Bunting S, Lindner JR. Molecular imaging of the initial inflammatory response in atherosclerosis: implications for early detection of disease. Arterioscler Thromb Vasc Biol. 2010;30:54–59.

201. Broisat A, Riou LM, Ardisson V, Boturyn D, Dumy P, Fagret D, Ghezzi C. Molecular imaging of vascular cell adhesion molecule-1 expression in experimental atherosclerotic plaques with radiolabelled B2702-p. Eur J Nucl Med Mol Imaging. 2007;34:830–840.

202. Deguchi J, Aikawa M, Tung CH, Aikawa E, Kim DE, Ntziachristos V, Weissleder R, Libby P. Inflammation in atherosclerosis: visualizing matrix metalloproteinase action in macrophages in vivo. Circulation. 2006;114:55– 62.

203. Sosnovik DE, Nahrendorf M, Deliolanis N, Novikov M, Aikawa E, Josephson L, Rosenzweig A, Weissleder R, Ntziachristos V. Fluorescence tomography and magnetic resonance imaging of myocardial macrophage infiltration in infarcted myocardium in vivo. Circulation. 2007; 115:1384 –1391.

204. Swirski FK, Pittet MJ, Kircher MF, Aikawa E, Jaffer FA, Libby P, Weissleder R. Monocyte accumulation in mouse atherogenesis is progressive and proportional to extent of disease. Proc Natl Acad Sci U S A. 2006;103:10340–10345.

205. Baigent C, Keech A, Kearney PM, Blackwell L, Buck G, Pollicino C, Kirby A, Sourjina T, Peto R, Collins R, Simes R. Efficacy and safety of cholesterol lowering treatment: prospective meta-analysis of data from 90,056 participants in 14 randomised trials of statins. Lancet. 2005;366:1267–1278.

206. Nissen SE, Nicholls SJ, Sipahi I, Libby P, Raichlen JS, Ballantyne CM, Davignon J, Erbel R, Fruchart JC, Tardif JC, Schoenhagen P, Crowe T, Cain V, Wolski K, Goormastic M, Tuzcu

EM. Effect of very high intensity statin therapy on regression of coronary atherosclerosis: the ASTEROID trial. JAMA. 2006;295:1556 –1565.

207. Aikawa M, Libby P. The vulnerable atherosclerotic plaque: pathogenesis and therapeutic approach. Cardiovasc Pathol. 2004;13:125–138.

208. Libby P, Aikawa M. Stabilization of atherosclerotic plaques: new mechanisms and clinical targets. Nat Med. 2002;8:1257–1262.

209. Aikawa M, Rabkin E, Okada Y, Voglic SJ, Clinton SK, Brinckerhoff CE, Sukhova GK, Libby P. Lipid lowering by diet reduces matrix metalloproteinase activity and increases collagen content of rabbit atheroma: a potential mechanism of lesion stabilization. Circulation. 1998;97:2433–2444.

210. Tang T, Howarth SP, Miller SR, Trivedi R, Graves MJ, King-Im JU, Li ZY, Brown AP, Kirkpatrick PJ, Gaunt ME, Gillard JH. Assessment of inflammatory burden contralateral to the symptomatic carotid stenosis using high-resolution ultrasmall, superparamagnetic iron oxide-enhanced MRI. Stroke. 2006 ;37(9):2266-70.

211. Chambon C, Clement O, Le Blanche A, Schouman-Claeys E, Frija G. Superparamagnetic iron oxides as positive MR contrast agents: in vitro and in vivo evidence. Magn Reson Imaging. 1993;11:509 –519.

212. Tahara N, Kai H, Ishibashi M, Nakaura H, Kaida H, Baba K, Hayabuchi N, Imaizumi T. Simvastatin attenuates plaque inflammation: evaluation by fluorodeoxyglucose positron emission tomography. J Am Coll Cardiol. 2006;48:1825–1831.

213. Folco EJ, Sheikine Y, Rocha VZ, Christen T, Shvartz E, Sukhova GK, Di Carli MF, Libby P. Hypoxia but not inflammation augments glucose uptake in human macrophages: implications for imaging atherosclerosis with 18fluorine-labeled 2-deoxy-D-glucose positron emission tomography. J Am Coll Cardiol. 2011;58:603–614.

214. Steinman DA, Image-based computational fluid dynamics: a new paradigm for monitoring haemodynamics and atherosclerosis, Curr Drug Targets Cardiovasc Haematol Disord. 2004;4:183-197.

215. Jolanda J. Wentzel, Yiannis S. Chatzizisis, Frank J.H. Gijsen, George D. Giannoglou, Charles L. Feldman, and Peter H. Stone. Endothelial shear stress in the evolution of coronary atherosclerotic plaque and vascular remodelling: current understanding and remaining

questions. Cardiovascular Research 2012;96:234–243.

216. Pedersen EM, Oyre S, Agerbaek M, Kristensen IB, Ringgaard S, Boesiger P, Paaske WP. Distribution of early atherosclerotic lesions in the human abdominal aorta correlates with wall shear stresses measured in vivo. Eur J Vasc Endovasc Surg. 1999;18:328 –333.

217. Wentzel JJ, Kloet J, Andhyiswara I, Oomen JA, Schuurbiers JC, de Smet BJ, Post MJ, de Kleijn D, Pasterkamp G, Borst C, Slager CJ, Krams R. Shear-stress and wall-stress regulation of vascular remodeling after balloon angioplasty: effect of matrix metalloproteinase inhibition. Circulation. 2001;104:91–96.

218. Davies PF, Polacek DC, Shi C, Helmke BP. The convergence of haemodynamics, genomics, and endothelial structure in studies of the focal origin of atherosclerosis. Biorheology. 2002;39:299 –306.

219. Buchanan JR Jr, Kleinstreuer C, Truskey GA, Lei M. Relation between non-uniform hemodynamics and sites of altered permeability and lesion growth at the rabbit aorto-celiac junction. Atherosclerosis.1999;143:27– 40.

220. Stone PH, Coskun AU, Kinlay S, Clark ME, Sonka M, Wahle A, Ilegbusi OJ, Yeghiazarians Y, Popma JJ, Orav J, Kuntz RE, Feldman CL. Effect of endothelial shear stress on the progression of coronary artery disease, vascular remodeling, and in-stent restenosis in humans: in vivo 6-month follow-up study. Circulation. 2003;108:438 – 444.

221. Shyy JY, Chien S. Role of integrins in endothelial mechano-sensing of shear stress. Circ Res. 2002;91:769-775.

222. Ohura N, Yamamoto K, Ichioka S, et al. Global analysis of shear stress-responsive genes in vascular endothelial cells. J Atheroscler Thromb. 2003;10:304-313.

223. Cheng C, van Haperen R, de Waard M, van Damme LC, Tempel D, Hanemaaijer L, van Cappellen GW, Bos J, Slager CJ, Duncker DJ, van der Steen AF, de Crom R, Krams R. Shear stress affects the intracellular distribution of eNOS: direct demonstration by a novel in vivo technique. Blood. 2005;106(12):3691-8.

224. Cheng C, Tempel D, van Haperen R, van der Baan A, Grosveld F, Daemen MJ, Krams R, de Crom R. Atherosclerotic lesion size and vulnerability are determined by patterns of fluid shear stress. Circulation. 2006;113(23):2744-53.

225. Kuhlmann MT, Cuhlmann S, Hoppe I, Krams R, Evans PC, Strijkers GJ, Nicolay K,

Hermann S, Schäfers M. Implantation of a carotid cuff for triggering shear-stress induced atherosclerosis in mice. J Vis Exp. 2012 Jan 13;(59):e3308.

226. Cheng C, Helderman F, Tempel D, Segers D, Hierck B, Poelmann R et al. Large variations in absolute wall shear stress levels within one species and between species. Atherosclerosis 2007;195:225–235.

227. Lardenoye JH, Delsing DJ, de Vries MR, Deckers MM, Princen HM, Havekes LM, van Hinsbergh VW, van Bockel JH, Quax PH. Accelerated atherosclerosis by placement of a perivascular cuff and a cholesterol-rich diet in ApoE*3Leiden transgenic mice. Circ Res. 2000;87:248 –253.

228. Traub O, Berk BC. Laminar shear stress: mechanisms by which endothelial cells transduce an atheroprotective force. Arterioscler Thromb Vasc Biol. 1998;18:677– 685.

229. Gimbrone MA Jr, Topper JN, Nagel T, Anderson KR, Garcia-Cardena G. Endothelial dysfunction, hemodynamic forces, and atherogenesis. Ann N Y Acad Sci. 2000;902:230 –239; discussion 239 –240.

230. Cunningham KS, Gotlieb AI. The role of shear stress in the pathogenesis of atherosclerosis. Lab Invest. 2005;85:9 –23.

231. Chatzizisis YS, Coskun AU, Jonas M, Edelman ER, Feldman CL, Stone PH. Role of endothelial shear stress in the natural history of coronary atherosclerosis and vascular remodeling: molecular, cellular, and vascular behavior. J Am Coll Cardiol 2007;49:2379–2393.

232. Tzima E, Irani-Tehrani M, Kiosses WB, et al. A mechanosensory complex that mediates the endothelial cell response to fluid shear stress. Nature 2005;437:426–31.

233. Cunningham KS, Gotlieb AI. The role of shear stress in the pathogenesis of atherosclerosis. Lab Invest 2005;85:9–23.

234. Dai G, Kaazempur-Mofrad MR, Natarajan S, et al. Distinct endothelial phenotypes evoked by arterial waveforms derived from atherosclerosis-susceptible and -resistant regions of human vasculature. Proc Natl Acad Sci U S A 2004;101:14871–6.

235. Yamawaki H, Lehoux S, Berk BC. Chronic physiological shear stress inhibits tumor necrosis factor-induced proinflammatory responses in rabbit aorta perfused ex vivo. Circulation 2003;108:1619–25.

236. Sheikh S, Rainger GE, Gale Z, Rahman M, Nash GB. Exposure to fluid shear stress

modulates the ability of endothelial cells to recruit neutrophils in response to tumor necrosis factor-alpha: a basis for local variations in vascular sensitivity to inflammation. Blood 2003;102:2828–34.

237. Sheikh S, Rahman M, Gale Z, et al. Differing mechanisms of leukocyte recruitment and sensitivity to conditioning by shear stress for endothelial cells treated with tumour necrosis factor-alpha or interleukin-1beta. Br J Pharmacol 2005;145:1052–61.

238. Chiu JJ, Lee PL, Chen CN, et al. Shear stress increases ICAM-1 and decreases VCAM-1 and E-selectin expressions induced by tumor necrosis factor-[alpha] in endothelial cells. Arterioscler Thromb Vasc Biol 2004;24:73–9.

239. Surapisitchat J, Hoefen RJ, Pi X, Yoshizumi M, Yan C, Berk BC. Fluid shear stress inhibits TNF-alpha activation of JNK but not ERK1/2 or p38 in human umbilical vein endothelial cells: inhibitory crosstalk among MAPK family members. Proc Natl Acad Sci U S A 2001;98:6476–81.

240. Partridge J, Carlsen H, Enesa K, et al. Laminar shear stress acts as a switch to regulate divergent functions of NF-kappaB in endothelial cells. FASEB J 2007;21:3553–61.

241. Virmani R, Kolodgie FD, Burke AP, Farb A, Schwartz SM. Lessons from sudden coronary death: a comprehensive morphological classification scheme for atherosclerotic lesions. Arterioscler Thromb Vasc Biol. 2000;20:1262–1275.

242. Lutgens E, van Suylen RJ, Faber BC, Gijbels MJ, Eurlings PM, Bijnens AP, Cleutjens KB, Heeneman S, Daemen MJ. Atherosclerotic plaque rupture: local or systemic process? Arterioscler Thromb Vasc Biol. 2003;23:2123–2130.

243. Chatzizisis YS, Coskun AU, Jonas M, Edelman ER, Stone PH, Feldman CL. Risk stratification of individual coronary lesions using local endothelial shear stress: a new paradigm for managing coronary artery disease. Curr Opin Cardiol 2007;22:552–564.

244. Traub O, Berk BC. Laminar shear stress: mechanisms by which endothelial cells transduce an atheroprotective force. Arterioscler Thromb Vasc Biol 1998;18:677–685.

245. Slager CJ, Wentzel JJ, Gijsen FJ, Schuurbiers JC, van der Wal AC, van der Steen AF et al. The role of shear stress in the generation of rupture-prone vulnerable plaques. Nat Clin Pract Cardiovasc Med 2005;2:401–407.

246. Li YS, Haga JH, Chien S. Molecular basis of the effects of shear stress on vascular

endothelial cells. J Biomech 2005;38:1949–1971.

247. Gimbrone MA Jr, Topper JN, Nagel T, Anderson KR, Garcia-Cardena G. Endothelial dysfunction, hemodynamic forces, and atherogenesis. Ann N Y Acad Sci 2000;902:230–239; discussion 239–240.

248. Brooks AR, Lelkes PI, Rubanyi GM. Gene expression profiling of human aortic endothelial cells exposed to disturbed flow and steady laminar flow. Physiol Genomics 2002;9:27–41.

249. Dai G, Kaazempur-Mofrad MR, Natarajan S, Zhang Y, Vaughn S, Blackman BR et al. Distinct endothelial phenotypes evoked by arterial waveforms derived from atherosclerosis-susceptible and -resistant regions of human vasculature. Proc Natl Acad Sci USA 2004;101:14871–14876.

250. Morigi M, Zoja C, Figliuzzi M, Foppolo M, Micheletti G, Bontempelli M, Saronni M, Remuzzi G, Remuzzi A. Fluid shear stress modulates surface expression of adhesion molecules by endothelial cells. Blood.1995;85:1696 –1703.

251. Chappell DC, Varner SE, Nerem RM, Medford RM, Alexander RW. Oscillatory shear stress stimulates adhesion molecule expression in cultured human endothelium. Circ Res. 1998;82:532–539.

252. Mohan S, Mohan N, Valente AJ, Sprague EA. Regulation of low shear flow-induced HAEC VCAM-1 expression and monocyte adhesion. Am J Physiol. 1999;276:C1100 –C1107.

253. Chatzizisis YS, Baker AB, Sukhova GK, Koskinas KC, Papafaklis MI, Beigel R et al. Augmented expression and activity of extracellular matrix-degrading enzymes in regions of low endothelial shear stress colocalize with coronary atheromata with thin fibrous caps in pigs. Circulation 2011;123:621–630.

254. Gambillara V, Montorzi G, Haziza-Pigeon C, Stergiopulos N, Silacci P. Arterial wall response to ex vivo exposure to oscillatory shear stress. J Vasc Res 2005;42:535–544.

255. Platt MO, Ankeny RF, Jo H. Laminar shear stress inhibits cathepsin L activity in endothelial cells. Arterioscler Thromb Vasc Biol 2006;26:1784–1790.

256. Platt MO, Ankeny RF, Shi GP, Weiss D, Vega JD, Taylor WR et al. Expression of cathepsin K is regulated by shear stress in cultured endothelial cells and is increased in endothelium in human atherosclerosis. Am J Physiol Heart Circ Physiol 2007;292:H1479–

H1486.

257. Chatzizisis YS, Jonas M, Coskun AU, Beigel R, Stone BV, Maynard C et al. Prediction of the localization of high-risk coronary atherosclerotic plaques on the basis of low endothelial shear stress: an intravascular ultrasound and histopathology natural history study. Circulation 2008;117:993–1002.

258. Koskinas KC, Feldman CL, Chatzizisis YS, Coskun AU, Jonas M, Maynard C et al. Natural history of experimental coronary atherosclerosis and vascular remodeling in relation to endothelial shear stress: a serial, in vivo intravascular ultrasound study. Circulation 2010;121:2092–2101.

259. Sipahi I, Tuzcu EM, Schoenhagen P, Nicholls SJ, Crowe T, Kapadia S et al. Static and serial assessments of coronary arterial remodeling are discordant: an intravascular ultrasound analysis from the Reversal of Atherosclerosis with Aggressive Lipid Lowering (REVERSAL) trial. Am Heart J 2006;152:544–550.

260. van Bochove GS, Straathof R, Krams R, Nicolay K, Strijkers GJ. MRI-determined carotid artery flow velocities and wall shear stress in a mouse model of vulnerable and stable atherosclerotic plaque. MAGMA. 2010;23(2):77-84.

261. Raschzok N, Muecke DA, Adonopoulou MK, Billecke N, Werner W, Kammer NN, Zielinski A, Behringer PA, Ringel F, Huang MD, et al. In vitro evaluation of magnetic resonance imaging contrast agents for labeling human liver cells: implications for clinical translation. Mol Imaging Biol 2011, 13:613–622.

262. Nkansah MK, Thakral D, Shapiro EM. Magnetic poly(lactide-co-glycolide) and cellulose particles for MRI-based cell tracking. Magn Reson Med 2011, 65: 1776–1785.

263. Perez-Balderas F, Davis BG, van Kasteren SI, Khrapichev A, Jefferson A, Bristow C, Serres S, Choudhury RP, Anthony DC, Sibson NR. New biodegradable multimeric MPIO contrast agent shows rapid in vitro and in vivo degradation and high sensitivity contrast. Proc Int Soc Magn Reson 2011, 19:1689.

264. Pharmaceutical Research and Manufacturers of America *Profile 2009*. Washington, DC: PhRMA

265. Derby B. Printing and Prototyping of Tissues and Scaffolds. Science 16 November 2012; 338(6109): 921-926.

266. Chang R, Nam J, Sun W. Direct cell writing of 3D microorgan for in vitro pharmacokinetic model. Tissue Eng Part C Methods. 2008; 14(2): 157-66.

267. Coatney S, Gandhi B, Park B S, Dzilno D, Tapia E M, Kamarthy G, Sidhu I. 3D bio-printing. Insights in Engineering Leadership White Paper, College of Engineering, University of California, Berkeley, 2013. Fung Institute for Engineering Leadership, Fung Technical Report No. 2013.04.17. Retrieved from http://www.funginstitute.berkeley.edu/sites/default/files/3D_Bio-Printing.pdf

# APPENDIX A

## Methodology of *In Vitro* Cell Culture Stage

The experimental design consisted of detection and characterisation of inflammatory markers (i.e. E-selectin and VCAM-1) on bovine aortic endothelial cells (bAEC) treated with TNFα. This was achieved by using immunocytochemistry, fluorescence and MRI using antibody-conjugated SPIO.

## A1 Growth Media and Cell Culture

### General Considerations

All cell experiments were performed under sterile conditions in a laminar flow hood (Class 2 Microbiological Safety Cabinet, Walker, UK) where practicably possible. The incubator used throughout was a Galaxy R $CO_2$ Incubator (Scientific Laboratory Supplies, Bucks, UK). Temperature was maintained at 37°C and $CO_2$ concentration at 5%.

### Growth Media

bAEC (Lonza Wokingham Ltd., UK) were seeded in an endothelial cell medium consisting of Dulbecco's Modified Eagle Medium (DMEM) containing 4500mg/L glucose, L-glutamine and pyruvate (Gibco BRL, UK), supplemented with 25µg/ml of gentamicin (Gibco BRL, UK), 2mM glutamine, 5% of fetal calf serum (FCS, Labtech International, Sussex, UK) 1µg/ml of hydrocortisone, 10 units of heparin, 10ng/ml of recombinant human epidermal growth factor (EGF) (PeproTech Ltd, London, UK) and 3ng/ml of recombinant human fibroblast growth factor (FGF)-basic (PeproTech Ltd, London, UK).

**Cell Culture**

bAEC were grown on poly-L-Lysine (PLL, 13µg/ml, Sigma®) coated flasks in endothelial cell medium and maintained at 37°C/ 5% $CO_2$ in an incubator throughout. This medium was changed every other day until the cells were 80% confluent, at which time they were either harvested and used for experiments or sub-cultured for further cultivation.

To sub-culture the cells, the first step was to free the cells from their adherence to the flask and bring them into a suspension by trypsinisation. The endothelial cell medium was removed and the flask was rinsed with phosphate buffered saline (PBS 1X, Gibco BRL, UK) to remove any residual medium as it contained endogenous trypsin inhibitors. After the initial washing step, 1ml of 0.05% trypsin supplemented with 4ml of ethylenediaminetetra acetic acid (EDTA) (0.5µmol/l), was used to free the cells from the flask. It is important to note that prolonged exposure to trypsin may cause cell damage and prevent cells from adhering to subsequent flasks. The flask was gently shaken to ensure the cells were in contact with the solution, which was then swiftly removed. In order to dislodge the attached cells, the flask was tapped gently. This process was observed under a microscope (x20 magnification). Once dislodged, 5ml culture medium was added to collect the cells and the suspended cells were transferred to a 15ml Falcon tube and centrifuged at 1800rpm for 3 minutes in a Rotina 35R Centrifuge (Hettich, Germany).

The resulting tight cell pellet was re-suspended in 2ml of endothelial cell medium and was then dispersed equally into two PLL coated 75cm$^2$ flasks, each containing 10ml of endothelial cell medium, ready for the bAEC to start growing again. The flasks were coated beforehand with PLL to assist the bAECs adherence to the new flasks. 5ml of PLL was added to the flask, which was placed in a 37°C / 5% $CO_2$ incubator for two hours. The PLL was removed and the flask was washed with PBS (1X) followed by endothelial cell medium prior to addition of the bAECs in their medium in the sub-culturing process. Therefore from each 75cm$^2$ flask of bAEC, two new flasks of cells were produced.

## A2 Induction of Inflammation on Endothelial Cells

## Plating and Growing Cells on Coverslips

1000 to 2000 bAEC were plated in a twenty-four well plate on sterile glass coverslips pre-coated with PLL as described above. It is important to note that the plating process would activate the endothelial cells by mechanical stimulation. Therefore, before inducing inflammation by TNFα, the cells were incubated at 37°C for 48 hours, allowing them to become 'silent'.

**Endothelial Cells induced inflammation by TNFα**

Inflammation was induced on bAEC by using recombinant rat TNFα (PeproTech Ltd., London, UK) at the following concentrations: 0.1ng/ml, 1ng/ml, 10ng/ml and 50ng/ml and at different incubation periods (4 hours, 24

hours and 48 hours). bAEC without any TNFα added were used as control cells. An illustration of the whole experimental layout is given on Figure A1.

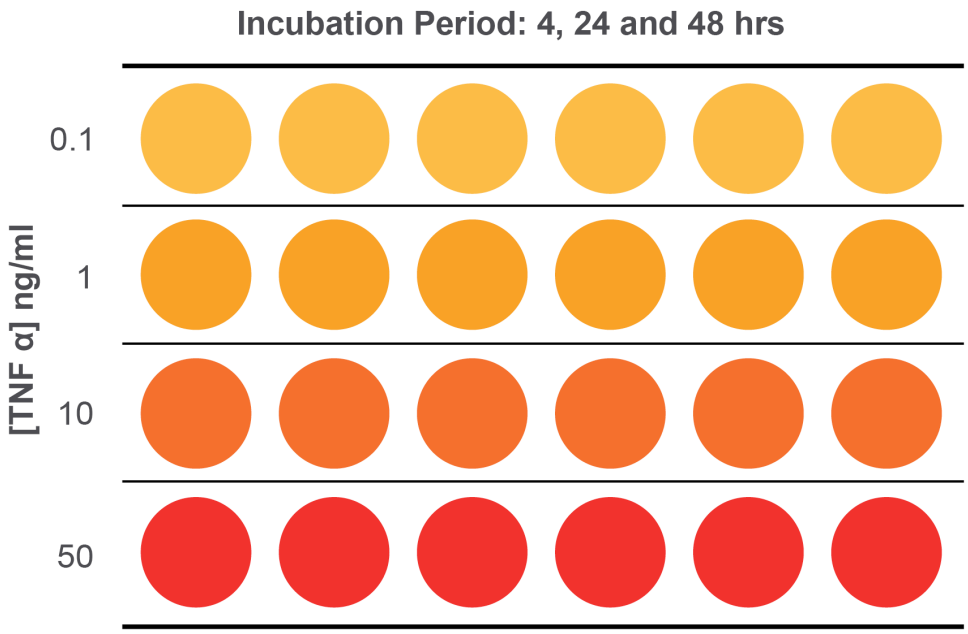



**Fig. A1. bAEC induced inflammation by TNFα of different concentrations (0.1ng/ml, 1ng/ml, 10ng/ml and 50ng/ml) with different incubation period (4 hours, 24 hours and 48 hours).** bAEC without any TNFα added were used as control cells.

## A3 Detection and Characterisation of Endothelial and Inflammatory Markers on bAEC by Immunocytochemistry

Endothelial markers such as the Von Willebrand Factor (vWF), vascular endothelial cadherin (VE cadherin), and inflammatory markers such as E-selectin and VCAM-1 were detected on bAEC by immunocytochemitry. Immunocytochemistry is a detection technique that is used to target specific receptors or markers in cells. This technique is based on an antibody-antigen coupling reaction. Two types of antibodies are used: the first unlabelled

antibody is specific for the expressed marker. The secondary antibody is usually fluorescently labelled and reacts with the primary antibody. Note that the secondary antibody must be against the immunoglobulin (Ig) epitope of the animal species in which the primary antibody has been raised.

Specific endothelial markers were detected using the goat anti-vWF and the goat anti-VE cadherin primary antibodies (Santa Cruz Biotechnology, CA, US) at a 1:200 dilution. Inflammation markers were detected by the goat anti-E-selectin and goat anti-VCAM-1 primary antibodies (Santa Cruz Biotechnology, CA, US) at a 1:200 dilution. The secondary antibody used was a rabbit anti-goat antibody, coupled to fluorescein isothiocyanate (FITC) which was a fluorescent marker with an emission wavelength of 518nm. Hence, this technique will allow the detection of inflammatory markers E-selectin and VCAM-1 and endothelial markers by fluorescence microscopy. The overview of detection and characterisation of inflammatory markers E-selectin and VCAM-1 on bAEC by immunocytochemistry is illustrated in Figure A2.

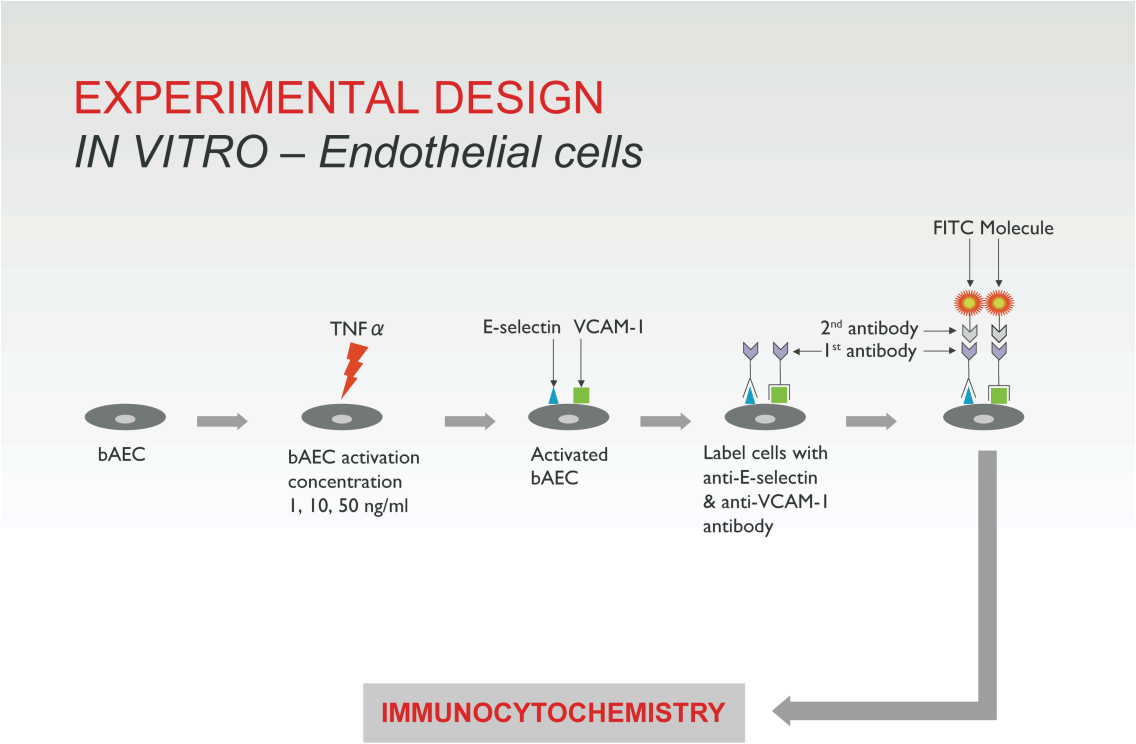



**Fig. A2. Detection and characterisation of E-selectin and VCAM-1 on activated endothelial cells by immunocytochemistry.**

After induction of inflammation, the TNFα was removed and each well was rinsed with PBS (1X). 50µl of 4% paraformaldehyde at 4°C (Sigma®) was added to each well to fix the cells. The twenty-four-well plate was then placed on the ice at 4°C for 20 minutes. The paraformaldehyde was removed and each well was washed three times with PBS (1X). 500µl of 10% rabbit serum was added to each well and the cells were then left at room temperature for 20 minutes. This allowed blocking of the non-specific sites on the endothelial cells.

Following the blocking step, the primary antibodies were added in the twenty-four-well plate as illustrated in Figure A3. The cells were incubated with the primary antibody overnight at 4°C in a humidified chamber.

**24-Well Plates for incubation of 4, 24 and 48 hrs**
**No TNFα is added to the control plate.**

| [TNF α] ng/ml | | | | | | |
|---|---|---|---|---|---|---|
| 0.1 | VWF | VECad | E-Selectin | E-Selectin | VCAM-1 | VCAM-1 |
| 1 | VWF | VECad | E-Selectin | E-Selectin | VCAM-1 | VCAM-1 |
| 10 | VWF | VECad | E-Selectin | E-Selectin | VCAM-1 | VCAM-1 |
| 50 | VWF | VECad | E-Selectin | E-Selectin | VCAM-1 | VCAM-1 |

**Fig. A3. Primary antibodies added to activated cells with different incubation periods with TNFα.** The anti-vWF antibodies and anti-VE Cadherin antibodies were used to characterise the specific markers on the endothelial cells, whilst the anti-E-selectin and anti-VCAM antibodies to characterise the inflammatory markers on the activated endothelial cells.

The coverslips were washed three times with PBS (1X) to remove any unbound primary antibodies. Then the secondary FITC conjugated anti-goat polyclonal IgG (dilution 1:200, Autogen Bioclear UK Ltd., Wilts, UK) antibody was added. The cells were incubated at room temperature for 4 hours in the humidified chamber, in the dark, to prevent photobleaching of the FITC label.

**DAPI staining**

4',6-diamidino-2-phenylindole (DAPI) is a fluorescent dye that has an emission fluorescence wavelength of 461 nm when bound to DNA. It is used to stain the nuclei of cells and appears blue in fluorescence microscopy. To allow the stain to enter the cell, the plasma cell membrane needs to be permeabilised beforehand.

The cells were washed three times with PBS (1X) to remove any unbound secondary antibodies and permeabilised with a 0.1% nonionic surfactant (Triton X-100 -Sigma®) for 1 minute at room temperature. Cells were washed in PBS 1X and nuclei were stained using 5% DAPI diluted in PBS (1X) for 30 minutes at room temperature in the dark. The coverslips were rinsed in PBS (1X) and ready to be mounted on slides.

**Preparation of Slides for Microscopy**

VECTASHIELD® mounting medium (Peterborough Vector Laboratories, UK,) was used for fluorescence microscopy. It prevents rapid loss of fluorescence during microscopic examination and retains anti-fading ability during long-term storage. One tiny drop of VECTASHIELD® mounting medium was dispensed onto each slide and coverslips were applied on the VECTASHIELD® mounting medium. The medium was allowed to disperse over the entire coverslip. Coverslips were then sealed on the slide with nail polish. The mounted slides were then used for microscopy (Leica DMIRE2 inverted microscope, Leica Microsystems Limited, UK). Mounted slides were stored at 4ºC in a dark room until further use.

## A4 Detection, Characterisation and Imaging of Inflammatory Markers on bAEC by Antibody-conjugated SPIO

The final phase of the *in vitro* work involved detection and characterisation of E-selectin on activated bAEC by antibody-conjugated SPIO as illustrated in Figure A4. In this phase, the cell culturing technique was the same as that described in section A1. The procedure of inducing inflammation on endothelial cells was similar to that described in section A2. The principles of detection and characterisation of inflammatory markers by antibody-conjugated SPIO were similar to that described in section A3.

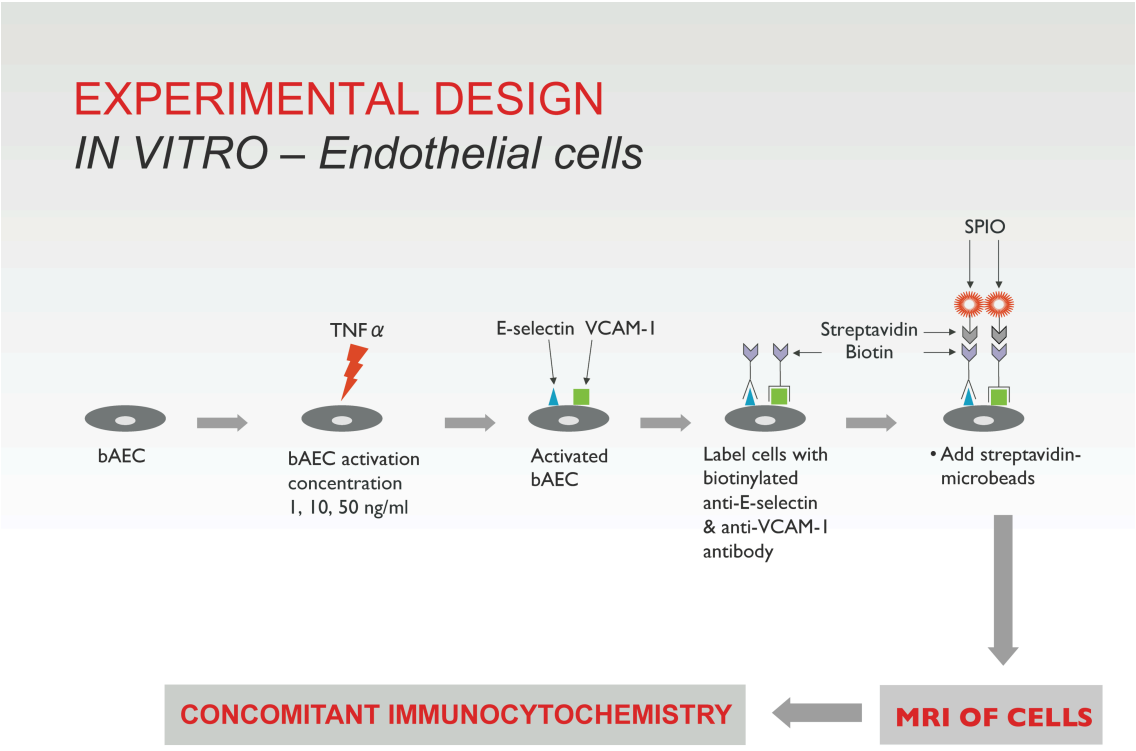



**Fig. A4. Detection and characterisation of E-selectin and VCAM-1 on activated endothelial cells by antibody-conjugated SPIO.**

**The Biotin-Avidin System**

Biotin is a vitamin B7 complex molecule and is often conjugated to a molecule or protein, for example, an antibody. This process is known as biotinylation.* In this experiment, biotinylated anti-E-selectin mouse monoclonal IgG (Vector Laboratories, Burlingame, USA) was used. Avidin is an egg-white derived glycoprotein which can bind up to four molecules of biotin simultaneously with a high degree of affinity and specificity.* Streptavidin is similar in properties to avidin but has a lower affinity for biotin.* Streptavidin microbeads (Miltenyi Biotec Ltd, Surrey, UK) used in this experiment are the magnetic beads (Iron oxide particles) conjugated to streptavidin. The E-selectin expressed on the activated bAEC can be detected by the biotinylated anti-E-selectin antibodies which are in turn bound to the high-affinity streptavidin microbeads. Therefore, these streptavidin microbeads can be used for magnetic labelling of the activated endothelial cells, thereby making these cells become 'MR visible'.

* *Diamandis EP, Christopoulos TK. The biotin-(strept)avidin system: principles and applications in biotechnology. Clin Chem 1991: 37(5): 625-636.*

**Activated Endothelial Cells Labelled with Biotinylated Anti-E-selectin Antibody**

bAEC were incubated with TNFα with different concentrations (1ng/ml, 10ng/ml and 50ng/ml) for 4 hours. 4 hours of incubation period was chosen because the optimal level of E-selectin expression had been achieved in the previous immunocytochemistry experiment in section A3.

Two negative controls were prepared:

*Control 1:* Unactivated cells only (cells without any TNFα _treatment)

*Control 2:* Unactivated cells with subsequent addition of biotinylated antibodies and streptavidin microbeads to assess any non-specific binding by the antibodies and non-specific labelling by the microbeads.

With trypsin and EDTA, a suspension of activated cells was prepared in the same way as described in section A1. This cell suspension was transferred to a 15ml Falcon tube and was washed twice by centrifugation at 1800rpm for 3 minutes.

The cells were then re-suspended and labelled at room temperature for 20 minutes with the biotinylated anti-E-selectin mouse monoclonal IgG (Vector Laboratories, Burlingame, USA) at a concentration of 10μg/ml diluted in 10% rabbit serum for labelling $10^6$ cells. Concomitant immunocytochemistry was performed as described in section A3 to correlate MRI data.

**Activated Endothelial Cells Labelled with Streptavidin Microbeads**

Following incubation, the cells were washed twice to remove unbound biotinylated antibodies with 2ml of labelling buffer composed of PBS (X1), supplemented with 2mM EDTA, and centrifuged at 1800rpm for 5 minutes. The buffer was kept at 4°C throughout the experiment to prevent capping of antibodies on the cell surface and non-specific cell labelling. The endothelial cell pellet was re-suspended and homogenised in 90μl of labelling buffer per $10^6$ cells and 10μl of streptavidin microbeads (Miltenyi Biotec Ltd, Surrey, UK)

per $10^6$ cells. The streptavidin microbeads were added to the three tubes of cells stimulated by TNFα of different concentrations (i.e. 1ng/ml, 10ng/ml, 50ng/ml). The cells were then incubated at 4°C for 15 minutes and washed to remove unbound streptavidin microbeads. The cells were re-suspended in 50µl of PBS for cell phantom MRI.

**Cell Phantom MRI**

A solution of 2% agarose (Sigma®, UK) in distilled water was prepared at 37°C and transferred into a bijou tube which was filled up to 80%. Seven empty eppendorf tubes held by a piece of parafilm were marked and placed in the agarose solution as illustrated in Figure A5. The parafilm was mounted onto the bijou tube to keep the eppendorf tubes in steady position in the agarose solution. The bijou tube was placed on ice for 4 hours to allow the agarose to solidify. Once the agarose settled, the parafilm was carefully removed. The seven empty eppendorf tubes were now securely placed in the agarose block.

50µl of 2% agarose solution was added to the 50µl of cell suspension prepared previously and was homogenised. This 100µl of new cell suspension was then transferred to the eppendorf tube. Three tubes contained the cells stimulated by TNFα of different concentrations (1ng/ml, 10ng/ml and 50ng/ml). The other two tubes contained the two negative controls. The remaining two eppendorf tubes were filled with 50µl of PBS and 50µl of streptavidin microbeads, each mixed with 50µl of 2% agarose solution, as controls as shown on Figure A5. The whole agarose block was placed in ice for 15

minutes to allow the agarose cell suspension within the eppendorf tubes to solidify.

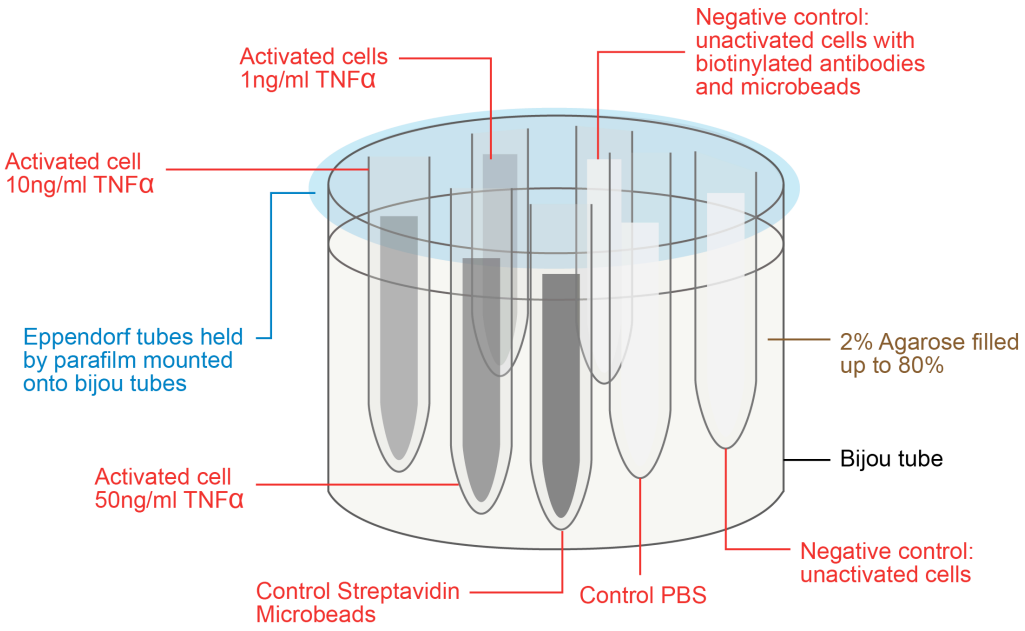



**Fig. A5. Cell phantom.** Seven samples were prepared. They are the activated cells stimulated by TNFα of different concentration (1ng/ml, 10ng/ml and 50ng/ml). The controls are unactivated cells with biotinylated antibodies and microbeads added as negative control, unactivated cells as negative contol, PBS and streptavidin microbeads.

The cell phantom MRI was performed using a 9.4 Tesla, horizontal bore scanner (Varian, Palo Alto, CA, USA). The sample was placed in a birdcage coil. T2 spin echo sequence was used with the following parameters: TR: 3500 msec; TE: 40 msec; FOV 40x40 mm; Matrix 256x256; Average: 40; Thickness 0.5mm; Number of slices: 30; plane: axial; Flip angle: 90°.

The MR images were analysed by Image J software (National Institutes of Health, http://rsb.info.nih.gov/ij/index.html). In each slice of image, both the signal in each sample and the background noise were measured and the

signal to noise ratio for each sample was calculated to allow comparison amongst the samples. The same quantification procedure was repeated in five consecutive slices of image. The average of the five signal to noise ratios in each sample was then calculated.

# APPENDIX B

## MRI of Cell Phantom

Bovine aortic endothelial cells (bAEC) were incubated with TNFα with different concentrations (1ng/ml, 10ng/ml and 50ng/ml) for 4 hours. Two negative controls were prepared. They were the unactivated bAEC only (cells without any TNFα treatment) and the unactivated bAEC with subsequent addition of biotinylated antibodies and streptavidin microbeads to assess any non-specific binding by the antibodies and non-specific labelling by the microbeads. The other two controls were the PBS, which was a vehicle solution in the experiment, and the streptavidin microbeads. The transaxial view of cell phantom MRI is illustrated in Figure 2.4 in Section 2.3.2.

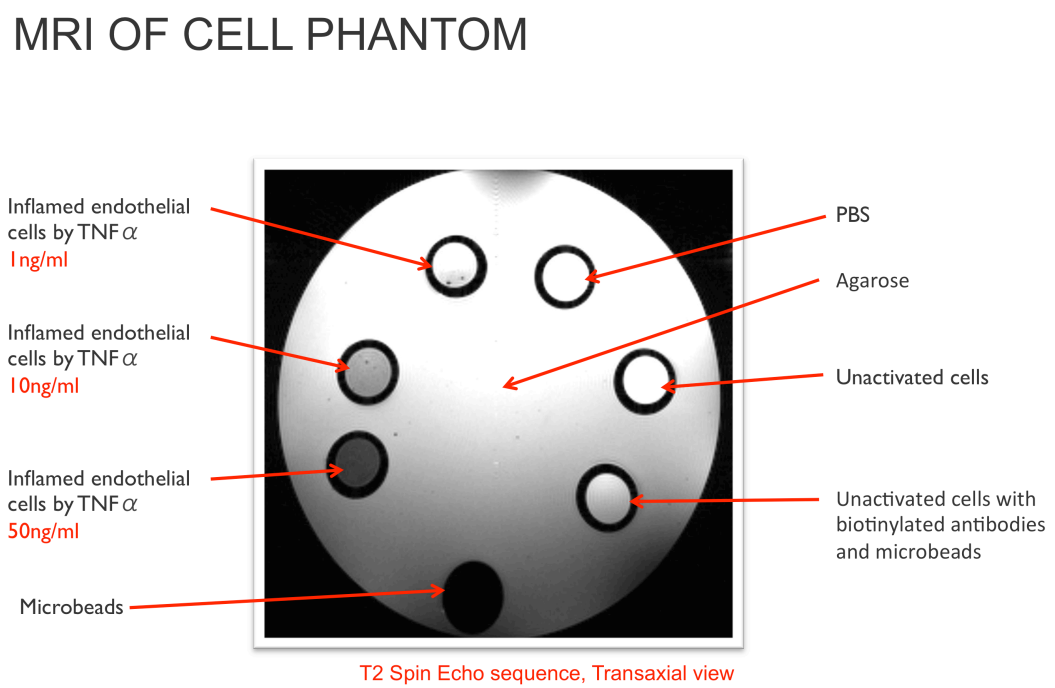



**Fig. 2.4 The transaxial view of MR image of cell phantom.** The streptavidin microbeads, positive control, were detected as signal void on the MR image using T2 spin echo sequence, and appeared to be the darkest amongst all the samples. The activated bAEC stimulated by higher concentration of TNFα were observed to produce greater signal void, and appeared darker on the MR image. The bAEC stimulated by 50ng/ml TNFα were observed to be the darkest amongst the three concentrations used, followed by 10ng/ml, and finally the least with 1ng/ml TNFα. By contrast, the negative controls: 1) PBS, 2) unactivated bAEC, and 3) unactivated bAEC added with biotinylated antibodies and microbeads were observed to produce minimal signal void, and appeared to be bright on the MR image.

In Figure 2.4, the streptavidin microbeads (iron oxide particles) were detected as signal void in T2 spin echo sequence by MRI. Therefore, the largest signal void (i.e. darkest) was seen in the microbeads control. It was observed that the activated cells stimulated by higher concentration of TNFα produced greater signal void and appeared darker in the MRI. The bAEC stimulated by 50ng/ml of TNFα appeared as dark grey colour, which was the darkest signal amongst the three concentrations used. This was followed by bAEC stimulated by 10ng/ml TNFα which appeared as grey colour in Figure 2.4. The bAEC stimulated by 1ng/ml TNFα appeared as light grey and produced the least signal void. Regarding the controls, both the PBS and the unactivated bAEC were observed to be the brightest and produced the least signal void amongst all the samples in this cell phantom MRI. The unactivated bAEC added with biotinylated antibodies and microbeads appeared to have a tinge of grey colour and had minimal amount of signal void.

In summary, it was observed that the activated bAEC stimulated by higher concentration of TNFα produced greater signal void and appeared darker in the MRI. The levels of E-selectin and VCAM-1 expression were observed to behave in TNFα dose-dependent fashion. The higher concentration of TNFα used to activate the cells, the greater extent of E-selectin and VCAM-1 expression observed in the immunocytochemistry (see Figure 2.3 in Section 2.3.1). Therefore, greater amount of streptavidin microbeads were bound to the biotinylated anti-E-selectin and anti-VCAM-1 antibodies. Hence, greater

signal loss detected by MRI and as a result, appeared to be darker in bAEC activated by higher concentration of TNFα.

## Signal to Noise Ratio of MRI of Cells

In order to quantify these observations, the mean of the signal to noise ratio (S/N) in each sample in 5 consecutive MRI slices was measured. The results are illustrated in Figure B1 and Figure 2.5 in Section 2.3.2.

| Samples | Mean signal to noise ratio | Standard deviation (S.D.) |
|---|---|---|
| Microbeads | 1 | 0.57 |
| Activated cells (TNFα 50ng/ml) | 24 | 2.23 |
| Activated cells (TNFα 10ng/ml) | 60 | 3.33 |
| Activated cells (TNFα 1ng/ml) | 101 | 6.47 |
| PBS | 134 | 4.63 |
| Unactivated bAECs | 129 | 4.53 |
| Unactivated bAECs with antibodies and microbeads | 115 | 4.73 |
| Agarose | 126 | 0.83 |

**Fig. B1. The values of signal to noise ratio of MRI of cell phantom.**

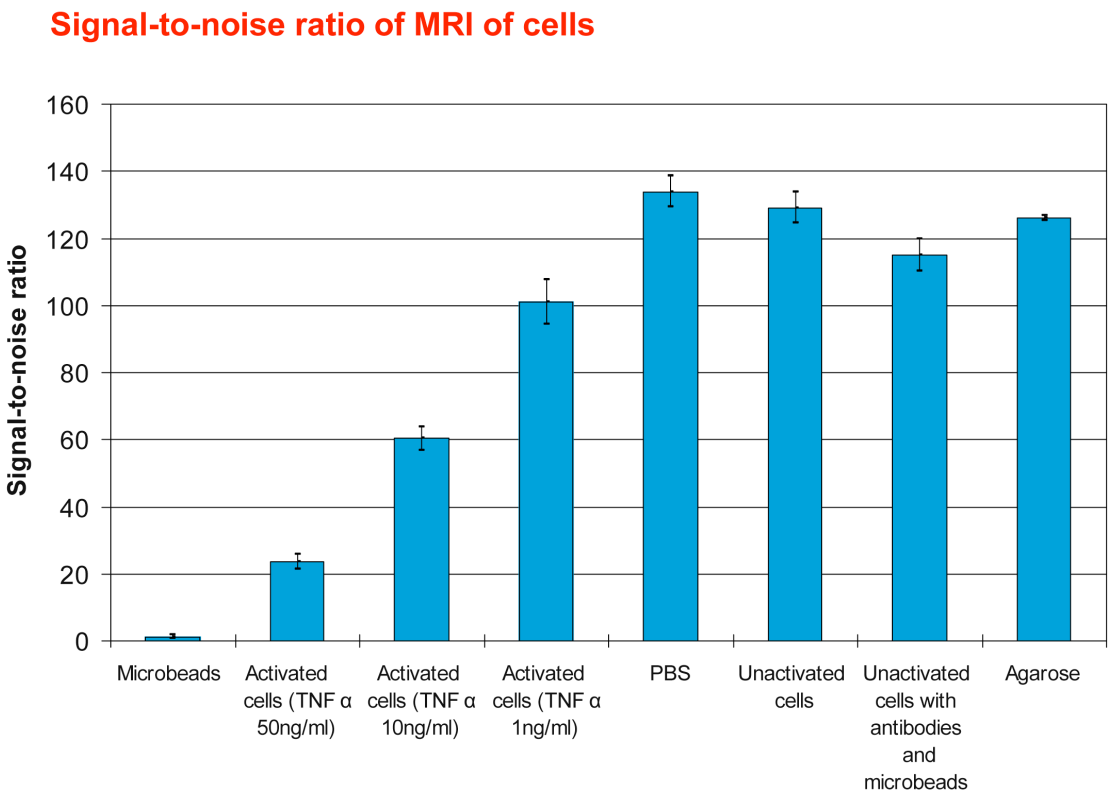



**Fig. 2.5 Signal-to-noise ratio of cell phantom MRI.** The S/N in streptavidin microbeads, positive control, was the smallest amongst all the samples. The activated cells stimulated by higher concentration of TNFα produced a lower S/N. By contrast, the negative controls: 1) PBS, 2) unactivated bAEC, and 3) unactivated bAEC added with biotinylated antibodies and microbeads produced high S/N.

The Image J software quantifies the “signal” in each sample by measuring its level of brightness or darkness. The darkest sample will give the smallest value as measured by Image J, and vice versa, the brightest sample will give the largest value. Therefore, in this study, the iron (microbeads), as a positive control, appears to be black (i.e. the darkest amongst all samples) in T2 spin echo sequence, giving the lowest level of brightness, hence the smallest “signal” value measured by Image J. The background noise was also measured by Image J. The concept is illustrated in Figure B2.



| Samples | Microbeads | Inflammed endothelial cells by TNFα 50ng/ml | Inflammed endothelial cells by TNFα 10ng/ml | Inflammed endothelial cells by TNFα 1ng/ml | Unactivated cells with biotinylated antibodies & microbeads | Agarose | Unactivated cells | PBS |
|---|---|---|---|---|---|---|---|---|
| | Positive Control | | | | ← Negative control → | | | |
| Signal value measured by Image J | 1 | 24 | 60 | 101 | 115 | 126 | 129 | 134 |
| Background noise value measured by Image J | 1 | 1 | 1 | 1 | 1 | 1 | 1 | 1 |
| Signal to Noise Ratio (S/N) Calculated | 1/1 = 1 | 24/1=24 | 60/1 = 60 | 101/1 = 101 | 115/1 = 115 | 126/1 = 126 | 129/1 = 129 | 134/1 = 134 |

**Fig. B2. Signal-to-noise ratio of cell phantom MRI.** The "signal", or the level of brightness or darkness, in each sample was quantified by Image J. The iron (microbeads), as a positive control, appears to be black (i.e. the darkest amongst all samples) in T2 spin echo sequence, giving the lowest level of brightness, hence the smallest "signal" value measured by Image J. On the contrary, PBS appears to be white (i.e the brightest amongst all samples), giving the highest level of brightness, hence the highest "signal" value measured by Image J. The background noise was also measured by Image J. Hence, the S/N in streptavidin microbeads, positive control, was the smallest amongst all the samples. The activated cells stimulated by higher concentration of TNFα produced a lower S/N. By contrast, the negative controls: 1) PBS, 2) unactivated bAEC, and 3) unactivated bAEC added with biotinylated antibodies and microbeads produced high S/N.

The S/N in microbeads control was 1, the smallest amongst all the samples. This was consistent with the observation that the microbeads control appeared to be the darkest amongst all samples. The activated cells stimulated by higher concentration of TNFα produced a lower S/N. The S/N in bAEC stimulated by 50ng/ml of TNFα was 24, the smallest S/N amongst the three concentrations used. This was followed by the bAEC stimulated by 10ng/ml of TNFα, whose S/N was 60. The bAEC stimulated by 1ng/ml of TNFα produced the highest S/N, i.e. 101, amongst the three concentrations used. These S/N also confirmed the previous observations that the bAEC stimulated by 50ng/ml TNFα appeared to be dark grey; those stimulated by 10ng/ml TNFα appeared

to be grey and those stimulated by 1ng/ml TNFα appeared to be light grey. As for the controls, the S/N of the PBS was 134, the highest amongst all the samples. This was followed by the unactivated bAEC and the agarose block, whose S/N were 129 and 126 respectively. These values were consistent with the previous observations that the PBS, the unactivated cells and the agarose block all appeared to be the brightest samples. The S/N of unactivated cells added with biotinylated antibodies and microbeads was 115, which could be due to a very small degree of non-specific binding by the biotinylated antibodies and non-specific magnetic labelling by the microbeads. Hence, tinge of grey colour was observed in Figure 2.4.

The higher concentration of TNFα used to activate the bAEC, the greater levels of E-selectin and VCAM-1 expression on these cells. Therefore, greater amount of streptavidin microbeads were bound to the biotinylated anti-E-selectin and anti-VCAM-1 antibodies. Hence, greater signal loss was detected by MRI and lower S/N in bAEC activated by higher concentration of TNFα. In addition, concomitant immunocytochemistry was performed and the results were consistent with those of MRI of cell phantoms. Greater level of E-selectin and VCAM-1expression were observed on the activated bAEC stimulated by higher concentration of TNFα in Figure 2.3 in Section 2.3.1.